THE UNIVERSITY *of* EDINBURGH

Magnetotelluric studies of the crust and upper mantle in a zone of active continental breakup, Afar, Ethiopia

Nicholas Johnson

THE UNIVERSITY
of EDINBURGH

Thesis submitted in fulfilment of
the requirements for the degree of
Doctor of Philosophy
to the
University of Edinburgh — 2012

Declaration

I declare that this thesis has been composed solely by myself and that it has not been submitted, either in whole or in part, in any previous application for a degree. Except where otherwise acknowledged, the work presented is entirely my own.

Nicholas Johnson

September 2012

Abstract

The Afar region of Ethiopia is slowly being torn apart by the Red Sea, Gulf of Aden and Main Ethiopian rifts which all meet at this remote, barren corner of Africa. Prior to rifting, volcanism probably started here some 30 million years ago, marked by the arrival of the Afar mantle plume and subsequent eruption of kilometres thick flood basalts. To the north and east the Red Sea and Gulf of Aden rifts have already progressed to become sea-floor spreading centres where new oceanic crust is produced. Active spreading on the Red Sea rift takes a landward step west into Eritrean Afar at approximately 15°N, after which divergence between the Nubian and Arabian tectonic plates is localised into 60 km long, 20 km wide magmatic segments that undergo periodic rifting cycles. This part of Afar is a unique natural laboratory where the process of transition from continental rifting to sea floor spreading can be studied. In September 2005 a dramatic rifting episode began on one such segment of the Red Sea rift in Afar (the Dabbahu magmatic segment), whereby a 60 km long dyke containing an estimated 2.5 km^3 magma was intruded in just two weeks, allowing opening of up to 8 m. Since then a further 13 smaller dykes have been intruded, some with fissural eruptions of basaltic lava. Subsidence observed via geodetic observations can only account for a small fraction of the magma supply required to inflate the dykes, suggesting a deep crustal or upper mantle source must exist.

The magnetotelluric (MT) method is a passive geophysical technique, used to

probe the Earth to reveal subsurface conductivity. The presence of fluids can dramatically increase conductivity by orders of magnitude making the MT method ideally suited to detecting them. MT data collected from 22 sites on profiles near to and crossing the active rift are analysed and interpreted in conjunction with seismic and petrological constraints. They reveal for the first time, the existence of both a mid to lower-crustal magma chamber directly below the rift, and an off-axis zone of partial melt well within the mantle. The volume of melt contained within the crust and upper mantle below the Dabbahu segment is estimated to be at least 350 km^3; enough to supply the rift at current spreading rates for almost 30 thousand years, assuming that both melt containing regions supply the rift. Vast amounts of highly conductive material, suggesting the existence of pure melt in places, are also required in the shallow crust close to Dabbahu volcano which lies at the northern end of the segment.

Further data collected on the currently inactive Hararo segment which is the next one to the south of Dabbahu, show a smaller zone of partial melt that appears to be pooling at the Moho, inferred seismically to be at about 22 km, but little or no melt is required within the mid-crust. The minimum amount of melt estimated to be contained here is just 21 km^3; an order of magnitude less than on the Dabbahu segment, but similar to estimates for melt within the crust found below the rift axis in the continental Main Ethiopian rift. This, along with other morphological evidence, suggests that this rift segment is less mature than the Dabbahu segment to the north, rather than it simply being at a different stage of a rifting cycle.

A wide spread layer of highly conductive sediments up to 2 km thick has been imaged at most locations. This was unexpected on the Dabbahu segment where the surface of the Earth is dominated by heavily faulted basalts erupted from fissures, which are seen as a resistive uppermost layer several hundred metres thick. The high conductivity of the sediments is attributed to high heat flow and the presence of brines.

Acknowledgements

First and foremost I would like to thank Prof. Kathy Whaler, my primary supervisor, for her continued support, efficiency in reading my work and for providing invaluable feedback and ideas. I am grateful for Kathy's patience at times when progress has been slow. My unofficial second supervisor, Sophie Hautot, has also been a great help particularly with providing codes and advice to help with data processing and plotting, and giving me the opportunity to work at the University of Brest for 3 months during which I learnt a lot and had great fun. Among others, Sophie added greatly to the cheerful atmosphere and smooth running of fieldwork, even when things were not going to plan.

On the subject of fieldwork, I would also like to thank Graham Dawes for his endless work in developing and preparing equipment and Mohammednur Dessisa for logistical preparatory work in Addis Ababa and helping us to communicate with guards, policemen, pastoralists and anyone else we came across in Afar. We were all very thankful of his ability to defuse tricky situations. Shimeles Fisseha, Tigistu Haile and Alf Ball were also very helpful in the field and Elias Lewi's time spent seeing to paper work for the import and export of our equipment was invaluable. Danny and Merron did an excellent job of seeing to our every need at camp and Dereje at Ethioder Tour and Travel was very accommodating when it came to our, sometimes complex, requirements for vehicles. Our drivers, in

particular Workneh, worked beyond their call of duty in showing us around and helping in the field.

I have been very lucky to have worked as a part of a diverse interdisciplinary group; the Afar Rift Consortium. I would like to thank all members who have regularly attended our lively meetings, and helped make them useful, informative and relaxed. Many people have been very generous in sharing their ideas and data sets. I would also like to thank my fellow PhD students in the School of GeoScience at the university of Edinburgh for making my time there enjoyable.

I would like to thank Dave Farbrother for two years of hilarious A-level geology classes that inspired me to study the subject at degree level. My parents have been supportive and interested in my work, for which I am grateful. My brother Dan and his wife Charlotte, have provided me with many an opportunity to escape Edinburgh and PhD life for which I have been very appreciative! I would like to thank my Auntie Ute for setting me a deadline to get this thesis written (and I look forward to claiming my prize from our small wager!). Finally I would like to thank Maddy for enduring the ups and downs and making lots of cups of tea, and without whom I would not be where I am today.

Contents

List of Tables

List of Figures

Chapter 1

Introduction

The Afar region of Ethiopia is a triple junction where three divergent tectonic plate boundaries meet. To the north and east are the sea floor spreading centres, the Red Sea and Gulf of Aden, and to the south is the northern most part of the East African Rift system, the Main Ethiopian Rift. Afar is triangular in shape covering some 60 thousand km^2 of low-lying (sometimes below sea level) land, mostly in Ethiopia but also including Djibouti and parts of Eritrea and Somalia. At its western and southern margins are large border faults where altitude rapidly increases into the cool Ethiopian highlands from the hot Afar depression. 30 Ma old flood basalts dominate the geology of the highlands, the eruption of which marks the beginning of volcanism in the area and also the probable arrival of the Afar mantle plume (Menzies et al., 1992; Ebinger and Sleep, 1998; Rochette et al., 1998; Ukstins et al., 2002; Wolfenden et al., 2005). Subsequent to the emplacement of the flood basalts, the Afar triangle has formed by stretching and thinning of continental crust, and the formation of new crust via magmatic processes (Hammond et al., 2011).

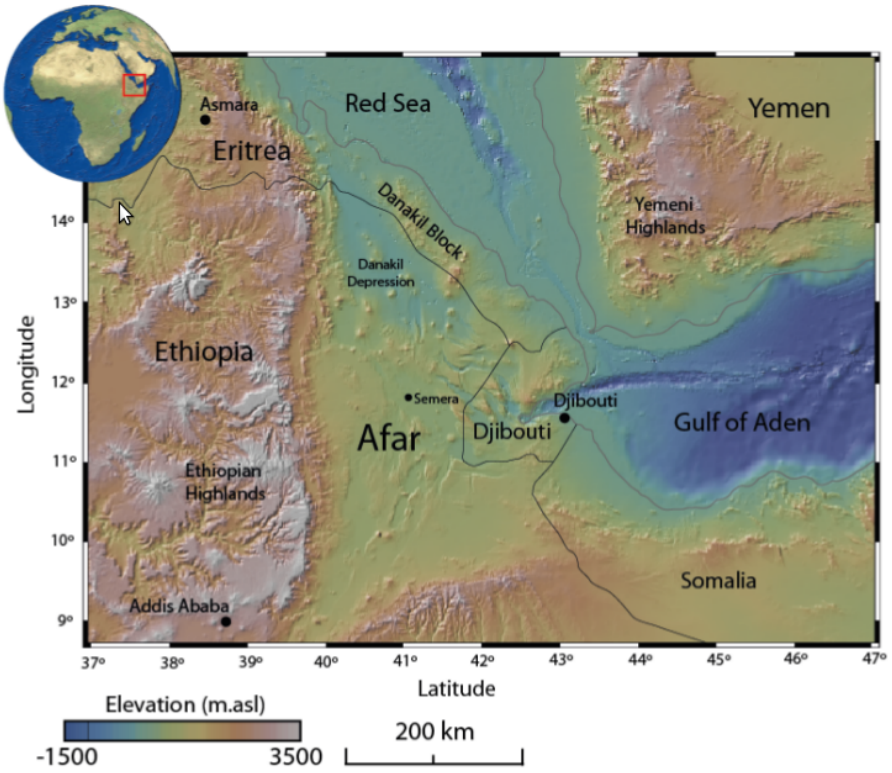

Figure 1.1: Topography map of Afar and surrounding regions. From Ferguson (2011).

This thesis is a study of the sub-aerial part of the Red Sea arm of the triple junction in Afar, where strain rates of approximately 20 mm/yr are accommodated on focussed magmatic segments, with length scales not dissimilar to those observed at mature oceanic spreading centres such as the Mid Atlantic Ridge (Ebinger and Sleep, 1998). Volcano-tectonic activity on these typically 60 km long segments in Afar is periodic; stress is built up over periods of time of the order of 100s of years due to far-field spreading, which is then relieved by a combination of seismic and magmatic processes during rifting episodes lasting 5-10 years (e.g. Wright et al., 2006). One such rifting episode began in September 2005 on the Dabbahu magmatic segment and is ongoing today. Initially, a so-called mega-dyke was intruded into the subsurface along the entire 60 km long segment, allowing upto 8 m of opening and requiring up to 2.5 km^3 of magma to fill the dike (Wright et al.,

2006; Ayele et al., 2007; Ebinger et al., 2008). Geodetic observations reveal only a small amount of subsidence that could be attributed to the deflation of magma chambers from where the material was sourced; this can only account for approximately 0.5 km^3 of the magma injected (Wright et al., 2006; Grandin et al., 2009). Since the rifting cycle began, a further 13 smaller dykes have been intruded, several accompanied by fissural eruptions, and the majority of which have shown no associated deflation of magmatic sources (Hamling et al., 2009; Ferguson et al., 2010), leading to speculation regarding the whereabouts of the 'missing magma' and the magmatic plumbing system of the rift. It is possible that some of the apparent lack of deflation of magma chambers in the crust can be accounted for by magma expansion caused by gas exsolving as the pressure in the chamber drops and/or the higher stiffness of the magma chamber in comparison to tensile fractures associated with dyke injection (Keir et al., 2009). Erupted products have fairly primitive, dry basaltic compositions although there are several large volcanoes which show more varied geochemistry; notably Dabbahu volcano at the northern end of the segment (Field et al., 2012), and the off-axis Badi volcano situated on a line approximately level with the middle of the segment (Ferguson, 2011), both of which have some rhyolitic lavas.

This thesis documents the collection, processing, modelling and interdisciplinary interpretation of magnetotelluric (MT) data from 43 sites, which provide information on subsurface electrical resistivity, with the primary aim of assessing magma supply and storage beneath the Dabbahu magmatic segment, and its less active counterpart immediately to the south, the Hararo magmatic segment. Controlled source transient electromagnetic (TEM) data were also collected at the majority of the sites to provide information on the very shallow subsurface resistivity. By studying both an inactive and an active rift segment it is possible to draw conclusions regarding rifting cycles. By comparing results to those from mature oceanic

spreading centres like the East Pacific Rise or Mid-Atlantic Ridge, and from continental rifts such as the Main Ethiopian rift it is possible to develop theories regarding the process of transition from continental to oceanic spreading.

The MT method has been developing since the early 50s as a method of mapping the conductivity structure of the subsurface (Cagniard, 1953). The presence of most fluids dramatically increases the conductivity of any medium, and so the MT method is very well suited to the study of magma-rich environments. Formulated around Maxwell's equations governing electromagnetic (EM) induction, the method involves recording naturally occurring variations of electric and magnetic fields at the surface of the Earth. These penetrate the subsurface inducing (telluric) currents whose strength and depth is dependent on electrical conductivity, which can then be deduced by studying complex ratios of the EM fields (Simpson and Bahr, 2005). The depth of penetration and hence the depth from which information can be recovered is dependent on the period of the measured field variations, so by simply recoding for longer amounts of time the depth of the investigation can be increased. The method has been successfully implemented to investigate the conductivity at mantle depths (e.g. Park et al., 1996; Baba et al., 2006a), and has been applied to many volcanic regions where zones of partial melt are of interest (e.g. Whaler and Hautot, 2006; Brasse and Eydam, 2008; Pommier et al., 2008; Navin et al., 1998). High conductivity values that are interpreted as being caused by the presence of partial melt can be used to estimate volumes of melt contained within the anomaly (e.g. MacGregor et al., 1998). This is a three stage process; (1) the conductivity of pure melt is estimated using geochemical constraints on composition, pressure and temperature (Pommier and Le-Trong, 2011); (2) this estimation is used in conjunction with the actual conductivity of the subsurface ascertained from the MT survey to calculate the fraction of melt within the otherwise solid rock matrix (Waff, 1974); (3) assumptions are made regarding the three-dimensional geometry of the anomaly so that its volume can

be calculated and the melt fraction deduced from steps (1) and (2) is used to calculate the volume of melt present.

This project has been carried out as a part of an interdisciplinary group called the Afar Rift Consortium. As such the rifting cycle that began in 2005 and the general morphological and subsurface structure of the rift is being studied using many techniques (seismology, geodesy, geochemical analysis of erupted lavas, remote sensing and observations of the rift architecture from field campaigns). This is the first such rifting episode to have occurred where modern geodetic data have been available (GPS measurements and interferometric synthetic aperture radar (InSAR)). Chapters 2, 6, 7 and 8 of this thesis discuss many aspects of the findings of other members of the consortium and where possible build up a picture of the structure of the subsurface and mechanics of the rifting using their results as well as those from this study. Of particular importance are constraints from seismic studies (e.g. Hammond et al., 2011; Belachew et al., 2011; Keir et al., 2011) and petrological investigations (e.g. Ferguson, 2011).

1.1 Layout of this thesis

- Chapter 2 outlines the tectonic history of Afar and the three rifts of which it comprises, gives details of the events leading up to and since the rifting cycle began in 2005 and presents a review of the research that has been carried out to date in the area, also comparing it to other active spreading centres around the world.

- Chapter 3 is a review of the MT method with derivation of the governing diffusion equations and details regarding how the data are processed and assessed with respect to dimensionality and distortion in this study.

- Chapter 4 gives details of the site locations and field procedures, before

presenting the processed data with analysis of its dimensionality and distortion.

- Chapter 5 includes a brief review of current inversion schemes for MT data, mostly focusing on modelling in 2 dimensions. Then, a suite of models for the data collected in Afar are presented with detailed discussion regarding sensitivity, the fit of the model responses to the data and non-uniqueness.

- Chapter 6 attempts to integrate the findings of the MT survey with those from seismic studies in the area. Particular attention is paid to looking at shallow seismic anisotropy and the 2-dimensionality that is evident in the MT data, before looking at evidence for melt in the crust and mantle inferred seismically.

- Chapter 7 has two parts. First, constraints from geochemistry are used to estimate the conductivity of pure melt, then a melt fraction is calculated to match the conductivity values inferred from the MT models. Finally, end-member assumptions are made about the 3-dimensional geometry of the zones of partial melt from which actual volumes melt can be estimated. In the second part of the chapter, comparisons are made between the volumes, locations and geometries of melt within the crust and upper mantle at the two segments studied in Afar and those at other spreading centres around the world. The implications for time-scales of rifting cycles and the transition from continental to oceanic rifting from our study are discussed.

- Chapter 8 summarises the findings of this study and synthesises them with the work of other members of the Afar rift consortium, before making recommendations for further work.

Chapter 2

The Afar region of Ethiopia

2.1 Introduction

This chapter gives an overview of the history of rifting at the Afar triple junction, and puts forward some established hypotheses explaining the range of possible forces which are driving the tectonic activity. Literature regarding the structure of the crust and upper mantle in Afar is reviewed. The sequence of events since the present day volcano-seismic crisis began on the Manda-Hararo rift segment of Afar is given, drawing on the already published results from various disciplines (seismic, petrological and geodetic studies) within the Afar Rift Consortium. Other examples where the conductivity structure below active spreading centres has been observed will also be discussed along with the characteristics of rifting in Iceland which is somewhat analogous to Afar.

2.2 Tectonic setting

The Afar region of Ethiopia contains the triple junction where the Nubian, Somalian and Arabian tectonic plates meet. All three plate boundaries of the triple junction are divergent with the continental-type Main Ethiopian rift (MER) to the south and the Red Sea and Gulf of Aden rifts to the north and east respectively (Figure 2.1). The MER is the northern extension of the East African rift system between Somalian and Nubian plates (Barberi et al., 1972). The Afar triangle which contains the triple junction is a low lying depression consisting of highly stretched crust containing a mixture of heavily faulted and intruded crystalline pre-Cambrian basement and proto-oceanic crust with some blocks of stable continental material, namely the Danakil microplate in NE Afar (e.g. Hammond et al., 2011). Continental rifting has dominated the geological evolution of Eastern Africa for the past 300 Ma (e.g. Lambiase, 1989); however, the present day tectonic environment around Afar, which is the topic of this thesis, only started to develop in mid-Tertiary times.

The onset of volcanism in north-west Ethiopia occurred before the Afar depression formed with the emplacement of flood basalts which now form high plateaux across western and south-eastern Ethiopia and in Yemen (i.e. on all three sides of what is now the Afar triangle). The basaltic pile on the plateau region to the west of the Afar triangle is up to 2000 m thick (although some authors estimate that as much again may have been eroded (Ukstins et al., 2002)) and has been consistently dated to 30-29 Ma (Rochette et al., 1998; Hofmann et al., 1997). Dating of rock samples and magnetostratigraphy both provide strong evidence to suggest that, like most other basaltic trap provinces, the period of emplacement for the bulk of the material was very small (<1Ma) (Rochette et al., 1998; Hofmann et al., 1997). Rochette et al. (1998) estimate the total volume of basalt to

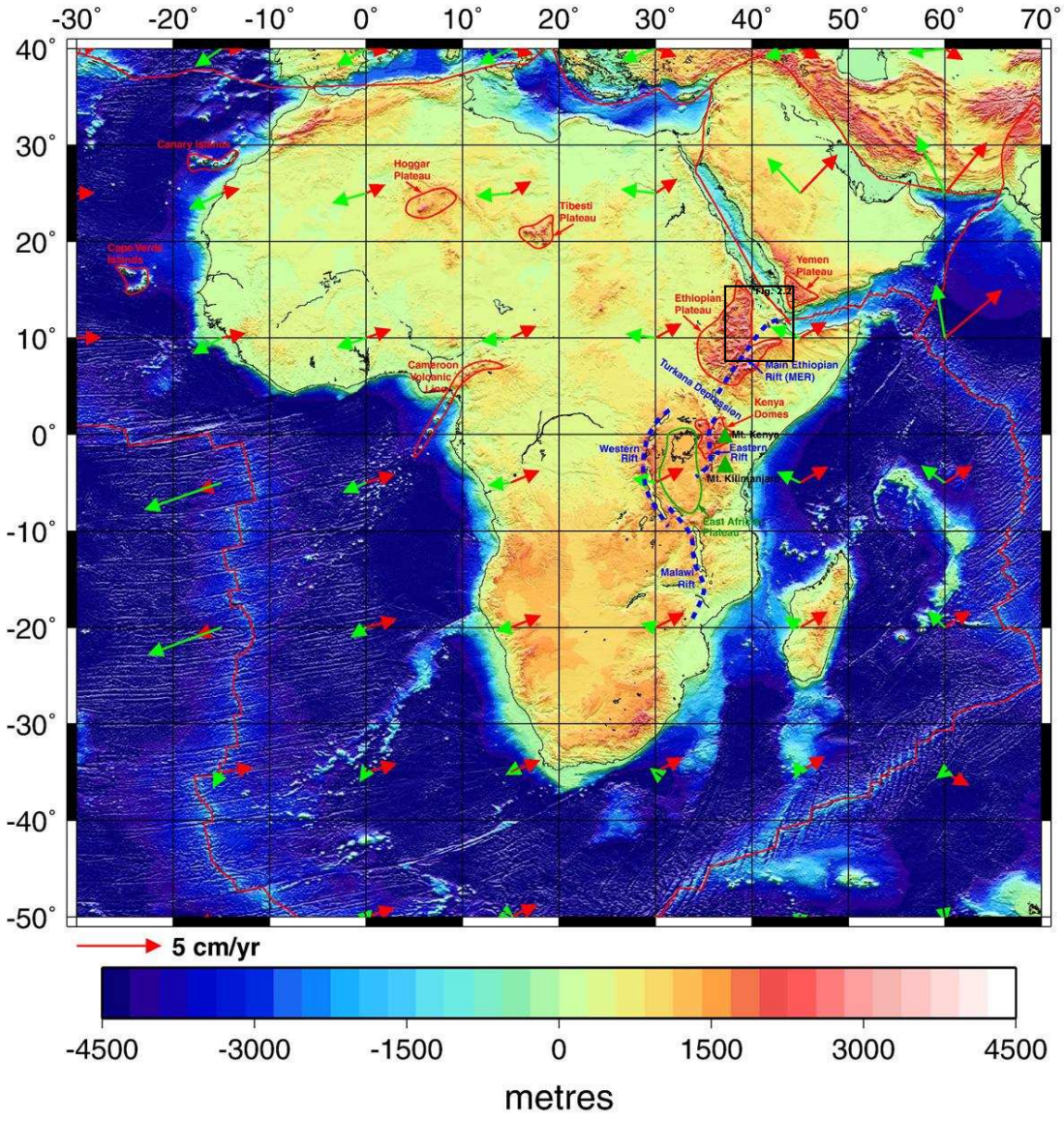

Figure 2.1: Tectonic structures of the African continent and surrounding oceans. The divergent Nubian, Arabian and Somalian plates are shown with absolute velocity vectors referenced to Pacific hotspot tracks (green arrows) and Indo-Atlantic reference frame (red arrows). Reproduced from Forte et al. (2010).

be of the order of 10^6 km^3. There is a systematic younging in the age of Ethiopian volcanics from north to south (Ukstins et al., 2002), however some authors report samples as old as 45 Ma in southern Ethiopia (e.g. Ebinger et al., 1993). Since the eruption of the flood basalts, volcanism in Afar has been ongoing to the present day with 2 distinct hiatuses between 25 and 20 Ma and again from 10.6 to 3.2 Ma. Ukstins et al. (2002) propose that they are related to the onset of rifting between Arabia and Nubia and then the transition to sea floor spreading in the Red Sea respectively.

Rifting in the Gulf of Aden and parts of the Red Sea north of 14°N progressed to sea floor spreading at 16.5 Ma and 4 Ma respectively (d'Acremont et al., 2005; Bonatti, 1985). Below 14°N on the Red Sea arm, rifting is offset subaerially into Afar jumping to the west side of the Danakil microplate (Figure 2.2). McClusky et al. (2010) show that strain accommodation moves from the Red Sea on the east side of the Danakil block in to Afar on the west side with a more or less linear transition between 16°N and 13°N. This therefore results in an anticlockwise rotation of the Danakil block which is estimated to be 1.5°/Ma (Vigny et al., 2007). From here down to the junction with the MER and Gulf of Aden, rifting is segmented into ∼60 km long, ∼10 km wide zones characterised by chains of aligned fissural flows, basaltic cones, stratovolcanoes and shallow seismicity where the majority of strain is accommodated magmatically (Ebinger et al., 2008, and references therein). The length scales of these segments are not dissimilar to those found at slow spreading oceanic ridges such as the Mid-Atlantic (Hayward and Ebinger (1996)). The northern most segments (Erta' Ale, Tat' Ale and Alyta) are topographically high (up to 700 m) consisting of axial volcanic ridges (Rowland et al., 2007). Segment terminations are recognised by topographic lows with faults curving from one segment into the next. Note that transform faults are not seen (Hayward and Ebinger, 1996). Further to the south is the Manda-Hararo

rift zone, comprising of the active Dabbahu magmatic segment (DMS) and the currently quiet Hararo magmatic segment (HMS) (see Figure 2.2), both of which are charactarised by a 35 km wide depression rather than the broad highs seen in the north (Rowland et al., 2007). These two magmatic segments are the focus of this thesis.

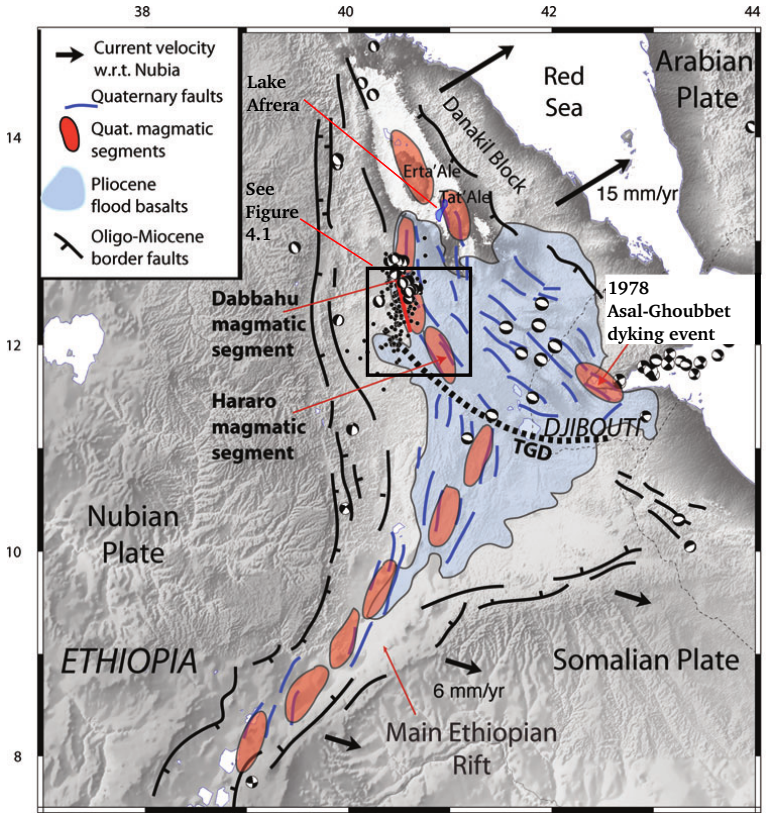

Figure 2.2: The Afar triangle showing present day magmatic segments. TGD= Tendaho Goba'ad Discontinuity. Arrows show plate motions relative to stable Nubia and focal mechanisms are from Global CMT database. Reproduced from Ebinger et al. (2008).

The appearance of the Ethiopian flood basalts around 30 million years ago is often presumed to mark the arrival of a mantle plume head (the Afar plume) at the crust (Ukstins et al., 2002; Menzies et al., 1997; Pik et al., 1998). The timing of the onset of rifting in Afar relative to the flood basalts is obviously key to differentiating between possible mechanisms for rift initiation, assuming that

the arrival of the flood basalts marks the impingement of the plume on the crust. Most authors suggest that the start of rifting was probably contemporaneous with the flood basalts, but that the main explosion of rifting did not take place until later at about 25 Ma and later still (approximately 15 Ma) further south in the Main Ethiopian Rift (Davidson and Rex, 1980; Wolfenden et al., 2005; ArRajehi et al., 2010) thus supporting a model of plume driven rifting. Simple evidence exists to support this in that the high flood basalt plateaux exist to the north of Afar (in Yemen) and to the south-west with the vastly stretched and thinned Afar depression between them, showing that the flood basalts were erupted first (marking the arrival of the plume), then later rifted apart. Wolfenden et al. (2005) propose a three stage model of rift progression in the southern Red Sea arm of the triple junction starting with basin formation bounded by large offset boarder fault systems from 29 to 26 Ma. This was accompanied by the eruption of rhyolites at volcanic centres located along the boarder faults. 25 to 20 Ma saw the localisation of strain to narrower zones containing basaltic flows and minor faults which is how the rifting continued until about 7 Ma. Thereafter, in the final and presently active mode of rifting in this area of Afar the majority of strain is accommodated by dyke injection and near surface faulting with occasional fissural eruptions.

2.3 Plate motions and driving forces

As the Arabian plate has moved to the north-east relative to Nubia and Somalia, forming the Afar triangle, the triple junction itself has moved to the north-east with it. Consequently the north-eastern most part of the MER cuts through old Red Sea and Gulf of Aden rift segments until it meets the present day Red Sea and Gulf of Aden rifts at the Tendaho-Goba'ad discontinuity (Figure 2.2, TGD). The TGD is fault scarp separating the E-W extending MER to the south from the

NE-SW extension to the north resulting from the north-eastward drift of Arabia (Ebinger et al., 2008).

Relative motions between the Nubian, Somalian and Arabian tectonic plates are constrained by GPS observations, plate reconstructions and global models of plate motions, and are again comparable to those found at slow-spreading ocean ridges. Far field spreading rates from GPS measurements between Nubia and Arabia, Arabia and Somalia, and Nubia and Somalia are approximately 20 mm/yr, 13 mm/yr and 4 mm/yr respectively (Bendick et al., 2006; McClusky et al., 2010; Vigny et al., 2007). Prior to the break-up of Arabia and Africa their rate of motion together, with respect to Eurasia, was between 20 and 30 mm/year, resulting in the closing of the Tethys ocean (Figure 2.3). When the Red Sea rift formed at 25 Ma, opening rates were 10-16 mm/yr, representing a deceleration of Africa with respect to Eurasia whilst Arabian motion remained constant (McQuarrie et al. (2003)).

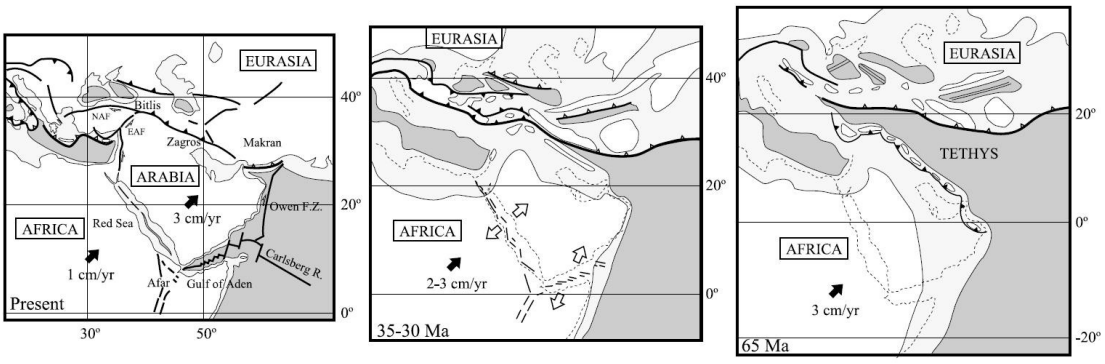

Figure 2.3: Tectonic evolution of the final stages of the closing of the Tethys ocean. Reproduced from Bellahsen et al. (2003).

Tomographic modelling of teleseismic signals passing through the mantle below Africa has shown a low velocity anomaly from the core-mantle boundary below southern Africa stretching north east to the top of the lower mantle with a complex 3D shape (Ritsema et al., 1999; Zhao, 2001; Montelli et al., 2006; Bastow et al.,

2008; Forte et al., 2010). Known as the African superplume, the northwards tilt of the anomaly is possibly caused by shear in the mantle from the northward migration of the African continent since the breakup of Gondwanaland[1] (Ritsema et al., 1999). It has been suggested that through heating of the lithosphere, the superplume has led to the development of the African superswell (Nyblade and Robinson, 1994) - a belt of anomalously high topography from South Africa to the Red Sea which exists without continental collision - the mechanism by which all other zones of such widespread elevated topography form. As well as elevated topography, East African plateaux are also characterised by long-wavelength negative Bouguer anomalies (Ebinger et al., 1989). These can be explained in terms of dynamic compensation, where the high plateaux are supported by hot upwelling mantle of low density (Ebinger et al., 1989). Globally, several other slow velocity zones exist throughout the mantle originating at the core-mantle boundary - classically, those associated with Hawaii, Iceland (although there is some controversy regarding the depth extent of the anomaly in Iceland (e.g. Foulger and Anderson, 2005)) and the volcanic islands of the South Pacific (Zhao, 2001) - all breaching beneath oceanic plates. None of these show the skewed geometry that the African Superplume exhibits - perhaps a reflection on the shearing power of a drifting continental plate which is thicker and has topography on the base of its lithosphere in comparison to an oceanic plate. Many authors have shown that the upper mantle below northern Ethiopia is also characterised by slow seismic velocities caused by the existence of the Afar mantle plume which is often considered to be a continuation of the African superplume (Benoit et al., 2006; Bastow et al., 2008). Slow seismic velocities of this sort are usually assumed to be caused by abnormally high temperatures, although other factors such as changes in chemical composition or partial melting, for example, can affect seismic velocities and cannot be directly differentiated.

[1] A Paleozoic super-continent

Naturally many authors have directly linked the Afar plume to the African superplume, some suggesting that it is one of several plumes or plumelets in East Africa (e.g. Montelli et al., 2006; Meshesha and Shinjo, 2008) others suggesting that the distribution and timing of magmatism and uplift throughout East Africa can be explained with the existence of a single plume (Ebinger and Sleep, 1998). Many continental rifts in their early stages are associated with the eruption of vast amounts of flood basalts forming large igneous provinces (LIPs) which are always linked to a thermal anomaly created by a nearby mantle plume (White and McKenzie, 1989; White, 1992; Courtillot et al., 1999). The initiation of rifting in Afar and the eruption of flood basalts there are undoubtedly linked to the existence of the Afar mantle plume (Ebinger and Sleep, 1998; Wolfenden et al., 2005; Dugda et al., 2007) although the extent of its influence today is debated (e.g. Rychert et al., 2012; Ferguson et al., 2012).

Of the forces which drive plate tectonics, several are considered important in the development of rifting around the Afar triple junction. ArRajehi et al. (2010) hypothesise that the driving force which initially caused Arabia to split from Nubia forming the Red Sea and Gulf of Aden rifts, is slab pull[2] from subduction associated with the closing of the Tethys ocean between Arabia and Eurasia (Figure 2.3). Further to this Bellahsen et al. (2003) add that stress is increased within subducting plates (ultimately leading to break up) where subduction is asymmetric. During closing of the Tethys ocean, subduction became asymmetric when the Arabian and Eurasian continents collided at the northern end whilst subduction of the Tethyan oceanic plate was still occurring further south. Bellahsen et al. (2003) conducted laboratory experiments to simulate the tectonic evolution described above and by Figure 2.3. They found that both a subduction zone locked asymmetrically by continental collision and a lithospheric

[2]Slab pull is the gravitational force exerted on a cold, dense, subducting oceanic plate as it sinks into the mantle below.

weakening (such as might be caused by the Afar plume) were required to create localised zones of extension similar to the Red Sea and Gulf of Aden rifts. Again, timing of events is critical to understanding cause and effect relationships. Some authors state that Arabian and Eurasian continental collision did not occur until as late as 10 Ma precluding it as a cause of continental rupture further south (e.g. McQuarrie et al., 2003), while others date the collision to be earlier than 25 Ma (e.g. Bellahsen et al., 2003). Either way, however, it is certain that the negative buoyancy-driven subduction of the Tethys oceanic plate created a tensional stress regime within the Afro-Arabian plate prior to breakup.

2.4 The structure of the crust and upper mantle in Afar

It is important to understand the geophysical constraints which can already be put on the structure of the lithosphere in Afar, particularly around the DMS, in order to make a consistent interpretation of the magnetotelluric data which are the subject of this thesis.

2.4.1 A seismological perspective

A simple three layer classification system of the crust in and around Afar was proposed by Prodehl and Mechie (1991) based on the results of seismic refraction surveys carried out in the 1970s and 80s (Berckhemer et al., 1975). This model consists of 'cover-rocks' (e.g. sediments, volcanics), upper crust and lower crust, with P-wave velocities of 2.2-4.5, 6-6.3 and 6.7-7.0 km s^{-1} respectively. Cover rocks are pervasive, up to 5 km thick in Afar, and can include large evaporite deposits the likes of which can be seen forming today around Lake Afrera to the

north east of the DMS (see Figure 2.2). Receiver function analysis uses arrival times of P waves, P-S wave conversions at the Moho and reverberations within the crust from teleseismic events to constrain both crustal thickness and the average ratio of P-wave to S-wave velocity (Vp/Vs) for the crust. Detailed modelling of receiver function waveforms at three seismic stations near the DMS support the model of Prodehl and Mechie (1991), showing between 3-4 km of cover rocks with substantial sedimentary layers (Hammond et al., 2011). The overall crustal thickness in Afar and the surrounding plateaux has been estimated using both the refraction surveys and receiver function analysis (See Figure 2.4). In the western south-eastern highland plateaux the crust is 35-40 km think, whilst in Afar it drops dramatically to 20-26 km thinning to just 16 km below magmatic segments in the Danakil depression of northern Afar where ground elevations drop to as much as 100 m below sea level (Hammond et al., 2011). At the currently active Dabbahu segment the crust is estimated to be 22-24 km thick. As mentioned previously the crust below the cover rocks can be split into upper and lower layers according to P-wave velocities (Prodehl and Mechie, 1991; Maguire et al., 2006; Hammond et al., 2011). The upper layer is variable in thickness from 20-25 km on the plateaux and in the MER, rapidly thinning to become virtually non existent in parts of central-northern Afar. It is interpreted as thinned Pan-African crystalline basement with proto-oceanic crust beneath magmatic segments (Maguire et al., 2006; Hammond et al., 2011). The lower crustal layer shows a similar trend of thinning into Afar and to the North but to a lesser extent varying from approximately 20 km in the highland to 8 km in northern Afar. It has been suggested that this seismological unit represents the emplacement of magmatic material in the lower crust sometimes referred to as under-plating (Maguire et al., 2006; Hammond et al., 2011). Below the Moho, the mantle shows relatively low P-wave velocities which can ultimately be linked to the Afar/African super-plume system and are associated with a thermal anomaly (see Section 2.3) (Bastow et al., 2008). Guidarelli et al. (2011) have carried out tomographic modelling of the crust

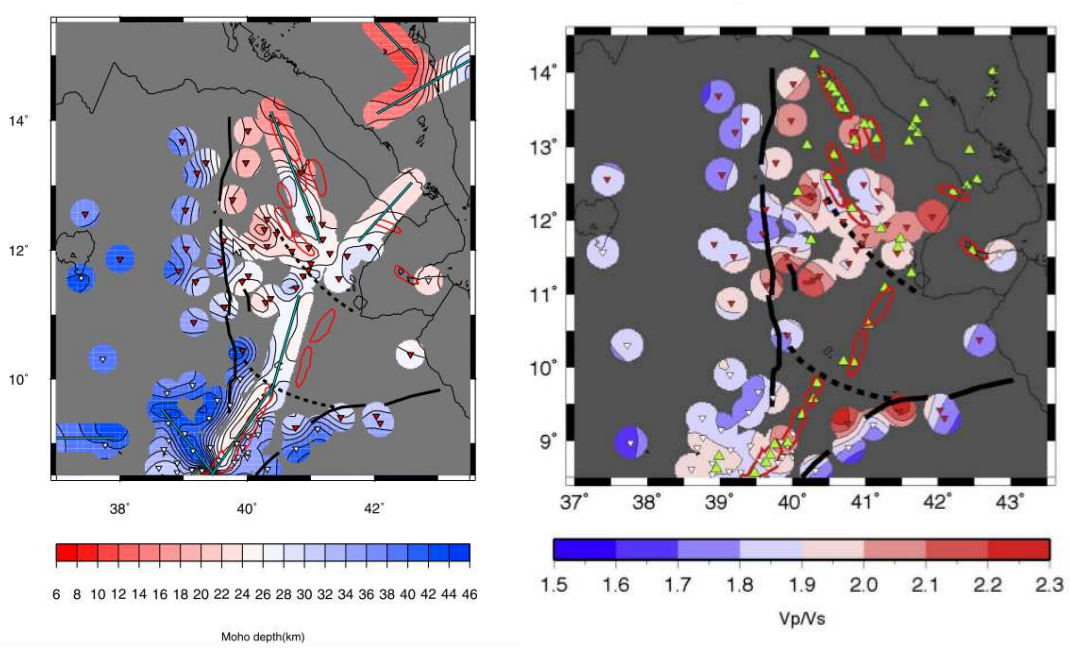

Figure 2.4: Crustal thickness (left) and Vp/Vs (right) in Ethiopia from receiver function analysis. Inverted triangles indicate the location of seismic stations. Green triangles show the location of active volcanoes. Black lines show the border faults separating Afar from the western and southeastern plateaus. Quarternary magmatic segments are shown by red lines. From Hammond et al. (2011)

using surface waves which are sensitive to the seismic velocy of the upper 30 km of the lithosphere. They find low velocity anomalies centred on currently active magmatic segments which are interpreted as regions of partial melt within the lower crust.

Vp/Vs ratios are used to discriminate between different rock types and they are particularly sensitive to the presence of fluids - unlike P-waves, S-waves are not transmitted through liquids hence high crustal Vp/Vs is indicative of some amount of a fluid phase within a medium. Typical crustal Vp/Vs are 1.75-1.85, with the higher values representative of mafic oceanic crust (Christensen, 1996). Bulk Vp/Vs for the crust in Afar and the MER are consistently above 1.9 (see Figure 2.4) (Hammond et al., 2011), requiring some fluid content in the crust, the obvious candidate being partial melt. Placing bounds on the quantity of melt is difficult as seismic velocities are also dependent on other factors (Hammond et al., 2011, and references therein). In several areas of Afar, generally below active volcanic systems or in some cases abandoned magmatic segments, Vp/Vs is considerably greater than 2.0.

Seismic anisotropy is another diagnostic tool used to discern different fabrics within the crust and mantle. It refers to a directional dependence in seismic velocity which causes S-waves to be split into two propagating waves aligned with the fast and slow axes of the anisotropy. On arrival at a seismic station, separate arrivals of the two modes are detected and the time lag between them and their orientation are used to estimate the strength and direction of the anisotropy. Studies have been conducted in Afar using SKS phase teleseismic waves which sample the mantle and crust (Hammond et al., 2010, 2011) and also using energy from local earthquakes which samples the upper 5-10 km of the crust alone (depending on hypocentral depth) (Keir et al., 2011). Studies using variations in different modes of surface wave have also been carried out in the MER which can be used to discriminate between causative fabrics (Bastow et al.,

2010). According to Bastow et al. (2010) three such fabrics exit below the MER as shown schematically in Figure 2.5: periodic layering of seismically fast and slow material in the upper 10 km, oriented melt pockets (OMP) in the lower crust and upper mantle, and lattice preferred orientation (LPO) predominantly of olivine crystals in the upper mantle and below. The mantle anisotropy below most of northern Ethiopia in oriented in a NE-SW direction parallel to the opening of the MER but seemingly uncorrelated with the opening directions of the Red Sea or Gulf of Aden. This has led to the suggestion that the anisotropy at mantle depths is predominantly controlled by mantle flow associated with the Afar mantle plume and African super-plume (Bastow et al., 2008). However Gashawbeza et al. (2004) argue that this is not the case because there is no radial flow observed where the plume reaches the lithosphere, and that instead the seismic anisotropy is largely caused by Proterozoic fabrics which are a legacy of the accretion of the Mozambique belt.

In Afar, shear wave splitting from local events relating to the shallow crust shows considerable variation in magnitude and direction which seems to be correlated with strain related near surface structures like faults (Keir et al., 2011). Close to magmatic centres or border faults at the Highland-Afar boundary, large magnitude, rift parallel anisotropy is observed. On the western highland plateau the magnitude is much smaller and the direction is uncorrelated to present day tectonics, instead probably reflecting metamorphic basement foliation (Keir et al., 2011). Interestingly some measurements made at stations just to the west of the DMS (on the MER side of the TGD) show very similar results to those of the western highland plateau which contrast sharply with those made within the DMS itself. This is perhaps evidence for small unaltered blocks of continental crust within the highly deformed Afar crust.

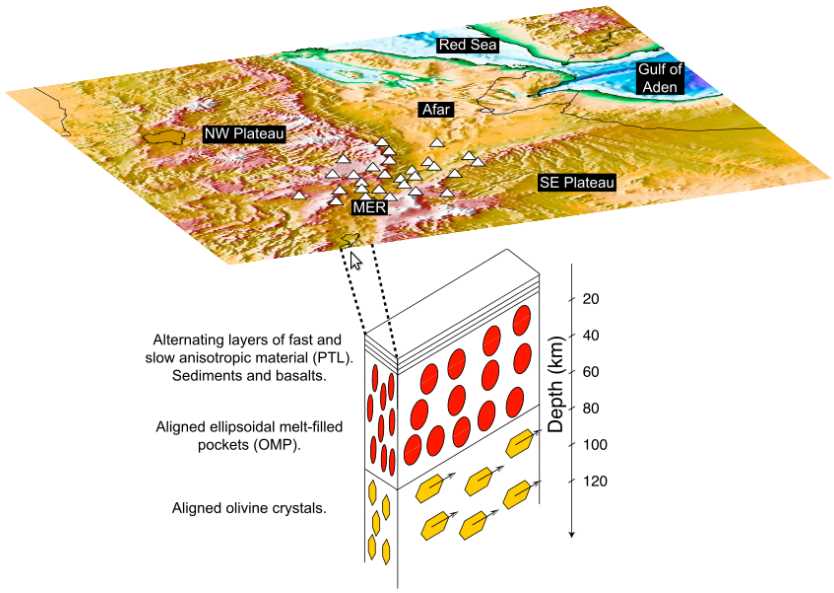

Figure 2.5: Schematic diagram showing causative fabrics of seismic anisotropy in the MER. From Bastow et al. (2008)

2.4.2 Near surface geology and tectonic structures

The near surface geology of the Afar region is dominated by a thick layer of basalt which is between 1-4 Ma, known as the Afar Stratoid Series (Figure 2.6) (Abbate et al., 1995). During their emplacement and subsequently, they have been fractured and faulted such that the landscape is dominated by broad grabens and horsts, aligned with and containing the present day magmatic segments (Acton et al., 2000; Bridges et al., 2012). Many such grabens have been periodically flooded, containing endorheic lakes (e.g. lake Afrera - see Figure 2.2), substantial units of lucustrine or fluvial sediments and evaporitic deposits, as well as younger volcanics (Bridges et al., 2012).

The DMS and HMS (where the data for this study were collected) have quite different surface appearances to one another. The active DMS to the north has young basaltic volcanics from fissural eruptions relating to the rift at the surface. The oldest of these lavas that has been dated is about 200 kyr and there is a

younging trend towards the present day morphological axis of the rift (Ferguson, 2011). A plot of distance from axis centre against age reveals a spreading rate that is approximately in agreement with the far field spreading rate (Ferguson, 2011). The lavas contain more than a thousand recognisable normal faults which have a mean strike direction of 333°, although there is considerable variation in this angle (Rowland et al., 2007). The mean fault length is 1.9 km and about 60% are downthrown towards the segment axis which is defined by an axial graben. Faults are closely spaced at about 500 m within 7 km of the axis and often have throw and opening displacements of 20 m and 1 to 3 m respectively. Deep fissures between footwall and hanging wall are common (Rowland et al., 2007) and often provide a path exploited by fissural eruptions (Ferguson et al., 2010). Slightly to the south of the segment centre is a silicic, central volcanic complex called the Ado'Ale Volcanic Complex (AVC) which is now bisected by the rift (Ferguson, 2011). The strike of the segment alters just north of the AVC from approximately 330° to 352°. At the northern end of the segment several other large volcanic edifices exist, most notably Dabbahu volcano after which the segment is named. Dabbahu is 1400 m high and displays lavas from basaltic to rhyolitic in composition (Field et al., 2012). There is also another large silicic volcano off-axis to the west of the DMS axis called Badi. Badi is approximately 20 km to the west of the axis at a latitude slightly north of the AVC, and reaches a maximum hight of 1200 m, some 600 m higher than its surroundings (Ferguson, 2011).

Most of the HMS is contained within the Tendaho Graben which is filled with lacustrine deposits that are up to 1.6 km thick (Abbate et al., 1995; Bridges et al., 2012). Some young volcanic centres exist within the graben (e.g. Kurub volcano). The graben is 50 km wide with very distinct and active border faults. In 1969 the village of Serdo on the NE border fault was destroyed by a magnitude 5.9 earthquake cause by strike-slip movement (Kebede et al., 1989).

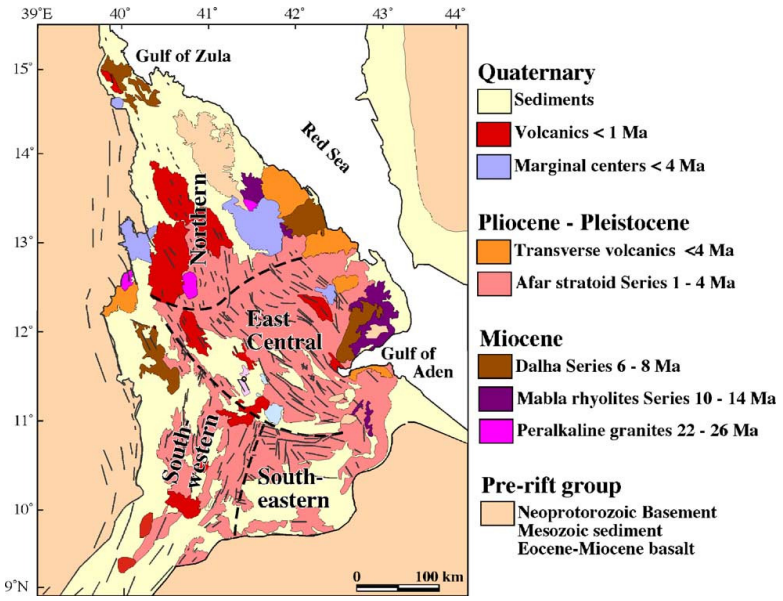

Figure 2.6: Geological map of the Afar depression. From Beyene and Abdelsalam (2005)

2.5 The 2005-present volcano-seismic event on the Dabbahu rift segment

In September 2005 the 60 km long Dabbahu rift segment ruptured, beginning with the injection of a so called mega-dyke along its entire length. The initial event occurred between the 14th September and 4th October and is well documented in Wright et al. (2006); Ayele et al. (2007); Ebinger et al. (2008). During this period, 163 earthquakes of magnitude >3.9 occurred. Wright et al. (2006) use radar data from the European Space Agency's Envisat satellite to form interferograms and range and azimuth offset maps that record the deformation owing to the dyking event, then using these scalar projections they estimate the three-dimensional displacement field. The horizontal component of displacement shows a maximum opening of 6 m at the surface in a direction perpendicular to the rift. There was a 25 km wide zone of uplift along most of the segment whilst a 2-3 km wide, well defined zone along the axis subsided by up to 2 m. Subsidense was

also observed at two locations at the northern end of the segment where shallow magma chambers are supposed to exist below Dabbahu and Gabho volcanoes. Simple elastic modelling of the displacement fields was carried out by Wright et al. (2006), where by the dyke was modelled as a tensile dislocation in an elastic half space discretised into rectangular patches from the surface to a depth of 10 km. Near surface normal faults were modelled as elastic dislocations dipping at 65 degrees and magma chambers associated with the volcanoes in the north were modelled at point deflation sources at 5 km depth as suggested by analysis of erupted pumice. Once model geometries were set, an inversion was carried out to constrain the amount of dyke opening and the volume of magma sourced from below the volcanoes. This showed dyke opening of up to 8 m with an average of 3.5 m between depths of 2 and 9 km. Since 2005 there have been 13 further dyke intrusions all considerably smaller in volume than the first (ranging from 2.4 to 6 % of the volume of the September 2005 dyke (Hamling et al., 2009)), two of which have been accompanied by fissural eruptions (Ferguson et al., 2010). There have also been two other fissural eruptions without dyke injection (Ferguson et al., 2010).

Both the seismicity and InSAR show that two magma supply zones were active during the emplacement of the mega-dyke. To begin with (before 25th September) most of the seismicity was on the northern half of the segment and centred around Dabbahu and Gab'ho volcanoes (Ebinger et al., 2008) where up to 3 m subsidence was observed (Wright et al., 2006). On the 26th September, a 500 m long 60 m deep volcanic vent opened up on the eastern flank of Dabbahu (Figure 2.7) with an explosive eruption. For the two days prior to this, nearly continuous seismic activity, including tremor, was recorded at the permanent seismic station in Addis Ababa (FURI). Analysis of the erupted pumice suggests a felsic source from 6 km below the volcano, reheated by injection of basaltic magma (Wright et al., 2006).

Clasts of up to 0.5 m were ejected and a small volume of rhyolite was extruded from the vent (Rowland et al., 2007).

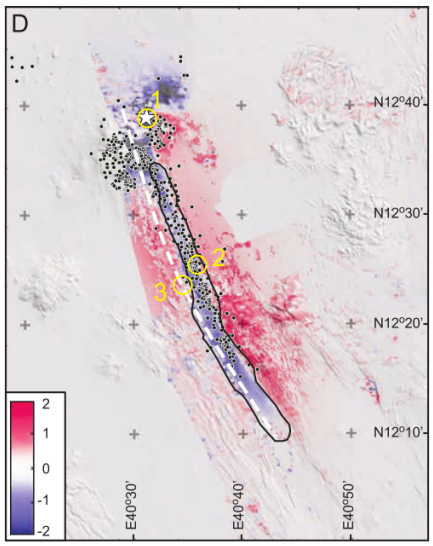

Figure 2.7: Subsidence on the Dabbahu magmatic segment after the initial 2005 dyke event. White dashed line is the rift axis, black dots are seismic events and the star at 1 marks the location of the vent which opened up. The area in blue shows subsidence directly above the dyke intrusion zone. Note that on the northern end of the segment the rift axis is offset to the west of the dykes. From Rowland et al. (2007)

Several authors have used geodetic data (GPS and InSAR) to constrain the 3-dimensional surface displacement from the 2005 dyke (Wright et al., 2006; Barisin et al., 2009; Grandin et al., 2009). These data have then been used in elastic modelling of the subsurface to estimate the geometry of the dyke and magma chambers that supply it. A 25 km wide zone centred on the rift showed uplift of up to 1.5 m on both flanks of the rift, whilst a 2-3 km wide zone directly above the dykes subsided by upto 2 m. Note that in the northern part of the segment dykes were injected to the east of the segment axis as shown in Figure 2.7. Barisin et al. (2009) showed that the uplift on the flanks was in fact asymmetric being 0.5 m higher on the west. The best fitting model to account for this showed

the dyke dipping at 80º to the west. High angle normal faults accommodate the strain in the top 2 km which explain the subsidence. Rowland et al. (2007) studied recent ground breaks (newly initiated and reactivated normal faults) showing that horizontal displacements are up to 3 m and vertical displacements are upto 5 m locally, but commonly 2 m. The maximum horizontal displacement at the surface was a total of 6 m of separation perpendicular to the rift axis. Modelling showed the maximum dyke dilation to be 8 m at approximately 5-6 km depth with an average opening of 3.5 m. No opening is required below about 9 km. Estimates of the total volume of magma injected are between 1.5 and 2.5 km^3, which is not balanced by an equivalent amount of deflation of the proposed shallow magma chambers beneath Dabbahu and Gab'ho which only show a total dilation of 0.5 km^3 (Wright et al., 2006; Grandin et al., 2009). Even when de-gassing of the magmas due to pressure reduction is accounted for the equation does not balance. It has been proposed that a large magma supply zones exists much deeper within the crust to supply magma to the rift, the deflation of which would be undetectable geodetically due to its depth and size (Ebinger et al., 2008; Hamling et al., 2009). The subsidence observed at Dabbahu and Gab'ho volcanoes has been modelled using both point deflation (Mogi) sources (Wright et al., 2006) and similar sill-like deflation sources (Grandin et al., 2009) which give depths to the magma chamber below Dabbahu of 5 and 9 km respectively. The seismicity associated with this deflation is clustered at a depth of 5 km (Ebinger et al., 2008), suggesting that the former may be a more accurate estimate.

The seismicity associated with dyke propagation can be used to accurately trace the path of the dyke within the subsurface (Belachew et al., 2011). Nine of the dykes emplaced after the initial one were recorded on temporary seismic arrays, all of which migrated north and south from a 5 km radius feeder zone at the mid-segment in the southern part of the AVC (Belachew et al., 2011) with a probable magma source in the lower crust or upper mantle (Keir et al., 2009). There is

also a very weak signal in the geodetic data to support supply from a deeper mid-segment feeder zone Grandin et al. (2009). Ebinger et al. (2008) suggest that magma injection from this deeper supply continued for 3 months after the main episode of the mega-dyke injection. Northward migrating seismicity progated with a velocity of between 0.45 and 0.53 m/s whereas those migrating to the south were slower with velocities of between 0.15 and 0.26 m/s (Belachew et al., 2011). Hamling et al. (2009) document 7 dyke intrusions occurring in 2006 and 2007. They show that successive dykes tend to relieve stress in sections of the rift where previous ones didn't.

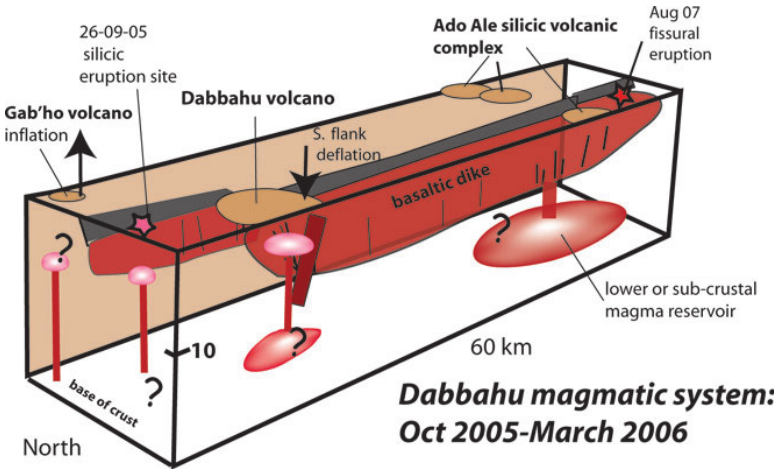

Figure 2.8: Schematic diagram showing the 2005 mega-dyke and proposed magma supply zones. Based on evidence from geodetic models and seismicity during the event. From Ebinger et al. (2008)

2.6 Rifting and magma supply at other spreading centres

The vast majority of magmatic divergent plate boundaries are submerged beneath the oceans, making direct observation difficult or impossible. Like Afar, Iceland offers an opportunity to study magmatic rifting on dry land and both locales

are also affected by plume activity. Iceland has over two dozen volcanic centres where the separation between the North American and European plates is accommodated, largely by magmatic rifting. Active periods on these segments last up to 10 years with quiescent times spanning 100-150 yeas (Gudmundsson, 1995). Morphology of the segments is similar to that of those found in Afar with typical lengths of 40-100 km, widths of 5-20 km and discrete magma supply zones from which lateral dyke injection propagates. A rifting event of similar scale to that currently ongoing in Afar happened on the Krafla segment in northern Iceland between 1975 and 1984 during which time an estimated 1.1 km^3 of magma was intruded or erupted through 20 dyking events and 9 eruptions (Sigmundsson, 2006). It has been speculated that both shallow crustal (1-3 km deep) and deep crustal (8-12 km deep) magma chambers were in operation during the event (Einarsson, 1978; Tryggvason, 1986; Gudmundsson, 1995; Buck et al., 2006). Later work using InSAR suggests that 10 years after the event an even deeper magma reservoir at 21 km depth at or near the crust-mantle boundary is inflating at a rate of 0.026 km^3/yr (de Zeeuw-van Dalfsen et al., 2004). The rifting episodes at Krafla between 1975 and 1984 and recently in Afar differ significantly in that at Krafla large amounts of subsidence were associated with dyke intrusions unlike in Afar, suggesting distinctly different magma supply regimes (Buck et al., 2006; Wright et al., 2006). Conductive material has been sensed between depths of 5 and 15 km across broad regions of Iceland (Árnason et al., 2010); however because there is no attenuation of seismic waves at equivalent depths (Menke et al., 1995) it cannot be interpreted in terms of partial melt, and its origins are not fully understood.

Seismic, and in some cases electromagnetic, surveys have been carried out at both the East Pacific Rise (EPR) and parts of the Mid-Atlantic ridge away from the Iceland hotspot in order to study crustal and upper mantle structures related to rifting (Baba et al., 2006a,b; Detrick et al., 1987; Singh et al., 1998; Kent et al.,

2000; Singh et al., 2006; Heinson et al., 2000; Sinha et al., 1997, 1998; MacGregor et al., 1998; Navin et al., 1998).

At the EPR, where spreading rates exceed 100 mm/yr (Detrick et al., 1987), a thin, vertically aligned sheet-like conductor is imaged electrically in the immediate vicinity of the ridge crest at one ridge segment but not another 150 km to the north. The crust and upper mantle is otherwise resistive to a depth of 60 km at which point conductivity rises to values indicative of 1 to 2% melt. Together, these observations are interpreted as evidence for rapid episodic melt transport from the mantle to the ridge where transient magma chambers may exist (Baba et al., 2006a,b). Shallow magma chambers in the crust have also been imaged seismically and again they are inferred to be narrow and immediately below the ridge crest (Detrick et al., 1987).

Shallow crustal magma chambers have also been imaged on the Mid-Atlantic ridge in two locations (Singh et al., 2006; Sinha et al., 1997, 1998; MacGregor et al., 1998; Navin et al., 1998). In this case, axial magma chambers tend to be about 3 km below the sea-floor and show sill-like geometries containing very high melt fractions which continue along the length of the ridge segment. MacGregor et al. (1998) use magnetotelluric data to show that below the axial magma chamber there is a zone of partial melt extending to the Moho which contains at least 20% melt. Like at the EPR, the very upper-most mantle is shown to be electrically resistive, containing little or no connected melt, although below 50 km resistivity decreases requiring a well connected melt fraction of 5% (Sinha et al., 1997). Again, Sinha et al. (1998) suggest that this is evidence for sporadic melt transport in highly porous conduits from the zone of melt production at approximately 50 to 100 km depth in the mantle to the crust below the ridge crest.

Chapter 3

The MT Method

3.1 Introduction

The MT method uses naturally occurring oscillations of the Earth's magnetic field as a power source to electromagnetically image the electrical conductivity (hereafter conductivity) structure of the subsurface. Broadly, it is based on Maxwell's equations which govern the induction of electric and magnetic fields due to time-varying magnetic fields and the flow of electrical currents respectively. The method is non invasive and can penetrate to great depths thanks to long period fluctuations of the Earth's magnetic field. The penetration depth of electromagnetic (EM) fields into the Earth is dependent on their frequency and on the conductivity structure itself, with higher conductivities reducing the penetration depth.

The parameter that the method is sensitive to is conductivity, which for Earth materials vary over a dozen or so orders of magnitude, with the likes of graphite or metal ores at the conductive end, and dry, unfractured igneous rocks at the other (e.g. Simpson and Bahr, 2005). The presence of even a small percent of (most)

fluids within an otherwise solid medium can increase conductivity dramatically especially when present as an interconnected phase (Sato and Ida, 1984). This study of Afar is concerned with the whereabouts of magma or partially molten rock within the crust, making MT ideally suited to our investigations where other more common methods such as seismic imaging may struggle due to attenuation of signals because of the presence of fluids (Whaler and Hautot, 2006).

This chapter will outline the basic principal of the MT method and the steps required, from data collection through to inversion, to carry out a successful MT experiment, although more detail of the specific methods used in this project will be given in the relevant chapters that follow. The MT method was realised in the early 1950's (Cagniard, 1953); however the historical development of the method is not key to this thesis and is therefore not generally given. The reader is referred to Simpson and Bahr (2005) and the references therein for more information on this subject. Simpson and Bahr (2005) and Chave and Jones (2012) are two complete treatise on the method covering all aspects from theoretical concepts to planning and implementing a field campaign and all of the steps that follow to gain a meaningful insight from the data. Unless referenced otherwise all of the following derivations and theory can be found there. Detailed descriptions of vector calculus and some vector identities used here are not given but can be found with specific application to electromagnetism, in, for example, Griffiths (1999).

3.2 Basic principals of the MT method

3.2.1 EM induction inside the Earth

The MT method is reliant on the Earth's magnetic field as a source of electromagnetic (EM) energy, but rather than the main part of the field which is created in the outer core, it utilises the fluctuating transient part which has its origins above ground. Electromagnetic fields with wave frequencies between 10^{-3} and 10^{+3} Hz have been used in this project; a range largely dictated by the capability of the equipment available. Naturally occurring EM field variations in this frequency range have two distinct origins.

First, the high frequency end of the spectrum from about 1 Hz results from meteorological activity (lightening strikes) which are distant from the study area (usually equatorial). EM waves are generated by these powerful cloud-to-Earth current discharges which then travel around the Earth in a waveguide whose boundaries are the surface of the Earth and the ionosphere at an altitude of 60 to 90 km during the day and night respectively. The other half of the frequency spectrum below 1 Hz (or above 1 s period) has its origins in interactions between the 'gusting' solar wind[1] and the Earth's magnetosphere[2] - fluctuations in the intensity of the solar wind cause contractions and dilations of the Earth's magnetosphere. It is assumed that primary fields from both source mechanisms impinge on the Earth's surface as harmonic plane waves with near vertical incidence and $e^{i\omega t}$ time dependence, where ω is angular frequency and t is time (Cagniard, 1953). The plane wave assumption is considered valid given that the fields are generated by large sheet-like currents in the ionosphere or by distant electric storms from which EM waves have been created and have subsequently

[1] A stream of charged particles emitted from the sun (mostly protons) which carry a magnetic flux

[2] The region of space around the Earth in which charged particles are influenced by the Earth's magnetic field

found their way to the measurement site in the Earth-ionosphere waveguide. The assumption may be violated in polar and equatorial regions where complex ionospheric current systems exist due to the equatorial and auroral electrojets. The equatorial electrojet (EEJ) is a non-uniform east-west flowing current that theory suggests could distort MT data with periods greater than about 10 s collected close to the magnetic dip equator (Padilha et al., 1997). Afar is located very close to the magnetic equator which is about 10 degrees north of the geographic equator in Africa. However, the strength of the EEJ is dependent on longitude with maxima over South America and South-East Asia not Africa (Chave and Jones, 2012). Further more, Padilha et al. (1997) conducted an experiment at the dip equator in Brazil to test the affect of the EEJ on MT data concluding that it is negligible. Similarly the data shown here did not appear to be distorted by this phenomenon.

MT data consist of measurements of the horizontal components of electric and magnetic fields at the surface of the Earth and it is the interaction between them within the conductive subsurface which form the basis of the MT method. Making use of vector calculus and its associated notation, interactions between electric and magnetic fields can be succinctly described by Maxwell's equations, which can be expressed as follows:

$$\nabla \times \mathbf{E} = -\frac{\partial \mathbf{B}}{\partial t} \tag{3.1}$$

$$\nabla \times \mathbf{B} = \mu_0 \mathbf{j}_f \tag{3.2}$$

$$\nabla \cdot \mathbf{B} = 0 \tag{3.3}$$

$$\nabla \cdot \mathbf{E} = \eta_f / \varepsilon_0 \tag{3.4}$$

where $\mathbf{E}$ is the electric field in Vm^{-1}, $\mathbf{B}$ is the magnetic induction in T, $\mathbf{j}_f$ is electric current density in Am^{-2} and η_f is the electric charge density due to free charges in Cm^{-3}. Here we have assumed that:

1. Variations in electrical permittivity (ε) and magnetic permeability (μ) are negligible in comparison to variations in bulk rock conductivity, and therefore free space values ($\varepsilon_0 = 8.85 \times 10^{-12}$ Fm^{-1} and $\mu_0 = 1.2566 \times 10^{-6}$ Hm^{-1}) can be used.

2. Time varying displacement fields owing to charge accumulation are negligible. This allows us to ignore the time dependent electric displacement term that would appear in the full version of Maxwell's equation for Ampère's law (3.2).

We have also used the relation $\mathbf{B} = \mu\mathbf{H}$ to express Equation (3.2) in terms of magnetic induction rather than magnetic intensity, $\mathbf{H}$ (which has units of Am^{-1}).

Equation (3.1) (Faraday's law) tells us that time variations in the magnetic field induce corresponding fluctuations in the electric field, forming a loop with its axis in the direction of the inducing field. Equation (3.2) (Ampère's law) tells us that a closed loop of current will have an associated magnetic field which is proportional to the flow of current. In words, Equation (3.3) states that the divergence of a magnetic field is zero or that magnetic monopoles do not exist.

Ohm's law states that:

$$\mathbf{j} = \sigma\mathbf{E} \tag{3.5}$$

where $\mathbf{j}$ is total current density and σ is conductivity. Using Ohm's law, Equation (3.2) can be rewritten:

$$\nabla \times \mathbf{B} = \mu_0\sigma\mathbf{E} \tag{3.6}$$

So together Equations (3.1) and (3.6) explain the essence of the method: naturally occurring, time-varying magnetic fields (right-hand side Equation (3.1)) induce

electric fields. In the conductive Earth the induced E-field causes a *telluric* current to flow in accordance with Ohm's law, whose magnitude is dependent on the conductivity, σ. In turn this induces a secondary internal magnetic field. What follows shows that, by measuring horizontal components of the electric and magnetic fields at the surface of the Earth we can gain an understanding of the conductivity structure below.

Two more assumptions are now needed:

1. The earth behaves as an Ohmic conductor, obeying Ohm's law (Equation (3.5))
2. No sources or sinks of current exist within the Earth ($\nabla \cdot \mathbf{j} = 0$)

Taking the divergence of Ohm's law and applying the above assumption 2:

$$\nabla \cdot \mathbf{j} = \nabla \cdot (\sigma \mathbf{E}) = 0 \tag{3.7}$$

Making use of a standard vector identity, this can be rewritten

$$\nabla \cdot (\sigma \mathbf{E}) = \sigma \nabla \cdot \mathbf{E} + \mathbf{E} \nabla \sigma = 0 \tag{3.8}$$

First taking the case of a homogeneous Earth ($\nabla \sigma = 0$) the divergence of $\mathbf{E}$ must also be zero i.e. the right-hand side of Equation (3.4) is equal to 0. This also holds for a 1-dimensional (1-d) Earth where conductivity varies only in the vertical direction.

By taking the curl of Equation (3.1), we can derive a wave equation solely in terms of $\mathbf{E}$ which shows how a time-varying electric field diffusively propagates into the Earth, and from which information about the conductivity structure can

be extracted:

$$\nabla \times \nabla \times \mathbf{E} = \nabla \cdot \nabla \cdot \mathbf{E} - \nabla^2 \mathbf{E} = -\nabla \times \frac{\partial \mathbf{B}}{\partial t} \tag{3.9}$$

Substituting in Equation (3.6) and assuming that $\nabla \cdot \mathbf{E} = 0$

$$\nabla^2 \mathbf{E} = \mu_0 \sigma \frac{\partial \mathbf{E}}{\partial t} \tag{3.10}$$

Through the same series of steps using Maxwell's equation for Ampère's law we find that:

$$\nabla^2 \mathbf{B} = \mu_0 \sigma \frac{\partial \mathbf{B}}{\partial t} \tag{3.11}$$

These are second order diffusion equations.

For a plane electromagnetic wave travelling in the z direction, electric and magnetic fields can be described by:

$$\mathbf{E} = \mathbf{E}_0 e^{i(\omega t - \mathbf{k}z)} \tag{3.12}$$

and

$$\mathbf{B} = \mathbf{B}_0 e^{i(\omega t - \mathbf{k}z)} \tag{3.13}$$

where $\mathbf{E}_0$ and $\mathbf{B}_0$ are initial amplitudes, ω is angular frequency (equal to $2\pi/T$, where T is the period), and $\mathbf{k}$ is the unknown wavenumber. With this in mind Equations 3.10 and 3.11 can be expressed in the frequency domain, giving:

$$\nabla^2 \mathbf{E} = i\omega \mu_0 \sigma \mathbf{E} \tag{3.14}$$

and

$$\nabla^2 \mathbf{B} = i\omega \mu_0 \sigma \mathbf{B} \tag{3.15}$$

3.2.2 Application to a homogeneous half-space

Starting with the simplest conceivable model of subsurface conductivity, a homogeneous half-space, we can look for solutions to the diffusion equations ((3.14) and (3.15)) derived in the previous section. First consider a plane E-field polarised in the x-direction, such that $\mathbf{E} = \hat{\boldsymbol{i}} E_x$ where $\hat{\boldsymbol{i}}$ is a unit vector in the x-direction. At any given moment $\mathbf{E}$ only varies in the z-direction such that:

$$\frac{\partial E_x}{\partial x} = \frac{\partial E_x}{\partial y} = 0$$

Hence Equation (3.14) can now be written:

$$\frac{\partial^2 E_x}{\partial z^2} = i\omega\mu_0\sigma E_x \tag{3.16}$$

By taking the second derivative with respect to z of Equation (3.12), and substituting into Equation (3.16) we find that:

$$k^2 E_0 e^{i(\omega t - kz)} = i\omega\mu_0\sigma E_0 e^{i(\omega t - kz)} \tag{3.17}$$

Thus solving for the unknown parameter k:

$$k^2 = i\omega\mu_0\sigma$$

$$\pm k = \sqrt{i\omega\mu_0\sigma} = \frac{1+i}{\sqrt{2}}\sqrt{\omega\mu_0\sigma} = \sqrt{\omega\mu_0\sigma/2} + i\sqrt{\omega\mu_0\sigma/2} \tag{3.18}$$

Substituting k back into Equation 3.12 we have a 1-dimensional (1-d) solution to the wave equation:

$$E_x = E_0 e^{i(\omega t \pm z\sqrt{\omega\mu_0\sigma/2}) \pm z\sqrt{\omega\mu_0\sigma/2}} \tag{3.19}$$

Assuming that the Earth does not generate any electromagnetic energy but only dissipates or absorbs it through Ohmic heating of conductive materials, we can

ignore the positive z terms to give:

$$E_x = E_0 e^{i(\omega t - z\sqrt{\omega\mu_0\sigma/2}) - z\sqrt{\omega\mu_0\sigma/2}} \tag{3.20}$$

We can now see that with increasing depth (z) and non-zero σ, the amplitude of an EM field penetrating the subsurface diminishes. Should $\sigma = 0$ (in the air layer between the ionosphere and Earth for example), then EM fields are not attenuated. From here we can derive the skin depth relation which gives the depth, for a given frequency, at which the amplitude of an EM field is reduced to $1/e$ of its initial value:

$$p(\omega) = 1/\mathrm{Re}(k) = \sqrt{\frac{2}{\omega\mu_0\sigma}} \tag{3.21}$$

which can be evaluated in terms of period, T, (in seconds) as:

$$p(T) = 503\sqrt{\frac{T}{\sigma}} \tag{3.22}$$

where p is in meters. In the MT method, electromagnetic fields are considered insensitive to conductivity structures at depths beyond one skin depth, so although the fields are not attenuated altogether, this is considered to be the penetration depth for a given period (T). The skin depth equation ((3.21) or (3.22)) shows that the penetration depth is not only dependent on the EM period, but also the conductivity structure itself, with more conductive substrata resulting in a shallower skin depth.

A plane polarised oscillation of the electric field in the x-direction (E_x) normally incident at the Earth's surface only induces a magnetic field in the perpendicular y-direction (from Equation (3.1)), assuming homogeneity. The wave equation for the magnetic field has the same form as Equation (3.20) but with a phase shift of $-\phi$:

$$B_y = B_0 e^{i(\omega t - \phi) - \gamma z} \tag{3.23}$$

where $\gamma = (1+i)(\omega\mu_0\sigma/2)^{\frac{1}{2}}$.

The MT impedance, Z, is defined as the ratio of electric to magnetic fields:

$$Z = \mu_0 \frac{E_x}{B_y} \tag{3.24}$$

which using Equations (3.20) and (3.23) can be expressed:

$$Z = \mu_0 \frac{E_0}{B_0} e^{i\phi} \tag{3.25}$$

So Z is a quantity that we can estimate using orthogonal measurements of electric and magnetic fields at the surface of the Earth. Note that for a 1-d conductivity structure using E_x, B_y or E_y, B_x yields the same result with a sign change. Given our plane polarised electric field E_x, Equation (3.1) can be rewritten:

$$\frac{\partial E_x}{\partial z} = -\frac{\partial B_y}{\partial t} \tag{3.26}$$

Taking the vertical derivative of Equation (3.20) and the time derivative of Equation (3.23) this becomes:

$$-\gamma E_x = -i\omega B_y \tag{3.27}$$

Combining this with Equation (3.24) gives an alternative expression for the impedance Z:

$$Z = \frac{1+i}{\sqrt{2}} (\frac{\omega\mu_0}{\sigma})^{\frac{1}{2}} = (\frac{\omega\mu_0}{\sigma})^{\frac{1}{2}} e^{i\phi} \tag{3.28}$$

Equation (3.28) shows that Z is a complex number with magnitude $\sqrt{\frac{\omega\mu_0}{\sigma}}$, and given that the magnitudes of its real and imaginary parts are equal, the phase, ϕ, is 45^o with the magnetic lagging behind the electric field.

3.2.3 The MT impedance tensor

Suppose we have a vertical contact in the subsurface whose strike is parallel to the x-direction, separating rock units of different conductivity within an otherwise 1-d subsurface. The current, j_y, across the vertical boundary must be continuous, so given that σ_y is discontinuous then in accordance with Ohm's law (Equation (3.5)) E_y must also be discontinuous. In this situation, Maxwell's equations decouple into two sets of equations (or modes) known as **E**-polarisation (otherwise known as the transverse electric or TE mode) incorporating electric fields parallel to strike, and **B**-polarisation (transverse magnetic or TM mode) incorporating magnetic fields parallel to strike. For **E**-polarisation describing currents flowing parallel to strike:

$$\begin{aligned} \frac{\partial E_x}{\partial y} &= i\omega B_z \\ \frac{\partial E_x}{\partial z} &= i\omega B_y \\ \frac{\partial B_z}{\partial y} - \frac{\partial B_y}{\partial z} &= \mu\sigma E_x \end{aligned} \tag{3.29}$$

For **B**-polarisation describing currents flowing perpendicular to strike:

$$\begin{aligned} \frac{\partial B_x}{\partial y} &= \mu_0\sigma E_z \\ \frac{-\partial B_x}{\partial z} &= \mu_0\sigma E_y \end{aligned}$$

$$\frac{\partial E_z}{\partial y} - \frac{\partial E_y}{\partial z} = -\omega B_x \tag{3.30}$$

In this case the impedance, Z, calculated using E_x and H_y will be different from that calculated using E_y and H_x and it now becomes convenient to express Z as a tensor such that

$$\begin{bmatrix} E_x \\ E_y \end{bmatrix} = \begin{bmatrix} Z_{xx} & Z_{xy} \\ Z_{yx} & Z_{yy} \end{bmatrix} \begin{bmatrix} B_x/\mu_0 \\ B_y/\mu_0 \end{bmatrix} \tag{3.31}$$

or

$$\mathbf{E} = \mathbf{ZB}/\mu_0 \tag{3.32}$$

This is the definition of the MT impedance tensor, $\mathbf{Z}$. The amplitude of the impedance can be scaled to have units of resistivity and is known as the apparent resistivity, (ρ_a):

$$\rho_{a_{ij}}(\omega) = \frac{1}{\mu_0 \omega} |Z_{ij}(\omega)|^2 \tag{3.33}$$

where i and j indicate either the x or y component of horizontal electric and magnetic field respectively. The phase of the impedance is given by:

$$\phi_{ij}(\omega) = \tan^{-1}\left[\frac{\mathrm{Im}\{Z_{ij}(\omega)\}}{\mathrm{Re}\{Z_{ij}(\omega)\}}\right] \tag{3.34}$$

Curves of apparent resistivity and phase plotted against log10(period), which is a depth proxy, are typically how MT data are viewed. Curves are expected to be smooth and in the case of a layered half-space Simpson and Bahr (2005) show that the apparent resistivity is a volume average of the subsurface to the depth of penetration of the frequency being considered. The impedance phase is one

of the most important MT parameters; as already shown it is equal to 45° over a homogeneous earth, however, if the resistivity of the subsurface increases with depth the phase drops below 45°. Conversely, if resistivity decreases with depth then phase values above 45° are observed. As well as being plotted as a function of period, MT data from multiple sites are often displayed as a pseudo-section, again using log10(period) as the depth proxy.

The off-diagonal elements of **Z** are known as the principal impedances and couple orthogonal electric and magnetic fields. The diagonal elements are known as the auxiliary impedances and couple parallel electric and magnetic fields, hence they are equal to zero in the case of a 1-d conductivity structure or a 2-d conductivity structure with the fields measured parallel and perpendicular to geoelectric strike (assuming perfectly noise free data).

If the subsurface conductivity structure is 3-d or if the fields are not measured perpendicular and parallel to the strike of the 2-d structure then electric and magnetic field are no longer orthogonal. The TE and TM modes are sensitive to different types of structures within the subsurface, for example, the TM mode tends to better resolve lateral resistivity contrasts and is less sensitive to along strike variations (3-d effects). So in summary, the 1-d impedance tensor (assuming noise free data) is:

$$\mathbf{Z_{1\text{-}d}} = \begin{bmatrix} 0 & Z_{xy} \\ -Z_{xy} & 0 \end{bmatrix} \tag{3.35}$$

Here, auxiliary impedances are zero and principal impedances have the same magnitude with the lower element being negative showing that the phase is in the third rather than the first quadrant. The 2-d impedance tensor expressed in strike coordinates is:

$$\mathbf{Z_{2\text{-}d}} = \begin{bmatrix} 0 & Z_{xy} \\ Z_{yx} & 0 \end{bmatrix} \tag{3.36}$$

Finally, the most general form of the impedance tensor where the subsurface conductivity structure is 3-d, is expressed as:

$$\mathbf{Z_{3\text{-}d}} = \begin{bmatrix} Z_{xx} & Z_{xy} \\ Z_{yx} & Z_{yy} \end{bmatrix} \tag{3.37}$$

In most cases, given a 2-d conductivity structure, the fields will not have been measured in the strike coordinate frame; however, if the angle (θ) between the measurement and strike coordinate frames can be estimated, then the 2-d impedance tensor can be recovered with a straight forward tensor rotation:

$$\mathbf{Z}(\theta) = \mathbf{R}(\theta)\mathbf{Z}\mathbf{R}^T(\theta) \tag{3.38}$$

where $\mathbf{Z}$ is the impedance tensor rotated into the strike reference frame and $\mathbf{R}$ is the rotational operator:

$$\mathbf{R} = \begin{bmatrix} \cos\theta & \sin\theta \\ -\sin\theta & \cos\theta \end{bmatrix} \tag{3.39}$$

corresponding to an anticlockwise rotation by an angle θ. This can be expanded

to give the elements of the rotated impedance tensor as:

$$\begin{aligned} Z'_{xx} &= Z_2 + Z_3 \sin 2\theta + z_4 \cos 2\theta \\ Z'_{xy} &= Z_1 + Z_3 \sin 2\theta - z_4 \cos 2\theta \\ Z'_{yx} &= -Z_1 + Z_3 \cos 2\theta - z_4 \sin 2\theta \\ Z'_{yy} &= -Z_2 - Z_3 \sin 2\theta - z_4 \cos 2\theta \end{aligned} \tag{3.40}$$

where

$$\begin{aligned} Z_1 &= (Z_{xy} - Z_{yx})/2 \\ Z_2 &= (Z_{xx} + Z_{yy})/2 \\ Z_3 &= (Z_{xy} + Z_{yx})/2 \\ Z_4 &= (Z_{xx} - Z_{yy})/2 \end{aligned} \tag{3.41}$$

3.3 Estimating the MT impedance tensor from electric and magnetic field measurements

Raw data may often amount to several gigabytes, representing the electric and magnetic fields recorded at high sampling rates, each in two orthogonal directions. The method used here by which these data are reduced to just eight numbers per frequency at each site (the real and imaginary parts of $\mathbf{Z}$) will be outlined, in brief, here. Full details can be found in Chave and Thomson (2004), along with the release notes from the code used, 'BIRRP: bounded influence, remote reference processing' which is freely available to the academic community.

The MT impedance tensor, sometimes referred to as a transfer function, relates an input (the magnetic field measurements) to an output (the electric field) via

a linear relationship. We aim to get an estimate of the MT impedance tensor, $\mathbf{Z}$, which is not biased by noise on either the input channel or the output channel. Assuming, for the moment, that noise only exists on the electric channel, this can be incorporated into Equation (3.32) such that

$$\mathbf{E} = \mathbf{ZH} + \mathbf{e_E} \tag{3.42}$$

where $\mathbf{e_E}$ represents noise on the output electric channel. Impedances can be estimated in the frequency domain by a least squares minimisation of $\mathbf{e_E}$, assuming the noise to be distributed in a Gaussian fashion. This proceeds by calculating power spectral densities of $\mathbf{E}$ and $\mathbf{H}$ field data via a Fourier transform, and using cross and auto spectra (e.g. Sims et al., 1971) such that at a given frequency

$$\mathbf{Z} = [\mathbf{H^T H}]^{-1}[\mathbf{H^T E}] \tag{3.43}$$

where the terms enclosed in square brackets are cross- and auto-power spectral matrices. This may be expanded for each component of $\mathbf{Z}$ as

$$Z_{ij} = \frac{(E_i H_j^* \cdot H_i H_i^* - E_i H_i^* \cdot H_i H_j^*)}{(H_x H_x^* \cdot H_y H_y^* - H_x H_y^* \cdot H_y H_x^*)} \tag{3.44}$$

In this case, because all noise is assumed to be on the electric channel, correlated noise on the magnetic channel leads to a downward biased estimation of Z_{ij} (artificially high denominator in Equation 3.44). By reversing the sense of input and output channels and assuming all noise to be associated with the magnetic field, an upward biased estimate of the impedance elements can be made (Jones et al., 1989). In reality the distribution of noise is unknown so these upward and downward biased estimated can be used to place bounds on the impedance, however the assumption that the noise is usually much greater on the electric rather than the magnetic channel is justified by Sutarno and Vozoff (1991), except where the magnetic field is contaminated by artificial noise such as power lines or electric

trains. At higher frequencies in particular, there usually exists an abundance of data, allowing stacking of spectral data from adjacent subsets or windows of the time series, hugely reducing the statistical error on impedance estimates. The subset size is chosen based on the lowest frequency of interest and a target value for the final number of degrees of freedom (Chave and Thomson, 1989). Data are typically recorded at different sampling rates which are used to give impedance estimates at a range of frequencies determined by the Nyquist frequency of that time series.

It has been recognised for some time that a Gaussian noise distribution is unrealistic, and that outliers can have a considerable affect on impedance estimates (e.g. Egbert and Booker, 1986; Chave and Thomson, 1989; Sutarno and Vozoff, 1991). To reduce the impact of this problem, so-called robust schemes have been developed to increase the precision of impedance estimates, in which unusual data in the response electric field (outliers) and the input magnetic field (leverage points) are iteratively down weighted in the estimation of the impedance (e.g. Egbert and Booker, 1986; Chave and Thomson, 1989). It has also been suggested that any upward bias due to a noisy magnetic channel can be circumvented by using measurements of the magnetic field at a remote site, where noise could be assumed to be uncorrelated between the two (Gamble et al., 1979; Chave and Thomson, 1989), however this does require that the magnetic field be measured simultaneously at two locations with a precise time-synchronisation between sets of recording equipment.

The processing code used here (Chave and Thomson, 2004) is applied as follows. First, the time-series of the two electric and two magnetic fields are visually inspected and, if they are excessively long such that some of the data can be discarded, the user may select a sub-section of the four time series which appear

to be of good quality. Very poor data are often recognisable at this early stage by large spikes (more often in the electric field) which appear not to be correlated to any signal in the magnetic field. Hereafter the process is fully automated. A pre-whitening filter is first used to remove artificial power spikes from the time series, after which they further split into windows according to the frequency of interest, then a data taper is applied to the ends of each data window to reduce spectral leakage. Fast Fourier transforms are then computed for each data window. Frequencies at which a response is computed are chosen to be equally spaced on a logarithmic scale, with five to ten frequencies per decade considered sufficient given the smooth variation of $\mathbf{Z}$ with frequency. Initially a simple least squares solution is sought (Equations (3.43) and (3.44)) and used to compute the residuals in Equation (3.42). Following this, an iterative process is used where impedance estimates with large residuals are down-weighted.

Estimating confidence intervals on the impedance can be done parametrically, however this has several problems associated with it, not least that it is even more sensitive to outliers than the least squares estimates themselves (Chave and Thomson, 1989). Many authors now use non-parametric methods, for example jackknife type estimations of the error (e.g. Chave and Thomson, 1989). It is this approach that is used in the algorithm used here (Chave and Thomson, 2004).

The electric field can be predicted using the calculated impedance and the measured magnetic field. The cross correlation of the predicted and measured electric field can be used to estimate the coherence between them at each frequency. This parameter is a good indicator of the quality of the recorded data in terms of the amount of noise and the assumed linear relationship between electric and magnetic fields. 'BIRRP' allows the used to define a minimum coherency threshold, where by estimates of the impedance showing lower coherency are rejected. This was generally set to 0.8, where a a value of 1 represents perfect coherency. However, where less data were available or very noisy (usually the long

period data for both reasons) this resulted in very few subsections of the available time series being used in the impedance calculation (there is a trade off between using a higher minimum coherence threshold and the number of data subsections being used). In this case the minimum coherence can be lowered and the code re-run.

3.4 A simple approach to determining the dimensionality of a data set

Given an MT impedance tensor that is clearly not of the 1-d form shown in Equation (3.35), Swift (1967) proposes that the following steps be taken to ascertain the degree of complexity of the dimensionality of the underlying structure. Additionally, if the tensor can be shown to be descriptive of a 2-d subsurface, he suggests a simple method to recover the angle between the measurement and principal axis, and hence the 2-d impedances.

A rotationally invariant parameter of a tensor is one that remains constant under rotation of the tensor. The rotationally invariant Swift-skew parameter, k, can be calculated from $\mathbf{Z}$, and gives an indication of the extent of departure from a 1-d or 2-d Earth. Calculated as follows:

$$k = \frac{|(Z_{xy} - Z_{yx})/2|}{|(Z_{xx} + Z_{yy})/2|} \tag{3.45}$$

k is zero in the 1-d and 2-d cases (with noise free data). If k is large (greater than 0.2 (Reddy et al., 1977)) then it is considered that 3-d effects prevail (or the data are very noisy) and there is no coordinate frame in which the MT modes de-couple.

However, if k is small (within the uncertainties of the data), then Swift (1967) suggests that the 2-d impedance tensor in a strike coordinate frame be estimated by rotating it, as previously described (Equation (3.38)), such that the diagonal elements are minimised (in practice they will not vanish due to noise in the data) and the magnitude of the off-diagonal elements is maximised. Hence the principal axes are defined as those which minimise the quantity:

$$|Z'_{xx}(\theta_0)^2 + Z'_{yy}(\theta_0)^2| \tag{3.46}$$

The expression for the necessary rotation (derived by looking for stationary points of the derivative of (3.46)) is given by:

$$\theta_0 = \frac{1}{4}\tan^{-1}\frac{(Z_{xx} - Z_{yy})(Z^*_{xy} + Z^*_{yx}) + (Z^*_{xx} + Z^*_{yy})(Z_{xy} + Z_{yx})}{|Z_{xx} - Z_{yy}|^2 - |Z_{xy} + Z_{yx}|^2} \tag{3.47}$$

where the asterisk denotes the complex conjugate of Z (Swift, 1967).

The angle of rotation at which the diagonal elements are minimised is the difference between the measurement reference frame and the strike-parallel reference frame. Note how rotating the impedance tensor through 180 degrees will yield two angles, 90° apart, at which the diagonal elements are minimised, with the off-diagonal elements are simply swapped, showing that there is a 90° ambiguity in determining the actual geo-electric strike direction. Or in other words it is not possible to determine from the impedance tensor alone, which of the principal impedances is the TE and which is the TM mode.

3.5 Advanced dimensionality analysis and galvanic distortion

The previous section showed how increasingly complex conductivity structures within the Earth manifest themselves in the MT impedance tensor. It is important to establish the level of complexity embedded within a data set because this will dictate how the data can be modelled and interpreted. This section describes an extra level of complexity, which has been shown to be common in many data sets, where the subsurface is 1-d or 2-d with the effects of small scale, local (by which we mean features of the subsurface with dimensions significantly less than the inductive scale length of the data) 3-d heterogeneities (e.g. Berdichevsky and Dmitriev, 1976; Bahr, 1988). They are sometimes referred to as scatterers because of the effect they have, principally on the E-field. Approaches to assessing and removing their effects on the data will be discussed.

Small scale local conductivity anomalies have undesirable effects on the MT impedance tensor, known collectively as galvanic distortion. As shown previously, due to the conservation of current at conductivity discontinuities, the electric field must be discontinuous which results in a non time-dependent build up of charge on the boundary. In turn the build up of charge distorts the amplitude of measured electric fields and alters the flow of telluric currents near to the boundary. This non-inductive effect distorts the regional impedance estimate, resulting in poor determination of the true regional geo-electric strike direction and an upwards or downwards parallel shift of apparent resistivity curves (know as *static-shift* - see Figure 3.1) due to the amplitude distortion of the electric field. Static-shifts of apparent resistivity curves can lead to major misinterpretation of the subsurface structure. Although electric charge will build up on any vertical conductivity boundary (assuming horizontal current flow) it only becomes a problem where the

distorting body is small and shallow enough such that it has no inductive contribution to the measured fields at the frequencies of interest. At greater depths, the inductive response is expected to dominate over galvanic effects (Groom and Bahr, 1992). Because of the time-independent nature of the phenomenon, the impedance phase is unaffected (Caldwell et al., 2004). Consequently, data affected by static shift are most easily recognised by looking for frequency bands where the apparent resistivity curves of the two modes are shifted apart and neither converging or diverging but the phase curves lie together (Simpson and Bahr, 2005) as shown in Figure 3.1. It should be noted that if a static shift is apparent there is no easy way of knowing which curve is correct and furthermore it is possible for both curves to be shifted together even if they appear to be coincident (Sternberg et al., 1988). The factor by which an apparent resistivity curve is shifted is not obtainable from the MT data alone.

For this case of a 1-d or 2-d regional (inductive) MT response with local 3-d effects, the principal impedances obtained by determination of the geo-electric strike and subsequent rotation of the impedance tensor as described previously will not be the regional inductive impedances, rather linear combinations of them (Groom and Bailey, 1989). In order to recover the true regional impedances, several schemes have been proposed (e.g. Larsen, 1977; Bahr, 1988; Lilley, 1998); however, the most commonly adopted method, in which the impedance tensor is decomposed into a series of matrix multiplications describing the distortion, was put forward by Groom and Bailey (1989) and is known widely as Groom-Bailey or GB decomposition.

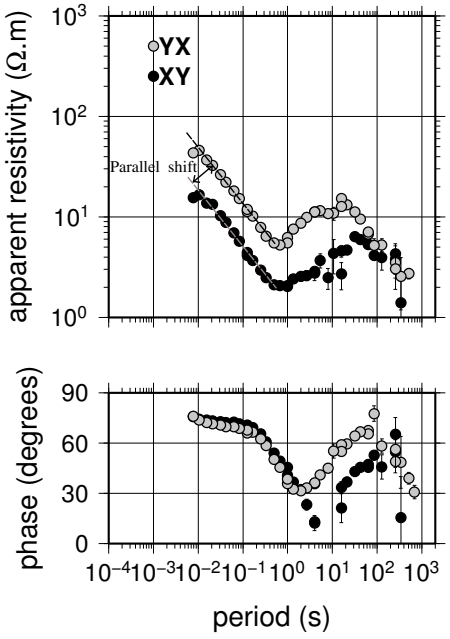

Figure 3.1: Apparent resistivity and phase data at a site affected by static shift. In the high frequency part of the resistivity curves there is a parallel shift between the orthogonal MT measurements. Notice how the phase for the two modes at these frequencies is coincident.

3.5.1 Groom-Bailey decomposition

An anomalous electric field due to charge build up not only distorts the measured electric field but also produces an anomalous current, in turn producing an anomalous magnetic field, all of which are in phase with the regional electric field (Groom and Bahr, 1992). However, in the GB approach, distortions of the electric field are assumed to be much stronger than those of the magnetic field **H**, because the magnetic field is determined by a weighted spacial average of the telluric current density (Groom and Bailey, 1989), hence $\mathbf{H}_m = \mathbf{H}_r$, where $\mathbf{H}_m$ and $\mathbf{H}_r$ are the measured and regional magnetic field. The measured electric field ($\mathbf{E}_m$) on the other hand is described by:

$$\mathbf{E}_m = \mathbf{C}\mathbf{E}_r \tag{3.48}$$

where **C** is a real distortion tensor with four independent elements and $\mathbf{E}_r$ is the regional electric field (Bahr, 1988). An analytical justification for this can be found in Groom and Bahr (1992).

So, given that:

$$\mathbf{E}_r = \mathbf{Z}_r\mathbf{H} \tag{3.49}$$

and

$$\mathbf{E}_m = \mathbf{Z}_m\mathbf{H} \tag{3.50}$$

it follows that

$$\mathbf{Z}_m = \mathbf{C}\mathbf{Z}_r \tag{3.51}$$

Extending this to the case where the regional conductivity structure is 2-d, and the EM fields are measured in a coordinate system other than that of the 2-d structure:

$$\mathbf{Z}_m = \mathbf{R}\mathbf{C}\mathbf{Z}_{2d}\mathbf{R}^T \tag{3.52}$$

where $\mathbf{R}$ is the rotation matrix described earlier. Equation 3.52 has 9 unknowns (the strike angle θ, four elements of $\mathbf{C}$, and the real and imaginary parts of the anti-diagonal elements of the 2-d impedance tensor, yet there exist only 8 known data (the complex elements of the measured impedance tensor), hence there is no unique solution to this decomposition. Groom and Bailey (1989) however suggest a factorisation of $\mathbf{C}$ which allows it to be separated into determinable and indeterminable parts each of which have a physical interpretation as follows (Groom and Bailey, 1989; Smith, 1995; Balasis et al., 1997):

$$\mathbf{C} = g\mathbf{T}\mathbf{S}\mathbf{A} \tag{3.53}$$

where g is a scalar and the tensors $\mathbf{T}$, $\mathbf{S}$ and $\mathbf{A}$ are given by:

$$\begin{aligned}
\mathbf{T} &= \begin{bmatrix} 1 & -t \\ t & 1 \end{bmatrix} \frac{1}{\sqrt{1+t^2}} \\
\mathbf{S} &= \begin{bmatrix} 1 & e \\ e & 1 \end{bmatrix} \frac{1}{\sqrt{1+e^2}} \\
\mathbf{A} &= \begin{bmatrix} 1+s & 1 \\ 1 & 1-s \end{bmatrix} \frac{1}{\sqrt{1+s^2}}
\end{aligned} \tag{3.54}$$

Each of the tensors is normalised (by the fraction on the right-hand side) to ensure that the elements remain bounded during computations. Remembering that the distortion tensor **C** actually acts on the electric field, it is possible to give each part of the factorisation physical meaning by considering its effect on an electric field measured in the coordinate frame of a regional 2-d structure.
First, the *anisotropy* tensor, **A**, stretches the electric field in orthogonal directions by different factors but in the same direction as the regional anisotropy. In fact it is impossible to distinguish between regional anisotropy and that caused by **A**. The aptly named *shear* tensor, **S**, has a shearing effect on the electric field, creating an anisotropy on axes which bisect the regional principal axes. Consequently an electric field pointing in the direction of the principal axes is not only stretched but also deflected by the shear angle defined as $\phi_e = \tan^{-1} e$. The *twist* tensor, **T**, rotates the electric field through an angle $\phi_s = \tan^{-1} t$. Finally, the *site gain*, g, scales the electric field equally in all directions and is necessary because the product of **T**, **S** and **A** will itself result in some scaling of the field due to the normalisation factors.

The cunning nature of this factorisation now becomes apparent. Neither g nor **A** are distinguishable from $\mathbf{Z}_{2d}$ (all having zero diagonal terms), hence if we allow them to be absorbed into the regional impedance tensor (effectively forming part of the static-shift) the decomposition becomes:

$$\begin{aligned} \mathbf{Z}_m &= \mathbf{RTSZ}'_{2d}\mathbf{R}^T \\ &= \begin{bmatrix} \cos\theta & -\sin\theta \\ \sin\theta & \cos\theta \end{bmatrix} \begin{bmatrix} 1-te & e-t \\ e+t & 1+et \end{bmatrix} \begin{bmatrix} 0 & Z'_{xy} \\ Z'_{yx} & 0 \end{bmatrix} \begin{bmatrix} \cos\theta & \sin\theta \\ -\sin\theta & \cos\theta \end{bmatrix} \end{aligned} \tag{3.55}$$

where normalisation factors in Equations 3.54 have been absorbed into g and

hence into $\mathbf{Z}'_{2d}$.

With seven unknowns Equation 3.55 theoretically allows us to determine the correct regional strike angle θ, and the two complex regional impedances (with unknown static shift) by fitting the seven unknown parameters to the eight known values of the measured impedance tensor. This is done by minimising the least-squared misfit, χ^2, between the data and model summary coefficients given by:

$$\begin{aligned} \alpha_0 &= Z_{xx} + Z_{yy} \\ \alpha_1 &= Z_{xy} + Z_{yx} \\ \alpha_2 &= Z_{yx} - Z_{xy} \\ \alpha_3 &= Z_{xx} - Z_{yy} \end{aligned} \tag{3.56}$$

and

$$\begin{aligned} \alpha_0 &= t\sigma + e\delta \\ \alpha_1 &= (\delta - et\sigma)\cos 2\theta - (t\delta + e\sigma)\sin 2\theta \\ \alpha_2 &= -\sigma + et\delta \\ \alpha_3 &= -(t\delta + e\sigma\cos 2\theta - (\delta - et\sigma)\sin 2\theta \end{aligned} \tag{3.57}$$

respectively, where

$$\sigma = Z'_{xy(2d)} + Z'_{yx(2d)}$$

and

$$\sigma = Z'_{xy(2d)} - Z'_{yx(2d)}$$

These two sets of equations ((3.56) and (3.57)) can be equated, giving four simultaneous complex non-linear equations which are solved for the seven parameters of the factorisation. Conventionally this is done on a frequency-by-frequency, site-by-site basis, iteratively constraining the estimates of twist, shear and regional strike in an attempt to find frequency independent values for each, with an acceptable level of overall misfit (Groom et al., 1993). This is a time-consuming process, leading to a suggested extension to the method by McNeice and Jones (2001) whereby a global solution is sought for a set of sites over a range of frequencies. The algorithm used to find the best fitting 3-d/2-d model is described in detail in McNeice and Jones (2001). Examples are given by Groom and Bailey (1989) to show that impedance tensors with large Swift-skew angles (previously thought to be indicative of 3-d induction) can be successfully decomposed by the proposed method, yielding regional 2-d impedances. Examples are also given to show how poorly estimated the regional strike can be in the presence of galvanic scatterers of the electric field, when the method of simply minimising the diagonal elements is adopted.

It is important that realistic estimates of the error on the regional 2-d impedances obtained from GB decomposition are sought. However, this is not straightforward because of the non-linear nature of the transformation between measured and 2-d regional impedances, and lack of knowledge about the distribution of impedance elements. Therefore Groom and Bailey (1991) suggest using a bootstrap procedure where by random Gaussian noise with variance equal to that of the impedance estimates is added to the measured impedance, and realisations of the 2-d impedance elements are made using the distortion parameters found in the decomposition. The scatter of the calculated 2-d impedances for a set of realisations is then used as an estimate of their error. This is also the procedure adopted by McNeice and Jones (2001).

3.5.2 Phase tensor analysis

As already shown, galvanic distortion is frequency independent and affects the amplitude relationships between measured electric and magnetic fields leaving the phase unaltered. Caldwell et al. (2004) define the magnetotelluric phase tensor and show that it can provide a distortion free assessment of the level of regional dimensionality and recover the regional geo-electric strike direction if the data are shown to be 2-d (or the closest equivalent if 3-d) without making any assumptions about the conductivity structure. In other words, unlike Groom-Bailey decomposition a 3-d regional conductivity structure can be accommodated with this method. They also suggest that the information contained within the phase tensor can be usefully displayed as an ellipse constructed using rotationally invariant parameters of the tensor. Data sets can then be visualised by constructing phase tensor ellipses at each frequency and site, to show lateral and depth variations in dimensionality.

Splitting the measured impedance tensor into real and imaginary parts gives:

$$\mathbf{Z}_m = \mathbf{X}_m + i\mathbf{Y}_m \tag{3.58}$$

From Equation 3.51:

$$\mathbf{Z}_m = \mathbf{C}\mathbf{X}_r + i\mathbf{C}\mathbf{Y}_r \tag{3.59}$$

where $\mathbf{C}$ is the unknown, real distortion tensor. The phase of a complex number is the ratio of its real and imaginary parts, hence Caldwell et al. (2004) define the MT phase tensor as:

$$\mathbf{\Phi}_m = \mathbf{X}_m^{-1}\mathbf{Y}_m \tag{3.60}$$

or from Equation 3.59:

$$\mathbf{\Phi}_m = (\mathbf{C}\mathbf{X}_r)^{-1}(\mathbf{C}\mathbf{Y}_r) = \mathbf{X}_r^{-1}\mathbf{Y}_r \tag{3.61}$$

Hence (3.60) and (3.61) can be equated:

$$\mathbf{\Phi}_m = \mathbf{X}_m^{-1}\mathbf{Y}_m = \mathbf{X}_r^{-1}\mathbf{Y}_r \tag{3.62}$$

showing that the phase tensor is, as expected, unaffected by the distortion tensor $\mathbf{C}$. Expanding Equation (3.60) in terms of the real and imaginary components of the impedance tensor, the phase tensor becomes:

$$\begin{bmatrix} \Phi_{11} & \Phi_{12} \\ \Phi_{21} & \Phi_{22} \end{bmatrix} = \frac{1}{det(\mathbf{X})} \begin{bmatrix} X_{22}Y_{11} - X_{12}Y_{21} & X_{22}Y_{12} - X_{12}Y_{22} \\ X_{11}Y_{21} - X_{21}Y_{11} & X_{11}Y_{22} - X_{21}Y_{12} \end{bmatrix} \tag{3.63}$$

where $det(\mathbf{X}) = X_{11}X_{21} - X_{21}X_{12}$ is the determinant of $\mathbf{X}$.

If the conductivity structure is 1-d with $\mathbf{Z}$ taking the form of Equation (3.35), making use of Equation (3.34) the phase tensor reduces to:

$$\mathbf{\Phi} = \begin{bmatrix} Y_{1-d}/X_{1-d} & 0 \\ 0 & Y_{1-d}/X_{1-d} \end{bmatrix} = (Y_{1-d}/X_{1-d})\mathbf{I} = \tan(\phi)\mathbf{I} \tag{3.64}$$

where $\mathbf{I}$ is the identity matrix. Hence the phase tensor is invariant under rotation and can be described by one scalar quantity, the tangent of the conventional MT phase for a 1-d structure.

For the more general case, as with any real rank 2 tensor, three coordinate invariants and a direction are required to fully describe the phase tensor. The simplest coordinate invariants are the trace, skew and determinant given by

$$\begin{aligned} tr(\mathbf{\Phi}) &= \phi_{11} + \phi_{12} \\ sk(\mathbf{\Phi}) &= \phi_{12} - \phi_{21} \\ det(\mathbf{\Phi}) &= \phi_{11}\phi_{22} - \phi_{12}\phi_{21} \end{aligned} \tag{3.65}$$

However, given that functions of the invariants are themselves invariant, Caldwell et al. (2004) suggest adopting a system used by Bibby (1986), which uses the maximum and minimum values of the tensor and the skew angle beta given by:

$$\Phi_{min} = (\Phi_1^2 + \Phi_2^2)^{1/2} - (\Phi_1^2 + \Phi_2^2 - det(\mathbf{\Phi}))^{1/2} \tag{3.66}$$

$$\Phi_{max} = (\Phi_1^2 + \Phi_2^2)^{1/2} + (\Phi_1^2 + \Phi_2^2 - det(\mathbf{\Phi}))^{1/2} \tag{3.67}$$

$$\beta = \frac{1}{2}\tan^{-1}\left(\frac{\Phi_2}{\Phi_1}\right) \tag{3.68}$$

where

$$\Phi_1 = tr(\mathbf{\Phi})/2 \tag{3.69}$$

$$\Phi_2 = sk(\mathbf{\Phi})/2 \tag{3.70}$$

The phase tensor can now be re-expressed in terms of these parameters:

$$\mathbf{\Phi} = \mathbf{R}^T(\alpha - \beta)\begin{bmatrix} \Phi_{max} & 0 \\ 0 & \phi_{min} \end{bmatrix}\mathbf{R}(\alpha + \beta) \tag{3.71}$$

where $\mathbf{R}$ is a rotational matrix of the form of Equation 3.39, and

$$\alpha = \frac{1}{2}\tan^{-1}\left(\frac{\Phi_{12} + \Phi_{21}}{\Phi_{11} - \Phi_{22}}\right) \tag{3.72}$$

The angle β is akin to the Swift-skew parameter of the impedance tensor and

gives a measure of the asymmetry of the phase tensor, becoming large where 3-d effects are significant. α expresses the tensor's dependence on the coordinate system and in a 2-d Earth it represents the geo-electric strike direction ($\pm 90^0$). These three coordinate invariants plus the angle α can be used to construct an ellipse (Figure (3.2)), graphically representing the phase tensor.

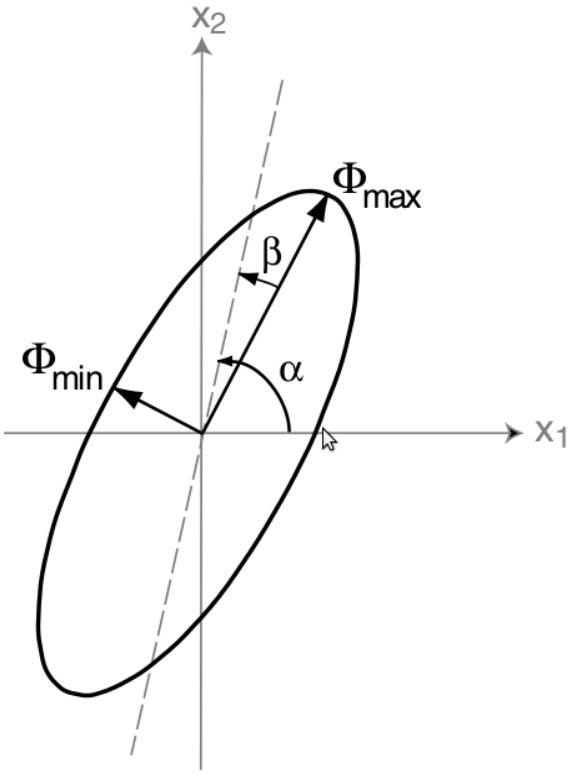

Figure 3.2: Graphical representation of the phase tensor. X_1 and X_2 are the axes of the measurement coordinate system. From Caldwell et al. (2004).

Where the subsurface is 1-d Φ_{max} and Φ_{min} become indistinguishable and the ellipse becomes a circle with radius equal to the conventional MT phase. In this situation, α becomes poorly defined. In a 2-d environment, the degree of ellipticity indicates the strength of the regional 2-dimensionality, with the major axis of the ellipse pointing in the direction of highest phase difference. β values greater than 3 are considered to indicate significant 3-d effects (Caldwell et al., 2004). Caldwell et al. (2004) point out however, that β values less than 3 cannot

be used to rule out 3-d effects, suggesting that rapid lateral variations of α are also a good indicator that they are present. Phase tensor ellipses can be plotted as a pseudo-section along a profile as a way of visualising the undistorted data over a range of frequencies. This type of analysis has become common place among MT practitioners and examples of its application can be found in Heise et al. (2007) and Hill et al. (2009).

3.5.3 Static-shift correction using independent data

Distorted amplitudes of the measured electric field caused by galvanic effects manifest themselves as vertical shifts of apparent resistivity curves when plotted against period on a log-log scale. If ignored, these can lead to significant misinterpretation where inverted resistivities are shifted by a factor equal to the amount of parallel shift of the apparent resistivity curves, and inverted depths are incorrect by a factor related to the square root of the resistivity shift (Simpson and Bahr, 2005).

One approach to correcting the static shift of apparent resistivity curves is to use an independent measurement of the shallow (relative to the depth of investigation of the MT survey) conductivity structure. Sternberg et al. (1988) suggest using a transient electromagnetic (TEM) sounding at each MT site. The TEM method uses a controlled magnetic source field and measures only the secondary magnetic field which is, as already discussed, largely unaffected by galvanic distortion. The depth of penetration of the complimentary TEM sounding needs to be deep enough both to image below any local inhomogeneities that may be causing the MT static shift and such that there is an overlap with the penetration depth of the MT data at the highest frequencies of the MT survey. The TEM method works in the time-domain: in very simplistic terms a magnetic field is produced by turning off the current in a stepwise fashion in a loop of wire laid out horizontally

on the ground (typically square with one side measuring between 50 and 500 m). As the magnetic field diffusely propagates into the ground it induces transient currents which attenuate the magnetic field. Transient currents produce a secondary magnetic field which is measured at the surface (as the transient voltage in a receiver loop) at specific integration times after the current has been switched off. The transient voltage data can then be converted into apparent resistivity at each integration time using the non-linear equation for EM fields due to a loop on a homogeneous half-space (Nabighian, 1988).

Sternberg et al. (1988) advocate the use of a simple scaling of the TEM sounding curve (i.e. apparent resistivity plotted against integration time). In this case, the TEM time scale or integration time (in ms) is simply divided by 200, which then allows direct comparison between TEM and MT apparent resistivity curves using the new time scale for the TEM data and the standard sounding period (in seconds) for the MT data (see Figure 3.3). This is justified using three different approaches by the authors. First it is shown empirically by the results of TEM and MT forward modelling of a layered subsurface (with no galvanic scatterers present). They show that for a large range of models the apparent resistivity curves of both methods overlap very accurately when this time shift is applied. Furthermore, they show that the method is not highly sensitive to the exact factor used. Second, they show that the frequency domain skin depth relations for the MT method differs from the time domain, TEM equivalent by a factor of 194 - remarkably close to their empirically derived time-shift factor. Finally, they static shift corrected some real data using this method, and then compared the results to those derived from joint inversion of the two data sets (where the inversion allowed for a static shift in the MT data). The static shift corrections were in agreement to better than one tenth of a decade at each site. This method for quantifying static shift in MT data does have some problems. Often the overlap

between the lowest frequency TEM data and highest frequency MT data is less than a decade which is not enough to reliably identify and quantify static shift especially if either data are noisy. The analysis carried out by Sternberg et al. (1988) is based on 1-d modelling and as such may not be reliable where the subsurface conductivity structure is multi-dimensional (Jiracek, 1990).

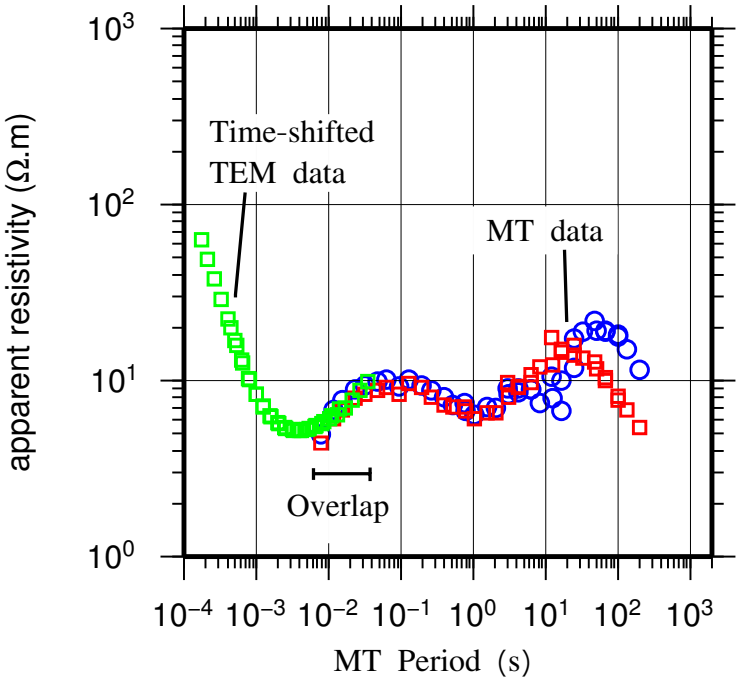

Figure 3.3: MT data (blue and red symbols) plotted with scaled TEM data (green

Chapter 4

Data collection, processing and distortion analysis

4.1 Introduction

Over 3 field seasons, MT data have been collected at a total of 43 sites (Figure 4.1) around the Manda-Hararo rift zone. Transient electromagnetic (TEM) soundings were co-located at 34 of the MT sites for static shift control. Broadly, two distinct regions have been targeted; the northern region of the rift zone (the Dabbahu magmatic segment or DMS) where active rifting has been observed since 2005, and an area further south which is morphologically similar but has not undergone any active rifting in very recent times (the Hararo magmatic segment or HMS). This chapter will give details of the site locations and rationale, data collection and processing, and an assessment of the dimensionality and distortion inherent within the data.

4.2 Site locations

Figure 4.1 is a map showing the site locations and nomenclature. The sites within each main area (DMS and HMS) are arranged as one long profile crossing the rift, and some extra sites (to the north in both cases) added to target specific features of interest as indicated in the detailed descriptions below.

4.2.1 The DMS profile

The DMS profile is an approximately linear set of seventeen sites which crosses perpendicularly to the centre of the currently active Dabbahu rift. The MT profile is 50 km long and sites are spaced seven kilometres apart at the edges reducing to about 3 km at the rift centre where higher resolution was desirable. However, linearity and spacing of the sites are not perfect due to the difficult nature of the heavily rifted terrain. The main objective was to constrain the location of partial melt supplying the dykes.

All sites except one were occupied during the 2008 field season, using helicopter access at most locations. The long period data at the western-most site (805) were of very poor quality, so a new site (106) was occupied during the later 2010 field campaign. The data from site 805 will not be used in any of the analysis described in later chapters.

4.2.2 The HMS profile

An equivalent profile across the HMS (approximately 60 km to the south) consisted of 15 sites. There has been no significant rifting events or volcanic eruptions along this segment in the recent past and so comparison of this with the DMS profile allows comparisons of the melt distribution below active and

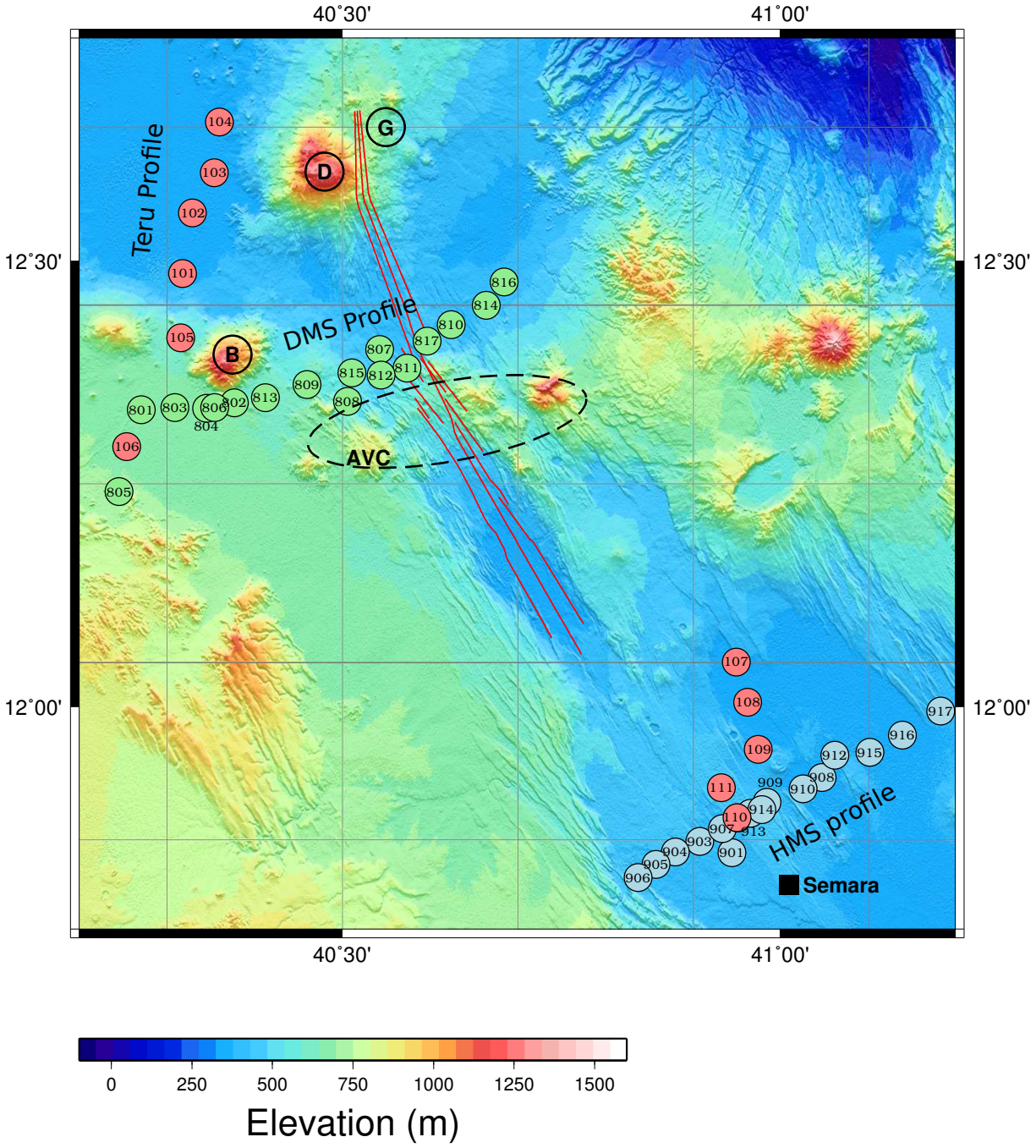

Figure 4.1: Locations of all MT sites from 3 field seasons with topography (from SRTM data). Sites are coloured according the the year in which they were collected, but largely; green = DMS profile, blue = HMS profile, (northern) red = Teru profile, (southern) red = Saha profile. Red lines show the extent of recent dyke events. D, G, B and AVC are Dabbahu, Gab'ho and Badi volcanoes and Ado'Ale volcanic complex. Semara is the regional capital of Afar. The villages of Digdiga and Teru are approximately coincident with sites 801 and 101 respectively. Magnetic declination is less than 2 degrees.

inactive rift segments. All sites were occupied during a field campaign in 2009 and were accessed by four-wheel drive vehicle from a base in Semara, the regional capital of Afar. Due to the relative ease of identifying and accessing suitable site locations, the site spacing is more regular forming a near perfect profile.

4.2.3 The Teru Profile

Five sites form a 22.5 km line (named the Teru profile after a small village lying on the profile) from the western end of the DMS profile, heading NNE and passing Dabbahu volcano on its western side. Due to the subsidence and vent opening seen at Dabbahu volcano in the initial September 2005 dyke event, it is known that shallow magma storage zones exist below Dabbahu volcano which are somehow connected to the rift (Wright et al., 2006). This part of the survey was conducted in an attempt to image the melt associated with Dabbahu volcano and look at the connectivity between inferred deeper supply zones of partial melt. The sites are somewhat distant from the summit of Dabbahu volcano which may be a limiting factor to the extent to which conclusions can be drawn.

4.2.4 The Saha profile

Five sites form a short transect through an area known as Saha, just to the north of the HMS profile. One site on this profile (110) is common to the HMS profile. InSAR imaging indicated that the region had been undergoing steady subsidence since the beginning of the rifting cycle (T. Wright, pers. comm., 2009). The wavelength of the signal suggests a deep source of deformation, with one hypothesis being that partial melt is migrating from here towards the active rift segment. With this in mind, four new MT sites were occupied in 2010 with the hope of

testing the idea that a deep zone of partial melt exists here. Unfortunately, unseasonably large amounts of rain fell prior to the fieldwork causing flooding of the Saha plain which limited how far north the sites could be deployed. However, given the deep crustal depth of the partial melt inferred from the InSAR studies, it was hoped that the long period data would still be sensitive to it.

Data that were collected from site 901 are not included in any of the profiles listed above as it was test site deployed to calibrate two different data recording systems and not intended for analysis (see Section 4.3). Aside from sometimes uncomfortable working conditions, Afar is in many ways an ideal location for an MT study due to the almost complete lack of technical civilisation. All of the sites in the north (DMS and Teru profiles) are located many tens of kilometres from the nearest power line or road, and the majority of the very small villages that exist do not have any kind of electricity supply; all things that normally make large contributions to noise in the recorded data. Sites further south (HMS profile) were all deployed at least 10 Km to the north-west of the main road and Semara. The magnetic declination from true north is less than 2 degrees in Afar, but was none the less corrected for in later analysis. The survey area does not generally have topographic features of a scale which might distort the MT response and the nearest ocean is sufficiently far away as to not affect the data. Vegetation cover is limited to a sparse number of small shrubs and trees which, where possible, were used to provide shelter from the sun for equipment and personnel!

4.3 Field procedures

SPAM Mk3 (Ritter et al., 1998) data acquisition systems were used to record the MT data in 2008, whilst in 2009 both SPAM Mk3 and newly developed Mk4

equipment were used. One test site was occupied with both systems in order to check consistency. In 2010 the data were collected using only SPAM Mk4 systems. Both systems are capable of real-time viewing of time-series and basic analysis (principally computation of transfer functions) which ensures that mistakes with equipment set-up or malfunctions (damaged cables, for example) can be rectified before the main run of data collection at each site. Three sets of MT equipment were taken into the field so the aim was to have two of them acquiring data at all times, however this was not always possible for logistical reasons. At the vast majority of sites data were recorded for 1-2 days.

Orthogonal components of the magnetic field were recorded using pairs of Metronix MFS05 or MSF06 broad band induction coils aligned to magnetic north and east, and buried to a depth of approximately 0.5 m to alleviate wind noise and carefully levelled so that only the horizontal component of the magnetic field was being measured. The vertical magnetic field was not measured due to the already difficult working conditions. The magnetic declination in Afar is very small (less than 2 degrees east) but was nonetheless corrected for when strike directions were computed. The electric field was measured using pairs of non-polarising Pb-PbCl porous pot electrodes with a dipole length of at least 50 m, but more usually around 100 m. For sites within the rocky rift, small (similar in scale to the dipole length) pockets of sedimentary material were identified on SPOT imagery and used to deploy the equipment, ensuring good electrical contact between electrode pairs. Most sites on the HMS, Teru and Saha profiles and those on the western end of the DMS profile were within sedimentary cover rocks. The extremely dry nature of the immediate subsurface meant that electrodes needed to be buried in a salty Bentonite mud mixture in order to maintain good electrical contact with the ground and keep the resistance between electrode pairs down. Prior to the

field work electrodes were put in pairs with similar self potentials.

All sensors feed into a *sensor box* located at the centre of the array. The sensor box filters the analogue signals to remove high frequencies before they are amplified and sent via cable to the *remote box*. At the remote box the signals are digitised and recorded in several user determined frequency bands each with its own sampling rate and digital high and low pass filters. This allows the data to be stored efficiently by only recording pre-scheduled blocks of the high frequency data whilst long period bands are recorded continuously.

TEM data were acquired using a Geonics PROTEM-37 system with a square source loop of 100 x 100 m and effective receiver loop size of 31.4 m^2. The time rate of decay of magnetic flux was recorded over integration times from 0.25 to 120 s. TEM data were not collected at all sites due to time or mobilisation constraints.

The equipment used were either purchased for this project (SPAM Mk4); loaned from NERC Geophysical Equipment Facility (GEF) (SPAM Mk3, MFS05 induction coils, TEM); or kindly loaned from the Geophysical Instrument Pool Potsdam (part of GeoForschungsZentrum) through the auspices of Oliver Ritter and Ulrich Kalberkamp (BGR, Hannover) (some SPAM Mk3 equpment in 2008, and MFS06 induction coils in 2010). Some electrodes were purchased for this project and some were from previous field work. All were manufactured by SDEC, France. Solar panels and 12 v batteries were used to power the equipment which were also loaned from NERC GEF.

Personnel in the field team included Prof. Kathy Whaler, Graham Dawes,

Mohammednur Desissa[1], Alf Ball (2009 only), and the author (2009, 2010) from the School of GeoSciences, University of Edinburgh; Sophie Hautot[2] from Université de Bretagne Occidentale (UBO), France; Shimeles Fisseha (2008, 2010) and Tigistu Haile (2010) from the Institute of Geophysics, Space Sciences and Astronomy, Addis Ababa University, Ethiopia and Yohannes Lemma (2008) from the Geological Survey of Ethiopia. Helicopter and pilot Chris Stewart were provided in 2008 by Everett Aviation (Kenya), and 4x4 vehicles and many drivers (who often helped in the field) were arranged via Ethio-Der Tour and Travel. Much logistical help in Addis Ababa, particularly with importing and exporting equipment, was received from Atalay Ayele, Shimeles Fisseha and Elias Lewi at the Institute of Geophysics, Space Sciences and Astronomy, Addis Ababa University.

4.4 Processed MT Data

All data were processed using Alan Chave's code BIRRP (Chave and Thomson, 2004), a description of which is given in Section 3.3. The transfer function estimations used here were computed by the author, with the exception of the 2008 data which were processed by Sophie Hautot. It was not possible to implement the use of a remote reference at all sites because there were not always two stations recording simultaneously; however, the lack of sources of artificial noise meant that none of the transfer function estimations used here were computed with a remote reference site. The range of frequencies for which good transfer functions were estimated was from 100 to 10^{-3} Hz (1000 s period) with approximately 60 percent of sites achieving data to the longest periods. At many of the sites where MSF06 coils were used (all data recorded in 2010), transfer function estimations

[1]now at Geological Survey of Northern Ireland
[2]now at Imagir, IUEM, France

at higher frequencies (up to 10,000 Hz) were possible. Figures 4.2 to 4.6 show the impedances as apparent resistivity and phase for all four components of the transfer functions at all sites, where the XY components are computed using the north-south electric and east-west magnetic fields and YX component the opposite pairs. The minor diagonal element data are plotted as pseudo-sections across the four main profiles with (log) period used as a depth-proxy which are shown in Figures 4.7 to 4.10. Note that major diagonal elements of the impedance tensor (shown by lighter colours in Figures 4.2 to 4.6) are much smaller in magnitude because there is little or no 3-d induction and there data have been recorded in a near strike coordinate system. Consequently diagonal element data tend to be more dominated by noise. Note that these data are not used in modelling.

4.5 Dimensionality and distortion

Before any modelling of the MT data can be undertaken its important to gain an intimate understanding of the dimensionality and possible distortion inherent within it; an interpretation based on a 1-d subsurface with no local distortion will lead to erroneous conclusions if the data are inherently 3-d in a local or regional context. Modelling tools for MT data are under continuous development. At present much effort is being put into the development of software whereby the subsurface is assumed to be 3-d, although 1-d or 2-d interpretation is still the norm. If analysis of a given data set suggests that a 2-d interpretation is applicable then arguably the most important parameter to recover accurately is the geo-electric strike direction (i.e. the horizontal direction in which conductivity is constant) (McNeice and Jones, 2001). The aim of the subsections that follow is to assess the validity of a 2-d interpretation of this data set, estimate the best fitting strike direction for the two main profiles and remove the effects of local

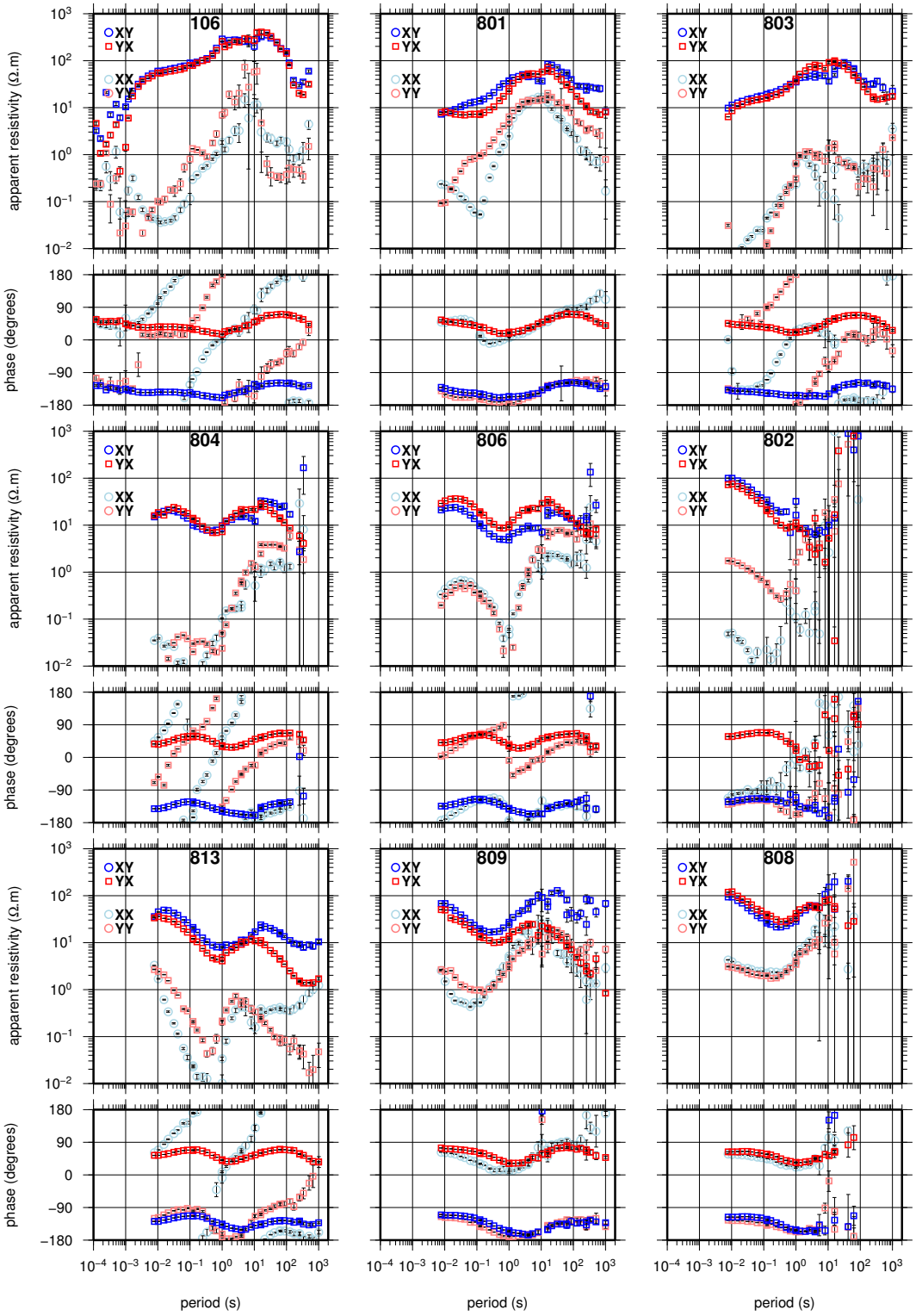

Figure 4.2: Transfer function estimations for the western sites of the DMS profile, with sites ordered from west (top left) to east (bottom right). Site numbers are shown at the top of each panel (see Figure 4.1 for locations).

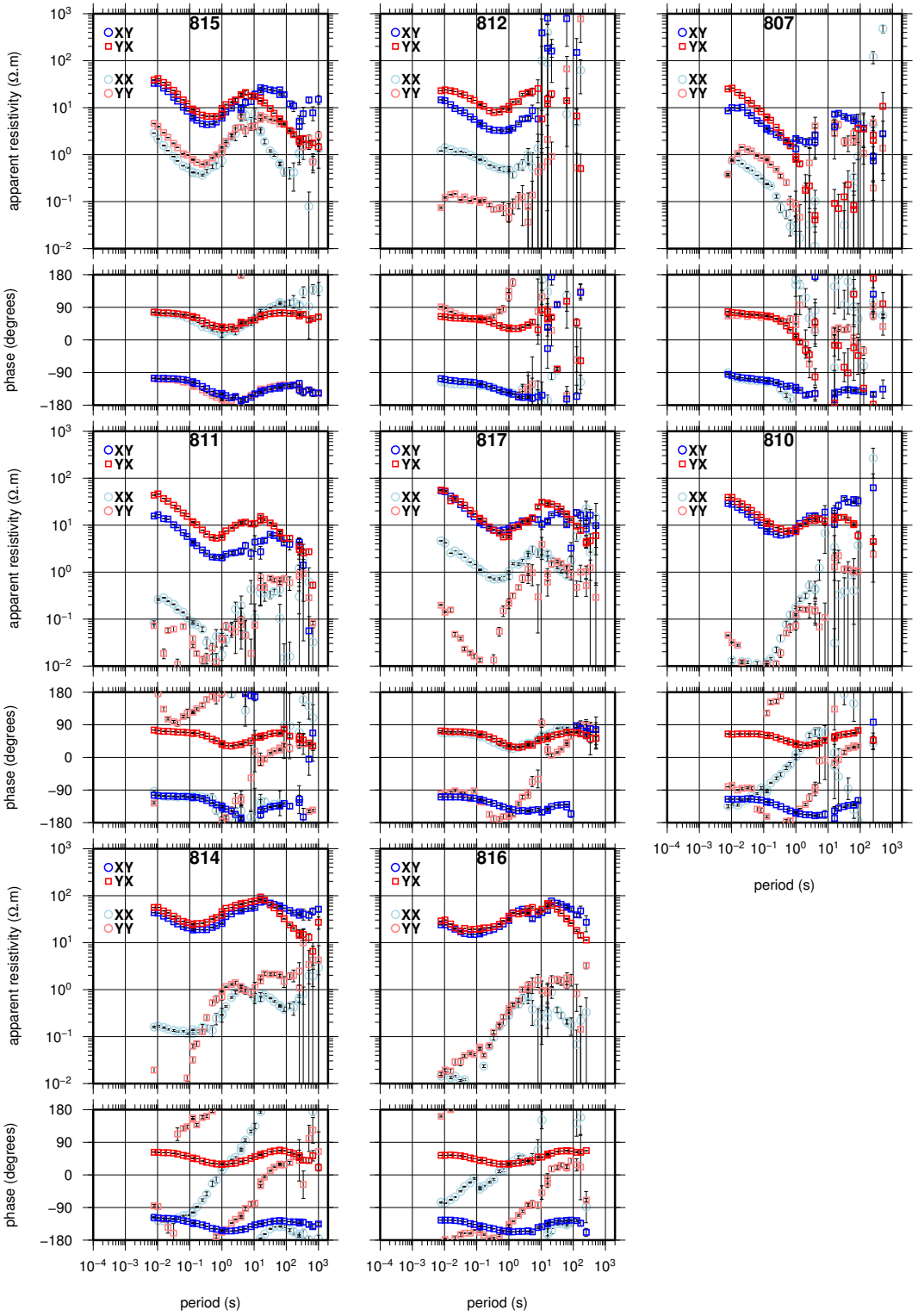

Figure 4.3: Transfer function estimations for the eastern sites of the DMS profile, with sites ordered from west (top left) to east (bottom right)

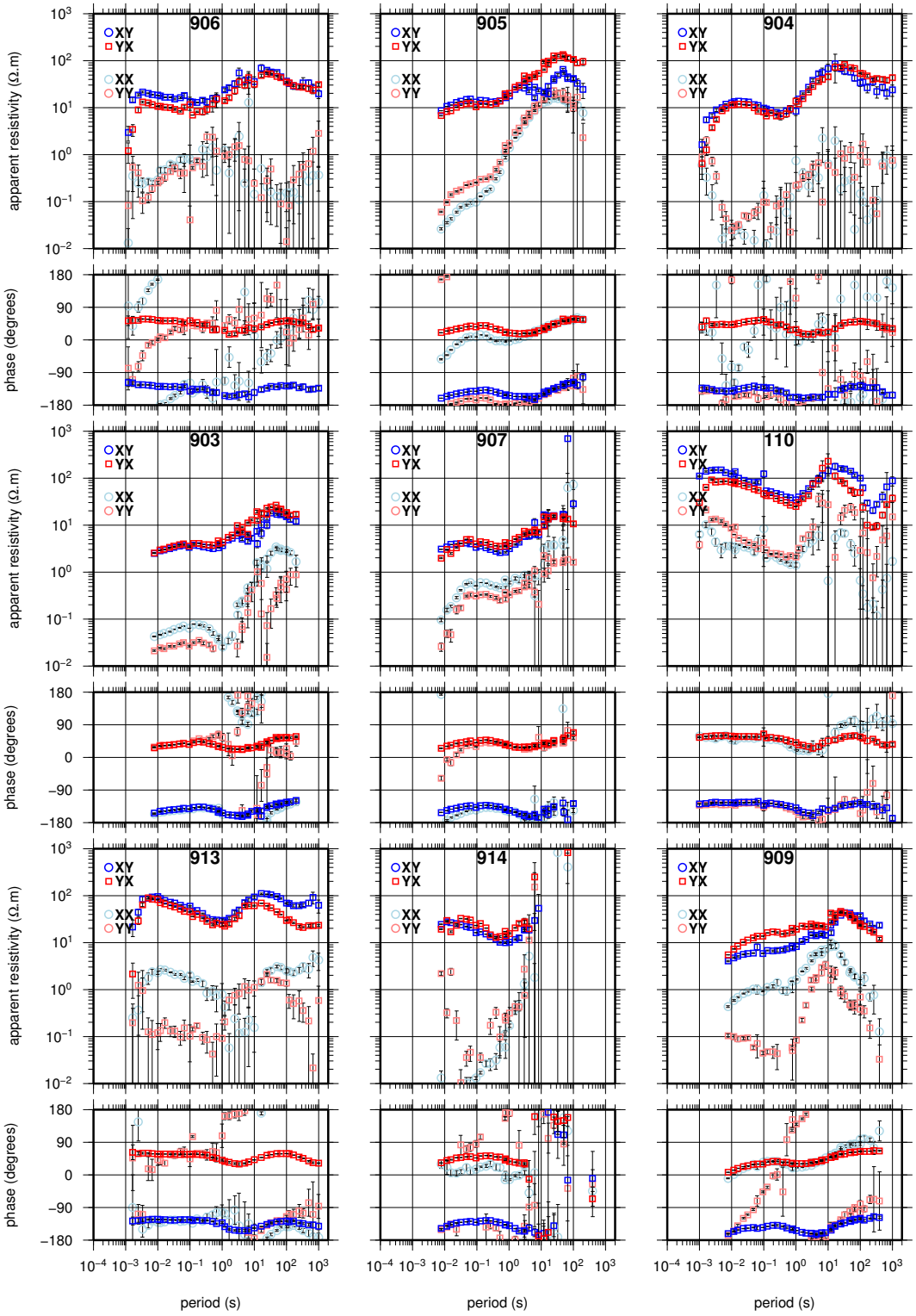

Figure 4.4: Transfer function estimations for the western sites of the HMS profile, with sites ordered from west (top left) to east (bottom right)

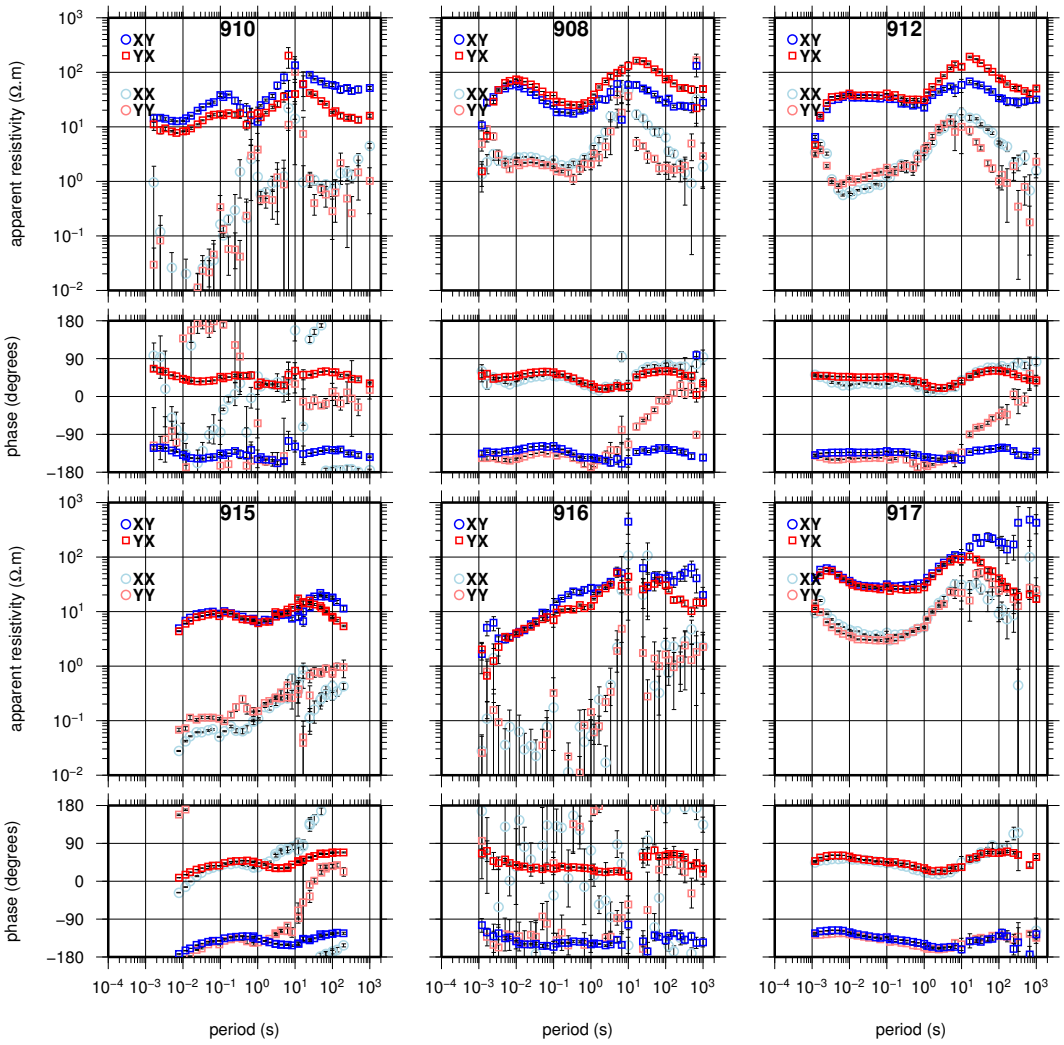

Figure 4.5: Transfer function estimations for the eastern sites of the HMS profile, with sites ordered from west (top left) to east (bottom right)

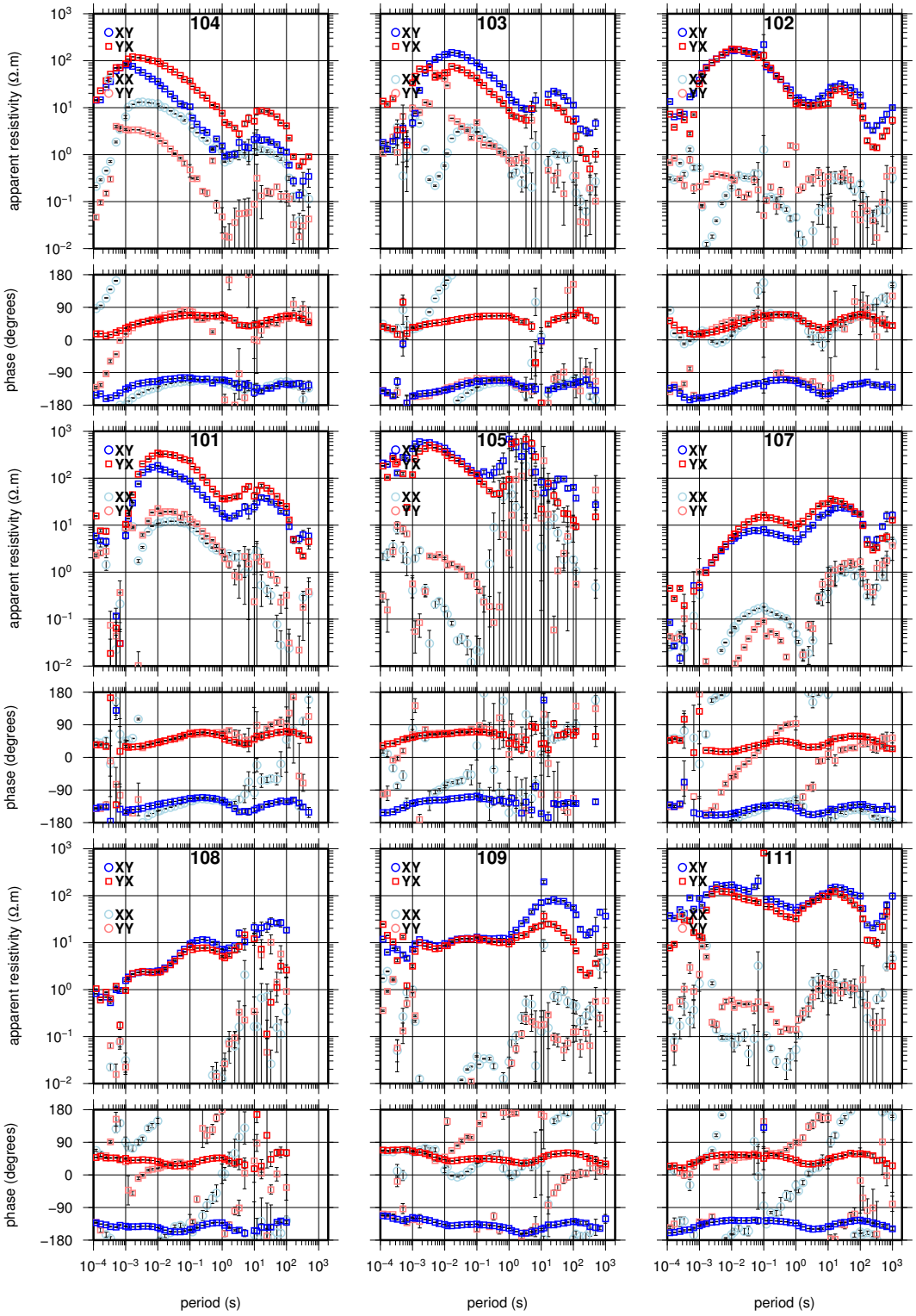

Figure 4.6: Transfer function estimations for the Teru and Saha profiles (with the exception of sites common to profiles shown in previous Figures).

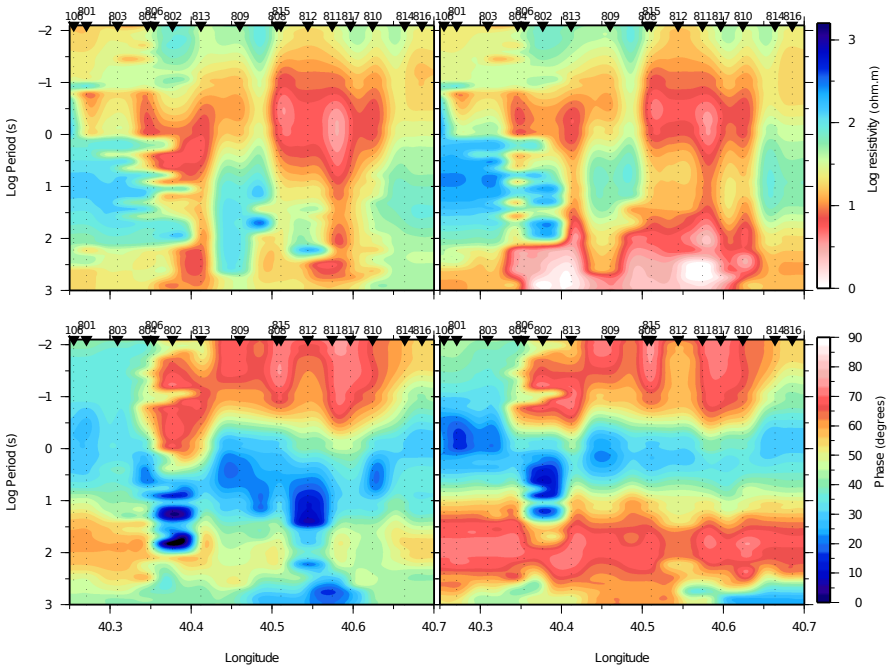

Figure 4.7: Pseudo sections of off-diagonal apparent resistivity (upper panels) and phase (lower panels) plotted against (log) Period for the Dabbahu profile from west (left) to east (right). XY components are shown on the left, YX on the right. Black dots show where data points exist.

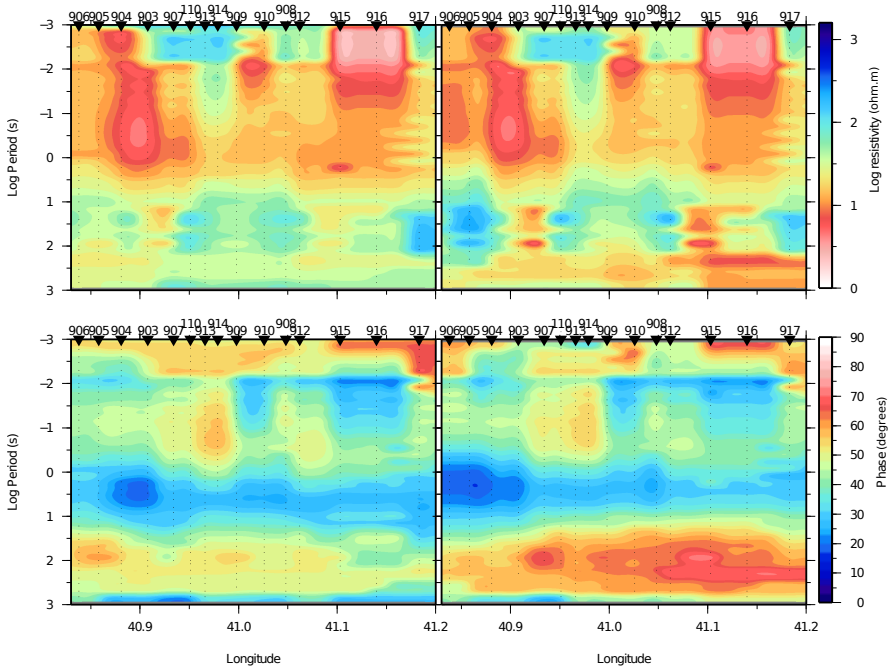

Figure 4.8: As Figure 4.7 for Hararo profile

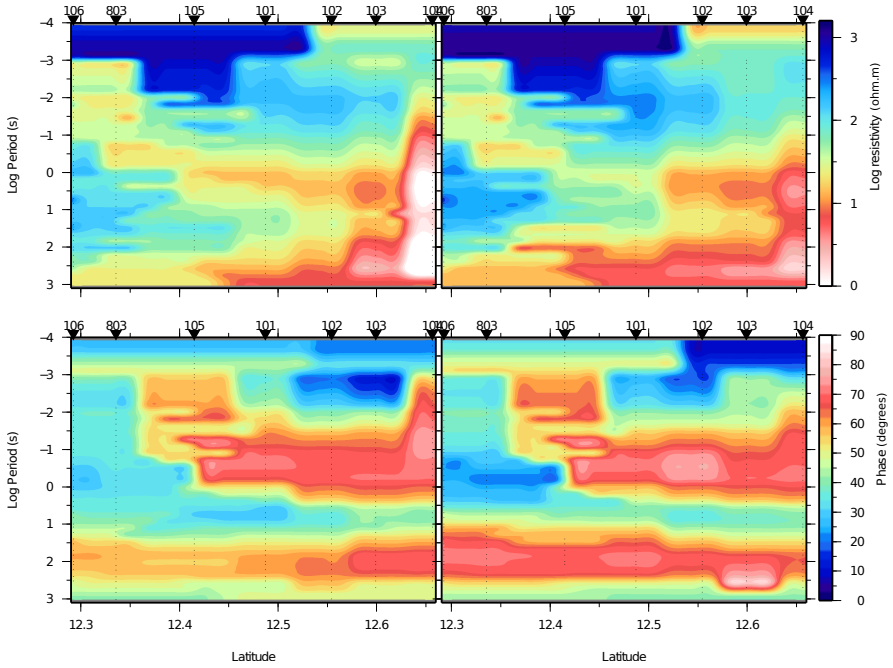

Figure 4.9: As Figure 4.7 for Teru profile, plotted from south (left) to north (right)

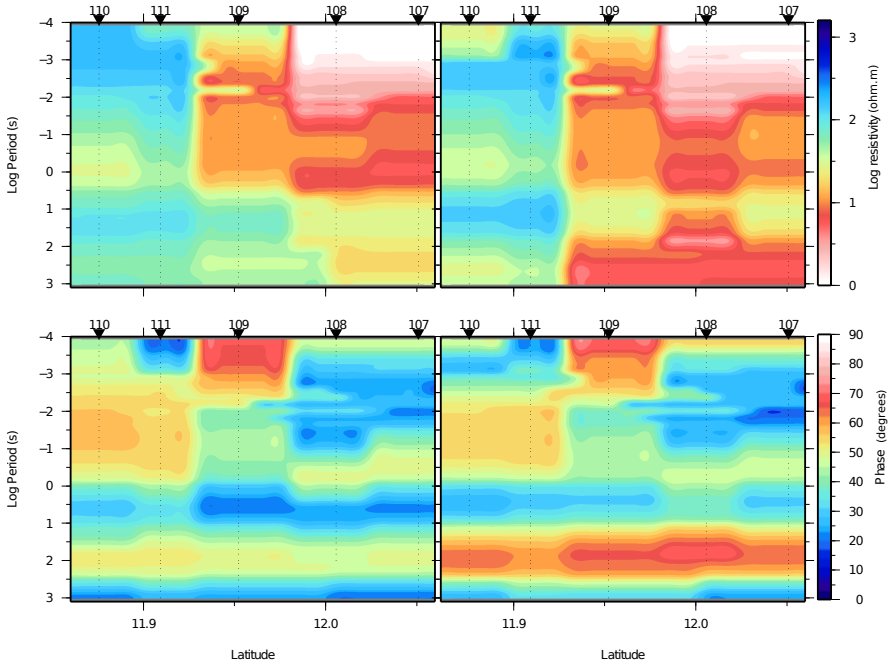

Figure 4.10: As Figure 4.9 for Saha profile

distortions of the electric field. The theory behind the methods used was given in Chapter 3.

4.5.1 Phase tensor analysis

Phase tensor analysis uses only the phase relationships of the complex MT impedances to estimate the level of complexity of the underlying structures and it is therefore unbiased by the effects of static shift. As shown by Caldwell et al. (2004), a convenient way of displaying the phase tensor information is as an ellipse whose major and minor axes are in the direction of, and scaled to the maximum and minimum, tensor values. In the 1-d case the phase will be approximately equal in all directions and departures from a circle are caused purely by data noise/errors. In the 2-d case the degree of ellipticity will be indicative of the strength of the 2-d structure, and the axes will point in a direction perpendicular or parallel to the geo-electric strike direction. If the subsurface conductivity

structure is 3-d then a third coordinate invariant parameter of the tensor is required to fully describe it. In this study an angle known as β will be used which was fully described in Section 3.5.2.

Phase tensor ellipses are commonly shown either for one given period in map-view where their orientation is easily interpreted (Figure 4.11) or for all data along a specific profile as a pseudo-section where frequency is used as a depth proxy (Figures 4.12 to 4.15). The ellipses can also be coloured to portray further information; in the following figures; this is either the minimum phase value or β.

In Figures 4.11 to 4.15 it can be seen that above 1 Hz at nearly all sites the ellipses appear to be circular with beta values ubiquitously below 5° with the exception of a few very high frequency measurements. Below this frequency most areas show a higher level of complexity; both the DMS and HMS profile data show a higher degree of ellipticity, particularly between 1 and 0.1 Hz, with principal axes generally aligning orthogonally to the structure of the rift which is highlighted by the red lines in Figure 4.11. At greater depths, especially on the HMS profile, the degree of ellipticity tends to reduce again. High beta values are common on the DMS profile particularly at sites located near to the rift axis. This is indicative of a 3-d structure, although such values may also arise due to poor data quality. For example sites 807 and 802 have very large error bars and considerable scatter beyond periods of 1 s (Figures 4.2 and 4.3) which correspond with large beta values and randomly oriented ellipses in Figure 4.7. Both of the shorter profiles tend to show more circular ellipses through the entire frequency range.

The minimum phase angle shown by the colour of the ellipses in Figure 4.11 indicates the conductivity gradient with depth where high values (above 45°) show increasing conductivity. Phase changes precede apparent resistivity changes

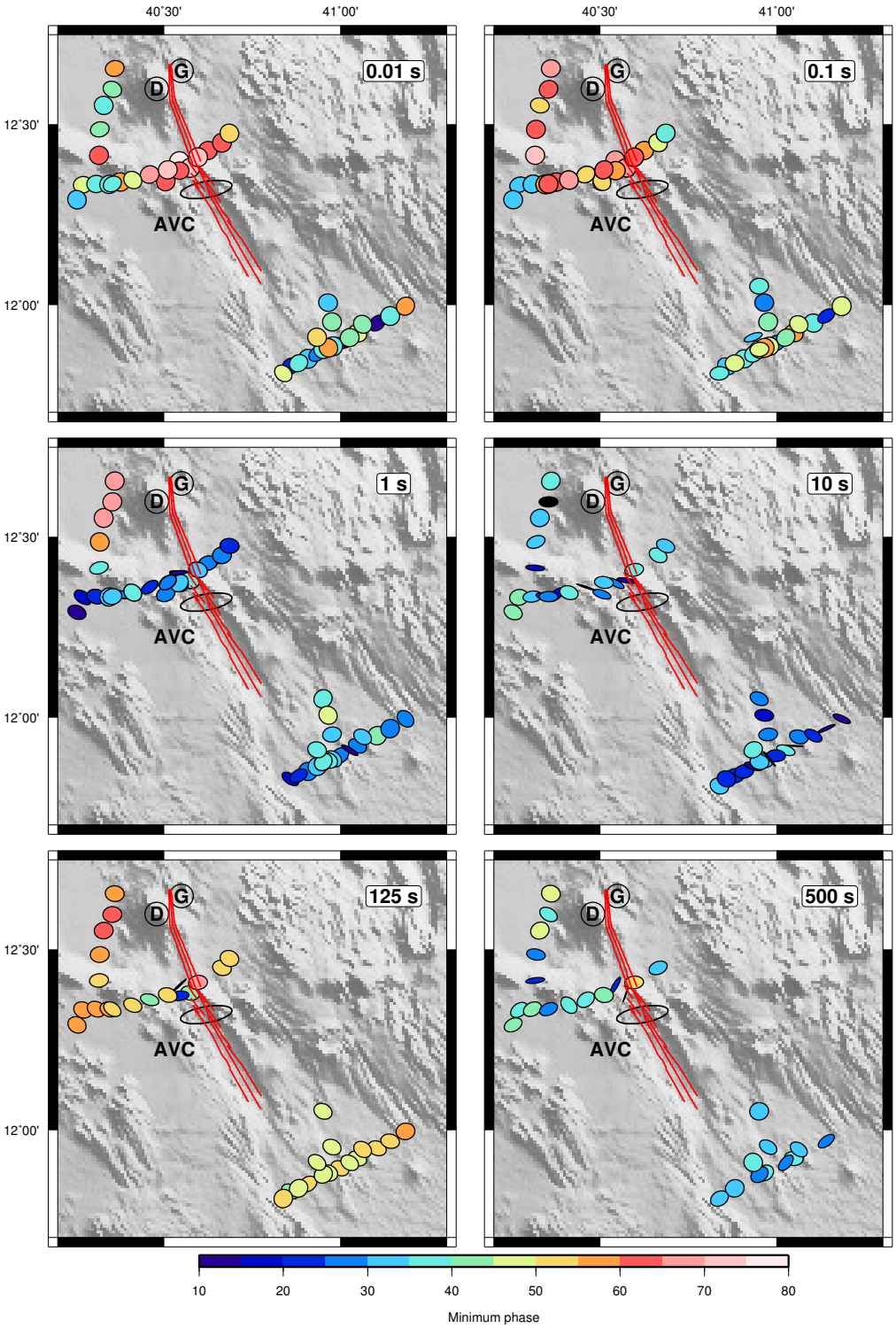

Figure 4.11: Phase tensor ellipses for all sites over a range of periods (given in seconds, top right corner of each plot). Ellipses are coloured according to their minimum phase angle using the scale shown at the bottom. Red lines show the location of dykes.

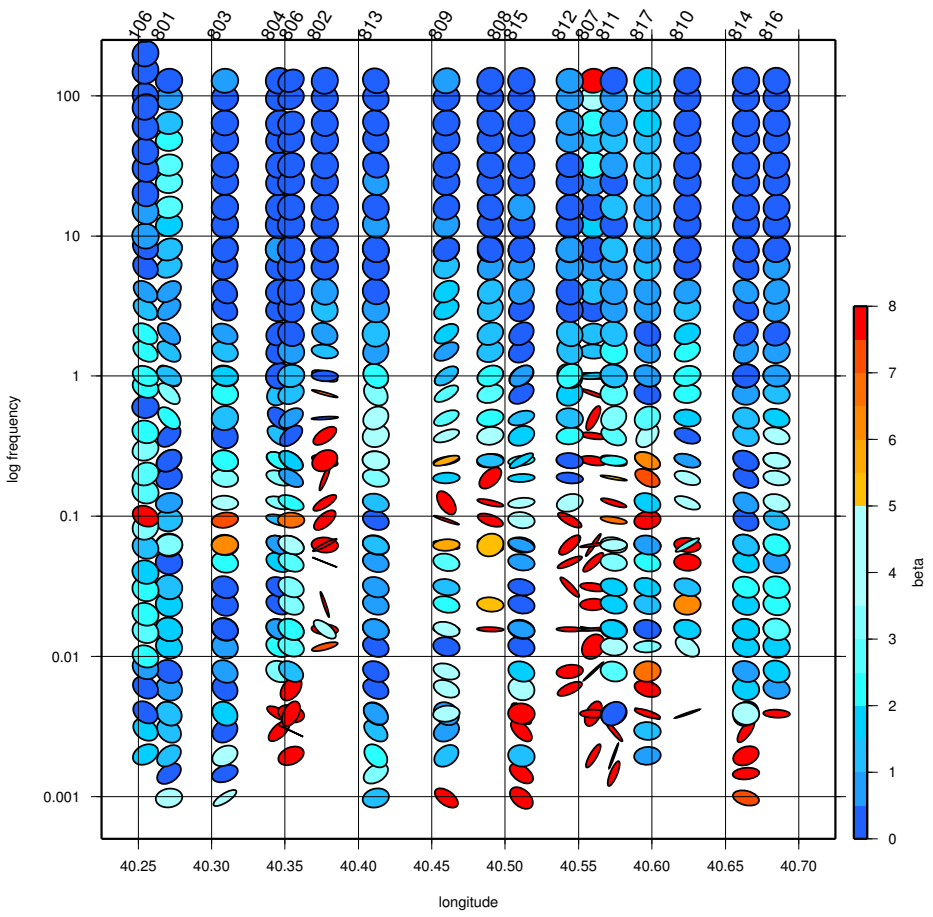

Figure 4.12: Phase tensor ellipses shown as pseudo section for DMS profile using log frequency as a proxy for depth. Ellipses are coloured by their beta angle values. Poor quality data cause large amounts of scatter and high beta values particularly in long period data at some sites, e.g. 802, 807 and 811.

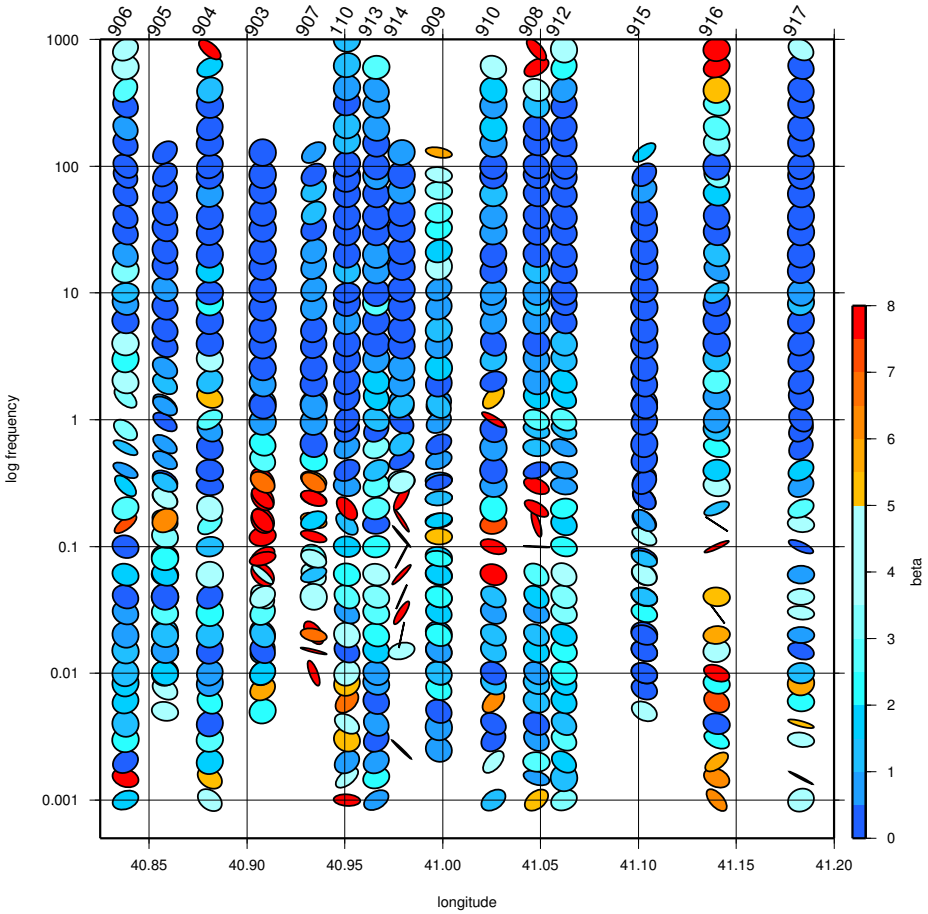

Figure 4.13: As Figure 4.12 for HMS profile.

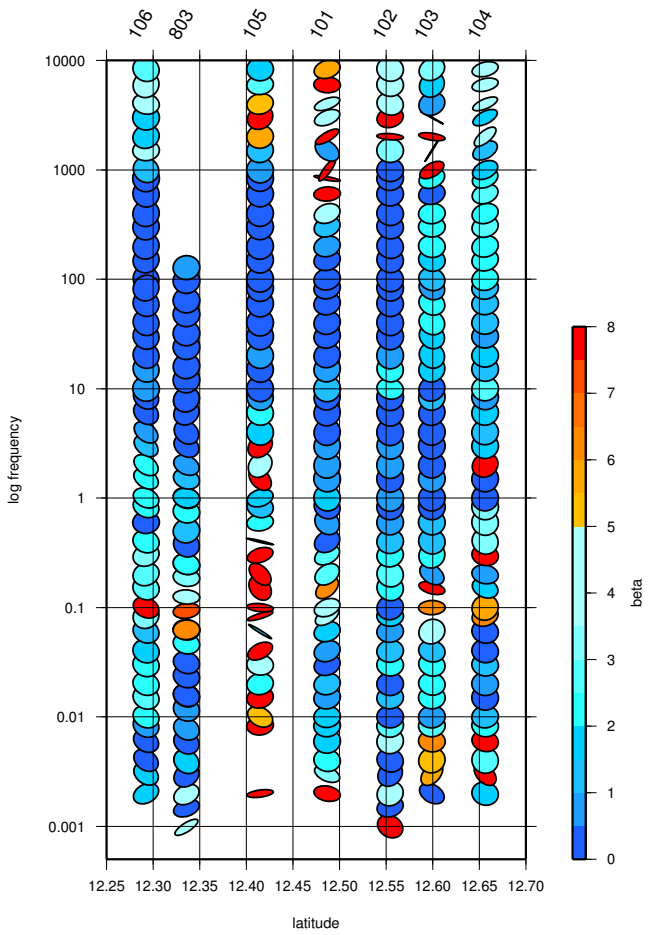

Figure 4.14: As Figure 4.12 for Teru profile.

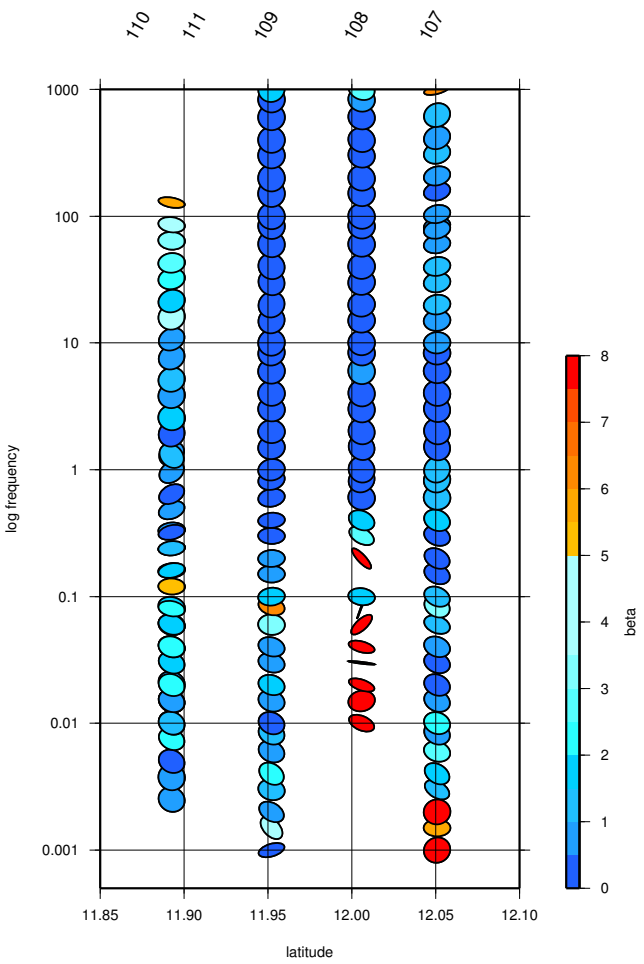

Figure 4.15: As Figure 4.12 for Saha profile.

(viewed as a function of increasing period). The pattern of this parameter is variable throughout the data set and can also be seen in the pseudo sections of Figures 4.7 to 4.10. Ignoring the very high frequencies that are only available at some sites, then general pattern seen is that of high phase in the high frequencies of the data (1-10 Hz), decreasing between 0.1 and 1 Hz, rising again from 0.01 to 0.1 Hz before finally decreasing again at the lowest frequencies. This is generally mirrored in the apparent resistivity pseudo sections which usually follow a conductive-resistive-conductive-resistive pattern, particularly over the DMS and HMS profiles.

Rose histograms showing the angles of the directions of major and minor axes at all sites and periods are given in Figure 4.16 for each of the four profiles. Given that the high frequency data appear to be more or less 1-d (and thus giving a meaningless strike direction) only data with periods of 1 second or longer are shown in the rose histograms. Along each profile a dominant strike direction is apparent with little scatter with the exception of the data from the Teru profile. For the sites along the southern profiles arms of the rose diagrams are clearly defined between -20° and -30° (and 90° repetitions thereof). On the DMS profile there is a distinct modal group of the rose diagram between -10° and -20°. The Teru profile shows no clear modal strike angle with the rose diagram showing two distinct maxima at -10° to -30° and 0° to 20°. This is probably because the data tend to retain a 1-d signature throughout the period range at many sites.

4.5.2 Groom-Bailey decomposition

Groom-Bailey (GB) decomposition is a type of distortion analysis whereby the subsurface is assumed to be 1-d or 2-d with local, near surface 3-d inhomogeneities which can cause the electric field to be distorted due to the build-up of charge on

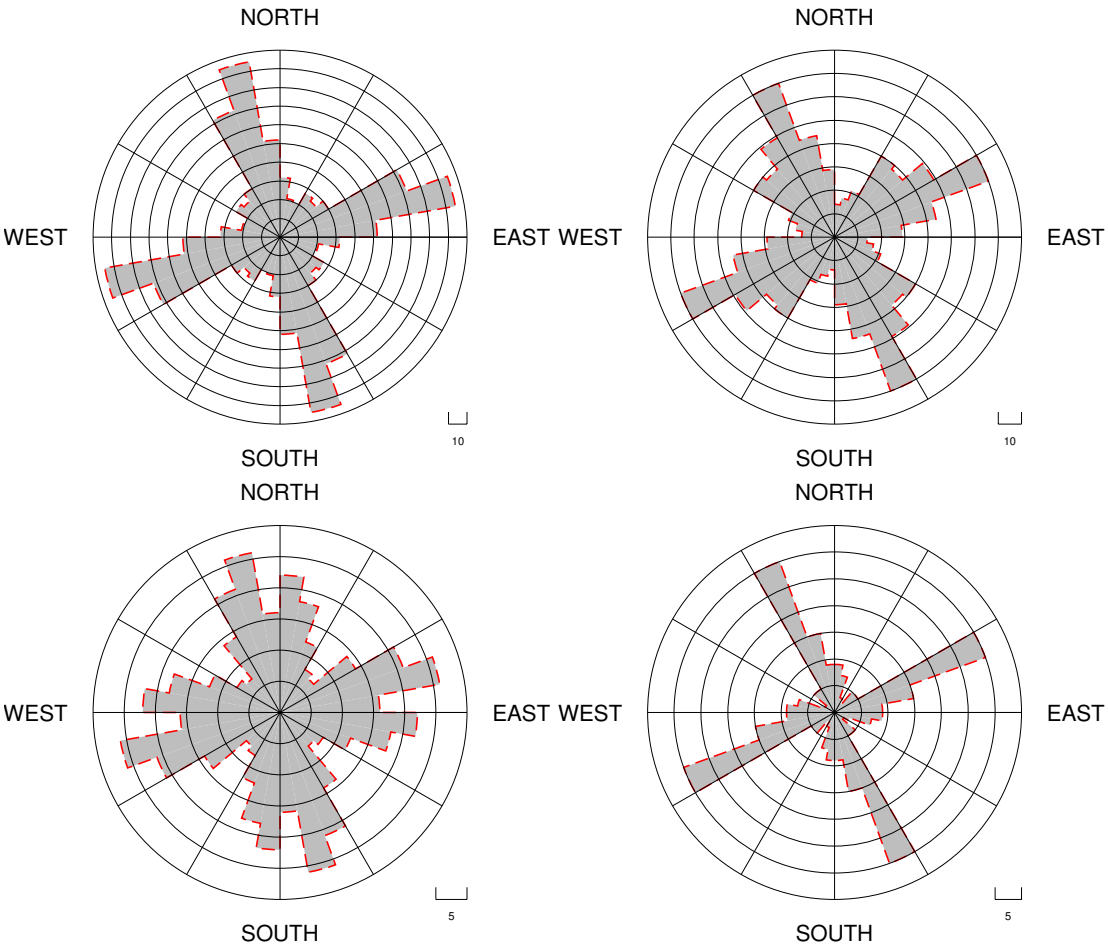

Figure 4.16: Rose diagrams showing the geo-electric strike angle according to phase tensor analysis using data at all periods longer than 1 second. Direction of both major and minor ellipse axes is shown for all periods at all sites on DMS and HMS profiles (top left & right), and Teru and Saha profiles (bottom left & right).

their surfaces (Groom and Bailey, 1989). The net effect in MT impedance data is known as galvanic distortion. As discussed in Chapter 3, in GB decomposition the measured impedance tensor is decomposed allowing the removal of some of the effects of galvanic distortion and accurate estimation of the regional geo-electric strike direction. A parameter known as 'site gain' cannot be determined by the method and if data are affected by galvanic distortion this manifests itself as a 'static shift' of apparent resistivity curves (see Figure 3.1 and surrounding discussion in Chapter 3).

Strike angles

The program 'strike' (McNeice and Jones, 2001) was first used on a site-by-site, period-by-period basis to gain a detailed understanding of the variation of Groom-Bailey decomposition parameters within the data set. The geo-electric strike angles obtained from this analysis are shown as vectors in Figure 4.17, with results averaged for all data points within the period band shown in the top right-hand corner of each plot. To reduce the cluttered appearance of such a figure only one of the possible two strike directions is shown, chosen to be the one most closely matching the geological strike of the rift at that location. The vectors are scaled according to the amount of split between the phase of the two MT modes in the decomposed transfer function. The phase split can be used as an estimate of the departure from a 1-d subsurface structure where no phase split is necessary (but not sufficient) for a 1-d subsurface conductivity structure. In the situation where the phase split is small (as shown by very short vectors in Figure 4.17), the computation of the strike angle becomes unstable and has no interpretable meaning.

In the high frequency data (0.1 to 1 s) the amount of phase split is small, as

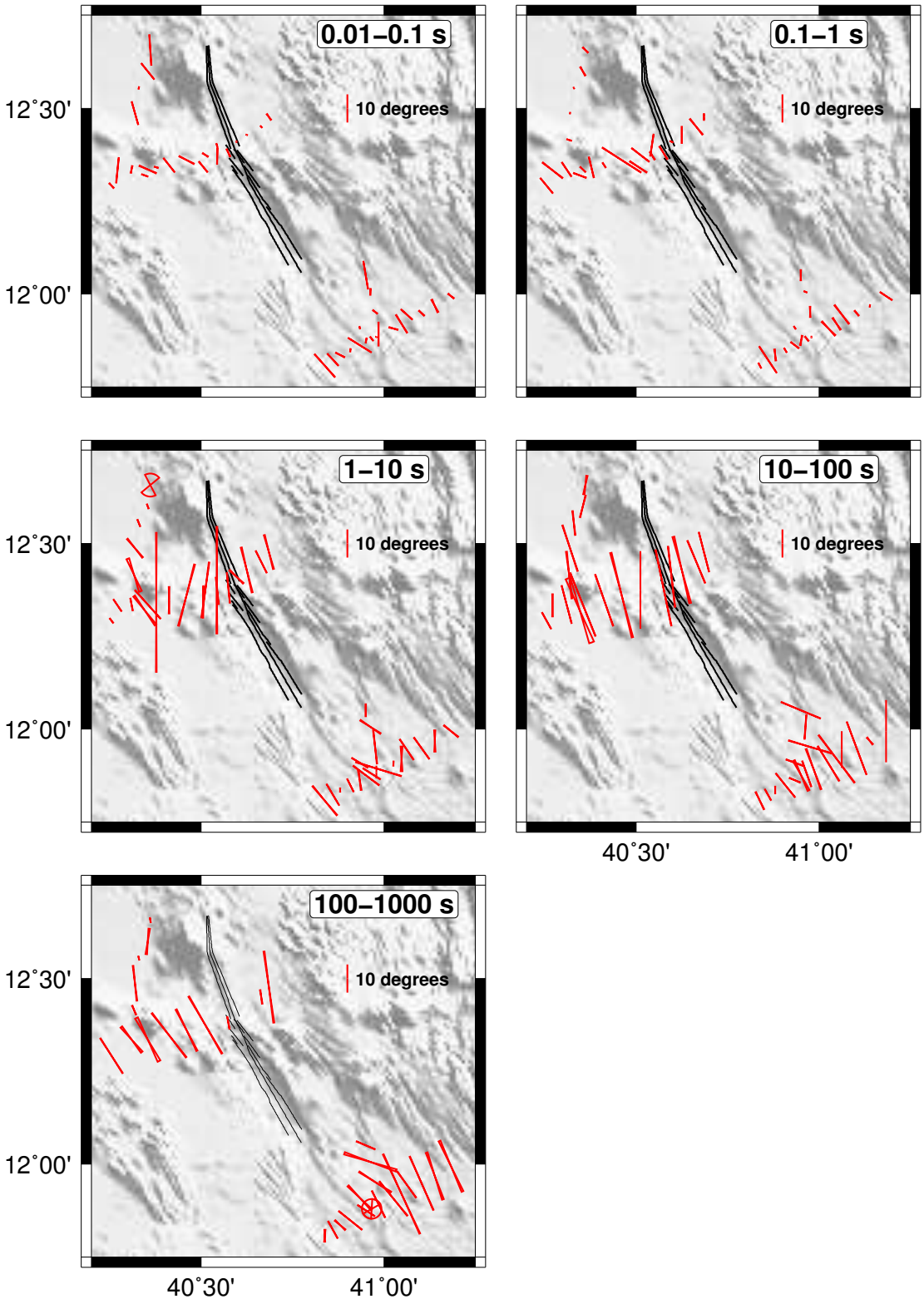

Figure 4.17: Strike angles calculated using GB decomposition. The vectors show the average strike angle for the period range shown is the top right-hand corner. The vector length is scaled according to the amount of split between the phase of the two modes. A vector representing a 10° phase split is shown for reference.

one would expect from looking at the high frequency phase tensor ellipses which are more or less circular. The strike direction is somewhat variable, which is not surprising for reasons given previously, however there is a fairly consistent SE to NW alignment. The most significant departures from this at these periods are found around the rift axis on the HMS segment, and on the western side of the DMS close to Badi volcano (shown on Figure 4.1).

At frequencies below 1 Hz there is, at most sites, a dramatic increase in the amount of phase split which generally persists to the lowest frequencies. Between 1 and 0.1 Hz there is again some scatter in the strike directions as with the shorter periods. However, below 0.1 Hz the strike direction tends to stabilise considerably with a SSE to NNW orientation seen at most sites. Sites on the Teru profile tend to display considerably less phase split throughout the frequency range than those on the DMS and HMS profiles, suggesting that the subsurface structures there are 1-d.

The program 'strike' can also be used to find the best fitting geo-electric strike direction for a set of sites over a range of periods. The best fitting strike angle found for the sites on the DMS and HMS profiles were -20° and -30° (anticlockwise from north) respectively (with 90 degree ambiguity as discussed in Section 3.4). For the sites on the Teru profile the strike angle is -44°.

Distortion parameters

As well as estimating new transfer functions in the reference frame of the recovered geo-electric strike direction, 'strike' also estimates the two parameters called twist and shear, which partially describe the effects of galvanic distortion, and furthermore these effects are removed from the new transfer function estimates (see Section 3.5.1 for details). Figure 4.18 shows a histogram for both of these

parameters using data from the DMS and HMS profiles in the regionally best fitting models of GB decomposition which yielded the strike directions given previously. The amount of twist at any site is never more than 10°, and 50 percent of the sites have a twist angle of less than two degrees. Similarly no site has a shear angle greater than 15°, and 50 percent of sites have a value less than 4°. These values for twist and shear are small in comparison to other studies where similar analyses have been carried out (e.g. Hamilton et al., 2006), and the distortion described by them is removed from the impedance data. Wu et al. (2002) state that shear angles less than 5° indicate an absence of local inhomogeneities, and that shear angles between 10° and 30° represent moderate distortion. Given that the twist and shear are so small suggests that galvanic distortion and therefore static shift, does not heavily influence the data.

RMS misfit

The final and very important parameter which is output from 'strike' is the RMS misfit to the decomposition model. This shows what is left over from the measured transfer functions once twist and shear are removed and the transfer functions are rotated into strike coordinates and is explained either in terms of data noise or 3-d induction. Although the RMS misfit is the accepted measure of how appropriate a model may be it should also be used with a little caution and in conjunction with inspection of the data. This is because the RMS does not give any indication of whether the misfit is randomly distributed or consistently biased one way or the other in which case it may be possible to act to reduce the bias. Figures 4.19 and 4.20 show the RMS misfit for every period at all sites on the DMS and HMS profiles once they are decomposed and rotated into into their respective strike coordinate reference frames. Values less than 2 are considered a reasonable fit to 2-d/3-d model of GB decomposition described in Section 3.5.1 without the need to introduce 3-d induction (e.g. Solon et al., 2005). The majority of data fall

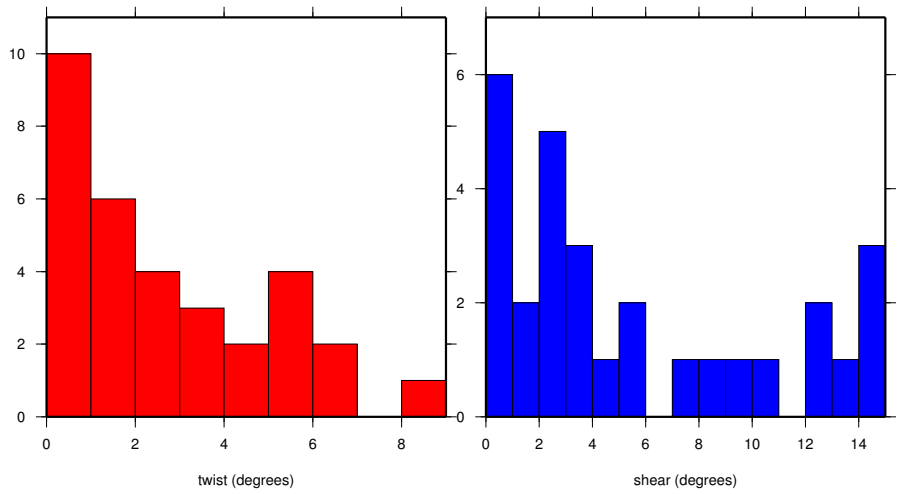

Figure 4.18: Histograms showing the distortion parameters, twist (left) and shear (right), recovered from GB decomposition, from sites on the DMS and HMS profiles.

within this boundary. The most notable exceptions are sites 809 and 909, and the long period data at sites 912 and 917.

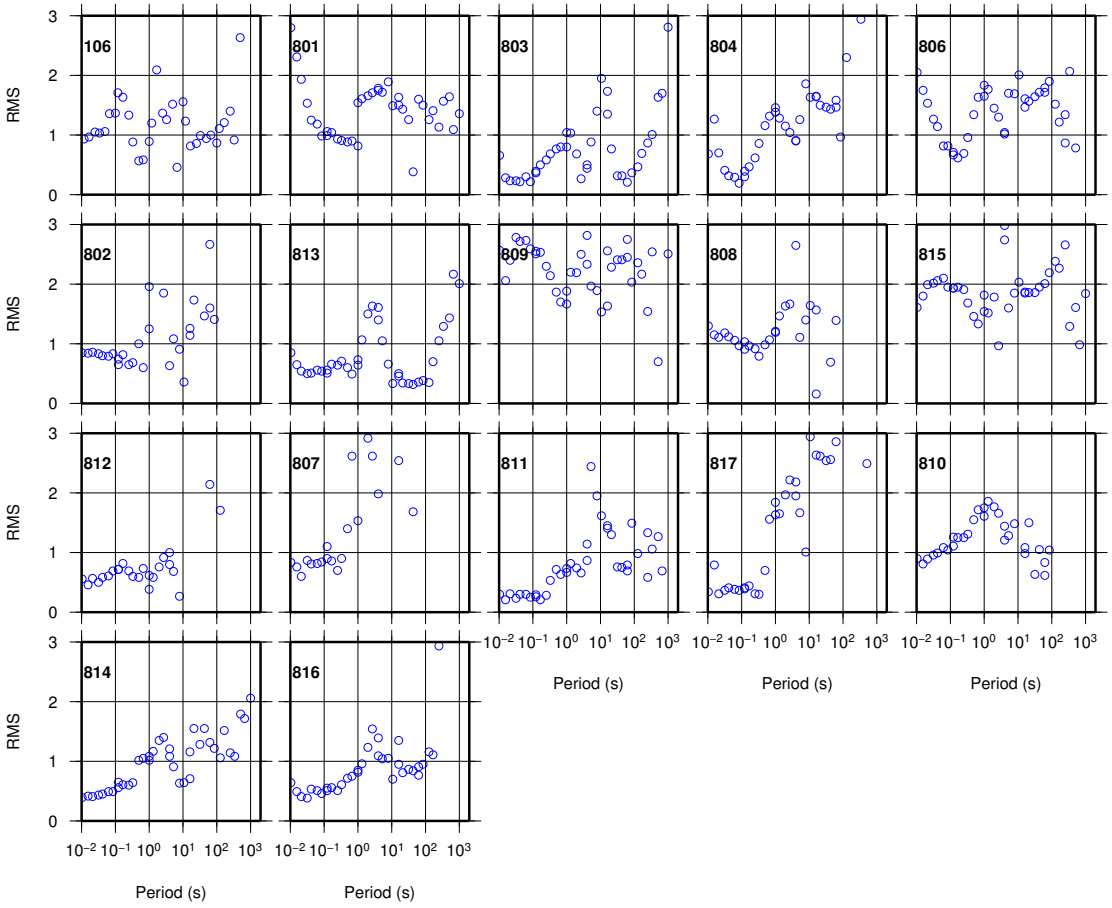

Figure 4.19: RMS misfit to the Groom-Bailey distortion model for all site on DMS profile (sites in order from west to east). A strike angle of -20° was used for all sites.

4.5.3 TEM soundings for static shift correction

The final step in assessing and correcting for the effects of galvanic distortion is to use the results of active source EM soundings to look at the static shift inherent in the MT apparent resistivity curves. The theory is laid out in Chapter 3, Section 3.5.3. Figure 4.21 shows a typical example of the raw TEM data (in this case from site 104) with the decay rate of magnetic field plotted against time after turn off

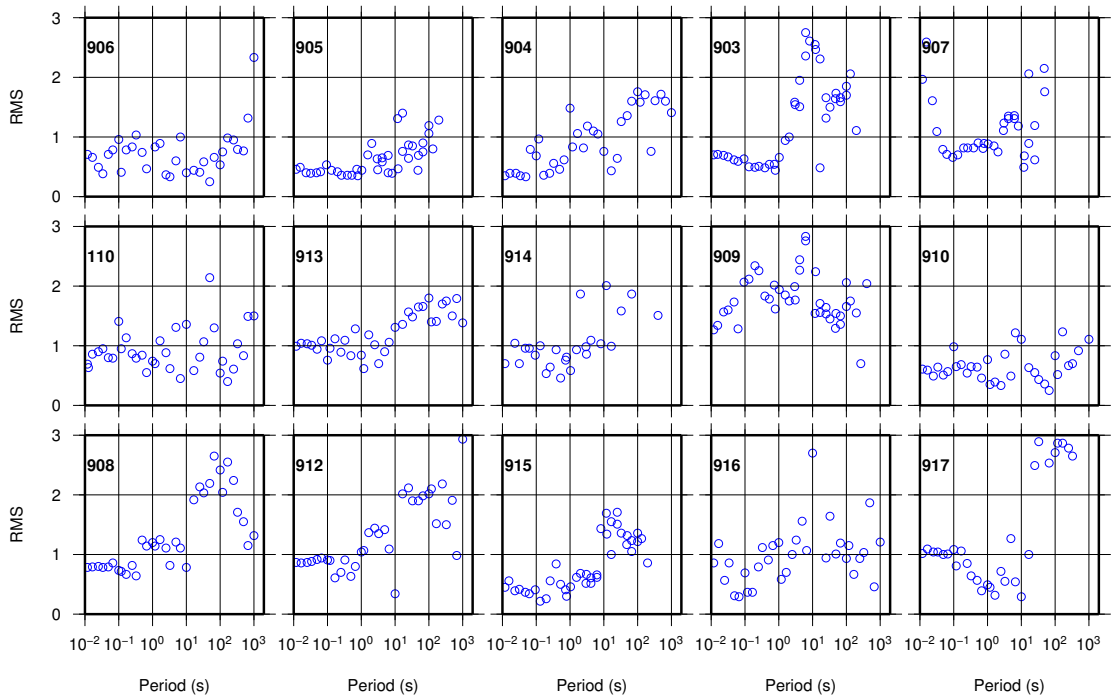

Figure 4.20: As Figure 4.19 for sites on HMS profile, using strike angle of -30°.

of the current in the transmitter loop. Curves for 4 different repetition frequencies are shown with a gradual decrease of data quality towards the lower frequencies. Figures 4.22 and 4.23 shown the direct comparison between the two data sets using the method of scaling the TEM integration time as advocated by Sternberg et al. (1988). Where the MT data are not affected by static shift the TEM and MT apparent resistivity curves should be coincident where they overlap in the high frequency part of the MT data; any discrepancy between the two suggests that local, time-independent distortions of the electric field have caused a static shift in the MT data. The method of comparing the two data sets by scaling the TEM integration time was tested by estimating a best-fitting 1-d model of the subsurface using the TEM data, then calculating the MT response of that model as suggested by Pellerin and Hohmann (1990). The result of this test is shown in Figure 4.24 where the apparent resistivity curves from both approaches are shown for site 803. It can be seen that in the frequency band where there is an overlap with the MT data, there is good agreement between the two approaches. Table

4.1 shows the results of the static shift correction using the TEM data indicating where the method failed and why.

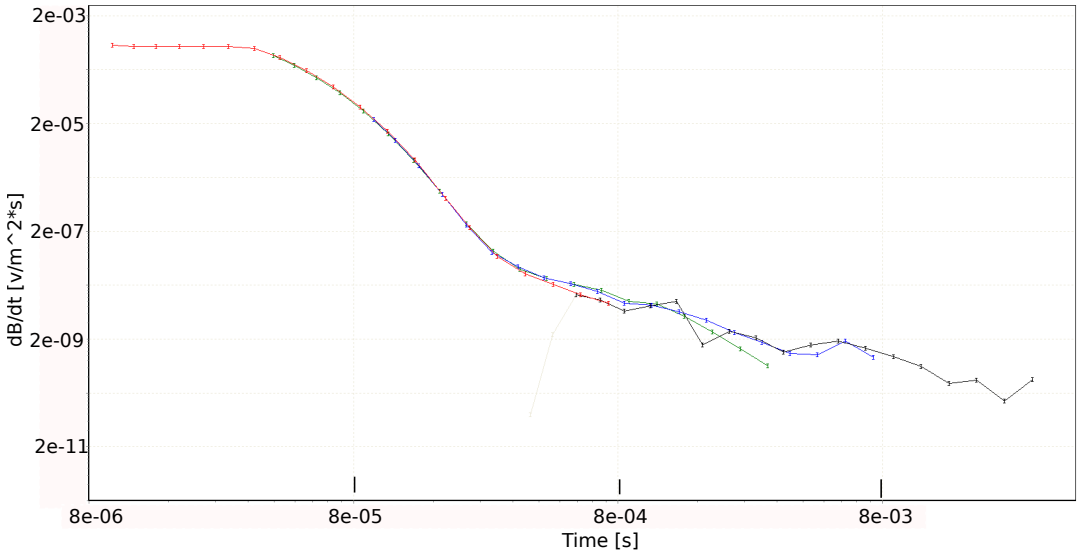

Figure 4.21: Transient decay curve for site 104. Red, green, blue and black curves show data recorded with repetition frequencies of 237.5, 62.5, 25 and 6.25 Hz.

4.6 Discussion

The preceding sections have shown the processed data and given details of several approaches used to assess the dimensionality of the underlying conductivity structure and quantify, and where possible correct for, the affects of galvanic distortion. The data are mostly of good quality with small uncertainties and extending to periods of a thousand seconds at approximately half of the sites. As expected, the level of uncertainty on the transfer function estimations tends to increase at the longest periods because the signal to noise ratio and volume of data to enable stacking decrease there. Broadly, the apparent resistivity and phase curves, and pseudo sections along the profiles, tend to reveal a resistivity structure that has a maximum in the very high frequency part, decreasing to a minimum, then rising

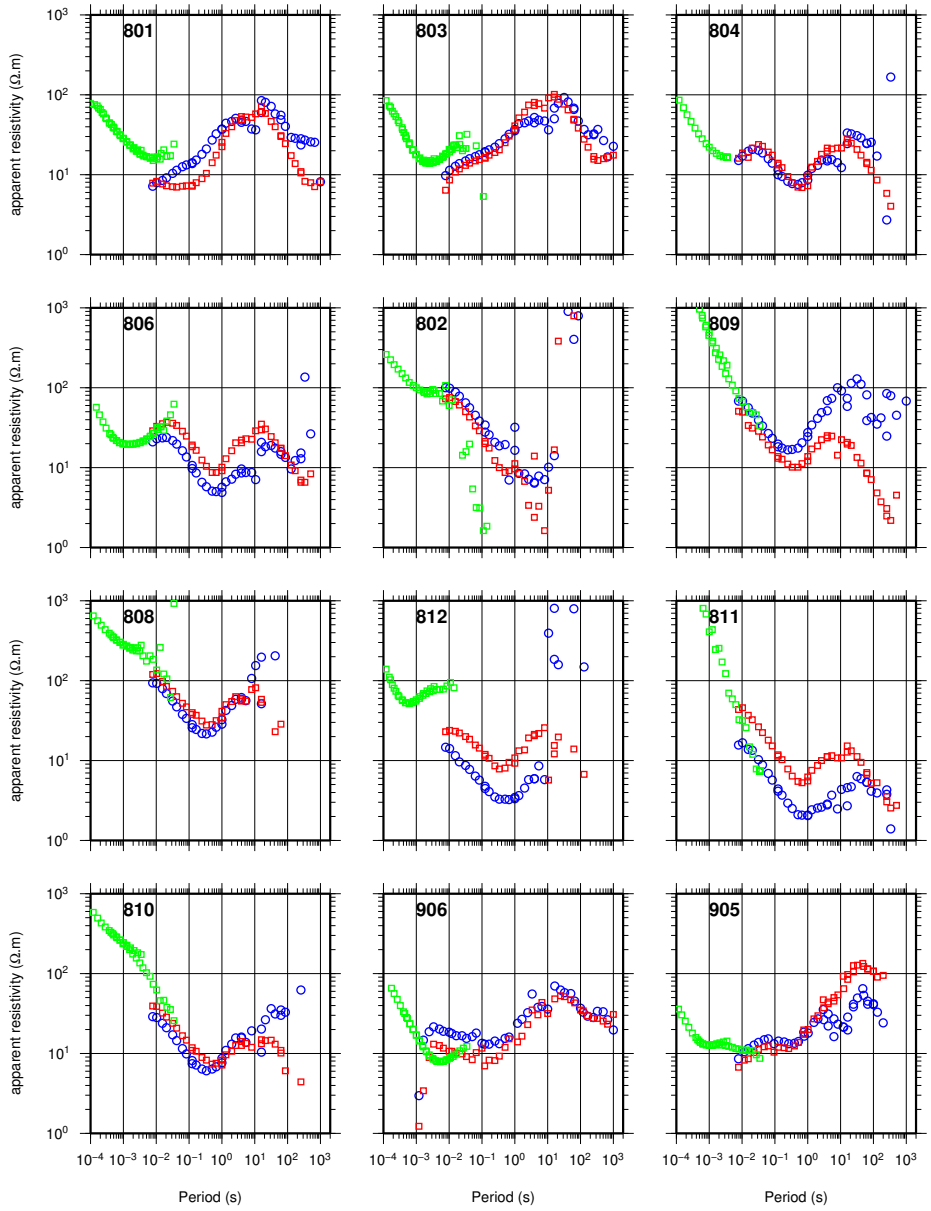

Figure 4.22: TEM data (green) plotted using timescale corrected to allow comparison to MT data (XY component = blue, YX component = red). Data shown for all sites where TEM data are available on DMS profile and 2 sites from HMS profile.

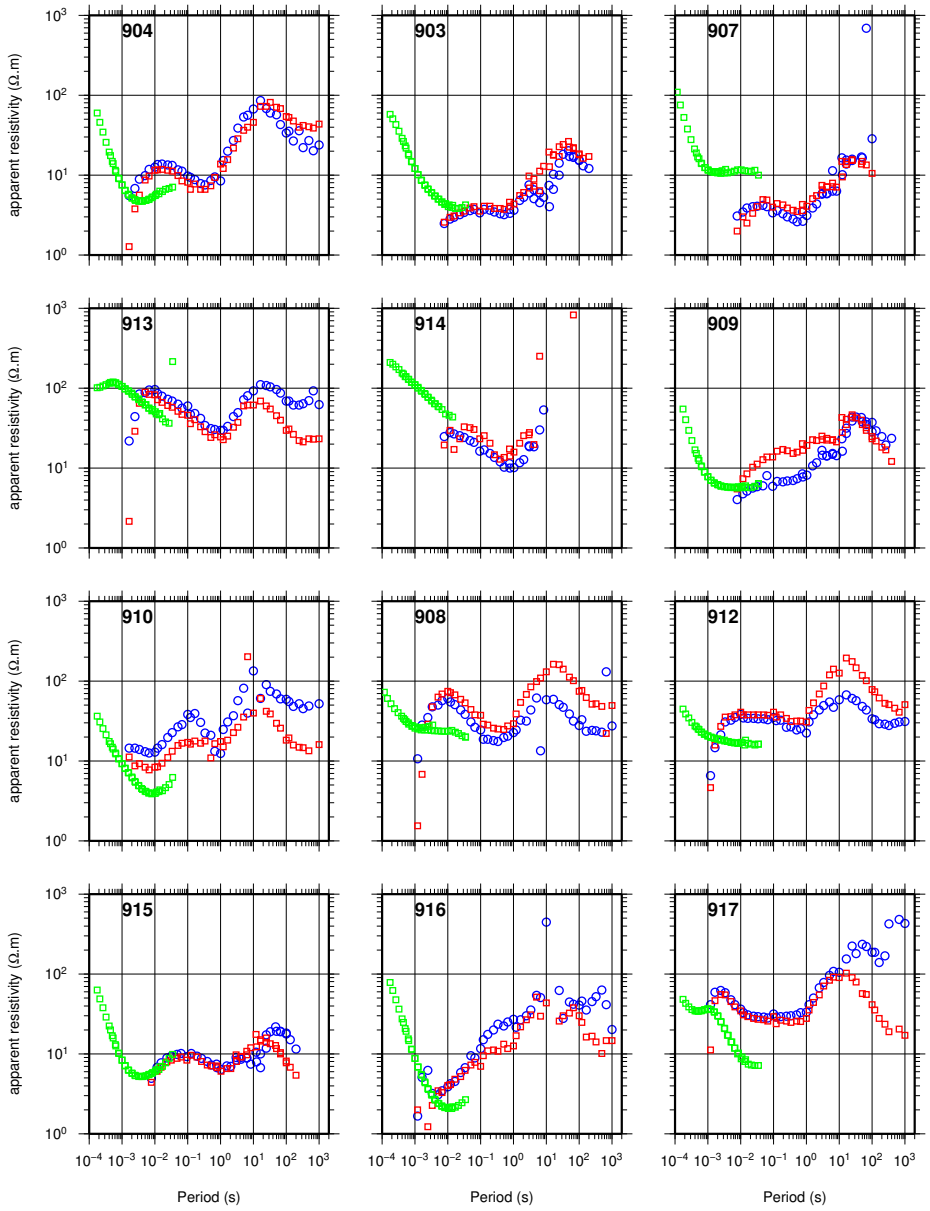

Figure 4.23: As Figure 4.22 for remaining sites on HMS profile.

Site	TE mode correction factor	TM mode correction factor	Comments
801	2	2	Very small overlap
803	1.8	2	
804	0	0	No overlap
806	0	0	
802	0	0	
809	0	0	
808	0	0	
812	7	4	
811	0	0	See discussion in Section 4.6
810	0	0	
906	-	-	Very poor correlation between TEM and MT data
905	0	0	
904	0.4	0.4	
903	0	0	
907	3.5	3.5	
913	0.6	0.7	
914	0	0	No overlap
909	0	0	Poor corelation between TEM and MT data
910	0.5	0.3	
908	-	-	Very poor correlation between TEM and MT data
912	0.5	0.5	
915	0	0	
916	0.5	0.5	
917	-	-	Very poor correlation between TEM and MT data

Table 4.1: Summary of static-shift correction factors

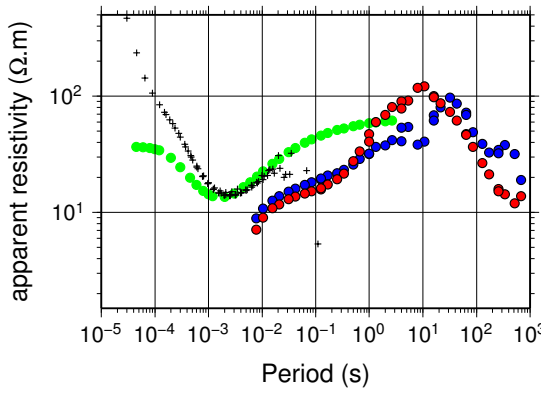

Figure 4.24: A comparison between using the simple time shift method (crosses) and forward calculation of the MT response of a 1-d model estimated from the TEM data (green dots) at site 803. MT data shown by blue (XY component) and red (YX component) dots.

to a second maximum before dropping again at the longest periods. Sometimes at the very longest periods the resistivity is seen to begin increasing again. For example, this pattern is typified by sites 813 or 815 on the DMS profile or sites 904, 908 or 913 further south on the HMS profile. This is of course a generalisation and there is much variation in the frequency at which maxima and minima are seen as well as their actual values. Indeed in a number of regions this general pattern is not seen at all.

The first conductor often reaches its lowest apparent resistivity values at about 0.3 to 1 seconds, which with some very rough skin depth calculations puts it no deeper than 4 km, assuming an average resistivity of not more than 64 Ωm which is an estimate of the regional apparent resistivity value at periods shorter than 0.3 to 1 s. It is most prevalent on the sites of the DMS profile with the exception of the first three sites which are different in that they do not have the initial resistor. The actual value of the minimum tends to be around 10 Ωm on the DMS profile. Many of the sites on the HMS profile do not show the same pattern in the

higher frequencies; like the first three sites on the DMS profile the initial resistor is commonly not seen and instead the resistivity curve starts at a low value of around 10 Ωm. Sites around Saha have very low initial apparent resistivity values, possibly a reflection of the fact that the sites were located in a sedimentary basin which had been recently flooded when we took the measurements. Sites on the Teru profile also have a distinctly different resistivity structure in the high frequencies, starting with higher than normal values then dropping rapidly to the first minimum. Apparent resistivity values at the highest frequencies vary over nearly two orders of magnitude among the whole data set, which is understandable when considering that some sites were located within vast sedimentary plains, whilst others were located on small sandy patches of ground surrounded by vast expanses of fresh igneous material within the rocky rift.

In the longer period, deeper part of the sounding curves the pattern is more consistent, although actual apparent resistivity values vary somewhat. At around 10 s there is almost ubiquitously a peak in apparent resistivity, with a corresponding change of phase values from below to above 45°. This transition is most clearly visible in the phase pseudo-sections. At longer periods the apparent resistivity drops by varying amounts with corresponding high phase values. The largest reductions of apparent resistivity (highest conductivities) are seen in the YX component of the DMS and Teru profiles, around the active rift and Dabbahu volcano respectively. The lowest apparent resistivity values are seen at the sites located closest to Dabbahu volcano such as 104 which drops to below 1 Ωm with phase values of between 70 and 80 degrees. Generally, the lowest apparent resistivity values in the long period data on the DMS profile are between 1 and 10 Ωm, whereas on the HMS profile the equivalent value tends to be between 10 and 100 Ωm.

Simply by looking at the data for the two MT modes one can gain an insight into the level of complexity of the causative structures. The data appear at most sites to be fairly 1D in the high frequency part (to 1 Hz) as the sounding curves for the two modes are coincident. At a very small number of sites a parallel shift, or static shift, between the apparent resistivity curves is seen (e.g. site 811), with phase curves remaining coincident, which implies that galvanic effects from local distorting inhomogeneities are present. At periods lower than 1 s some amount of divergence between the apparent resistivity and phase curves of the two modes is common, suggesting a higher level of complexity. At the majority of sites the diagonal elements of the impedance tensor are an order of magnitude or two lower than the off-diagonal elements, implying that the measurements have been taken in a near strike coordinate system, and that 3-d effects do not, in general, prevail. There are some sites, notably 809, 815, 905 and 104 where, in the long period data, the diagonal elements are as large as the off-diagonal elements. They may be reduced by rotating into a coordinate system that differs considerably from the measurement coordinate frame, but if these sites require a geo-electric strike angle which is significantly different from surrounding sites then the causative structures are, by definition, 3-d. Large diagonal elements can also exist as a direct consequence of 3-d induction because primary and secondary fields are no longer orthogonal.

Two further methods, phase tensor analysis and GB decomposition, were implemented to quantify the dimensionality of the subsurface and define the geo-electric strike direction, supposing that one exists. The phase tensor ellipses support the fact that the data are to all intents 1-d down to a period of approximately 1 s at nearly all sites, as shown by very low beta values (less than 1) and near circular ellipses (Figures 4.11 to 4.15). Beyond this, just as a split between apparent resistivity and phase curves of the MT modes is seen, the phase tensor ellipses

gain a degree of ellipticity. This is particularly prevalent in the data from the central parts of the main profiles crossing the rift. This is indicative of a conductivity structure which is at least two dimensional. At periods longer than 10 s, again particularly over the central part of the DMS profile, some sites display high beta values, either as a result of poor data quality or 3-d regional induction. Comparing the sites and periods at which high beta values are observed to the transfer function estimations, often the data have large error bars and the phase and apparent resistivity curves do not vary smoothly with period, suggesting that it is the quality of the data causing the high beta values rather than 3-d induction. For example the most consistently high beta values seen on the DMS profile are at sites 802, 812 and 807 at periods longer than 1, 10 and 1 second respectively. However, data points with large error bars and often a degree of scatter are observed at those sites and periods. If true 3-d induction were causing beta values to rise then we should still expect transfer functions to vary smoothly with period, and it would not be reason in itself for large uncertainties on the estimations. In some cases high beta values are observed over a limited frequency band, for example at sites 811 or 903. Again there seems to be a corresponding band of transfer function estimates with outliers and larger uncertainties than at surrounding frequencies.

Groom-Bailey dimensionality analysis assumes a 2-d/3-d model of the subsurface where that the regional induction is at most 2-d but local 3-d effects which distort the data are accounted for. If the regional structure is in fact 3-d, this will show up as high RMS misfit to the 2-d/3-d model. Solon et al. (2005) suggest that regional 3-d effects become significant when RMS misfit values over 2 are encountered. Figures 4.19 and 4.20 show the RMS misfit for all sites on the DMS and HMS profiles, when the data are in the regionally best fitting strike coordinate system (actual geo-electric strike directions will be discussed shortly). In general, the data can be explained satisfactorily with the 2-d/3-d model with a few isolated

cases where misfit seems to be above the acceptable level. Most notably, site 809 shows high RMS misfit throughout the frequency range, which is odd given that, in the high frequency part, the data appear 1-d with low beta values from phase tensor analysis. The RMS misfit shown for that site in Figure 4.19 uses the best fitting regional geo-electric strike direction, however if we look for the best fitting direction for that site alone, it is 33° away from the regional strike. Using this new geoelctric strike direction for that site, the RMS misfit is greatly reduced as shown in Figure 4.25. This analysis supports the earlier observation that, unlike surrounding sites, large diagonal impedance elements are seen in the measurement coordinate system. This also suggests that site 809 requires a significantly different geo-electric strike direction than the rest of the data set, which is in itself an admission of a 3-d subsurface in that area. At some other sites, particularly 817, 908, 917 and 903, high RMS misfits are also seen but here they are instead isolated to a small part of the period range (usually the longest periods), and again this coincides with poor data quality.

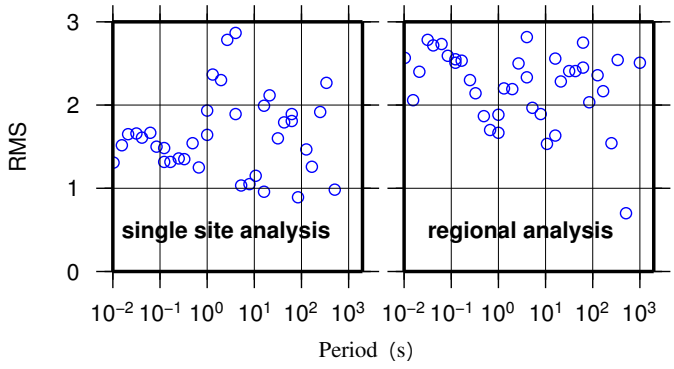

Figure 4.25: RMS misfit to 2-d/3-d GB model at site 809 using the regional best fitting strike angle, and that which best fits site 809 alone.

Groom-Bailey decomposition not only shows where the effects of galvanic distortion are present, but removes them from the ideal 2-d impedance tensor, except for the static-shift associated with apparent resistivity. The amount of distortion

removed is quantified by the frequency independent twist and shear parameters output from the decomposition algorithm, which are shown for all sites on the DMS and HMS profiles as histograms (Figure 4.18). Twist and shear do not exceed 10° and 15° respectively for any of the sites, and 50 percent of the sites take values less than 2° and 4° (twist and shear respectively). These values are very low in comparison to other studies where similar analyses have been carried out (e.g. Hamilton et al., 2006). The effects of galvanic distortion are removed from the impedance tensor by GB decomposition, with the exception of the amplitude effect known as static-shift, as discussed in the previous chapter. Given that the twist and shear are so small it is reasonable to assume that causative, local 3-d inhomogeneities either do not exist or are having little effect; therefore, it is possible to assume that static shift effects will also be small (Wu et al., 2002).

Both phase tensor analysis and GB decomposition (implemented using the multi-site, multi-frequency function of the program *strike*) are used to define the best fitting regional geo-electric strike direction for the four profiles. From GB analysis the best fitting strike direction for the DMS profile is 20° west of north[3], which is in good agreement with the phase tensor analysis where the modal strike direction, as shown in Figure 4.16, is between 10° and 20°. The rose histogram representing the phase tensor result for this profile shows an even distribution of strike directions at many frequencies, which is due to the contribution from the high frequency data which appear to be 1-d, hence the strike direction is an unstable parameter. There is, however, a well defined modal group between 10° and 20°, which is the contribution from the longer period data. The strike direction found from GB analysis for the HMS profile is 32° west of north which, again, compares very well to that found using phase tensor analysis where, this time, the strike angle appears to be better defined throughout the frequency range as

[3]Note that at this stage all strike directions are subject to the 90° ambiguity discussed in the previous chapter.

shown by the very distinct arms of the rose histogram.

As well as using *strike* to determine frequency and site independent estimates of the geo-electric strike for the sites making up the profiles, it was also used to study the variation in this parameter from site to site and through the frequency range. Figure 4.17 shows that where there is little split between the phase of the MT modes (shown by small vector lengths), there is often some variation in the strike angle, which is not surprising as the data are probably 1-d. Between 1 and 10 s some phase split becomes apparent, particularly over the rift axis on the HMS profile, and around Badi volcano on the DMS profile. However, beyond 10 s the strike direction becomes more or less independent of site location, especially between the sites making up the DMS and HMS profiles crossing the rift.

Without vertical magnetic field data it is not possible to resolve the 90^o ambiguity in the determination of geo-electric strike direction, and therefore define TE and TM modes, from the MT data alone. The approach used here is to make a simple assumption that the geological strike of the structures forming the rift also defines the geo-electric strike direction. This seems reasonable given that one of the two possible electric strike directions aligns perfectly with the strike of the rift (see Figure 4.26). The mean strike of the faults on the DMS is 27^o west of north, however there is considerable variation along its length (Rowland et al., 2007). To add to this, Keir et al. (2011) invert upper crustal shear-wave splitting results from local earthquakes for fracture parameters. They find that at a seismic site (ALEE) very close to MT site 817, the fracture strike is 15+/-10^o west of north. To the north of the central Ado' Ale volcanic complex the strike of the faults becomes 8^o west of north, reflecting a change in the orientation of the rift axis. There is a 12^o difference between the electric strike direction on the DMS and HMS profiles; a swing that is also seen in the alignment of the rift giving further confirmation that the two are aligned. The TE mode is defined as the one which

incorporates electric fields parallel to strike, hence in Figures 4.2 to 4.10 and 4.22 to 4.24 the XY component (blue symbols) represents the TE mode, whilst the YX component (red symbols) represents the TM mode.

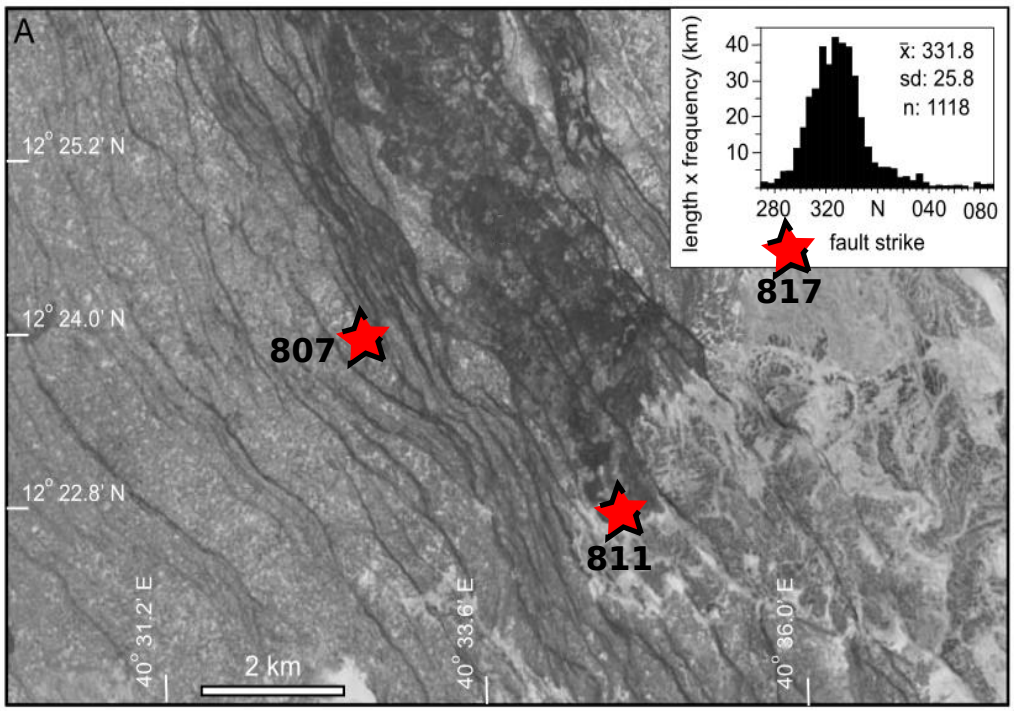

Figure 4.26: Map showing faults at the rift axis, which passes through site 811, and a histogram of fault orientation. Modified from Rowland et al. (2007)

The strike angle along the other two profiles which do not cross the rift, but run perpendicularly to it, appear to be less well defined according to phase tensor analysis, particularly the Teru profile. The data making up this profile (sites 101-105) tend to appear more 1-d to the longest periods than those crossing the rift, as shown by the small split between the resistivity and phase curves of the modes, and near circular phase tensor ellipses. In this situation, as already mentioned, the notion of a strike direction is meaningless. The best fitting, frequency and site independent geo-electric strike direction for this profile is 44° west (or east given the ambiguity) of north. This seems to fit poorly with the result from phase tensor analysis, which shows two distinct modal groups in the rose-histogram, between

10° and 20° west of north, and between 0° and 20° east of north. In Figure 4.17 there appears to be little systematic change in strike angle from site to site or through the frequency range at these sites, but again this Figure does show that the phase split (vector length) is smaller than at the sites crossing the rift, supporting the 1-d argument. Similarly, GB analysis estimates the geo-electric strike angle for the Saha profile to be 70° west of north (or 20° east of north), which agrees poorly with the estimate from phase tensor analysis.

The final step taken in this primary assessment of the data was to compare the high frequency part of the MT resistivity data to active-source TEM data, in order try to quantify and control static-shift. At all the sites occupied in 2008 and the majority of those occupied in 2009 where TEM data are available the overlap between the TEM and MT curves is small (often half a decade or less - see Figures 4.22 to 4.23), which does not allow for accurate estimation of the static shift. Sternberg et al. (1988) state that the magnitude of the static shift is most accurately estimated on a part of the curve with little or no gradient, which given the very small overlap is not always possible with the exception of a few fortuitous sites like 905 for example. Given these limitations, quantification of small scale static shifts will not be possible for most sites. However the results do give an insight into which sites might be affected by larger scale static shifts. Table 4.1 gives static shift correction factors according to this method.

Of the sites on the DMS profile where TEM data are available only one, 812, seems to show a significant static shift of 0.7 and 0.4 decades for XY and YX components respectively. At all other sites the shift does not appear to exceed 0.2 decades which is considered within the uncertainties on the data, given the small overlap between MT and TEM data. At several sites there is clearly a small split between the MT modes (site 811 for example) suggestive of some amount of static shift, however the amount of split is again smaller than accuracy of the

method used to correct the static shift. For example taking case of site 811, the MT and TEM apparent resistivity curves overlap where the gradient is steep and they are not parallel; the TEM curve lies approximately midway between the MT modes but with a different gradient making it impossible to say whether it is the XY, YX or indeed both curves which are shifted.

According to the TEM data two sites on the HMS profile show an unambiguous static shift (907 and 912). In both cases however the two MT curves are coincident at high frequencies suggesting that both are affected by an equal static shift (i.e. both curves need shifting by the same amount in the same direction). Whilst not impossible this seems statistically unlikely, especially at more than one site.

Static shift can be separated into anisotropy and site gain (See Chapter 3, Section 3.5.1). The anisotropy or curve splitting can be corrected for by shifting the TM and TE apparent resistivity curves to their geometric mean as advocated by Marquis et al. (1995) and Solon et al. (2005), leaving only the site gain unresolved. Given the ambiguity and uncertainty surrounding the correction of the data using the TEM data, and the fact that the very small amounts of twist and shear detected suggest that galvanic effects are small, the data used for subsequent modelling were only corrected for anisotropy.

In conclusion to this chapter, the primary analysis of the MT data detailed here suggests that it will be possible to proceed with caution to carry out 2-d modelling of the data for the two main profiles crossing the rift. At the majority of sites where 3-d effects appear to prevail the data quality is low, usually due to poor signal to noise ratios at the longest periods; however, larger data uncertainties account for these inaccuracies. At the worst sites where there are clearly outliers in the transfer function estimations (e.g. at sites 802, 807 and 914) some data

may need to be rejected before modelling can take place. Where there genuine 3-d regional induction appears to be present, like around site 809 for example, caution must be exercised with regard model interpretation.

Chapter 5

Modelling

5.1 Introduction

The previous chapter showed that the data are mostly consistent with the assumption that the causative geo-electric structures are 2-d; that is that there exists one horizontal direction in which conductivity is approximately constant. Therefore, this chapter concentrates on the use of a 2-d inversion algorithm to produce a suite of models which are most likely to be representative of the subsurface. Unlike many other geophysical methods, the MT method is not inherently non-unique; Bailey (1970) showed that for noise free, 1-d data over a continuous range of frequencies only one model will fit. In reality however, MT data are affected by noise, only available at discrete frequencies and rarely, if ever, conform to a perfect 1-d subsurface, in which case a large variety of models will all fit the data equally well. The approach used here to narrow down the range of possible models is to to search for one which not only fits the data well, but does so with the least amount of structure possible. The first inversion scheme to employ this sort of search on EM data was described by Constable et al. (1987)

who named it Occam's inversion after the the fourteenth-century scholar, William of Ockham who was famed for the principle of Occam's razor; '*it is vain to do with more what can be done with less*'. The process of removing unnecessary, possibly spurious structure from a model is named regularisation and tends to make inversion algorithms more stable (Siripunvaraporn and Egbert, 2000). Before data were inverted the ρ^+ algorithm was used to perform a consistency check between the phase and apparent resistivity data at each site and frequency as suggested by Jones et al. (2003), and at that stage obvious outliers were removed from the data. This chapter begins with a description of the code used to invert the data before going on to detail the parametrisation of the model space and finally show the models produced. The fit of the model responses to the data will be discussed along with some basic interpretation and comparisons between the profiles, however detailed interpretation will be left to Chapters 6 and 7.

5.2 2-d inversion method

The 2-d inversion scheme used here was chosen because it was freely available at the time of the investigation, can easily be run on a standard PC, and is fast, stable and easy to use. The code is called REBOCC and is based on a data space (as opposed to model space) varient of the original OCCAM's inversion (Siripunvaraporn and Egbert, 2000). A summary of the inversion method is given here.

The aim of all inversion methods is to find a model of the subsurface which minimises the misfit between the measured data $\mathbf{d} = [d_1, d_2..., d_N]$ where N is the number of data and the theoretical model responses $\mathbf{F[m]}$. Here, the model space is discretised into M blocks of constant resistivity $\mathbf{m} = [m_1, m_2..., m_M]$. A measure of the root-mean-square (RMS) fit of the model responses to the data is

given by

$$X_d^2 = (\mathbf{d\text{-}F[m]})^T \mathbf{C_d}^{-1} (\mathbf{d\text{-}F[m]}) \tag{5.1}$$

where X_d is the RMS misfit, $\mathbf{C_d}^{-1}$ is the diagonal data covariance matrix containing the statistical errors on the data, $\mathbf{e} = [e_1, e_2..., e_N]$ and the superscript T denotes the matrix transpose. For a model that fits all the data within the errors $X_d^2 = N$ giving an RMS misfit of 1. As mentioned in Chapter 4, the RMS misfit should not be used alone to judge the appropriateness of a model or compare between two models; the data and model response curves should also be closely inspected because the RMS gives no indication of how the misfit is distributed.

Inversion schemes which seek the minimum structure model (which includes most of them) also need to minimise some model norm, X_m, that quantifies the amount of structure. This can be given by

$$X_m^2 = (\mathbf{m\text{-}m}_0)^T \mathbf{C_m}^{-1} (\mathbf{m\text{-}m}_0) \tag{5.2}$$

where $\mathbf{m}_0$ is a prior model and $\mathbf{C_m}^{-1}$ is a model covariance matrix characterising the expected magnitude and smoothness of resistivity variations relative to $\mathbf{m}_0$. In reality an RMS misfit of 1 will not be achievable so the aim of the inversion is to minimise X_m^2 subject to $X_d^2 = X_*^2$ where X_*^2 is a user defined maximum desired misfit.

The minimisation problem is solved by introducing a Lagrange multiplier λ^{-1} which controls the 'trade off' between misfit and smoothness. The unconstrained functional for the inversion is given by

$$U(\mathbf{m}, \lambda) = (\mathbf{m\text{-}m}_0)^T \mathbf{C_m}^{-1} (\mathbf{m\text{-}m}_0) + \lambda^{-1} \{ (\mathbf{d\text{-}F[m]})^T \mathbf{C_d}^{-1} (\mathbf{d\text{-}F[m]}) - X_*^2 \} \tag{5.3}$$

for which stationary points with respect to $\mathbf{m}$ and λ are sought. $\mathbf{F}[\mathbf{m}]$ is non-linear in the MT case meaning that a solution is found by approximate iterative methods. The OCCAM inversion is based on linearising $\mathbf{F}[\mathbf{m}]$ by using the first two terms of a Taylor series expansion such that

$$\mathbf{F}[\mathbf{m}_{k+1}] = \mathbf{F}[\mathbf{m}_k + \delta\mathbf{m}] = \mathbf{F}[\mathbf{m}_k] + \mathbf{J}_k(\mathbf{m}_{k+1} - \mathbf{m}_k) \tag{5.4}$$

where k is the iteration number, $\mathbf{m}_k$ is the model of the previous iteration (or starting model in the case of the first iteration), $\mathbf{J}_k = (\partial\mathbf{F}/\partial\mathbf{m})|_{\mathbf{m}_k}$ is the $M \times N$ Jacobian or sensitivity matrix. Substituting this into Equation (5.3) gives

$$U = (\mathbf{m}\text{-}\mathbf{m}_0)^T\mathbf{C}_\mathbf{m}^{-1}(\mathbf{m}\text{-}\mathbf{m}_0)+\lambda^{-1}\{(\hat{\mathbf{d}}_k-\mathbf{J}_k(\mathbf{m}_{k+1}-\mathbf{m}_0))^T\mathbf{C}_\mathbf{d}^{-1}(\hat{\mathbf{d}}_k-\mathbf{J}_k(\mathbf{m}_{k+1}-\mathbf{m}_0))-X_*^2\} \tag{5.5}$$

where $\hat{\mathbf{d}}_k = \mathbf{d} - \mathbf{F}[\mathbf{m}_k] + \mathbf{J}_k(\mathbf{m}_k - \mathbf{m}_0)$. This expression can then be minimised by differentiating with respect to $\mathbf{m}$ and setting the result equal to zero, giving an iterative expression

$$\mathbf{m}_{k+1}(\lambda) = [\lambda\mathbf{C}_\mathbf{m}^{-1} + \mathbf{J}_k^T\mathbf{C}_d^{-1}\mathbf{J}_k]^{-1}\mathbf{J}_k^T\mathbf{C}_d^{-1}\hat{\mathbf{d}}_k + \mathbf{m}_0 \tag{5.6}$$

At each iteration, Equation (5.6), is solved for a series of trial values of λ and the misfit for each is evaluated by solving the 2-d forward problem (Siripunvaraporn and Egbert, 2000). The model with the lowest misfit is taken as the basis for the next iteration until the condition $X_d^2 = X_*^2$ is met. This process is known as phase I (Parker, 1994). Once the desired misfit is reached (which may never happen in which case it is recommended that it is raised and the inversion re-run), then

OCCAM performs a search through λ to find the model with the lowest model norm whilst keeping the misfit at the desired level. This is known as phase II. This is the basis of the original occam inversion (Constable et al., 1987; de Groot-Hedlin and Constable, 1990). For larger 2-d data sets, the method has large computational costs in terms of CPU time to calculate the sensitivity matrix and solve the $M \times M$ system of equations at each iteration and in terms of memory. The REBOCC algorithm reduces both of these requirements by re-casting the problem in the $N \times N$ data space rather than the $M \times M$ model space, given that the number of model parameters (M) usually far exceeds the number of data (N). Further computational savings are then made by only calculating a subset of the rows of the sensitivity matrix. This is where the inversion scheme gets its name - the REduced Basis OCCam's inversion - and the approximation results in little loss of detail because MT data are smooth and 'redundant' (Siripunvaraporn and Egbert, 2000). It is up to the user to define which data points are used to determine the representers of the sensitivity matrix. Siripunvaraporn and Egbert (2000) suggest either all data at every p^{th} period where p should be in the region of 2 to 6, or a checkerboard where every p^{th} period at every s^{th} station is used. The second option maybe risky where station spacing is sufficiently large that the lateral variation of the data may not be smooth. As p or s are reduced computational time will, of course, be increased.

The forward modelling part of the code is used to calculate the sensitivity matrix and the model responses from which the misfit to the data is calculated. Accurate forward modelling is thus key to the success of the inversion. The second-order Maxwell's equations described in Chapter 3 are solved using a finite difference method. A basic description is given in Siripunvaraporn and Egbert (2000), and full details can be found in Smith and Booker (1991).

Calculating the inverse of the model covariance matrix required in Equation (5.6) is not computationally practical; however, the data space method requires

the model covariance matrix itself rather than its inverse. REBOCC does not calculate the full model covariance matrix but rather the correlation length scale is altered throughout the model space to reflect the loss of resolving power of the data at depth and at the model space boundaries of the model space. Known geological structures are easily incorporated into the model with this scheme, for example, by letting the correlation length scale go to zero at a fault. Full details regarding the calculation of the model covariance matrix are given by Siripunvaraporn and Egbert (2000).

As mentioned previously, during phase I the inversion searches for λ which minimises the RMS misfit. In the first instance three trial values of λ are used and corresponding misfits calculated in order to establish if a higher or lower value is required (unless a minimum in the misfit is bracketed in this first guess). Then, λ is increased or decreased until a minimum in misfit is found. This then becomes the middle value (of three) that λ takes in the next iteration and the process is repeated (Siripunvaraporn and Egbert, 2000).

5.3 Parametrisation of the model space

In order to satisfy boundary conditions, the model space is extended beyond the region to which the data are sensitive, both laterally and with depth. The model space is split into blocks of constant conductivity whose dimensions change according to the resolution of the data such that blocks are small at the surface in the region containing the sites, becoming larger at greater depth. If the grid is too coarse then it may not be possible to include sufficient structure to fit the data; if the grid is very fine, the computational costs will be increased. Here, an initial grid was designed based on some 'rules of thumb' suggested by Weaver (1994), then tested by making it finer and observing whether the model has changed

(with associated improvement in fit). The first layer should be approximately one tenth of the skin depth of the highest frequencies, increasing by a factor of 1.2-1.5 until a total model depth of at least twice the maximum skin depth is reached. The thickest cells should not exceed half of the maximum skin depth. A series of air-layers are also required for the calculation of the TE mode response. The first of the 10 air layers above the air-Earth interface is 10 m thick, increasing by a factor of three such that the 10th layer is 30 km think. Vertical grid-lines need to be as evenly spaced as possible with sites located on a node. The nodes between the sites were spaced as close as possible to 500 m. Outside the region containing the sites node spacing was increased by a factor of approximately 1.5 until a distance equal to twice the maximum skin depth was reached. Following these rules for the DMS profile, the first layer was 10 m thick and the total depth extent of the model space was 130 km divided into 33 layers. The horizontal model space was divided into 127 columns with a total of 82 km beyond the sites to the east and west. This gave a total of 4191 cells. The grid used for the HMS inversion was designed in the same way but only contains 3500 cells because the profile is shorter. Trial and error testing showed that a finer vertical node spacing was needed in the area immediately beyond the region containing the sites, but otherwise this parametrisation worked efficiently and gave enough freedom to satisfactorily fit the data. The maximum penetration depth of the data was assessed through sensitivity tests which will be described in Section 5.7.1.

Once the geo-electric strike direction for each of the profiles is established the sites are projected onto a strike-perpendicular line to get the distances along the profile for each site to be used in the inversion. For the DMS and HMS profiles the difference between actual and projected distances between sites is very little; however, because the Teru profile is oblique to the strike-perpendicular line, once

projected onto that line the distances between sites become considerably shorter than actual distances.

5.4 Data used in the inversions

The processed data shown in the previous chapter were decomposed and fitted into the regional 2-d coordinate frame using the program 'strike' (McNeice and Jones, 2001), and then the ρ^+ algorithm (Parker and Booker, 1996) was used to check for consistency between the phase and apparent resistivity data, putting bounds on outliers or missing data (Jones et al., 2003). Obvious outliers in both phase and apparent resistivity and very noisy data were removed. The data in the figures showing the model response curves (5.5 to 5.10 and 5.14) are those that were used in the inversion of the DMS, HMS and Teru profiles.

The REBOCC algorithm allows the user to define an error floor for each of the data types (phase and apparent resistivity) for each mode. Should the statistical error of any datum be less than this then the error floor value is taken. Initially, a 10 percent error floor was used, a value commonly taken among similar studies (e.g Hill et al., 2009). The error floor is often used to down-weight the apparent resistivity over the phase if static shift type distortion is likely to be present, or, for example, to down-weight the TE- over the TM-mode in the presence of 3-d effects.

5.5 Results: DMS and HMS rift perpendicular profiles

The same basic strategy was adopted for inverting the DMS, HMS and Teru profile data sets. REBOCC was run using the TE and TM modes alone and as a joint inversion of both modes. Tests were carried out in which the resistivity of the homogeneous starting model was varied, using values of 10, 100 and 1000 Ωm. Generally, the effect was to change the number of iterations required to reach a model that achieved the desired misfit, with 100 Ωm requiring the fewest iterations. However in some cases (TE mode and joint inversions where the inversion seemed to struggle to converge), using different staring models altered the final outcome. In this situation the 100 Ωm starting model always produced the model with the lowest misfit levels. Hence in all cases, the starting model was a homogeneous half-space of 100 Ωm. Another preliminary test that was carried out, was to invert the data that were allocated as TE mode in a TM mode inversion in order to check the mode allocation. REBOCC was not able to fit the data with this reversed sense of mode, and the models that were produced were not geologically interpretable with extreme resistivity values and sharp contrasts, thus confirming the original assignment of modes (which was based on geological structure of the rift). Initially p was set to 4 such that every 4^{th} period (at all sites) was used in the calculation of the sensitivity matrix. Each iteration ran in less than 10 s so it was not deemed necessary to use a larger value, and increasing the amount of data used did not alter the models produced but rather just slowed down the inversion considerably. During the inversion of the DMS data, the first iteration required a total of 5 values of the Lagrange multiplier λ to be used to find a minimum in the RMS misfit. After this, most iterations found a minimum from just four values. REBOCC can optionally incorporate static shifts of apparent resistivity as additional model parameters estimated by the inversion.

However, when allowed this seemed to give unreasonably large static shifts, even for sites that previous analysis suggested were unaffected by galvanic distortion, that were unstable between iterations. Therefore, static shift corrections were not incorporated in the inversion.

The inversion was run initially with a desired RMS value of 1.5. However, in many cases it was never reached and hence phase II of the process (searching for the Lagrange multiplier that gave the smoothest model) was not implemented. As suggested by Siripunvaraporn and Egbert (2000), the desired RMS was then increased until it could be achieved and the smoothing process could take place. Generally the desired RMS was achieved after between 3 and 5 iterations. During the joint mode inversions there tended to be some issues with stability or convergence of the model which would often be seen to alternate from iteration to iteration between two slightly different models: one more resembling the TE mode only model and the other the TM mode one. In this situation there was also a significant alternation between a lower and higher overall RMS and hence the model with the better overall misfit is shown here.

Figures 5.1 to 5.10 show the preferred models and the model response curves along with the data for TE, TM and joint inversions of the DMS and HMS profiles. Equivalent models for both profiles are shown in one panel to allow for easy comparison later. The overall normalised RMS misfit is shown at the bottom of each model.

Very broadly, similar structures are seen in the equivalent models for the two main profiles shown here. The TE mode models show structures with vertical boundaries because the telluric currents which this mode senses travel along the strike of 2-d structures. This mode also tends to more extreme resistivity values particularly at the high end (notice that the scale used for this mode is different from others). Conversely, the TM mode inversions show structures with stronger

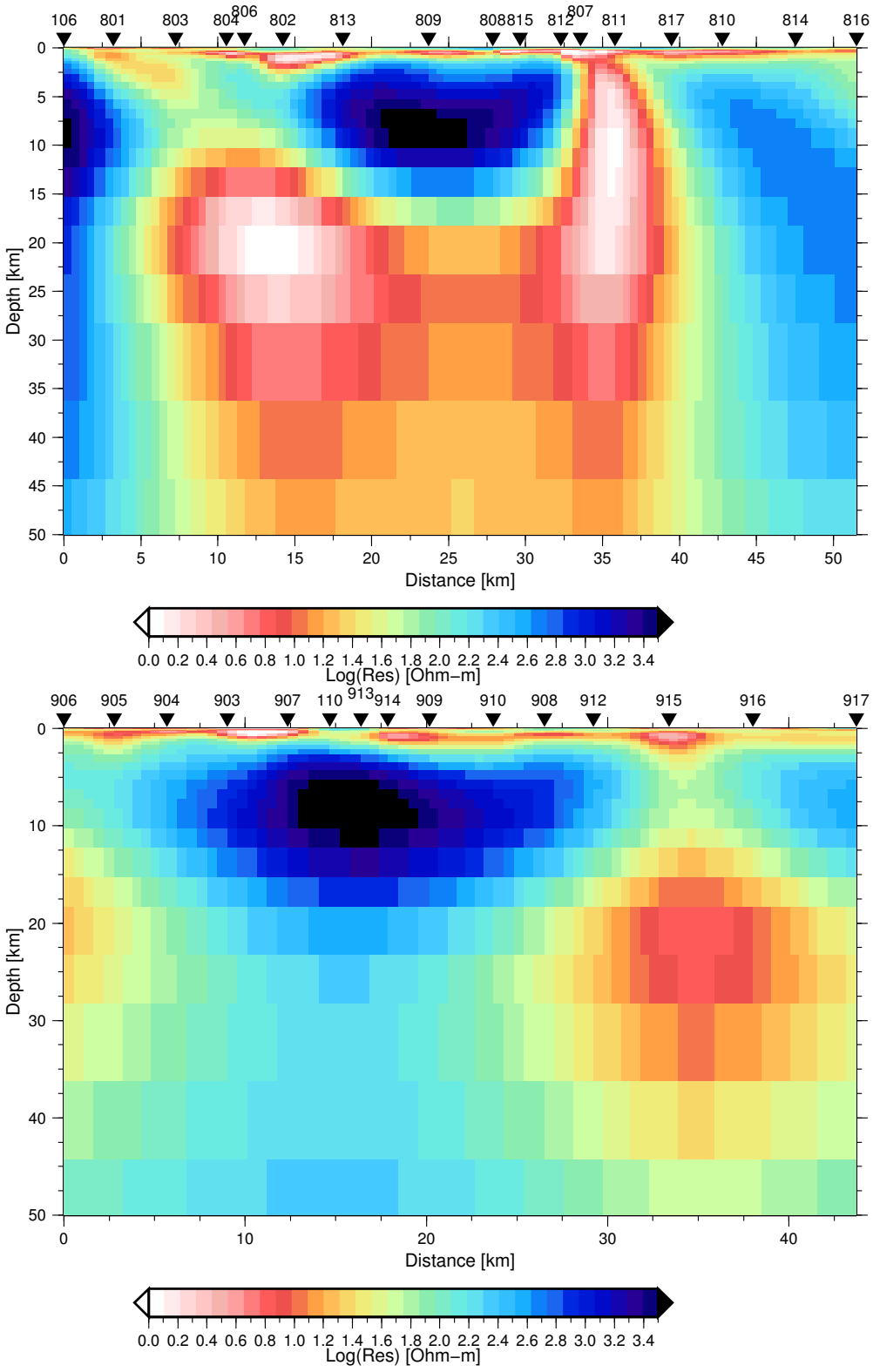

Figure 5.1: TE mode inversions for DMS (top) and HMS (bottom) profiles. Normalised RMS were 2.43 and 1.58 respectively

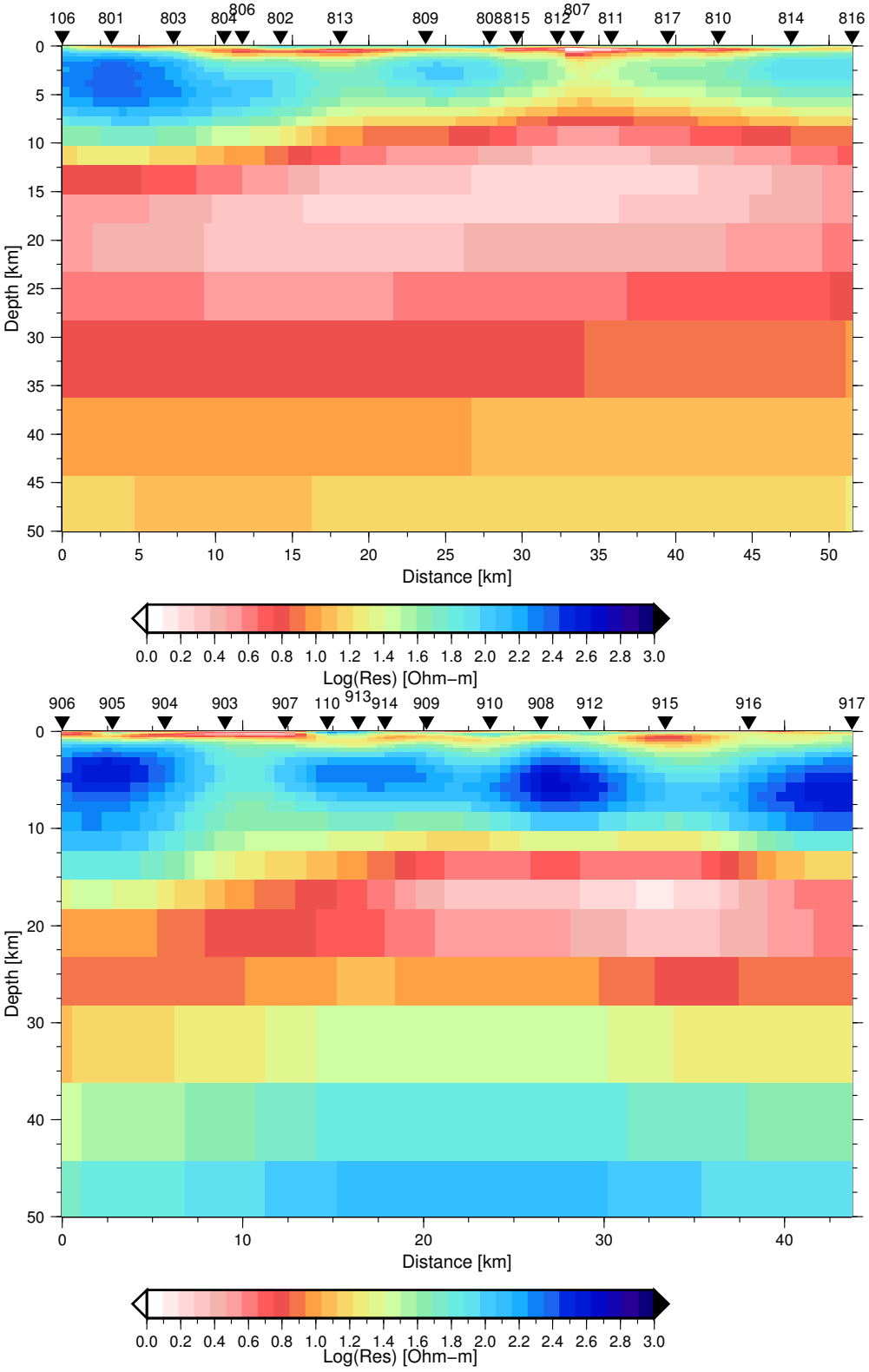

Figure 5.2: TM mode inversions for DMS (top) and HMS (bottom) profiles. Normalised RMS were 1.98 and 1.02 respectively

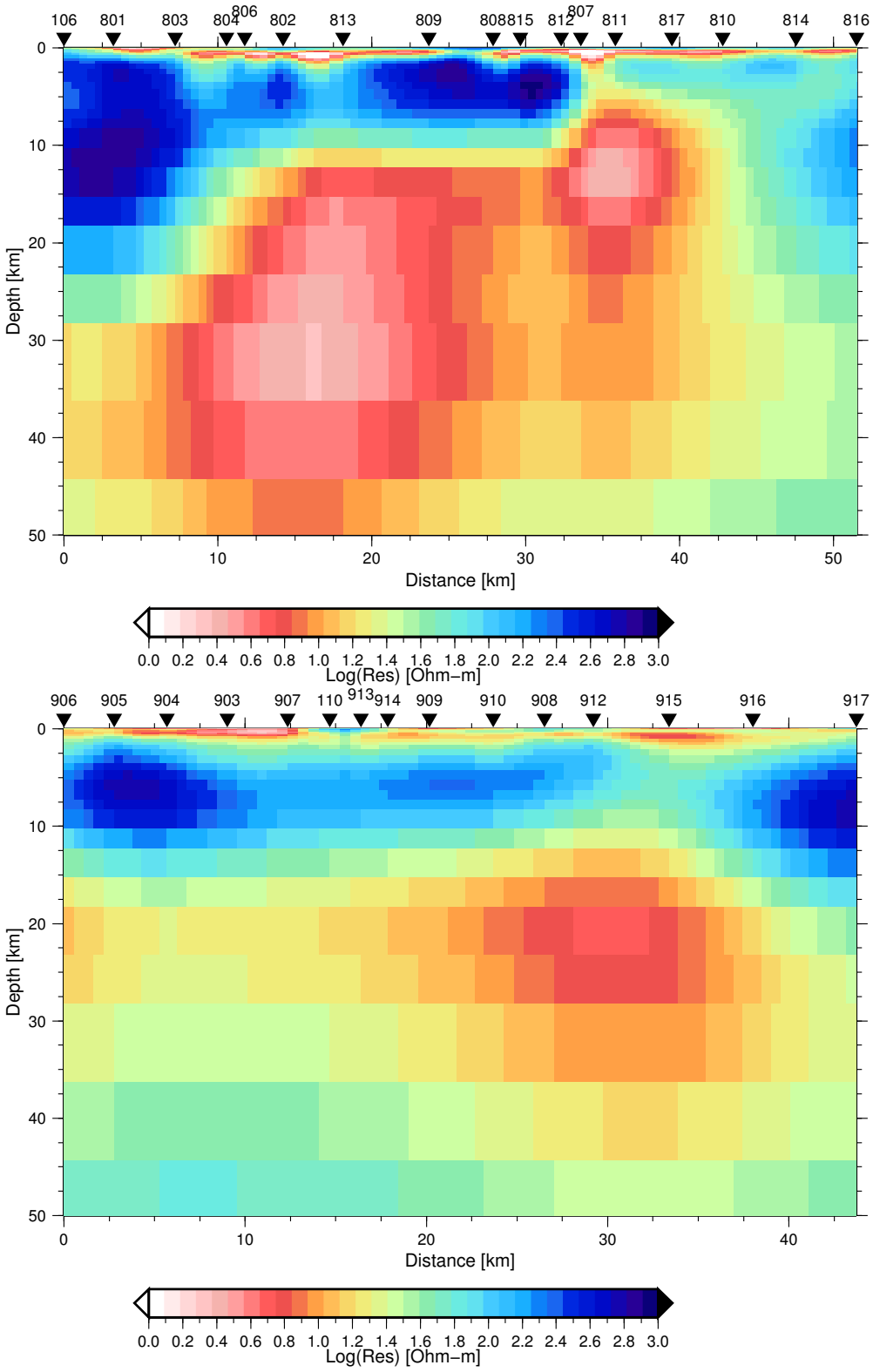

Figure 5.3: Joint inversions of both modes for DMS (top) and HMS (bottom) profiles. Normalised RMS were 2.61 and 2.35 respectively

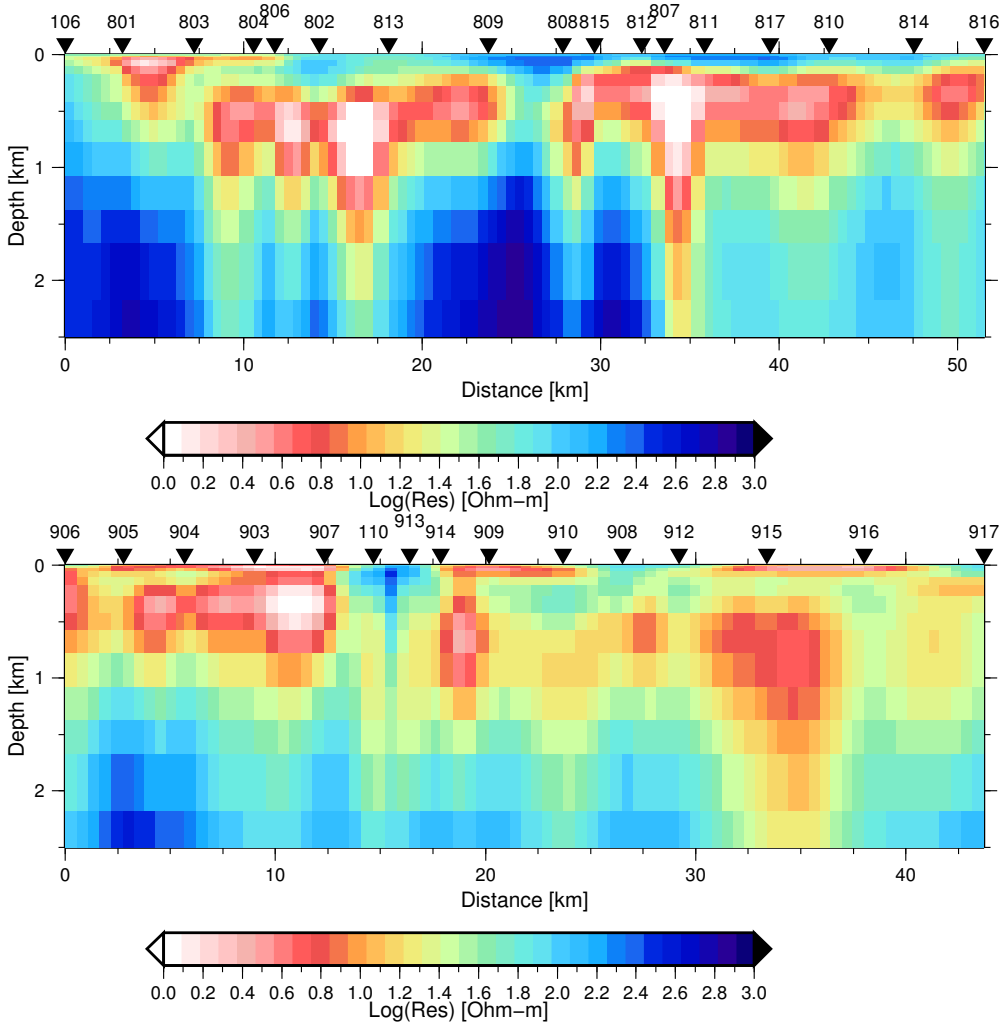

Figure 5.4: Upper 2.5 km of the joint inversion models shown in Figure 5.3. DMS profile shown at top, HMS profile at bottom.

horizontal boundaries, and generally produce a smoother model. The joint mode inversions have elements of both.

All three models for the DMS profile show a highly conductive layer in the uppermost 2 km, an expanded view of which is shown in Figure 5.4. Here it is possible to see that the conductive layer is pervasive across the entire profile with the exception of a small interruption between sites 809 and 808 and below site 106. It is also possible to see that in the western part of the model between sites 106 and 806, the conductive layer is present from the surface, whereas elsewhere there appears to be a 100 to 200 m thick resistive layer. Generally, the resistivity of the conductive material is between 1 and 10 Ωm. Below this initial conductor is a resistor which, in accordance with the joint mode inversion, can be split into three sections which get progressively thinner and less resistive from west to east. To the west of site 804 the resistor appears to thicken dramatically from 10 to 20 km, with resistivity values of between 300 and 1000 Ωm. In all three of the models shown for the DMS profile this is the largest single resistor seen, although the TM mode inversion seems to favour conductors and so it is not so pronounced in that model. In the central part of the model, between sites 804 and 812, the resistor extends to about 12 km in the joint inversion. Moving further east, there is an intriguing structure which is pervasive in all models; a conductive pathway which forms a break in the otherwise resistive layer between sites 807 and 811. The feature is most prominent in the TE mode model, as one might expect given its vertical interface nature, but it does appear in both other models as well. To the eastern extreme of the model the resistor thickens again, but resistivity values never exceed about 200 Ωm.

At depths greater than the base of the resistive layer (i.e. below between 10 and 20 km except where the conductive pathway extends to the surface), there exists an extensive region of very conductive material which is core to answering the key questions of this thesis. The conductive region is split into two distinct zones; the

more western one appears to start at approximately 12 km and is 20 km wide at 30 km depth. The more eastern conductor is smaller and shallower, appears to be circular in shape with a diameter of 8 to 12 km centred on a depth of about 12 km. The lowest resistivity in both conductors is below 3 Ωm and both show resistivities rising again at their lowermost extent, which, although at the lower limit of the penetration depth of the data, is believed to be required to fit the data (see Section 5.7.1).

The HMS profile models also show high conductivity material in the upper 2 km of the subsurface which, at the majority of sites, extends all the way to the surface, with little resistive cover as seen further north on the DMS profile. Again, this is followed by a resistor which is of a more uniform thickness of 12 to 15 km except in the far east where it extends below 20 km. The resistivity values are variable and mostly not quite as high as in the equivalent unit on the DMS profile, taking values between 80 and 600 Ωm. Like the DMS profile, at greater depth there is a conductive zone which is centred on the eastern side of the profile below sites 910 to 916. The conductor tends to begin at depths between 12 and 18 km (deeper than on the DMS profile), and the amount of conductive material above 15 km is far less than that seen further north. The lowest resistivity values are not as low as on the DMS profile, reaching 5 Ωm, and the area covered by very conductive material is not as extensive. In the western half of the profile the resistivity does not go below about 15 Ωm in the joint inversion.

Figures 5.5 to 5.10 show the model responses and the data used for the inversions which allow for detailed examination of where the models do and don't fit the data well. Figures 5.11 and 5.12 are the data and responses in pseudo-section format for the joint inversions. As indicated by the RMS misfit figures summarised in Table 5.1, the single mode TM inversions provide the best fit, followed by the TE mode only and then the joint mode inversions, with the HMS profile data generally being better fit than the DMS data. The worst data fits tend to be to

Model	RMS misfit values					Model Norm
	Overall	TE ρ_a	TE ϕ	TM ρ_a	TM ϕ	
TE DMS	2.44	3.14	1.42	-	-	80
TM DMS	1.98	-	-	2.08	1.86	21
Joint DMS	2.61	3.76	1.75	2.72	1.63	68
TE HMS	1.58	1.76	1.38	-	-	48
TM HMS	1.02	-	-	0.98	1.06	38
Joint HMS	2.35	3.20	1.76	2.21	1.98	29
TE Teru	1.46	1.58	1.32	-	-	23
TM Teru	1.48	-	-	1.52	1.44	19
Joint Teru	1.75	1.75	1.19	2.28	1.58	51
DMS RB 23 km	2.88	3.95	1.76	3.30	1.91	123
DMS Sills	2.74	3.75	1.75	3.13	1.17	-

Table 5.1: Summary of RMS misfit values and model norms for all models discussed.

the longest period data and in this case the fit of both the apparent resistivity and phase data is poor. There are some examples where the phase data are fit but the apparent resistivity are not (for example sites 106 and 801, TE mode inversion), but rarely is there a good fit to the apparent resistivity with a poor fit to the phase.

On the DMS profile the worst fit sites tend to be where the data are of poor quality as shown by their large error bars (sites 802, 812 and 807); however, there are a small number of sites where the data appear to be of good quality, yet the model does not fit the data. First, site 106 long period data are poorly fit in single mode and joint inversions in both phase and apparent resistivity, with the model predictions for TE resistivity too low, and too high for the TM mode, with correspondingly high and low phases respectively. The Groom-Bailey analysis for this site did not show a high misfit to the 2-d model and regional strike direction suggesting that 3-d effects are not prevalent. Site 809 also appears to have good quality data, yet the fit of the TE mode in both apparent resistivity and phase, and in single and joint mode inversions is very poor. This is likely to be a localised 3-d effect as indicated by the high misfit from GB decomposition and the fact that the fit of the TE mode is much worse than TM (the TE mode

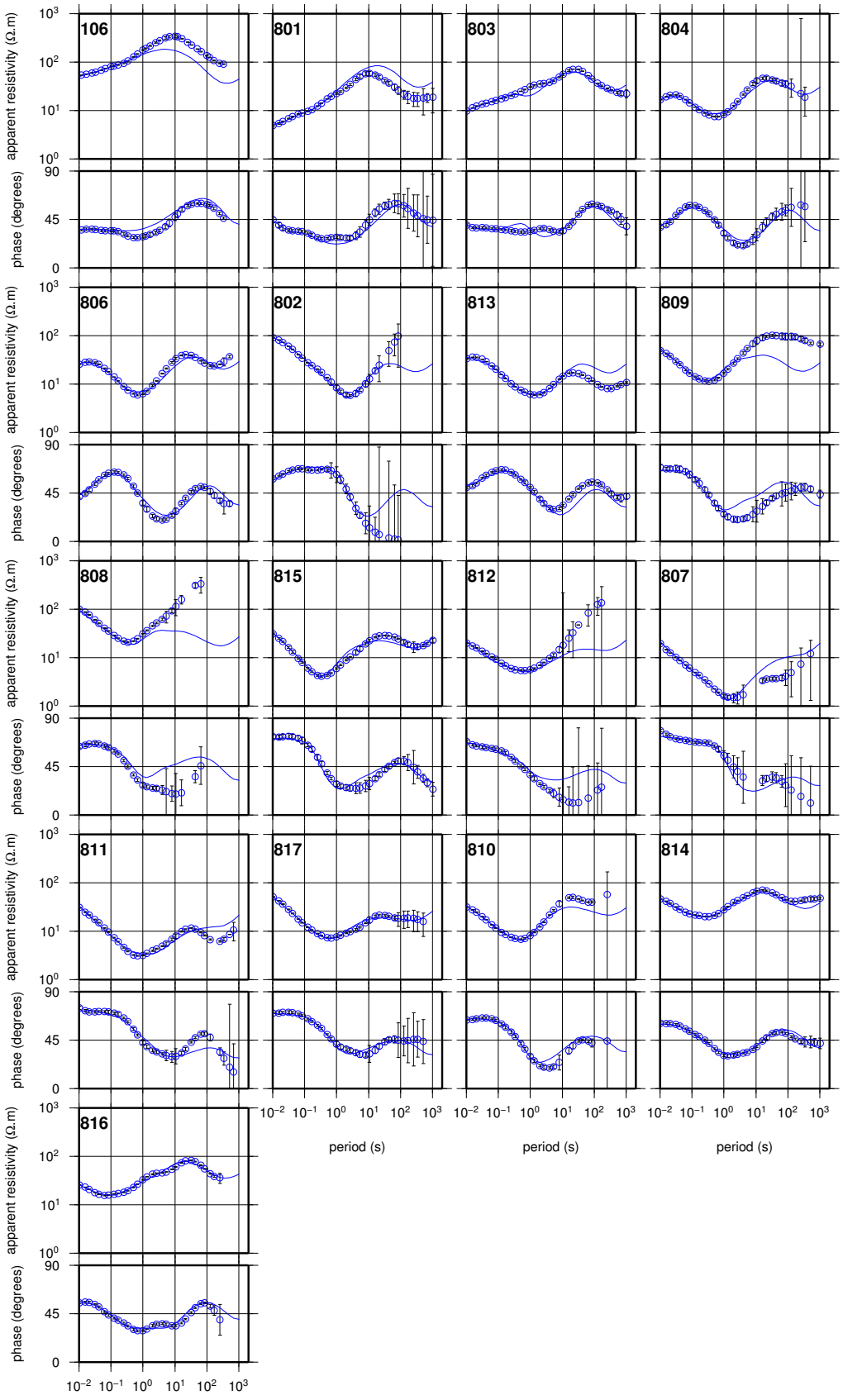

Figure 5.5: Model responses (solid lines) and data for the single TE mode inversion of the DMS profile.

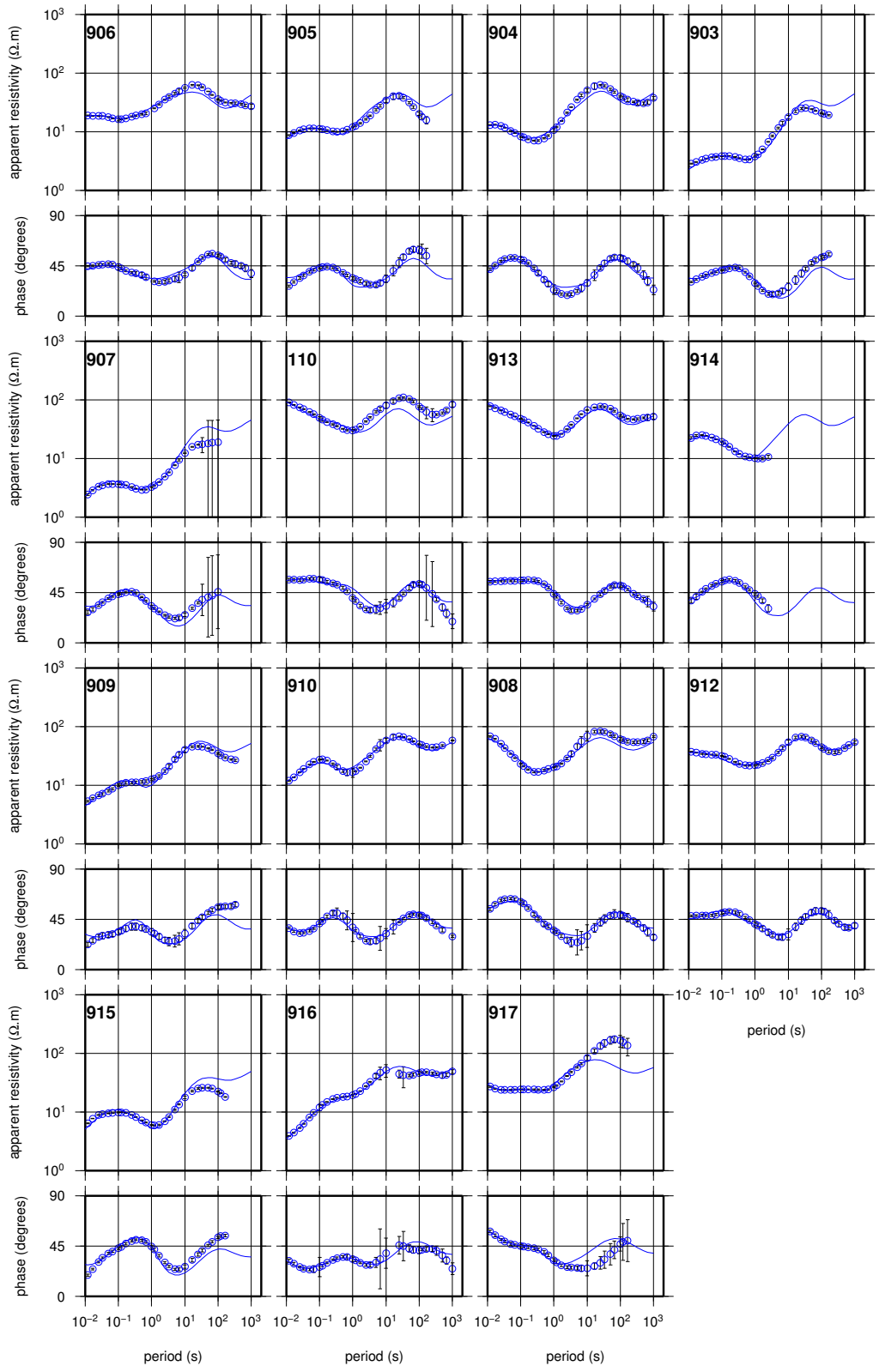

Figure 5.6: Model responses (solid lines) and data for the single TE mode inversion of the HMS profile.

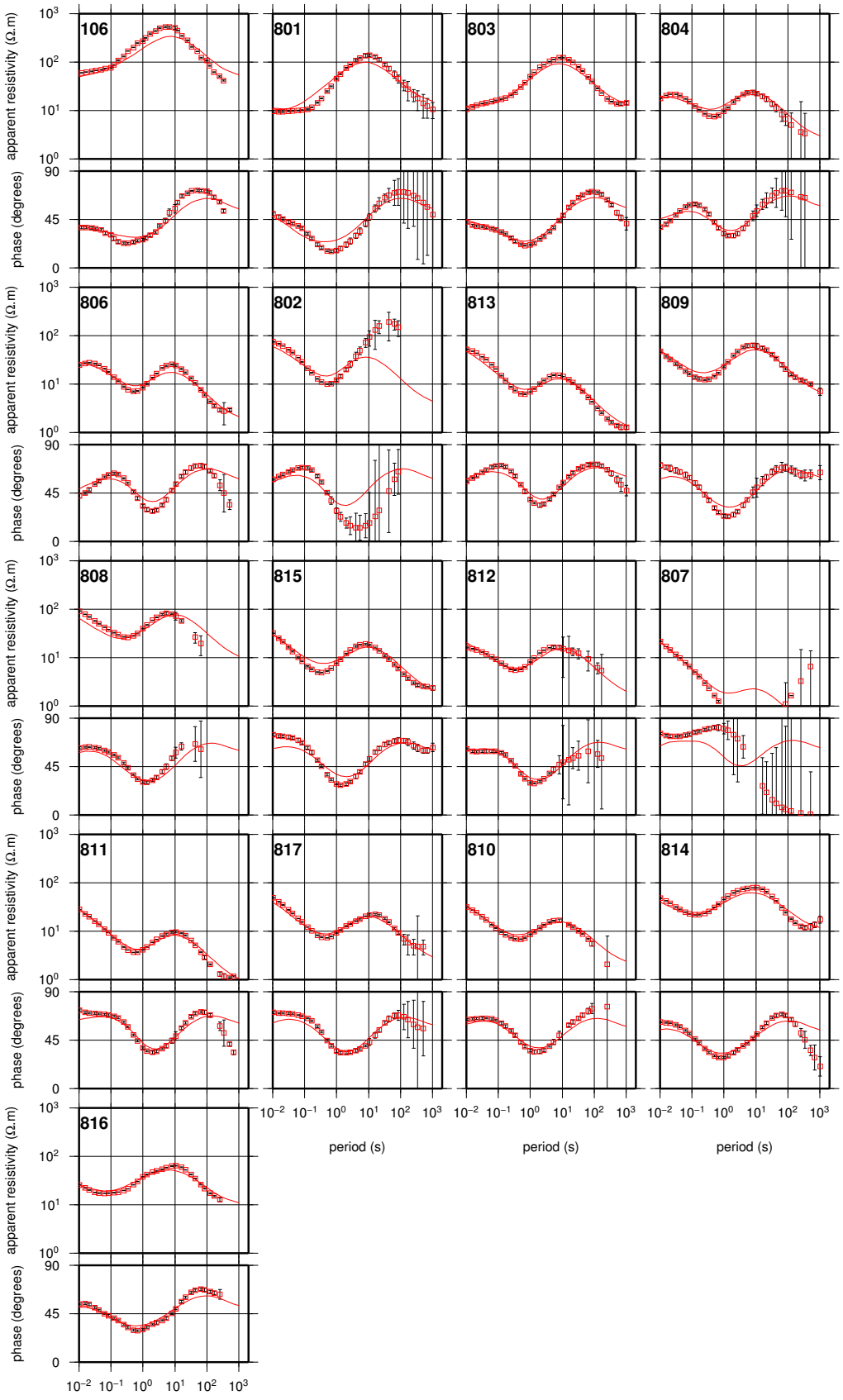

Figure 5.7: Model responses (solid lines) and data for the single TM mode inversion of the DMS profile.

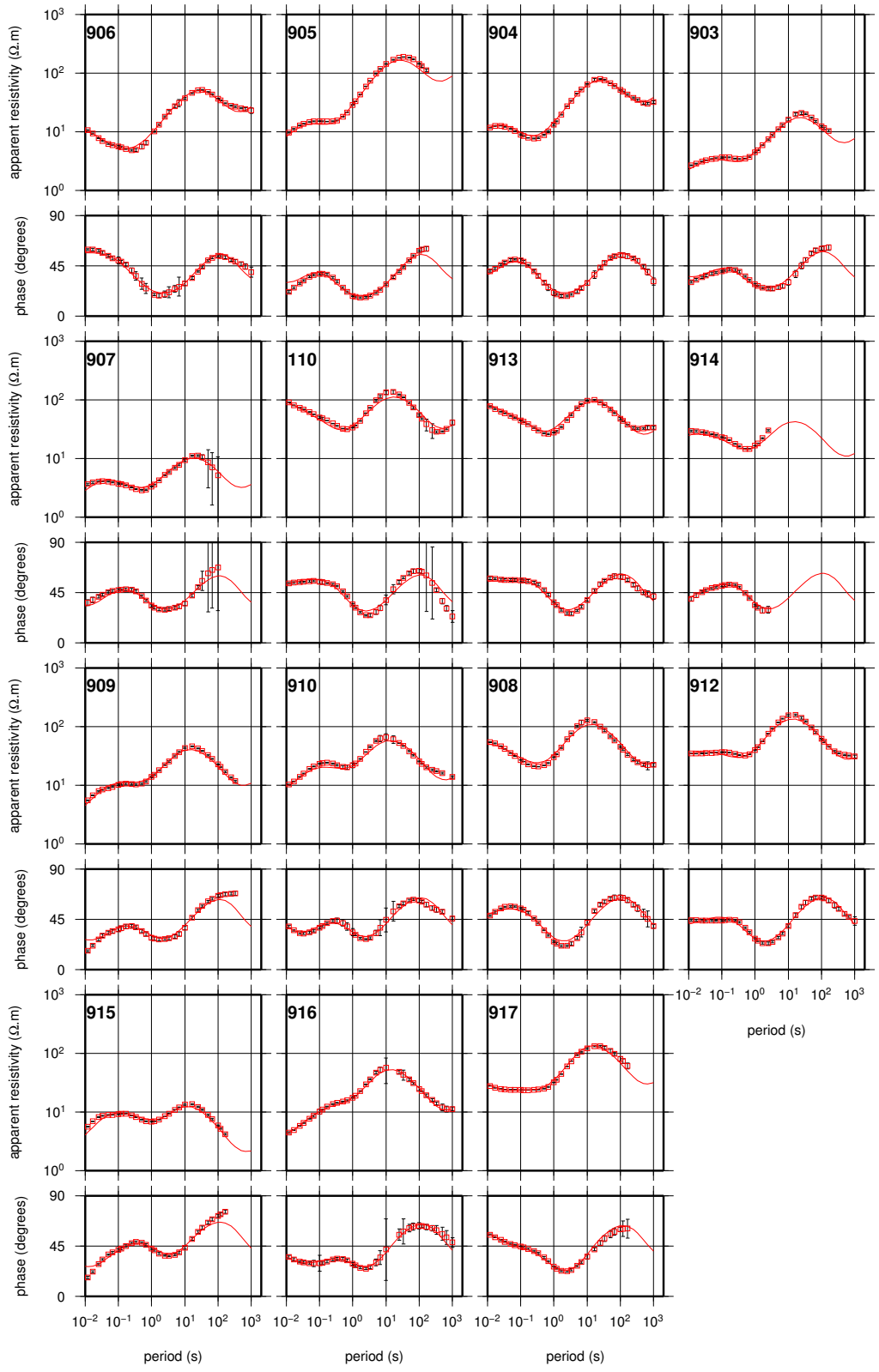

Figure 5.8: Model responses (solid lines) and data for the single TM mode inversion of the HMS profile.

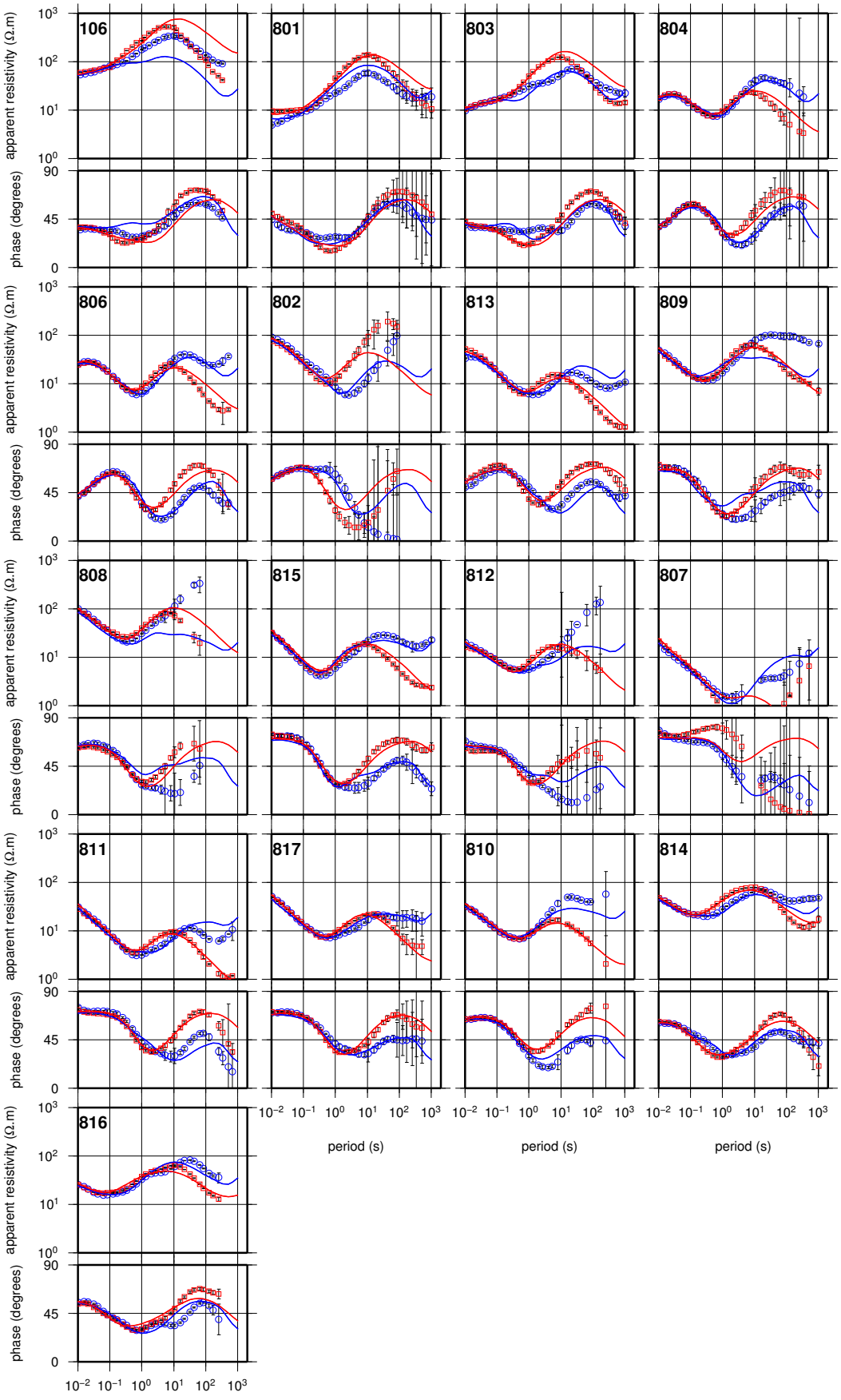

Figure 5.9: Model responses (solid lines) and data for the joint inversion of the DMS profile. Red lines or symbols are TM mode, blue are TE mode.

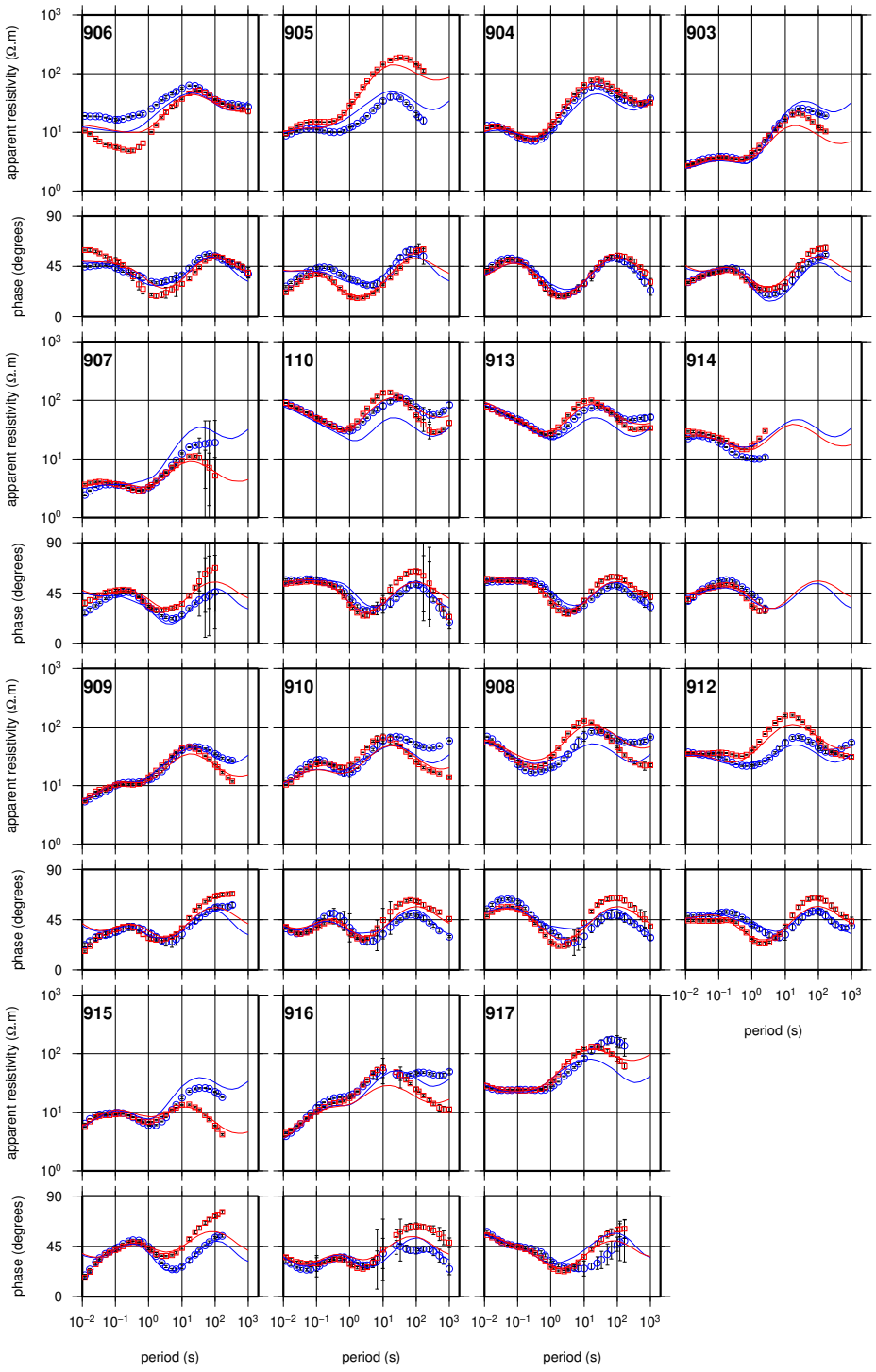

Figure 5.10: Model responses (solid lines) and data for the joint inversion of the HMS profile.

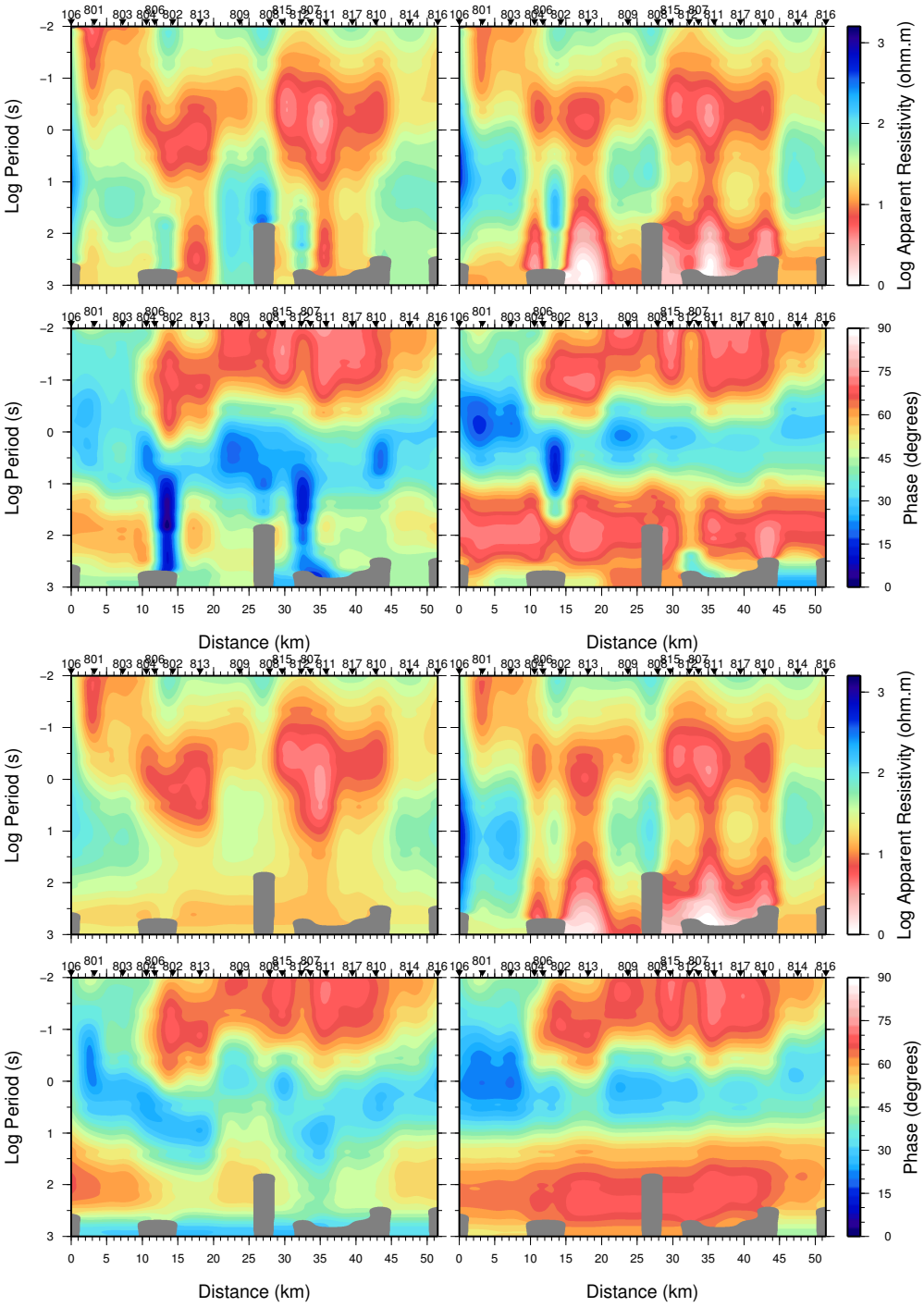

Figure 5.11: Pseudo-section of data (top) and joint inversion model responses (bottom) for the DMS profile. Upper panels are apparent resistivity, lower panels are phase, LHS is TE mode, RHS is TM mode. Greyed out areas show where there are no data.

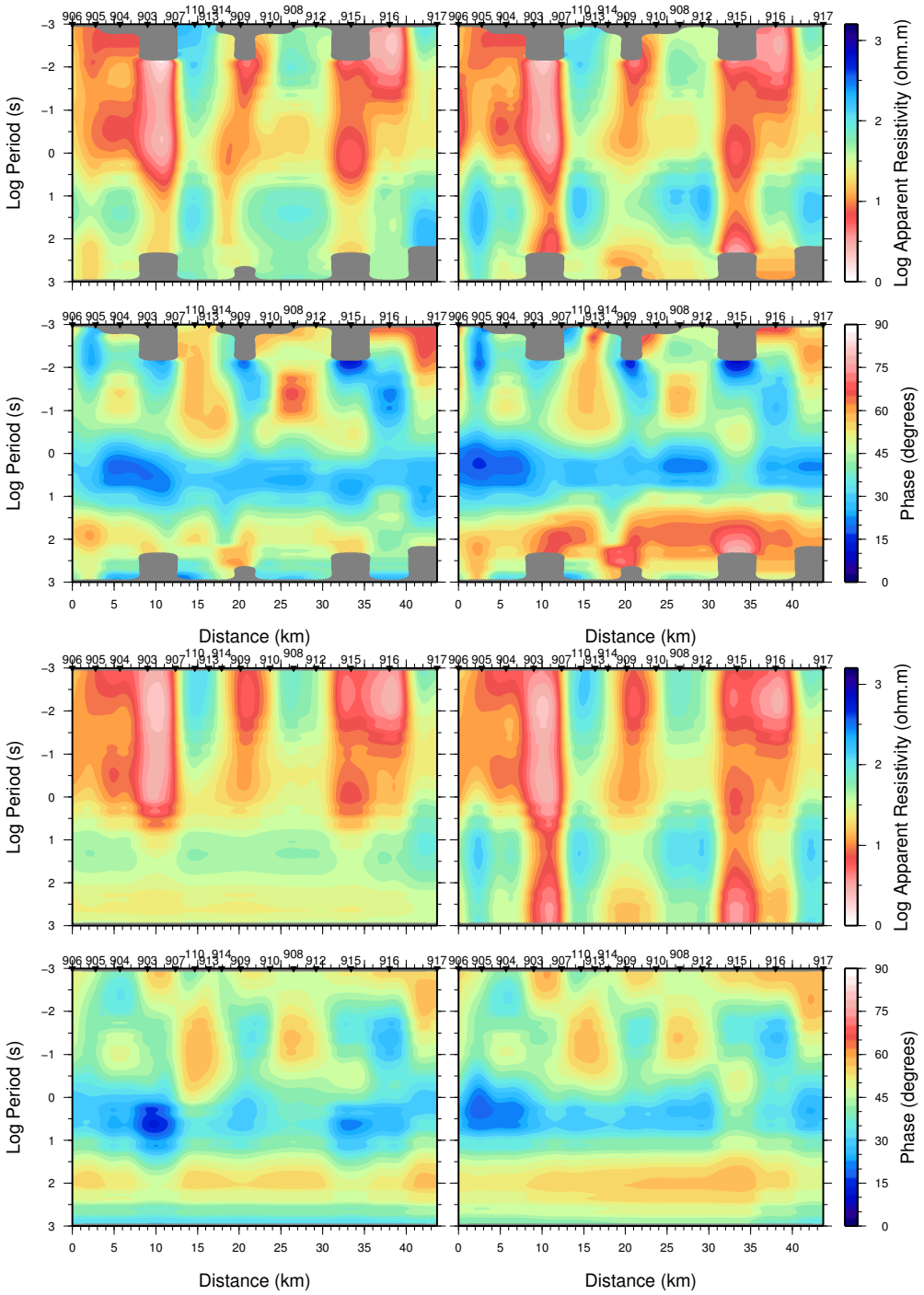

Figure 5.12: As Figure 5.11 for HMS model

being more sensitive to 3-d effects for reasons given previously). Looking at the fit more broadly by inspecting the pseudo-sections (Figure 5.11), the main features of the TM mode are very well reproduced, particularly the band of high apparent resistivity and low phase centred on 10 s and 1 s respectively, as well as the low apparent resistivity and high phase that follow. Some features of the TE mode are not quite as well reproduced. First, the magnitude of the high apparent resistivity and low phase band at 30 and 3 s is marginally lower in the data than in the model responses. This can be seen explicitly in the response curves of sites 801 and 813 although the effect is, at most, 0.1 of a decade. Also, the data show some sharp contrasts in phase in the lower part of the pseudo-section below sites 802 and 807 that are not well reproduced by the model. However both of these features are associated with very noisy data with correspondingly large error bars.

Again, the main features of the data pseudo-section for the HMS profile are well reproduced by the model. The long period TM mode phase tends to be higher in the data than the model responses, particularly on the western side of the profile (sites 908 to 917), although the apparent resistivity appears to well reproduced here. The long period, TE mode apparent resistivity data are collectively the worst fit part of the data set with model predictions significantly lower than the data at sites 110, 913, 908 and 917.

5.6 Results; the Teru profile

The data from the five sites making up the Teru profile were inverted having undergone Groom-Bailey decomposition and rotation into the best fitting strike angle of -44° west of north. This strike direction is not parallel to the strike of the rift at this latitude. However, this is not surprising given that the profile does not actually cross the rift and the dominant tectonic structures here are probably

somewhat different, especially given the complexity of the area which is heavily influenced by Dabbahu, and to some extent Badi, Volcanoes. Also, the data at all sites appear to be very 1-d as indicated by the lack of split between the two modes in apparent resistivity and phase curves and phase tensor analysis (see Chapter 4, Section 4.6). In this case mode allocation is irrelevant because transfer functions estimated with alternate orthogonal pairs of magnetic and electric fields give the same results. Indeed when the data are inverted with modes swapped the results are very similar.

Figure 5.13 shows the results of TE-only, TM-only and joint mode inversion for this profile, and Figure 5.14 shows the corresponding MT responses of those models. Similarly to the DMS and HMS profiles, the upper 2.5 km of all models have a conductive layer 1 to 2 km thick which appears to be thinning to the south. Like the DMS model this is overlaid by a thin resistive veneer which conversely to the conductor, appears to thin to the north. As seen previously, below this the TE and TM mode models show quite different structures, with the joint mode model having features of both. The TM mode model is not dissimilar to that of the DMS or HMS profiles having a moderately resistive layer to about 10 km depth, followed by a conductor approximately 20 km thick with minimum conductivity in the region of 3 Ωm. On the other hand, the TE mode model has, at its northern limit, a very conductive body that is broader, shallower and more conductive than any such feature seen on the DMS or HMS profiles. It begins at about 2.5 km depth, is more or less circular in shape with an approximate diameter of 10 km, extending to the north of the profile and its lowest resistivity value is below 0.1 Ωm. This feature also appears in the joint mode inversion.

The data for the Teru profile are generally very well fit by the model responses as shown by Figure 5.14 and in Table 5.1. The TE mode is slightly better fit than TM and phases are better fit than apparent resistivities. The worst fit site in all

inversions is 101, which is the site where there appears to be most departure from a 1-d subsurface.

5.7 Discussion

5.7.1 Sensitivity tests

Many tests have been carried out to test how well constrained by the data a given feature of the model is. These tests are carried out by using the forward modelling part of REBOCC to calculate the response of the model when, for example, the structure of the model that we are interested in is manually removed or altered. If the alteration has a detrimental effect on the fit of the model to the data, then the data are considered to be 'sensitive' to the existence of that feature, or put in other words, the feature is constrained or required by the data. Park et al. (1996) rightly point out that even if the misfit is increased that is not to say that an alternative resistivity structure may be able to compensate for the alteration, which must be tested by re-running the inversion with the altered feature of the model fixed, and reassessing the misfit once more.

Hammond et al. (2011) use receiver function analysis to show that the depth to the Moho in the vicinity of the DMS and HMS is around 22 km. Arguably the most important feature of the MT models to test was the depth to which the data are sensitive, and in doing so test whether such large volumes of conductive material are required at depths below the Moho, particularly on the DMS profile. To this end, a resistive basement of 1000 Ωm was fixed at 54 km depth, then the inversion was run as usual (rather than just imposing the structure on the favoured model then using forward modelling to calculate the response). The process was repeated with the resistive basement at 44, 36, 28, 23 and 18 km and

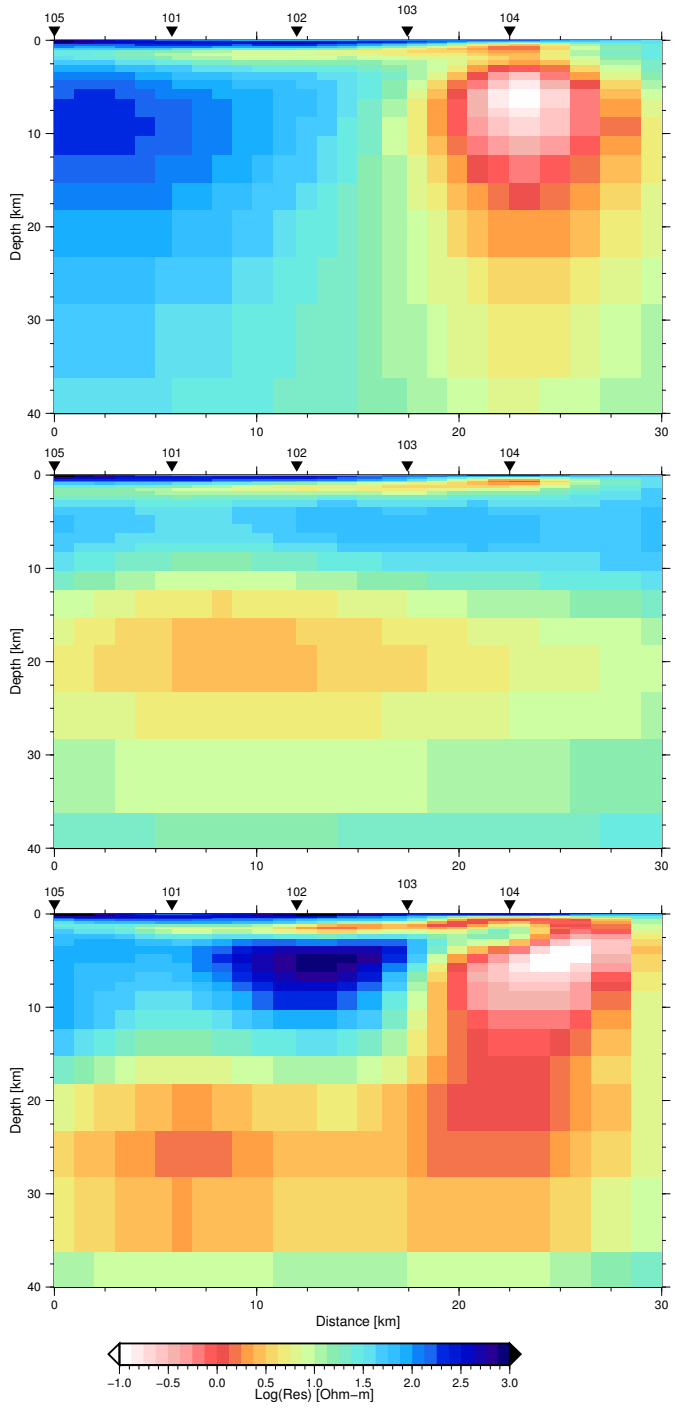

Figure 5.13: TE mode (top), TM mode (middle) and joint mode (bottom) inversion results for the Teru profile, with normalised RMS misfits of 1.45, 1.47 and 1.83 respectively. Note that the colour scale used here is different to previous models to accommodate a larger range of resistivities and some of the model space to the north of the profile is shown. The vertical scale is half that of the horizontal. The southern end of the profile is on the left. Dabbahu Volcano lies to the west of sites 103 and 104.

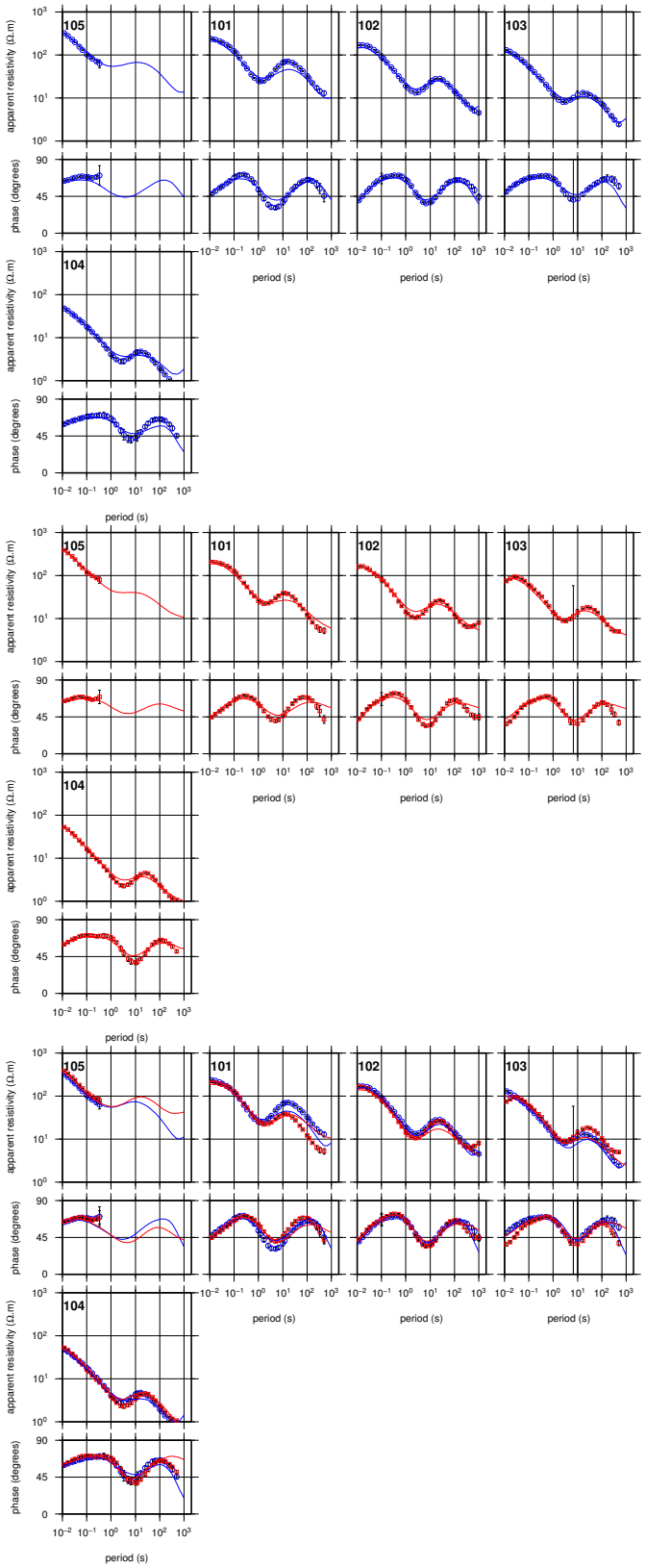

Figure 5.14: Response curves for the models shown in Figure 5.13, plotted with data. Red symbols or lines = TM mode data or responses, blue symbols or lines = TE mode data or responses

the responses were studied at each depth allowing detailed analysis of the depth to which the data are sensitive. The effect on the model responses is virtually undetectable with the resistive basement at a depth of 54 km; however, changes in both the model and the responses are seen at all shallower depths. Included here are the results from the test where the top surface of the resistor was fixed at a depth of 23 km. In this test the best fitting model had an RMS misfit value of 2.88, a significant increase from 2.61 achieved by the unconstrained model. The response curves of the TM mode were worst affected, mostly, as one might expect, in the long period data (see Figure 5.16). Furthermore, the model itself (Figure 5.15) requires extreme resistivity contrasts with values as low as 0.2 Ωm (similar to sea water) at 20 km depth which if interpreted in terms of magma would require pure melt with no solid matrix (See Chapter 6). The model is also much rougher, with a norm of twice that of the model shown in Figure 5.3.

The maximally smooth model naturally shows the deep, high conductivity regions as undifferentiated zones, however a test was performed to establish whether or not the MT data could support a model whereby they were separated by resistive bands. One such model is shown in Figure 5.17 with model responses shown in Figure 5.18. The resistive bands are compensated for by even lower resistivities within some of the conductive bands, keeping the overall conductance similar. Figure 5.18 shows that the fit is not compromised at any sites.

The exact structure of the upper conductive layer shown in Figure 5.4 seems to be very well constrained by both TE and TM modes. Any alteration of this layer results in dramatic changes to the model responses which then no longer fit the data. On the other hand the conductive pathway which appears to connect the upper conductor to the lower one below sites 807 and 811 does not seem to be very well constrained. This can be seen in Figure 5.15 where the subsurface below these sites is comparatively resistive without a severe effect on the fit. It is

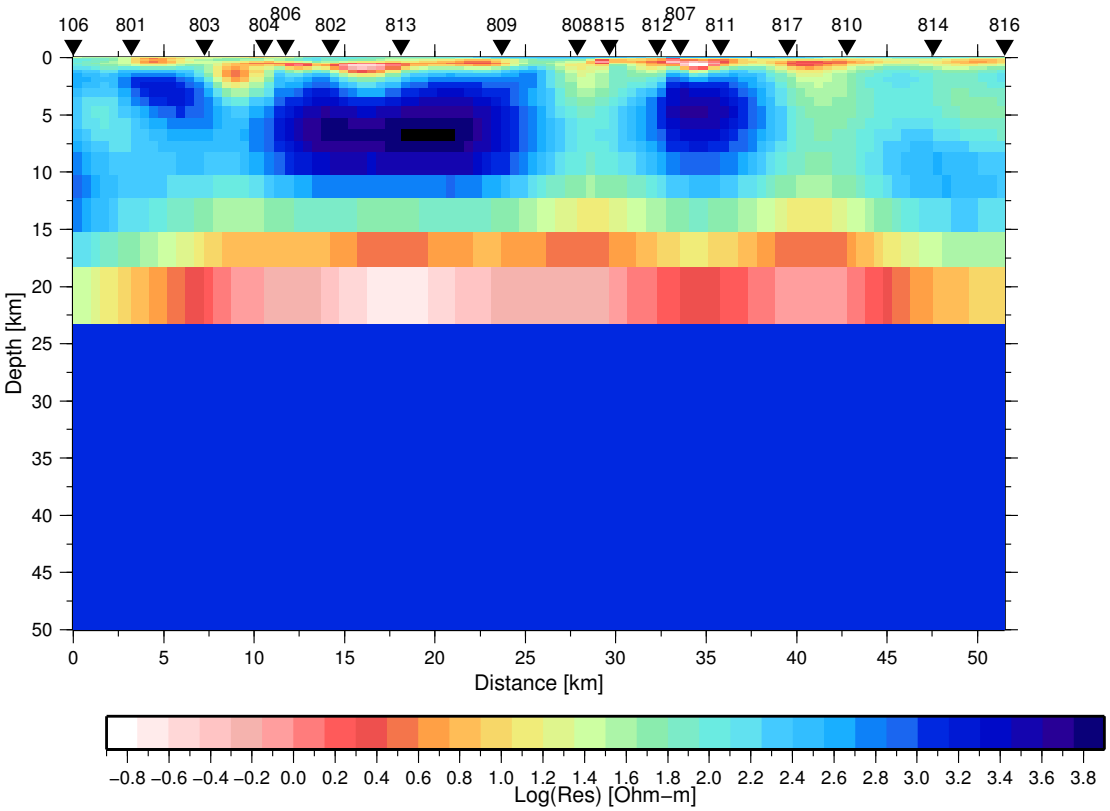

Figure 5.15: Best fitting model with a resistive basement of 1000 Ωm at 23 km depth. Note the colour scale used is different to previous models to accommodate the large range of values in this model. Overall RMS misfit is 2.88

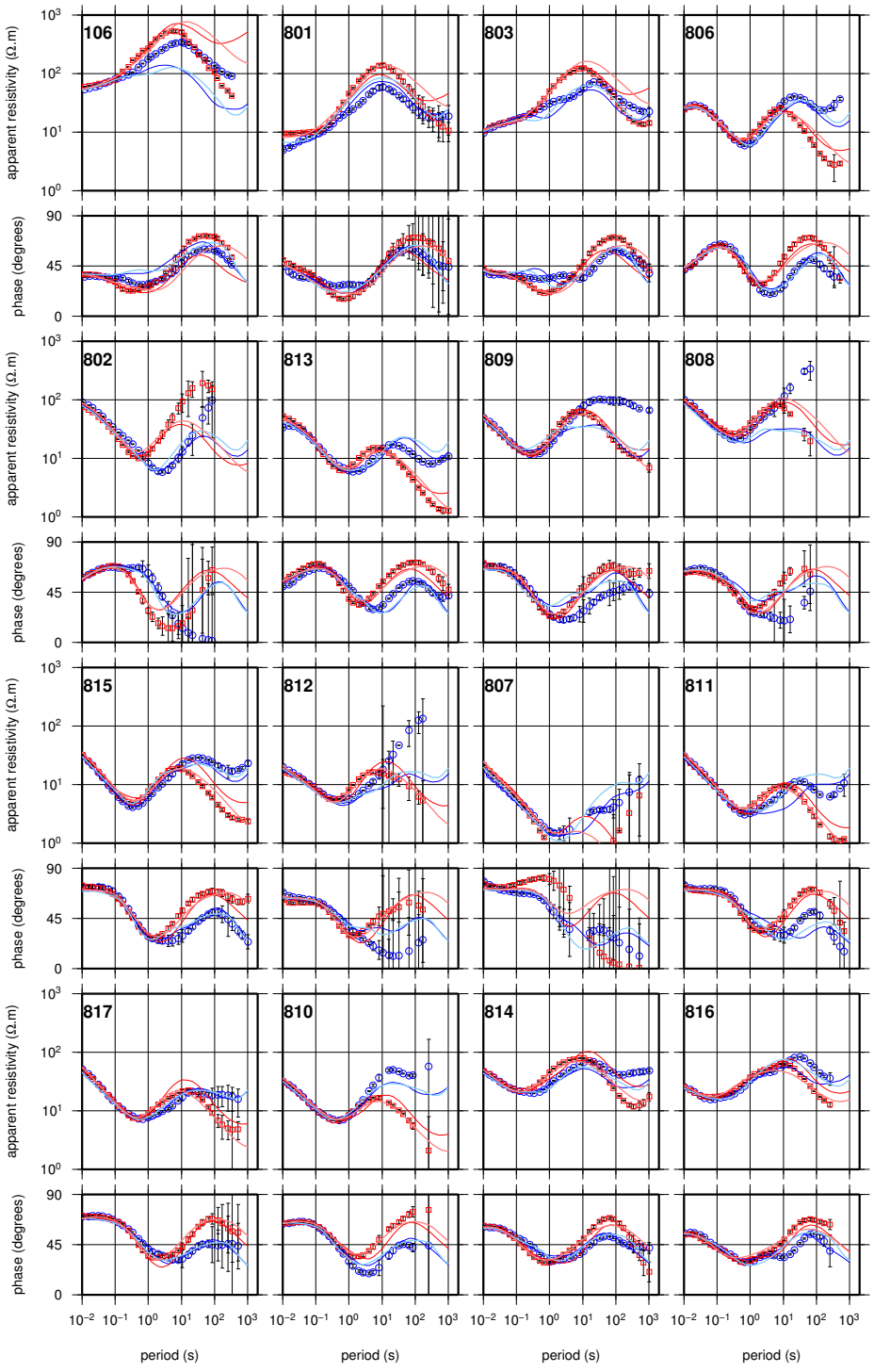

Figure 5.16: Responses for both the original model (light colours) and that shown in Figure 5.15 (dark colours). Data are also shown as symbols. TE mode = blue, TM mode = red. Site 804 is not shown but response curves for that site are very similar to site 806.

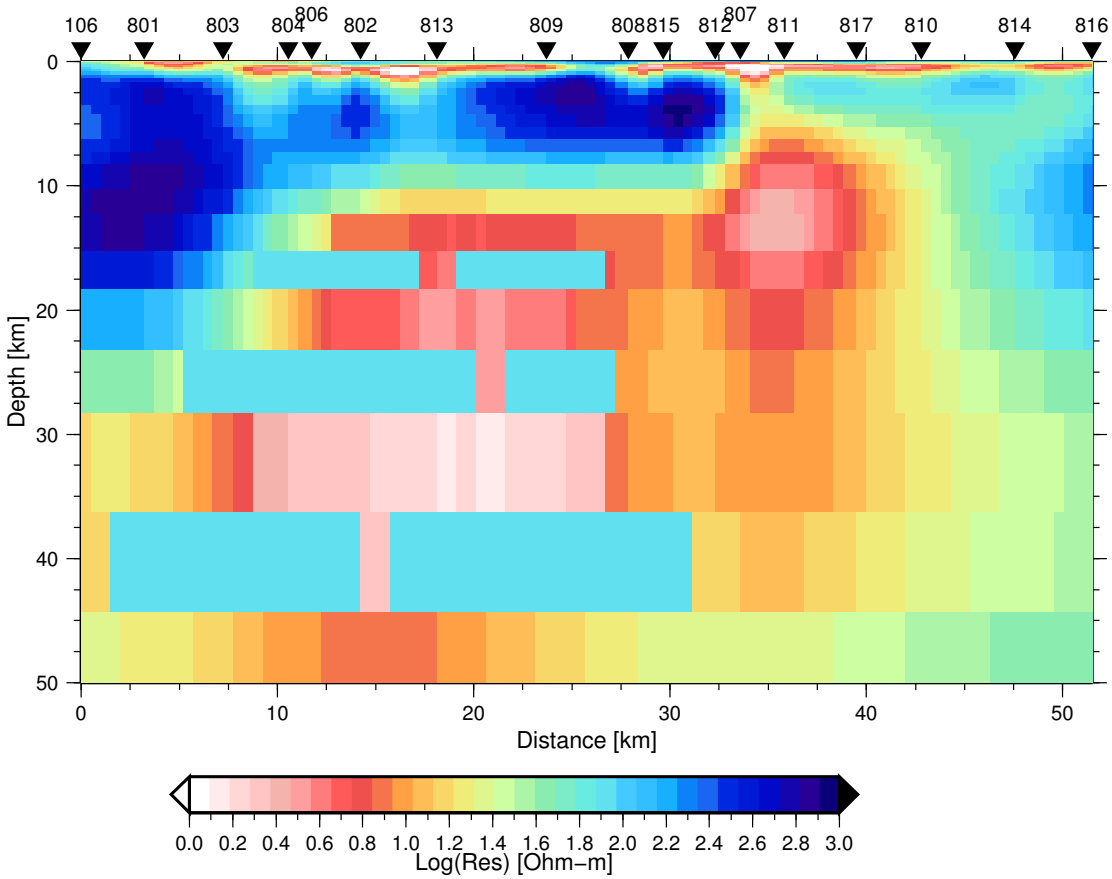

Figure 5.17: Joint inversion of both modes showing the deep conductor separated by resistive bands. RMS misfit = 2.73

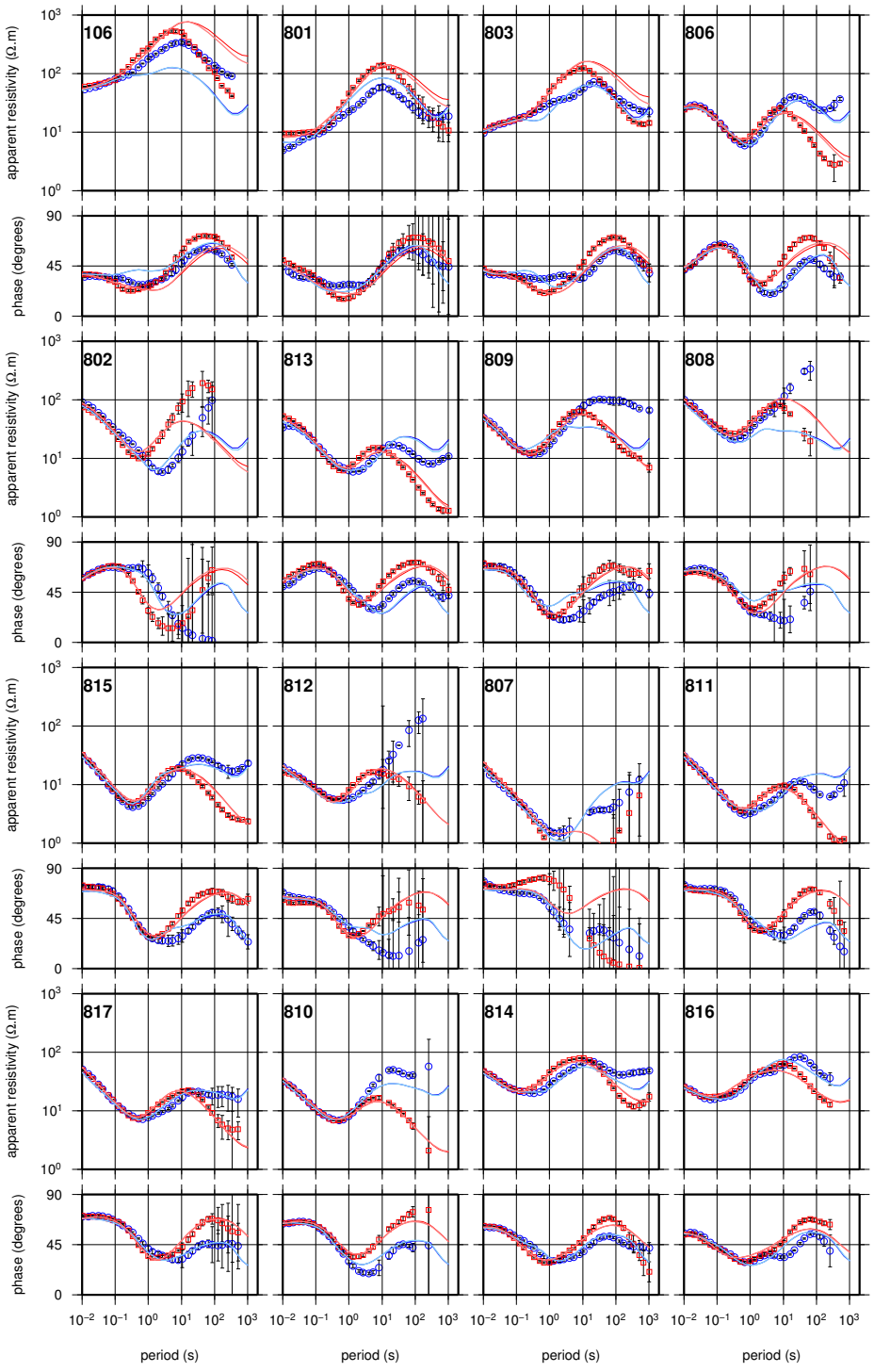

Figure 5.18: Responses for both the original model (light colours) and that shown in Figure 5.17 (dark colours). Data are also shown as symbols. TE mode = blue, TM mode = red.

possible that this feature of the model appears due to the data at site 807 which are of very poor quality.

It is common for lower error floors to be used for the TM mode and/or the phase data due to their being less or un-affected by 3-d structures and static shift respectively (e.g. Hill et al., 2009; Miensopust et al., 2011), thus giving them more influence on the model. However this was not deemed necessary here because those data were being preferentially fit regardless (see Table 5.1). For instance individual RMS misfits for the joint inversion of the DMS profile were 3.7 and 1.7 for the TE apparent resistivity and phase, and 2.8 and 1.6 for the TM apparent resistivity and phase. Some tests were performed nonetheless using a lower error floors for the TM mode and phase data; however, this was considered to skew the fit too much in favour of those data.

5.7.2 Interpretation

The existence of extensive sedimentary deposits was to be expected on the HMS profile given the nature of the sediment filled Tendaho Graben which it crosses. Bridges et al. (2012) anticipate sediments to be more than 1 km thick, interspersed with fissure basalts, and a borehole drilled at Dubti (north east Tendaho) found 1500m of lacustrine sediments (Abbate et al., 1995). This model is in excellent agreement with the upper 2 km of the HMS MT model as shown in Figure 5.4, where the highly conductive regions are caused by the sediments, and the resistive blocks at the surface between sites 110 and 914, and 908 and 912 are related to fissure basalts. This is consistent with field observations; most sites were located on sedimentary plains, with the exception of those previously mentioned which were located on more rocky terrains. As with the HMS profile, the most reasonable explanation for the upper conductive layer seen across the DMS profile is also sediments, which were not necessarily expected prior to this study with the

exception of the western sites located on the Digdiga plain (sites 106 to 804 - see Figure 5.19). To the east of Badi volcano the surface of the rift is characterised by heavily faulted fissure basalts which are seen in the DMS MT model as a resistive layer of just 100 to 200 m thick. In the field there is no evidence on the surface of the kilometre or so of sediments which underlie the fissure basalts and lava flows. According to the modelling carried out by Grandin et al. (2009) and Wright et al. (2006) the 2005 mega-dyke stopped at 1 to 3 km below the surface after which spreading was accommodated by slip on normal faults. Thus the dykes probably do not penetrate the sedimentary layer. The lowest resistivity seen in the sediments is less than 1 Ωm which is low given that typical resistivities in marine sediments are between 1 and 10 Ωm (Chave and Jones, 2012). Two factors are likely to contribute to the very low resistivities seen; first pore fluids may be very saline (large salt deposits are seen at Afdera and Dallol to the north of Dabbahu), and second the geothermal gradient is high here (Gianelli et al., 1998) and elevated temperatures cause pore fluid conductivity to rise (Chave and Jones, 2012). The two regions of the conductive layer which exhibit the lowest resistivities are located immediately next to Badi volcano and within the rift axis where high heat flows should be expected (see Figure 5.20). Sites 101 to 104 on the Teru profile were located on what seemed like extensive sedimentary plains similar to those at Digdiga. Therefore it is surprising that the resistivity structure below these site does not show the conductor extending all the way to the surface as it does at many sites on the HMS and those located on the Digdiga plain on the DMS. From this observation it is presumed that the sediments observed in the field at sites 101 to 104 are a very thin superficial deposit and frequencies recorded during this project were not high enough to detect them.

The resistive units seen in most areas below the conductive sediments down to a depth of 10 to 15 km are consistent with fractured and faulted igneous upper crust. Evidence from the seismicity associated with the 2005 dyke injection (Belachew

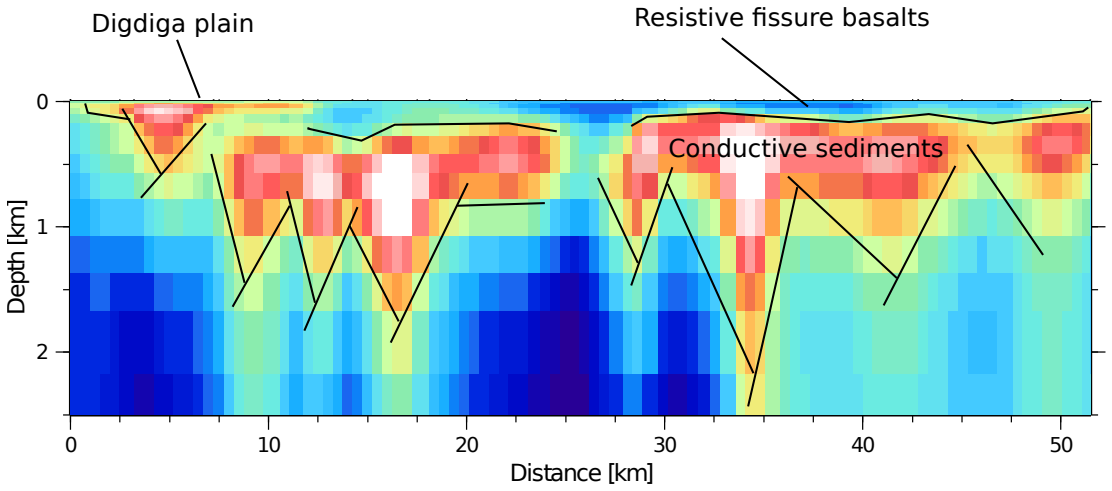

Figure 5.19: Interpretation of upper part of Dabbahu Model. Vertical exaggeration = 2.6.

et al., 2011) and modelling of geodetic data (Wright et al., 2006; Grandin et al., 2009) suggests that there is no dyke opening below 10 km and the maximum opening occurs at 4 to 6 km. These depths are concurrent with the resistive layer seen in the models so it is likely that this part of the crust is composed, at least in part, of frozen dykes emplaced during this late stage of continental breakup. Resistivity values in this zone lie between 100 and 1000 Ωm which are low in comparison with normal values for dry igneous rock, in the region of 10^3 to 10^7 Ωm (Simpson and Bahr, 2005). Miensopust et al. (2011) magnetotellurically imaged the massive Okavango Dyke Swarm in Botswana and reported resistivity values of 10^4 Ωm - an order of magnitude higher than seen here. In the DMS, fracturing and faulting of this upper crustal layer as well as abnormally hight heat flow may be responsible for lowering the resistivity. The conducting pathway seen below sites 807 and 811 may be a result of increased fracture and fault density seen here as shown in Figure 5.20.

Below the resistive upper crust on the DMS and HMS profiles we see broad regions of conductive material, which can only be explained in terms of partial melt in this

tectonically active region. This is the first time these huge reservoirs of magma have been imaged because at these depths teleseismic imaging does not have the power to resolve them (e.g. Bastow et al., 2008; Hammond et al., 2011), and yet they are too deep to be imaged in detail by seismic methods using local sources of energy or modelling of geodetic data (e.g Keir et al., 2009; Wright et al., 2006). All of the above methods do however infer their existence and comparisons will be looked at in more detail in Chapter 6. The Moho (the boundary between the crust and mantle) around the Dabbahu segment is estimated to be at a depth of 20 to 24 km (Hammond et al., 2011). The deep conductor seen on the DMS profile is split into two distinct regions both of which straddle the Moho. The smaller and shallower of the two is largely located in the crust between 8 and 25 km directly below the location of the recent dykes, spanning approximately 8 km in width. The other larger conductive zone is further to the west and largely below the Moho, between 12 and 45 km, reaching its maximum at 30 km. Because the depth of penetration is reduced in conductive material, the bottom of this conductor is not very well resolved. However, the data, particularly of the TE mode, at sites 806 and 813 clearly show the resistivity curve rising and the phase below 45 degrees at the longest periods suggesting that the data are sensitive to its lower extent. The bottom surface of the conductor shown on the HMS profile is better resolved because long period data are available at more sites and tend to be of slightly better quality, and because the total conductance is considerably lower the depth of penetration is increased. The highest conductivities outside of the sedimentary deposits are seen in the very shallow crustal conductor near to Dabbahu volcano on the Teru profile. Large parts of the Chapters that follow will be devoted to discussing in more detail the interpretation of these conductive bodies with regard to melt fractions and their wider implications.

The shallow crustal conductor seen on the Teru profile is intriguing. Several authors suggest that a magma supply exists under Dabbahu volcano between 2

and 6 km depth Ebinger et al. (2008); Field et al. (2012). The conductor imaged here is centred on about 4 km and is more or less circular with a diameter of 10 km (using an approximate 9 Ωm contour). The lowest resistivity values seen in the joint inversion of both MT modes is less than 0.1 Ωm and although the profile does not actually traverse Dabbahu volcano, sites 103 and 104 are only 10 km from the summit. Given the evidence from other studies that suggest that magma storage zone exist in the crust below Dabbahu, it seems reasonable to interpret the conductive material seen here as partial melt.

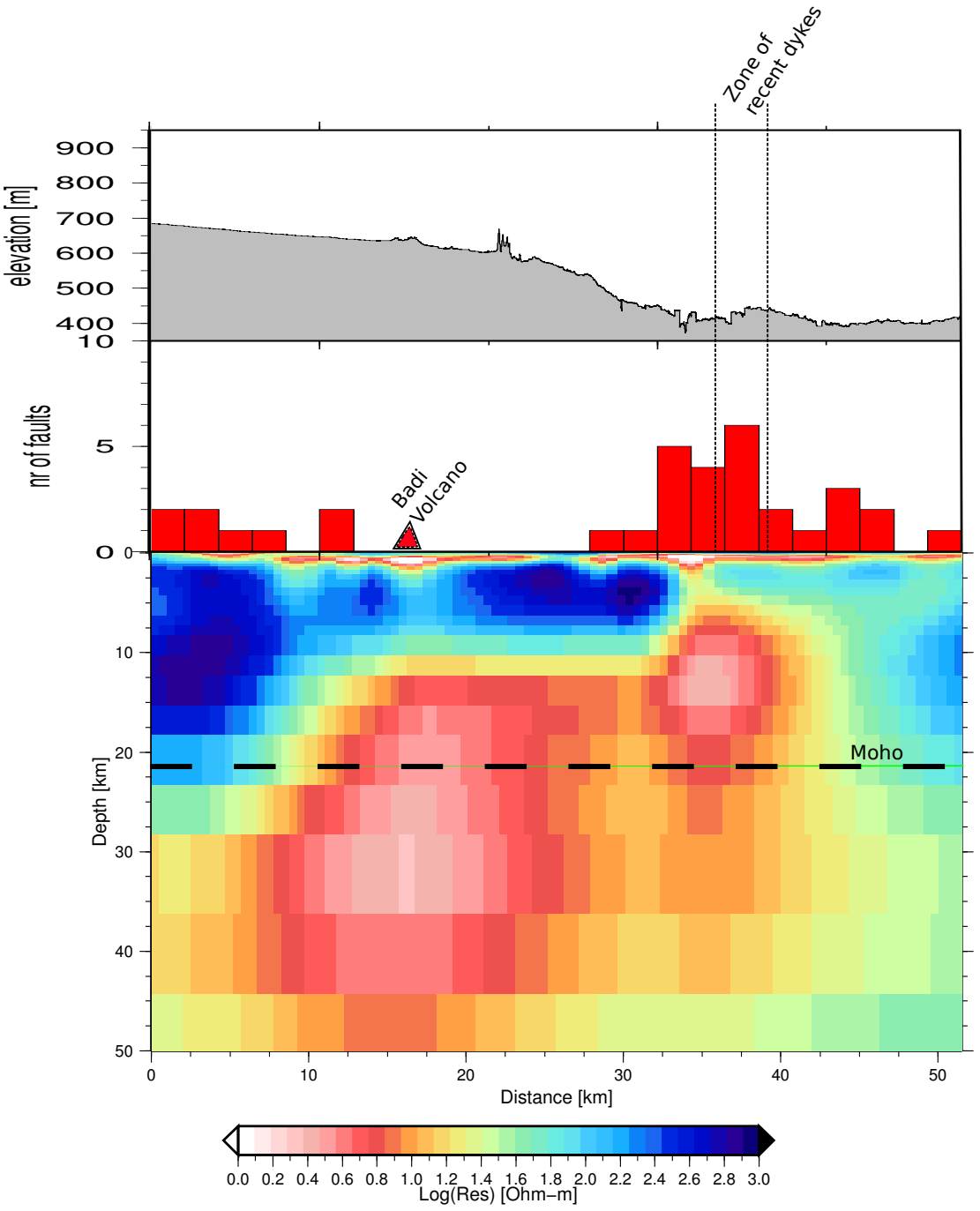

Figure 5.20: Joint inversion DMS model shown with histogram of faults, elevation along the profile and locations of Badi volcano and recent dykes. The Moho is indicated by the dashed black line.

Chapter 6

Integration with seismic studies

6.1 Introduction

The mega-dyke intrusion of September 2005 was recorded seismically by a sparse array of permanent seismometers in Ethiopia, Djibouti, Eritrea and Yemen. Since then a temporary array of broadband seismometers has been deployed, the data from which have been used in many studies by members of the Afar Rift Consortium. From accurately locating in time and space the seismic events (seismicity) associated with later dyke intrusions, to sampling the seismic velocities of the crust and mantle using teleseismic energy, this chapter looks at some detailed comparisons between some of the results obtained from these studies and the results given in the previous chapters of this thesis. Such comparisons are interesting because both methods are capable of sensing, for example, fluid phases within the Earth but the physical parameter measured is different for each method (conductivity and seismic wave velocity). The chapter is generally arranged such that the depth of interest increases throughout, starting with a

look at seismic and electrical anisotropy of the upper crust and ending with a discussion of seismic velocities and conductivity of the upper mantle.

6.2 Comparing seismic anisotropy with geo-electric strike direction

Comparing seismic anisotropy with electrical anisotropy can provide a useful insight into possible strain related fabrics within the crust and lithospheric mantle (e.g. Padilha et al., 2006; Hamilton et al., 2006), which are pertinent in this study. By electrical anisotropy, in the broadest sense, we mean that the conductivity of the subsurface is dependent on the orientation in which a current is flowing (Wannamaker, 2005). This may be a result of regional 2-d structures that are resolvable by the data, or a 2-d fabric such as a series of dykes or oriented melt pockets within a host of differing resistivity where the fabric itself cannot be resolved. The latter is known as shape preferred orientation (SPO). Finally, it may be caused by an intrinsic, microscopic effect such as anisotropic hydrogen diffusivity in olivine crystals (applicable to mantle depths) which is known as lattice preferred orientaion (LPO) (Schock et al., 1989). Without knowledge of the vertical magnetic field (not recorded during this study) it is not possible to discriminate between such causative structures from the MT impedance data alone (Hamilton et al., 2006), and they all manifest themselves as a contribution to the 2-dimensionality of the data set. Here, the geo-electric strike direction attained from GB analysis is used on a site-by-site and period-by-period basis to assess the variation in electrical anisotropy and compare it with results from studies of seismic anisotropy. The amount of split between the TE and TM mode phase is used as a measure of the magnitude of electrical anisotropy as suggested

by Hamilton et al. (2006) and Padilha et al. (2006).

The physical parameter to which seismic waves are sensitive is the velocity with which they travel through a medium, hence seismic anisotropy is defined as an azimuthal dependence of that property within the Earth. On entering a seismically anisotropic medium, shear waves split into two polarisations travelling parallel and perpendicular to the fast direction, which then develop a time delay between them as they travel at different speeds through the volume. SKS waves (shear waves that pass through the core as longitudinal waves and re-emerge as shear waves) from teleseismic events are used to study seismic anisotropy accrued between the the core-mantle boundary and seismic station. The delay time between fast and slow shear waves and the direction of the fast axis of the waves are used to estimate the magnitude and direction of anisotropy respectively. This method recovers information from depths that are generally beyond the maximum penetration depth of the MT data. However, upper crustal anisotropy has been measured in Afar using shear wave splitting from local earthquakes (Keir et al., 2011). In their study, Keir et al. (2011) use 78 seismograms from 34 stations, eight of which are within the vicinity of our MT profiles (Figure 6.1). Most of these eight sites estimate the anisotropy from only one earthquake with the exception of the two north-western most sites, located within the active rift, where 36 earthquakes were used collectively. The depth of the earthquakes varies between 3.6 and 13.5 km at the eight stations located close to the MT profiles. A plot of ray-path length versus delay time at station ALEE (where 30 measurements were made), produces a linear pattern (Figure 6.2) showing that seismic anisotropy is accrued uniformly through this part of the crust (Keir et al., 2011). Therefore in the results of this study, shown in Figure 6.1, delay times are normalised by the ray-path length. Note that seismic station ALEE is coincident with MT site 817.

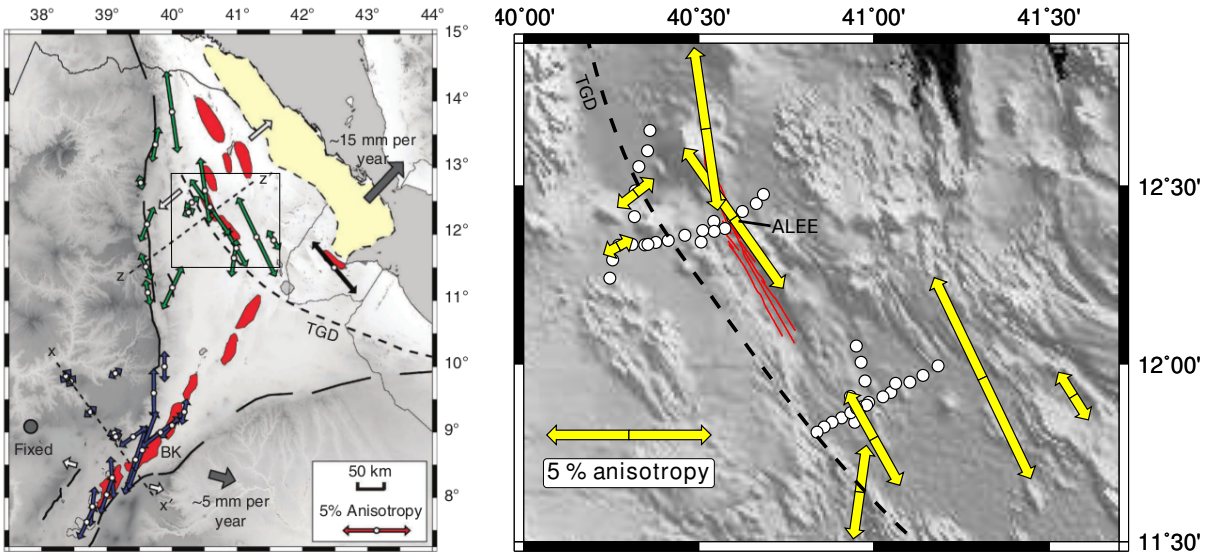

Figure 6.1: Crustal anisotropy estimated using shear-wave splitting from local earthquakes (Keir et al., 2011). Vectors point in the fast direction. Regional results shown on left, and results from seismic stations located near to MT profiles on right. TGD = Tendaho Goba'ad Discontinuity. White circles = MT sites.

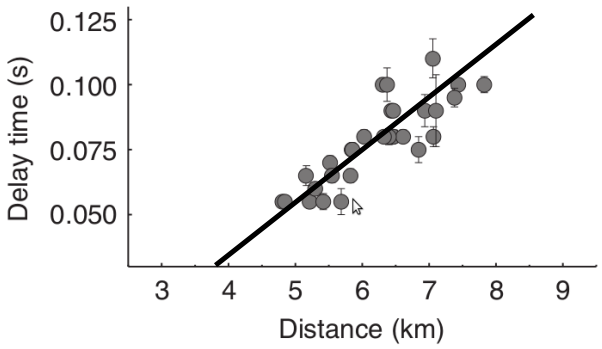

Figure 6.2: Ray-path length vs. delay time for shear-wave splitting results from station ALEE which is co-located with MT site 817. Reproduced from Keir et al. (2011).

The fast directions of anisotropy shown in Figure 6.1 are variable and closely parallel large scale Earth structures such as the Oligo-Miocene border faults. They are not always perpendicular to the opening direction (direction of minimum horizontal stress) as would be expected if the anisotropy was caused by dilatancy of micro-cracks in response to the extensional environment. Dilatency of micro-cracks can also be ruled out by the fact that anisotropy caused by this would be expected to reduce with depth as cracks close up due to increasing confining pressure. The magnitude of anisotropy is also variable and seen to increase dramatically into the Quaternary-Recent magmatic segments and around areas of active volcanic activity. This increase is most simply explained by the coincident increase in macro-scale dyke-induced faulting towards the axis of magmatic segments. The highest magnitude anisotropy is seen at stations located on active volcanoes where shallow magma chambers are inferred to exist from geodetic studies (e.g. Wright et al., 2006) or geochemical analysis of rock samples (e.g. Field et al., 2012). Here, some contribution from oriented melt pockets is likely to add to the amount of seismic anisotropy. Oriented melt within the upper crustal dykes themselves is unlikely to have an effect on the magnitude of anisotropy away from active volcanic centres because these approximately metres-wide structures freeze within day- to week-long time-scales after emplacement. Keir et al. (2011) interpret these observations of crustal anisotropy as evidence that strain in Afar is mainly accommodated by localised dyke intrusion and shallow faulting rather than by movement on detachment faults.

The Tendaho-Goba'ad Discontinuity (TGD), which marks the threshold between NW-SE extension on the Main Ethiopian Rift (MER) and NE-SW extension on the Red Sea-Gulf of Aden rift systems, seems also to form a boundary between very different seismic anisotropy characteristics. To the west of the TGD within Afar, the magnitude of anisotropy is greatly reduced and more or less perpendicular to the rift parallel anisotropy just 40 or so km further east in the

rift axis. This is good evidence in support of the TGD partitioning separation between the Arabian plate and Africa to the NE, and Nubian and Somalian plates to the SW.

The MT method has much more potential for measuring variation of anisotropy with depth by analysing the variation in strike direction and 2-d indicators as the sounding period increases. Here, data within decade-wide period bands are analysed at each site in terms of the strike direction attained from GB analysis (carried out using 'strike' (McNeice and Jones, 2001)), and the average amount of split between the TE and TM mode phase once the data are rotated into the best fitting strike direction for that band. By looking at the pseudo section of apparent resistivity in conjunction with the 2-d model shown in the previous chapter it is possible to estimate the depth within the subsurface to which a given period band relates. Figure 6.3 shows these results with the local shear-wave splitting results superimposed. Note that, given the 90^{o} ambiguity in estimating geo-electric strike direction, the direction shown in Figure 6.3 is that which most closely matches the assumed 2-d geoelectric strike direction used in 2-d modelling.

In order to make a comparison between the observations of seismic and electrical anisotropy, it is important to know which period bands have penetration depths that are comparable to the depth of earthquakes used in the seismic analysis. For the eight sites located close to the MT profiles the earthquake depth range was between about 4 and 13 km with the vast majority at a depth of less than 10 km. The MT model in Figure 6.4 shows that these depths fall within the upper resistor and, with the possible exception of the sites on the rift axis, are not deep enough to reach the lower-crustal/upper-mantle conductors. The seismic station ALEE which is located just to the east of the zone of recent dykes and is coincident with MT site 817 (see Figures 6.5 and 6.6), did not record any earthquakes deeper than 6 km which again is not within the conductor directly below, and the same can be said of the station further south, near to the HMS profile. Now looking at the

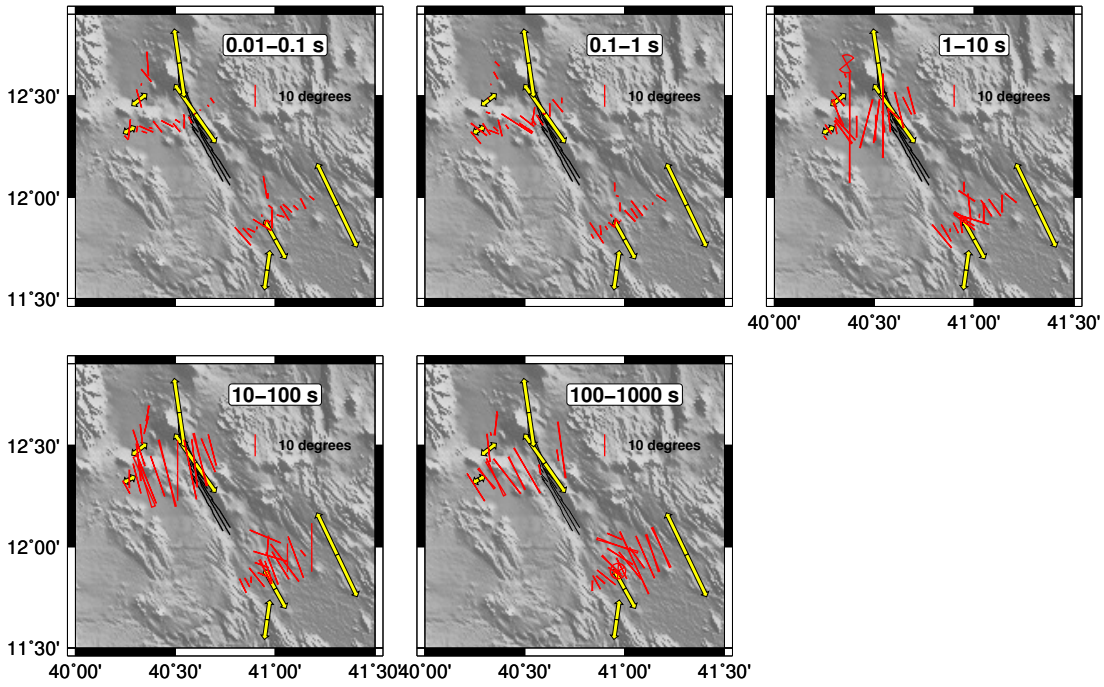

Figure 6.3: Electrical and seismic anisotropy. Each panel shows the best fitting geo-electric strike direction for each site for the period band indicated at the top of each panel. Vector lengths are scaled by the average amount of split between the phase of the two modes in that period range. Seismic anisotropy is also plotted as per Figure 6.1

pseudo-section shown in Figure 6.4, it can be seen that the period range which contains the data exhibiting the higher resistivities pertaining to these depths is approximately between 1 and 100 s (this is very similar regardless of which mode or which of the two main profiles are studied). Therefore, it is observations at this period range and shorter that will be used to compare to the seismic results.

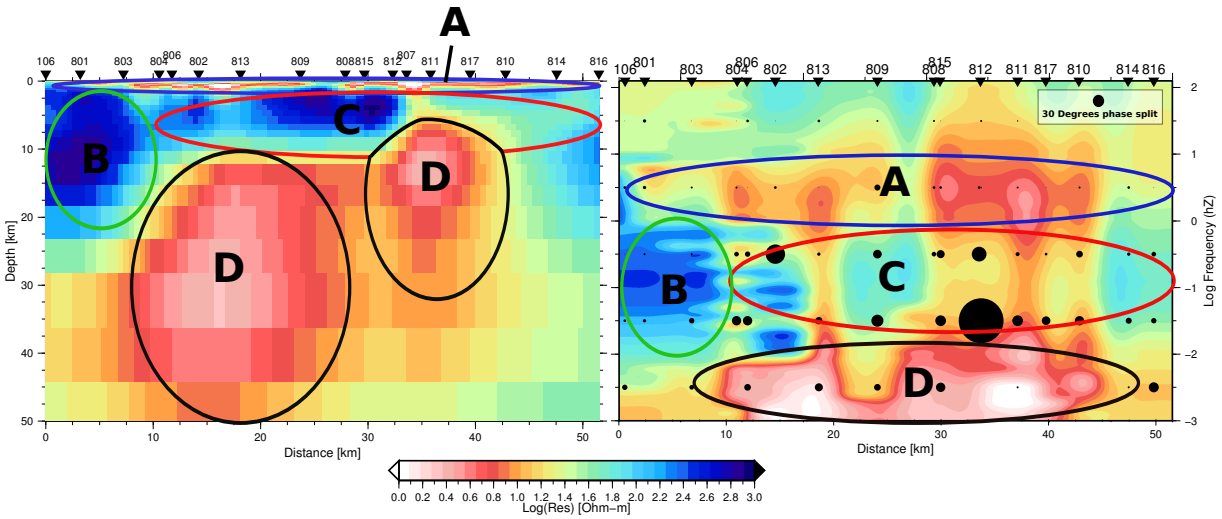

Figure 6.4: 2-d joint inversion model (left) and pseudo-section of TM mode apparent resistivity (right). Coloured ellipses indicate where features of the data manifest themselves within the model, allowing an approximate comparison between frequency and depth. Black circles plotted on the pseudo-section are scaled to show the amount of phase split at each site and period band.

In the two shortest period bands of the MT data which penetrate the shallow conductive sedimentary layer, the amount of phase split in the data is very small and the strike direction variable suggesting the sediments are consistent with a 1-d conductivity structure. It seems likely that this layer is seismically isotropic also, because a plot of delay time vs. ray path length at the rift central station ALEE produces a linear trend which does not pass through the origin (Figure 6.2), but rather at zero delay time the ray-path length is approximately 4 km. Beyond these period bands the MT data in most areas exhibit a dramatic increase in the amount of phase split. Like the seismic anisotropy, sites located to the west of the

TGD show much smaller magnitude phase splits than those within the heavily rifted region. Given that the seismic anisotropy is oriented perpendicularly to the rift here there might be an argument to suggest that the actual geo-electric strike is also oriented that way (given the 90 degree ambiguity in determining geo-electric strike direction). However, the TGD is itself a regional 2-d structure that is parallel to the strike of the rift and therefore the assumed geo-electric strike direction. The MT data will be sensitive to this 2-d structure even if they are somewhat displaced from it (unlike seismic energy) so it is still likely that the actual geo-electric strike direction for the sites east of the TGD is rift parallel.

Between 1 and 10 s period the strike direction at sites located in the rift is still somewhat variable. Generally the sites on the DMS seem to show a clockwise rotation away from the strike of the rift and the direction of the seismic anisotropy at station ALEE. This may be explained by the fact that the rift itself turns to the north, approximately at the point at which the MT profile crosses (Rowland et al., 2007) so it is possible that the MT data are more sensitive to the features of the rift to the north rather than the south. This rotation is seen as a change in orientation of seismic anisotropy between the two north-western most sites. Likewise, the sites on the HMS profile in this period band show considerable phase split with a slightly variable but generally rift parallel orientation which is in reasonable agreement with the seismic results.

In the next period band between 10 and 100 s, the amount of phase split increases and the direction becomes slightly more consistently parallel to the rift, in better agreement with the seismic results. The simplest plausible mechanism to cause the electrical anisotropy, or 2-dimensionality, in this resistive layer is undoubtedly large scale fractures and faults related to the rifting. This is supported by the fact that the magnitude of anisotropy is greatly reduced to the west of the TGD. The resistor labelled B and C in Figure 6.4 is interrupted by some sub-vertical structures of slightly lower resistivity which are probably caused by zones of higher

fault density (Rowland et al., 2007). These are most notably found between sites 803 and 813 where Badi volcano is located and the TGD is expected to cross the profile, and again between sites 812 and 816 where the highest density of faults can be found (see Figure 5.20). Likewise, similar structures can be found on the HMS profile between sites 912 and 916, and 907 and 914, for example.

Both the seismic and electrical anisotropy are most likely to be caused by fractures and faults associated with the rift, and yet there is not always perfect agreement in the orientation of the anisotropy. The fault systems, particularly near to the DMS profile are rather complex as show in Figure 6.5 and documented by Rowland et al. (2007). Given that most of the seismic observations are from one event only and hence sample the Earth via only one ray path, where the MT data are sensitive to a larger volume below and around the site, it is maybe not surprising that there is some discrepancy between them. Also it should be remembered that the length scales over which fracture patterns change is quite short and only one of the seismic stations is co-located exactly with an MT site. Looking at this site (seismic station ALEE, MT site 817) where many earthquakes were used in the seismic analysis we see that the orientation of anisotropy is actually in reasonable agreement between the two methods as shown in detail in Figure 6.5. Here, MT results are shown for the 1 to 10 s period range, the strike direction being 46 ± 3 degrees west of north, compared to 33 ± 10 degrees for the seismic anisotropy.

6.3 Seismicity and receiver function analysis

The seismicity related to the initial mega dyke intrusion was recoded by a regional array of seismometers in Ethiopia, Eritrea, Djibouti and Yemen. Between October 2005 and April 2006 immediately after the initial September 2005 dyke emplacement a temporary network of 6 seismometers was deployed to record

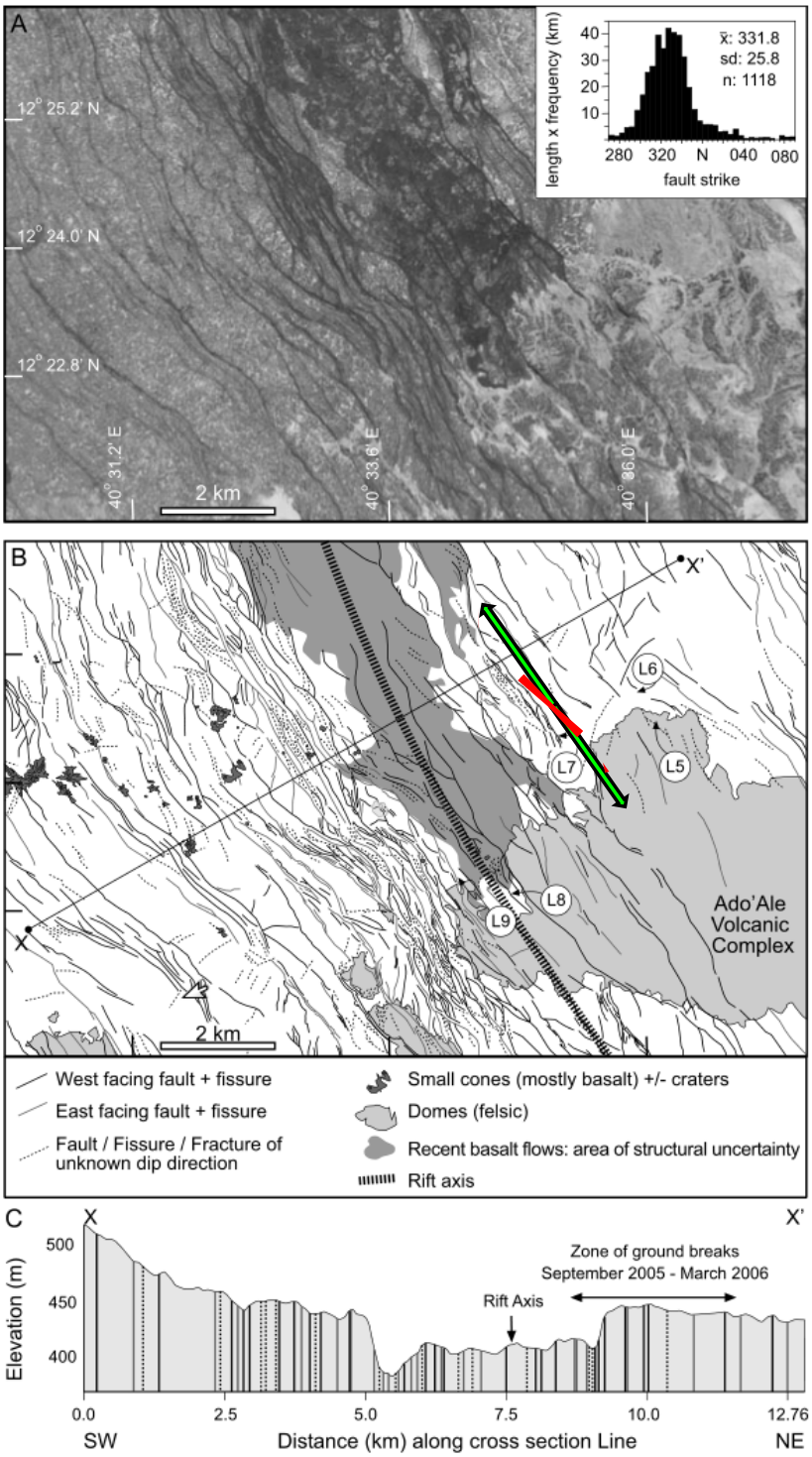

Figure 6.5: Corona image (A), structural interpretation of A with seismic and electrical anisotropy (green and red vectors) at stations ALEE and 817 respectively (B), and structural cross-section C. The locations labelled L5 to L9 are sites visited and reported upon by Rowland et al. (2007) and have no significance to this study. Modified from Rowland et al. (2007)

the ongoing activity (Ebinger et al., 2008). After that, from March 2007 there has been an array of up to 44 seismometers deployed in Afar as a part of the collaborative efforts of the Afar Rift Consortium. Consequently, the seismicity associated with many of the later dykes has been captured by this network and is documented in detail by Belachew et al. (2011). The timing and location of the micro-seismic events during dyke intrusion can be used to accurately map out the movement of magma through the subsurface. In September 2005, seimicity began around Dabbahu and Gab'ho volcanoes although this did not signal the beginning of the actual dyke intrusion (Ayele et al., 2007). Instead, after a short lived hiatus in activity it jumped 30 km south to the AVC after which bidirectional migrating seismicity was observed, thought to be caused by the propagation of the dyke. Little subsidence has ever been observed at the AVC (Hamling et al., 2009) suggesting that the majority of dykes are fed from this location via a deep source. Belachew et al. (2011) also state that all subsequent dykes have propagated from the feeder zone at the southern end of the AVC and not from the volcanoes to the north. The feeder zone is located between about 12.24 to 12.3 degrees north - some 11 to 18 km south of the MT profile. Northward moving dykes propagate at a rate of between 0.45 and 0.53 ms^{-1}, where southward ones travel more slowly at between 1.6 and 2.6 ms^{-1}. The seismogenic zone associated with the dykes is about 5 km wide - much wider than the 1 to 3 m wide dykes themselves, even when the 1 km uncertainty of the hypocentral locations is taken into account (Belachew et al., 2011). This is however consistent with the width of the zone of deformation observed at the surface (Rowland et al., 2007). Earthquakes are observed between the surface and a depth of 8 to 10 km, which is consistent with the depth down to which dyke opening is required from modelling of geodetic data (Wright et al., 2006; Hamling et al., 2009; Grandin et al., 2009). Earthquakes continue for several days after the dyke migration has ceased. Figure 6.6 shows the preferred MT model documented in Chapter 5, Section 5.5, superimposed with the seismicity from 2007 to 2009, during which time seven dykes were intruded

(Belachew et al., 2011). Earthquakes from a distance of 5 km either side of the profile are projected onto it (data courtesy of M. Belachew). Here, the seismogenic zone extends down to a depth of 8 km at which point there appears to be a sharp cut-off. This discontinuity may be artificially sharp due limitations of the velocity model used in locating the earthquakes (Belachew et al., 2011). The vast majority of the earthquakes fall within the zone of dykes shown by the vertical red lines, and the dense cluster of them form an approximate 'v' shape as one might expect from normal faulting associated with a dyke intrusion. The lower extent of the seismogenic zone is coincident with the start of the upper conductor seen in the MT model. A much smaller number of deeper earthquakes extend to Moho depths, which generally demarcate the eastern margin of the upper conductor. These mostly form part of the intra-dyke seismicity as do the small cluster of earthquakes located on the south-west flank of Badi volcano (Belachew et al., 2011).

Given the coincidence of the bottom of the dykes and our upper conductor it is tempting to suggest that the former are directly fed by the latter. However the MT profile crosses the rift some 15 km north of the supply zone inferred by the seismicity data which leaves several possible configurations for the connection between the upper conductor and the supply of magma to the dykes (see Figure 6.7). First, the upper conductor shown by the MT model is actually displaced somewhat to the south and therefore close enough to the supply zone to act as a direct source of magma (Figure 6.7A). Second, the upper conductor is a longitudinal feature which exists directly below the MT profile, but which is only actually connected to the dykes via the central supply zone (Figure 6.7B). Or third, it may be arranged as in the latter suggestion but directly connected to the dykes along their length (Figure 6.7C). 3-d modelling of the MT data (Hautot et al., 2012), shows a conductor between 8 and 13 km depth that is displaced to the south of the DMS profile approximately 5 km between sites 815 and 817.

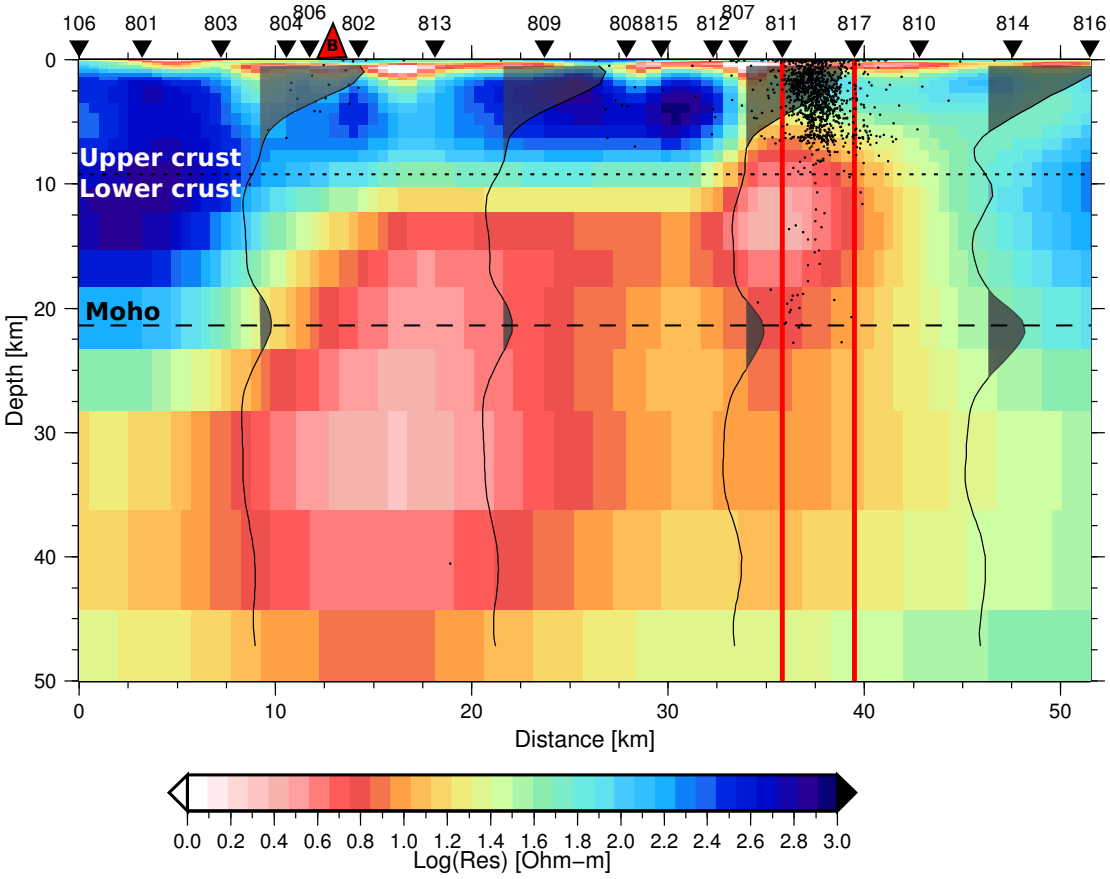

Figure 6.6: 2-d joint inversion model superimposed by migrated receiver functions and seismicity data projected onto the profile from 5 km either side of it (black dots) (Hammond et al., 2011; Belachew et al., 2011). Upper and lower crust defined by wave-form modelling of receiver functions (Hammond et al., 2011). B = Badi volcano.

This, therefore, supports the first hypothesis (cartoon A, Figure 6.7). The last hypothesis where an elongate body directly supplies the dykes along its length is not in agreement with the seismicity data which show all of the dykes originating from one location. Whilst it is not impossible that they all originate from the feeder zone to be then fed along their length from below as they propagate, it would seem unlikely that if the upper conductor is directly connected along the length of the dykes, that the location from which they originate is not more varied. So, from 2-d modelling alone, it seems more likely that the plumbing system depicted by cartoon B (Figure 6.7) where by the upper conductor is an elongate feature of the subsurface but with a connection to the surface only at one point, is closest to reality. Magma plumbing systems will be discussed further in the following chapter along with constrains from geochemical analysis of erupted lavas and geodetic observations, and comparisons to other similar regions such as NE Iceland.

Figure 6.6 shows migrated receiver functions also projected onto the MT profile. The signal from the Moho is highly attenuated (in comparison to surrounding regions) where we image high conductivities assumed to be the result of large amounts of melt, and the bulk crustal Vp/Vs ratio here is between 1.85 and 2.2 (Hammond et al., 2011) which can only be explained by large amounts of a fluid phase. In other areas of Afar a clear mid-crustal receiver function signal is seen, which is consistent with the two layer model of the crust proposed as a result of the seismic surveys carried out in the 70's and 80's (Makris and Ginzburg, 1987; Prodehl and Mechie, 1991). This however is not seen in the migrated receiver functions in the vicinity of the DMS segment, which maybe a result of a genuine change of the structure of the crust, or it may be due to reverberations within sedimentary layers masking the signal (Hammond et al., 2011). Detailed modelling of receiver function waveforms could only be carried out at 3 stations within Afar due to excessive sedimentary cover at most sites. Two of the sites at

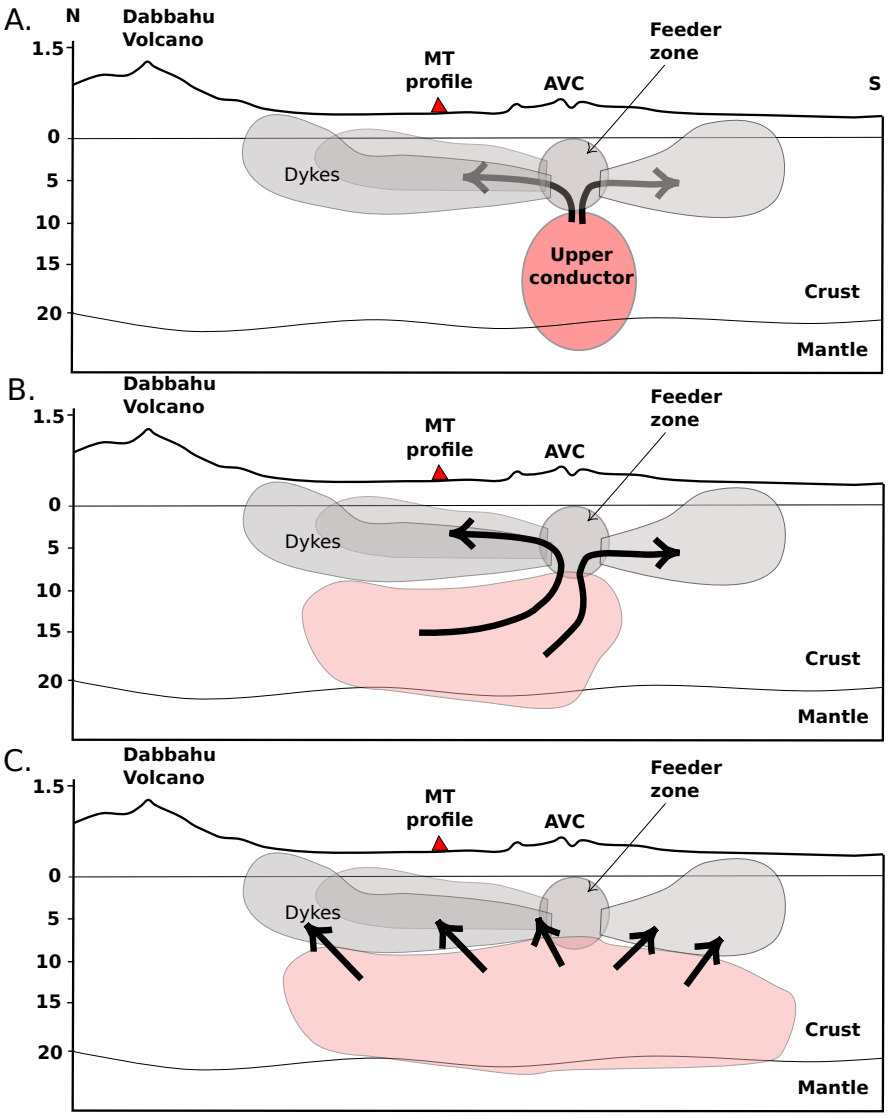

Figure 6.7: N-S section through the DMS rift schematically showing possible magma plumbing systems

which this analysis was carried out (SILE and FINE) were located approximately 60 km to the west and east of the DMS and the other (AFME) was considerably further north on the Afdera volcanic segment. The stations either side of the DMS show 3 to 4 km of cover rocks, considerably thicker than the sediments imaged magnetotellurically, but this also includes pyroclastics and lava flows. The upper crust at these sites is 4 to 8 km thick and the lower crust 11 to 16 km thick with a thinning trend from west to east. Stations SILE and AFME actually show a reduction in S-wave velocity at the upper-lower crustal boundary which explains why this mid-crustal contact is not seen in the migrated receiver functions shown in Figure 6.6 (Hammond et al., 2011). Extrapolating between stations SILE and FINE to approximate the crustal structure at the DMS gives thicknesss of 3.5, 6 and 13.5 km for the cover rocks, upper and lower crust respectively as indicated on Figure 6.6. The Vp/Vs ratio for the lower crustal layer was between 2.1 and 2.25 for the three stations - an exceptionally high value only explicable by large amounts of partial melt which does extend into the mantle (Hammond et al., 2011).

6.4 Seismic and geodetic constraints on the nature of the upper mantle

A study of P_n seismic waves has been made to asses the P-wave velocity of the upper mantle (Stork et al., 2012). The seismic P_n phase refers to energy from near earthquakes (in this study, 200-1500 km away from the temporary array of seismic stations in Afar) that is refracted below the Moho. Globally, in continental settings V_{P_n} has an average value of 8.1 kms^{-1} (Christensen and Mooney, 1995). Results from the Afar region are dominated by two broad regions of low velocity

taking values of down to 7.2 kms^{-1} which are similar to those expected at mid-ocean ridge environments (e.g. Dunn et al., 2005). They are located below and to the west of the Dabbahu Manda-Hararo rift system and below and to the north of the Erta'Ale rift segment as shown in Figure 6.8. Outside of the two anomalous regions, the velocity abruptly returns to more normal continental values.

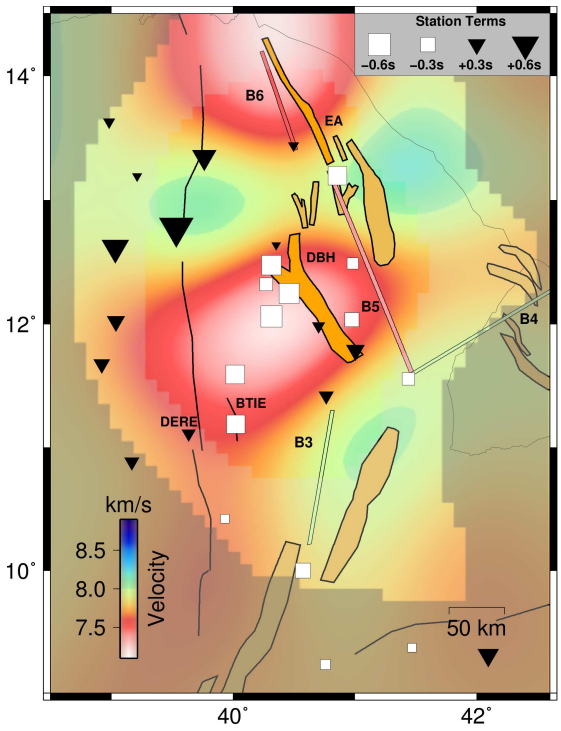

Figure 6.8: V_{P_n} in Afar. Profiles B3 to B6 show mantle P-wave velocities from refraction surveys (Makris and Ginzburg, 1987). Brown regions are magmatic segments (DBH = Dabbahu, EA = Erta Ale). From Stork et al. (2012).

Station delay terms shown in Figure 6.8 indicate crustal thickness, with large magnitude positive terms representing thicker crust. These results are in good agreement with the receiver function study of Hammond et al. (2011). Stork et al. (2012) suggest that their result, showing a reduction of P_n velocity of up to 12 percent, cannot be explained solely with a thermal anomaly, instead around 3 percent partial melt is required. They suggest that the partial melt evidenced by their study is due to lithospheric thinning and up-welling of the mantle. The low

velocity anomaly shown in Figure 6.8 reaches its maximum close to the centre of the DMS and reduces sharply at the southern end of the HMS. Similarly, the amount of conductive material below the Moho also decreases considerably from the DMS MT profile to the HMS profile (see Figure 5.3 in the previous chapter). A discussion of the amount of partial melt required by the conductivities shown in the MT models will be given in the next chapter, but it should be kept in mind that the resolution of the study of P_n velocities discussed here is not as high the MT survey. Hence the 3 percent partial melt amount suggested by Stork et al. (2012) is somewhat a regional average for the zone containing the anomaly.

Nooner et al. (2009) used GPS measurements to constrain spreading rates at the DMS after dykes have been injected. They find that they are considerably faster than the secular divergent plate motion suggesting that this is caused by relaxation in the viscoelastic mantle as a result of the stress change imparted by dyke injection. Modelling of the GPS data show that they are consistent with a viscoelastic upper mantle with a viscosity of approximately 5 X 10^{18} Pa.s, overlain by 12 - 14 km of elastic crust, thus supporting the existence of a hot upper mantle rich in partial melt.

Chapter 7

Discussion

7.1 Introduction

This chapter has two distinct parts; first estimations of the volume of melt within the crust and upper mantle are made. This is a three stage process involving using geochemical constraints on magmatic compositions, temperatures and pressures to estimate the conductivity of pure melt, then taking the magnitude of conductivity anomalies and using them to estimate the melt fraction of partial melts, and finally making assumptions regarding the 3-d geometry of melt zones to calculate volumes of melt. Second, the exact nature of the magma supply system is discussed, drawing on hypotheses regarding other spreading centres around the globe. Comparisons are also made between amount and geometry of melt below the currently active (Dabbahu) and inactive (Hararo) segments in Afar and the Main Ethiopian rift as documented by Whaler and Hautot (2006).

7.2 Calculating melt volumes contained within the crust and upper mantle

The two lower crustal/upper mantle resistivity anomalies seen in the MT models are assumed to be caused by some amount of partial melt, that is a two-phase medium consisting of melt within a solid rock matrix. The previous chapter has shown that there is a great amount of evidence from other disciplines to support a large amount of partial melt at these depths. Resistivity values of anomalies caused by partial melt estimated from MT experiments (or other methods used to estimate electrical conductivity), along with geochemical constraints from analysis of erupted lavas can be used to place constraints on the amount of melt within the crust (e.g. Brasse and Eydam, 2008; Hill et al., 2009; Pommier et al., 2008). The overall resistivity of the two phase medium is not strongly dependent on that of the solid rock matrix (Glover et al., 2000), but it is necessary to accurately estimate the resistivity of the melt component (which is heavily dependent on composition, temperature and pressure) before the percentage of melt can be estimated via one of several two-phase mixing models (Roberts and Tyburczy, 1999).

7.2.1 Estimating the conductivity of the fluid phase (melt)

Silicate melt is shown to be a semiconductor by Shankland and Waff (1977), with conductivity largely controlled by ionic mobility, usually of just one or two ionic species (Pommier et al., 2008). The dominant charge carrier for silicate liquids is found to be sodium, the mobility of which is increased with the addition of water (Gaillard, 2004; Gaillard and Marziano, 2005). A semiempirical approach is used by Pommier et al. (2008) to quantify the conductivity of silicate melts as a function of pressure (P), temperature (T), composition and water content. Many previous

studies have shown that changes in pressure have less effect on the conductivity than temperature (Shankland and Waff, 1977; Tyburczy and Waff, 1983; Maumus et al., 2005); however, it is usually taken into account and, like temperature, its effect on conductivity is described by an Arrhenius law (Tyburczy and Waff, 1983; Gaillard, 2004; Pommier et al., 2008). Increasing pressure reduces conductivity, particularly of liquid phases, whilst increasing temperature raises conductivity. Pommier and Le-Trong (2011) provide a web-based portal called SIGMELTS, which calculates the conductivity of silicate melts, using an Arrhenius law to include the effects of T and P, and experimental results (see references in Pommier and Le-Trong, 2011) to quantify compositional dependence.

Petrological analysis of rock samples is used to estimate the composition and volatile content of the melt within the crust and mantle. Samples have been collected from the Ado Ale volcanic complex and Badi volcano (Ferguson, 2011), recent basaltic eruptions within the rift (Ferguson et al., 2010), Dabbahu volcano (Field et al., 2012) and Erta Ale volcano (Field et al., submitted). The geochemistry of erupted lavas from around the DMS varies greatly from mafic and undifferentiated compositions from fissure eruptions and axial flows, to evolved silicic material erupted at Dabbahu and Badi volcanoes as well as the now bisected Ado Ale volcanic complex. Carbonatite-type magma is extremely conductive (Gaillard et al., 2008) and is common in some less mature parts of the East African Rift system (Dawson, 1992), however there is no evidence of its existance in Afar. Field et al. (2012) suggest that the mostly rhyolitic lavas of Dabbahu volcano are compatible with protracted fractional crystallisation from a basaltic parent magma. Making the logical assumption that the deep conductors imaged magnetotellurically supply the rift with magma during dyke injections then the best estimate for the composition of the melt within the conductors comes from the basalts from fissure eruptions associated with some of the dyke intrusions. Estimating the composition of the melt imaged in the conductor close to Dabbahu

is harder because the historic range of compositions of erupted at the volcano is large. The most recently erupted products (including those from the vent which opened up in September 2005) are felsic (silica rich) in composition (Wright et al., 2006; Field et al., 2012).

Estimating the H_2O content of erupted basalts is difficult because, due to its volatile nature, it is usually lost from magmas upon eruption. However, analysis of melt inclusions (MI) within phenocrysts can be used to estimate water content of the melt at the time of crystallisation for the host mineral, but unfortunately such work has not been carried out using the DMS basalts. A study of MI from chemically evolved lavas around Dabbahu volcano however, suggest that water content is generally low, although there is much variation between MI from different host minerals. For example, olivine crystals show 0.28 to 0.57 wt.% water, whereas feldspars and clinopyroxines show between 2.29 and 5.8 wt.%. Field et al. (2012) suggest that low silica content of the olivine-hosted MI show that they were trapped at an early stage of fractionation from the basaltic parent melt, hence these estimates of water content represent the best approximation for the melt within the crustal/upper mantle conductors. Another approximation comes from MI analysis of basalts from the Erta Ale range which, although distant from the DMS, is assumed to be compositionally similar to the basaltic melt within the conductors. Here, Field et al., (submitted) estimate that the pre-eruptive magmas contain less than 0.13 wt.% water. Pommier and Le-Trong (2011) state that the increase in conductivity for melts containing water only becomes significant with wt.% greater than 4, so for the purposes of the calculations that follow an average of 0.4wt.% H_2O from the olivine MIs from Dabbahu is used.

Estimates of SiO_2 and Na_2O are 48.2±1.2% and 2.71±0.32% from whole rock analysis of 29 basaltic lavas collected from the AVC and Badi volcano (errors based on one standard deviation) (Ferguson, 2011). It is unlikely that these

compositions represent exactly those of the melt within the deep conductor due to fractionation and crustal contamination prior to eruption. Ferguson (2011) uses a modelling technique to estimate the composition of the primary melt (that is, primary liquids that separate from the mantle due to partial melting prior to any crystallisation or chemical modification). It would be reasonable to assume that actual melt compositions within the crustal/upper mantle conductors lie somewhere between the compositions of primary melts and the erupted basalts. SiO_2 and Na_2O concentrations estimated for primary melt are 47.08% and 1.99% respectively, whilst melt fractions are estimated to be 10 to 15% and the depth of melting between 75 and 100 km. The most recently erupted lavas from Dabbahu volcano to the north of the MT profile are much more silicic (70 to 75% SiO_2), having evolved in shallow magma storage zones (Field et al., 2012). Basalts erupted in 2010 from Erta Ale volcano contain less than 50% SiO_2 and around 2.6% Na_2O (Field, in press).

As well as composition, the pressure and temperature of the melt need to be estimated in order to calculate its conductivity. The pressure is easily estimated because the depth of the conductive body is known. The upper (axial) and lower (off-axis) conductors are centred on approximately 12 and 30 km respectively, giving rise to pressures of about 300 and 750 MPa (Ferguson, 2011). Rough bounds are put on these estimations by calculating the pressure at the upper and lower depths of the conductive regions (see Table 7.1). Ferguson (2011) uses thermodynamic modelling of lava compositions to estimate the melting conditions in the crust and mantle around the DMS. He finds significantly different chemical signatures (and therefore melting conditions) for on-axis lavas erupted through fissures directly linked to the rifting process, and off-axis lavas (from around Badi and Dabbayra volcanoes). He suggests that melt is more efficiently transported from the mantle to the axial- rather than the off-axis storage zones. Liquidus temperatures for axial lavas are from 1165 to 1230°C. For Badi lavas the liquidus

Conductor	SiO_2	Na_2O	H_2O	Pressure (MPa)	Temperature (°C)	Conductivity (Sm^{-1})
Axial	48.2±1.2	2.71±0.32	0.425±0.145	300±100	1197±32.5	2.42
Off-axis	48.2±1.2	2.71±0.32	0.425±0.145	750±250	1245±6	3.69
Teru (evolved magma)	72.1±1.4	5.9±0.41	0.425±0.145	250±100	1197±32.5	1.28
Teru (evolved magma)	72.1±1.4	5.9±0.41	5.8	250±100	1197±32.5	6.23

Table 7.1: Summary of magma compositions, temperature, pressure and conductivity. Compositions all given as wt.%. Errors are one standard deviation.

SiO_2 +/-	Na_2O +/-	H_2O +/-	Pressure +/-	Temperature +/-
1.67-3.51	2.37-2.42	2.45-2.36	2.45-2.39	3.05-1.76

Table 7.2: Sensitivity analysis of conductivity calculations for the on-axis magma chamber. Numbers are conductivity (Sm^{-1}) calculated using upper and lower bounds on compositional constraints, P and T.

temperatures lie between 1239 and 1251°C. There is a lack of geochemical analysis of erupted products from the HMS. Given that the depth of our conductor there is similar to the deeper conductor seen on the DMS, the composition and temperature of the melt shall be assumed to be the same.

All of the above estimates for the composition, P and T of the melt within the conductive anomalies are summarised in Table 7.1, along with the conductivities of the melt from SIGMELTS. Varying T, P and the compositional constraints within their standard errors, reveals that the estimation is very sensitive to the SiO_2 content and T and little affected by variations within the probable uncertainty of P, H_2O and Na_2O. This is demonstrated by the figures in Table 7.2 which show the conductivity for the axial magma chamber (where the uncertainties on temperature are large) using upper and lower bounds on T, P and composition. The maximum and minimum conductivity values attainable for the on-axis and off-axis magma chambers are 4.53 and 1.24 Sm^{-1}, and 5.75 and 2.20 Sm^{-1} respectively, which give ranges of 0.57 and 0.46 on a logarithmic scale.

7.2.2 Melt beneath Dabbahu volcano

As magmas become more evolved due to fractional crystalisation the silica content increases. Evolved magma (or lava) such as the youngest rhyolite erupted at Dabbahu volcano typically contains about 70% SiO_2. The data in Table 7.2 show that magma conductivity is extremely dependent on SiO_2 with higher concentrations leading to lower conductivities. Table 7.1 shows the conductivity for an evolved magma, typical of Dabbahu volcano, which is considerably lower than those of the primitive melts. Naturally, this means that a conductor containing partial melt of those compositions must have a higher melt fraction than a conductor of the same conductivity that contains a more primitive melt. The conductivity of even the most primitive pure melt in the shallower axial conductor is less than the maximum conductivity seen in the maximally smooth model for the Teru profile. However, Field et al. (2012) find that the H_2O content using MI from alkali feldspars can be as high as 5.9%. This is more likely to be representative of the evolved melt below Dabbahu volcano rather than the estimates based on MI from olivine because the feldspars crystallise much later than olivine. Using this upper estimate of water content, conductivity values for pure, evolved melt are closer to those seen in the Teru profile model.

7.2.3 Constraining melt fractions using mixing models

The conductivity of a two-phase medium is very dependent on the geometry or connectivity of the conductive part of the mixture. The very low resistivities seen in the MT models suggest a well connected melt configuration; melt contained in isolated pockets is virtually undetectable by the MT method (Waff, 1974; Roberts and Tyburczy, 1999; Ten Grotenhuis et al., 2005). The conductivity of such a system can be calculated using the Hashin-Shtrikman lower bound

(HS^-) (Hashin and Shtrikman, 1962). At the opposite end of the spectrum, the conductivity of a perfectly connected conductive phase is given by the Hashin-Shtrikman upper-bound (HS^+) (Hashin and Shtrikman, 1962), which is commonly used where partial melt has been imaged via EM methods (e.g. Park et al., 1996). Interpreted in terms of partial melt, the very high conductivities seen in the MT models from this study can only be explained in terms of a well connected molten phase, without invoking extremely high melt fractions. Waff (1974) showed that for $\sigma_f >> \sigma_m$, where σ_f, σ_m are the conductivities of the fluid phase and solid rock matrix, HS^+ can be approximated as;

$$\sigma_{bulk} = \frac{2}{3}(\phi\sigma_f) \tag{7.1}$$

where σ_{bulk} is the conductivity of the bulk material and ϕ is the fraction of melt.

Several authors have also derived formulae (theoretically and empirically) for geometries of a conductive phase which lie between the extreme end members of the HS upper and lower bounds. Slightly lower melt fractions are found for a given σ_f and σ_{bulk} if it is assumed that the melt forms a series of stacked layers or continuous parallel pathways (Roberts and Tyburczy, 1999; Chave and Jones, 2012). In this case the bulk conductivity parallel to the layers is given simply by

$$\sigma_{bulk} = \phi\sigma_f + (1-\phi)\sigma_m \tag{7.2}$$

Table 7.3 contains the estimate of the melt fraction for the two conductors seen in the subsurface below the DMS profile and that below the HMS profile, based on the highest conductivity values found at the centre of the anomalies. As discussed in Section 7.2.2, the highest conductivities seen around Dabbahu volcano suggest that pure melt exists there. Estimates in Table 7.3 are given for both the HS^+

Conductor	σ_{bulk} (S/m)	% melt HS^+	% melt parallel pathways
DMS, off-axis	0.42	17.2	11.5
DMS, axial	0.38	34.0	22.6
HMS	0.19	7.8	5.2

Table 7.3: Percent melt calculations for each of the deep crustal/mantle conductors according the Hashin-Shtrikman upper bound and parallel pathways model.

and parallel pathways models. Melt fractions calculated with other models of geometry are extremely high. For example the connected tube model of Schmeling (1986) requires the off-axis DMS anomaly to contain more than a third melt at its centre, to produce the bulk conductivities seen. It would seem unreasonable to think that a fluid phase making up one third of a volume of material would not be more or less perfectly connected. The parallel pathways model is appealing given that significant amounts of seismic anisotropy at these depths has been attributed to oriented melt pockets (Bastow et al., 2010), and for the reason that this model gives the most conservative estimations of the amount of melt when the fraction of melt is already extremely high in comparison to other studies in extensional tectonic settings, for example just 4% melt was required in a magma chamber imaged below the East Pacific Rise (Baba et al., 2006a).

7.2.4 Estimating volumes of melt

In order to estimate the amount of melt contained within the conductive bodies, the bulk conductivity of material with 3 and 8% partial melt is estimated using the parallel pathways mixing model described in Section 7.2.3. These are 0.11 (3%) and 0.30 (8%) Sm^{-1} for the deeper conductors on the DMS and HMS profiles and 0.08 (3%) and 0.22 (8%) Sm^{-1} for the DMS axis conductor. Then, contours are plotted on the MT models relating to these conductivities and the area of the anomaly within each contour is estimated (see Figure 7.1). A volume is then

calculated by making an assumption about the lateral (along-rift) extent of the anomaly, and the corresponding volume of melt is derived using the mid-value melt fraction for the area enclosed by the contour. For example, the inner contour of the axial conductor has a maximum melt fraction of 22% at its center (see Section 7.2.3) and a melt fraction of 8% at its outer extent, so the melt fraction used for that region is 15%. Depending on what assumption is made about the along rift extent of the zone of partial melt, this generally leads to a conservative estimate of the amount of melt because regions with less than 3% melt are not considered. Because the lateral extent is not known, it is initially assumed that the conductive regions are spherically symmetric, rather than extending to infinity as per the 2-d assumption. Figure 7.1 shows the areas of the nested contours for 8% and 3% partial melt, approximated as circles of diameter 22 and 9 km for the lower off-axis conductor, and 10 and 5 km for the axial one, leading to total volumes of melt of 320 and 35 km^3 respectively. By the same method, the conductor seen on the HMS profile (which does not have parts containing as much as 8% partial melt as shown by Figure 7.2) contains 21 km^3 of melt. The shallow crustal conductor near to Dabbahu volcano has some regions where conductivity is high enough to support the existence of pure melt as shown by Figure 7.3. An approximate estimate of the amount of melt contained there by using ellipsoids rather than spheres (due to the shape of the contours) is in excess of 200 km^3.

The approximation of spherically symmetric zones of partial melt leads to minimum estimates of the amount of melt for the conductors below the rift segments, because it is probable that they extend further along the rift as per the 2-d assumption. Also, other authors who have imaged axial magma chambers below spreading centres suggest that they are, to some extent, continuous along the length of the segment (e.g. Sinha et al., 1997, 1998). On the other hand, the approximation of a spherically symmetric magma chamber is arguably supported in the case of the shallow axial magma chamber on the DMS profile, assuming

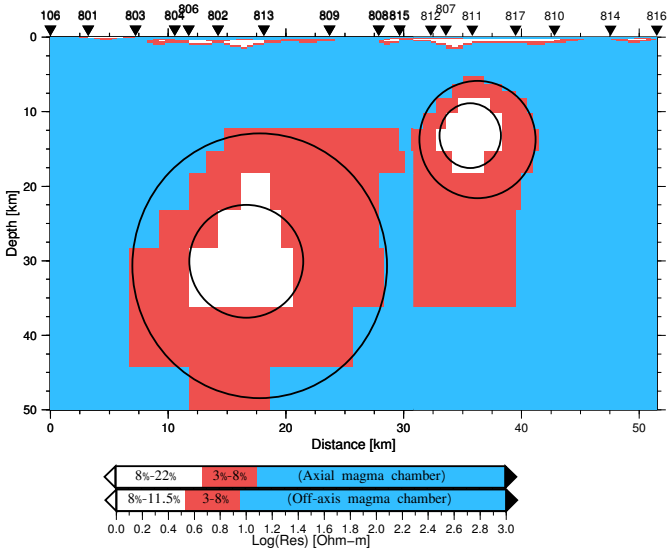

Figure 7.1: Contours showing 3% and 8% partial melt on the DMS profile. Note the different scales used for the axial and off-axis magma chambers.

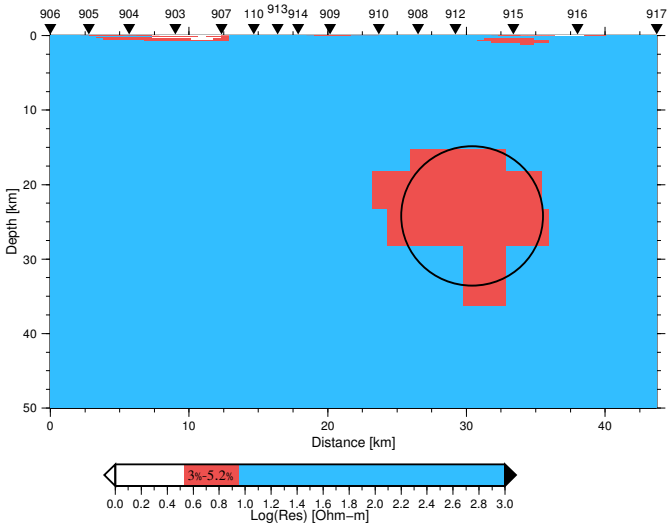

Figure 7.2: As figure 7.1 for HMS profile

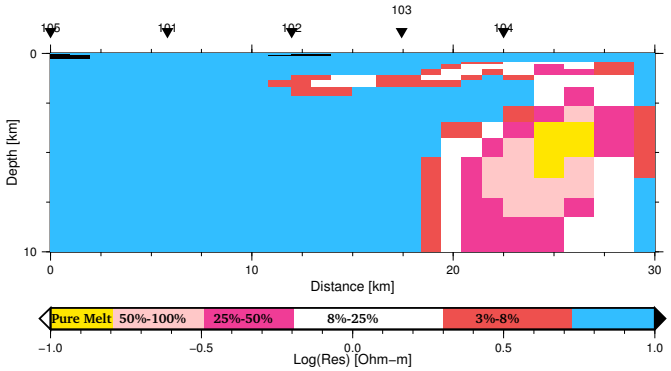

Figure 7.3: As figure 7.1 for Teru profile, now showing contours for 3%, 8%, 25%, 50% and pure melt.

that it supplies the dykes directly, given that there is strong evidence showing that they are fed from a discrete central source rather than along their entire length (Belachew et al., 2011). However, its seems likely that there is some amount of melt distributed continuously at around the crust-mantle boundary beneath the rift segments given the regionally high Vp/Vs ratios (Hammond et al., 2011) and slow seismic velocity anomaly as shown by the P_n study of Stork et al. (2012). Another approach leading to an upper limit on the melt volume, would be to assume that the magma chambers are continuous along the length of the rift, thus calculating their volume as cylinders whose length is equal to that of the rift segment (approximately 60 km for both DMS and HMS) and cross-sectional areas shown in Figures 7.1 and 7.2. In this case the melt volumes at the Moho are approximately 1400 km^3 and 200 km^3 for the DMS and HMS profiles, and the axial magma chamber would contain 6 km^3 per km of rift, or a total of 370 km^3. Given the lack of indicators of 2-dimensionality in the data close to Dabbahu volcano, and the fact that at such shallow depths the conductor there it not associated directly with the rift, the spherically symmetric assumption seems reasonable for that conductor.

The MT method is better at resolving conductance (the product of conductivity

and thickness) rather than conductivity itself (Simpson and Bahr, 2005). Consequently a conductor evident in the data may be equally well fit (in terms of model responses) by a layer of given thickness and conductivity or a thinner layer of a higher conductivity. An example of this is shown by Figure 5.17 where the large off-axis conductor on the DMS profile is replaced by a series of layers reminiscent of sills of higher conductivity without serious detriment to the fit of the model responses to the data. If the sills model is used to estimate the volume of melt results are similar to those using the single conductor because although the overall volume is smaller, the conductivity and hence fraction of partial melt they contain is higher. In the sills model the highest conductivity seen is 0.74 Sm^{-1} which gives a melt fraction of 20% (nearly twice that seen with one large conductor). However, if the volume of melt is calculated, again assuming that the sills are continuous along the length of the rift, the volume is approximately 1700 km^3; only 300 km^3 more than the previous estimate.

7.3 Plumbing and melt configurations for the DMS, and other examples of melt beneath spreading centres

Ferguson (2011) uses geochemical and isotopic analysis of basaltic and silicic lavas erupted on and off the rift axis to suggest that both are derived from melting of the mantle at 100 to 75 km depth. The amount of mantle melting is between 4 and 6 %. However, significant differences in their geochemistries do exist, which reflect differences in the transportation and storage (or fractionation paths) of magma between the mantle melting zone and the surface at which they are erupted. Based on modelling of liquid compositions produced by fractionation of the estimated primary mantle melt compositions, he suggests that axial lavas have undergone

a two stage fractionation path, first being modified in a deep storage region at about 45 km depth, then in a shallow storage region at approximately 8 km depth beneath the rift axis. Ferguson (2011) then suggests that the off axis magmas have undergone a single stage fractionation process with melt stalling at the base of the crust at about 25 km depth. Figure 7.4 shows schematically the melting and fractionation system implied from geochemical evidence (Ferguson, 2011). This model is in good agreement with the zones of partial melt imaged in this study. It does, however, suggest that the two distinct conductors supply different volcanic edifices and are not, or are at most poorly, connected, and hence the recent dyke intrusions are only supplied by the upper axial magma reservoir. During the initial mega-dyke intrusion of the current phase of activity an estimated 1.5-2.5 km^3 of magma was injected into the crust (Wright et al., 2006; Grandin et al., 2009), with a further 0.5 km^3 from the seven subsequent dyke intrusions up to November 2007 (Hamling et al., 2009). The average cumulative opening along the DMS from this series of dyke intrusions is estimated to be approximately 4 m (Hamling et al., 2009). Without the further addition of more melt from the mantle the current axial magma chamber therefore contains an amount of magma to supply the rift for approximately a further 50 m of opening assuming 100% efficient melt extraction (calculation carried out using the minimum melt calculation assuming a spherical axial magma chamber). Taking present day, far-field spreading rates between the Nubian and Arabian plates to be 20 mm/yr (Vigny et al., 2007), this is enough magma to supply the rift for 2500 years.

In the initial dyking event, the amount of subsidence seen around volcanoes at the nothern end of the rift segment could only account for a fraction (approximately one fifth) of the magma required to fill the dyke (Wright et al., 2006), and with only one exception, none of the subsequent dykes were accompanied by any measurable subsidence at volcanic centres within the rift (Hamling et al., 2009). During the dyke injection of June 2006 an estimated 0.12 km^3 was intruded from

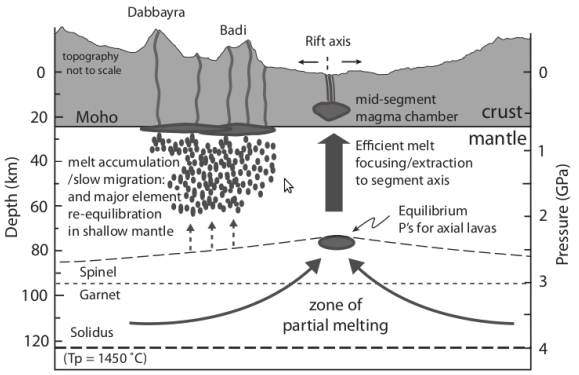

Figure 7.4: Schematic diagram of melt and fractionation system below the DMS from geochemical evidence. Reproduced from Ferguson et al. (2012)

the central supply zone at the AVC (Hamling et al., 2009; Belachew et al., 2011). Hamling et al. (2009) state that should this magma have been supplied from a melt zone at 15 km depth (roughly equivalent to the depth of the axial conductor), according to modelling using a deflating Mogi source, an associated subsidence of approximately 15 cm should have been observed over a broad area. However, no such signal was recorded. This is not the only example of 'missing magma'; Owen et al. (2000) reported a difference by a factor of approximately 3.8 between dyke inflation and reservoir deflation at Kilauea, Hawaii. Such discrepancies have been explained in terms of magma compressibility and the difference in compliance between dyke and magma chamber (Johnson et al., 2000; Rivalta and Segall, 2008), magma supply rate into the reservoir equalling drainage through dyke injection (Mériaux and Jaupart, 1995) or a magma reservoir that is deep enough such that deflation is not detectable at the surface (Hamling et al., 2009). The large conductor imaged here at approximately 12 km depth rules out this last hypothesis. Although not supported by the geochemical evidence of Ferguson (2011) (outlined in the previous paragraph and shown schematically in Figure 7.4), it is possible that the deeper, off-axis magma chamber is connected to the axial supply zone, and that during dyke injection melt migrates between the two. Hamling et al. (2009) suggest for subsidence to go undetected, a supply zone should be

at a depth greater than 33 km, thus consistent with the depth of the deeper conductor. The conductivity between the axial and off-axis magma chambers is high enough for partial melt with at least a 2% melt fraction, and thus supports the idea that they may be connected, allowing melt migration via percolation. It is also possible that transient, highly porous melt conduits exist to transport magma which, as described by Sinha et al. (1998), are of a scale not detectable by the MT method. Continuing with this hypothesis, the amount of melt between the two magma chambers combined (using the minimum melt volume estimations from spherically symmetric magma chambers) is enough to supply the rift with no replenishment from the mantle, for approximately 25,000 years; an order of magnitude longer than for the axial chamber alone. The other alternative possibility is that a highly porous conduit from the 80 km zone of mantle melting continuously supplies the upper magma storage zone. With either of these hypotheses, for there to be no subsidence or uplift as the upper magma chamber is recharged or drained during dyke injection, the influx or replenishment must exactly match the magma demand from the dykes. To achieve a perfect balance between supply and demand would seem harder as the supply zone becomes more distant from the upper magma reservoir, hence this would be easier to achieve assuming that the off-axis zone of partial melt rather than the mantle melting zone is feeding the upper magma chamber.

It is widely accepted that the Red Sea rift in Afar has moved north-east over approximately the last 8 Ma to accommodate plate motion at the triple junction. (e.g. Wolfenden et al., 2005). Hammond et al. (2011) suggest that there is evidence in the receiver function analysis to suggest that this does not occur evenly through time, but rather the rift axis takes discrete jumps. This leaves some blocks of slightly thicker crust that have probably undergone less intrusion (thus has a more continental signature) and contains less partial melt, in between the present

day and paleo-rift axes. This may be an explanation for the asymmetry of the conductors seen below the DMS profile; it is possible that at a previous time the active rift axis was further to the west and hence the large deeper conductor, also to the west, would have previously supplied the rift.

There are clearly some uncertainties regarding the exact magma supply regime around the DMS. It is useful, therefore, to look at evidence showing the location of melt in the crust and upper mantle at other magmatic spreading centres. Electromagnetic imaging of the crust and mantle has been carried out along two profiles crossing the fast spreading East Pacific Rise (EPR) (Baba et al., 2006a,b). A highly focussed, vertically aligned, narrow zone of high conductivity was seen at 17°S, estimated to contain up to 4% melt Baba et al. (2006a), yet no such feature was seen 150 km to the north at 15°45'S (Baba et al., 2006b). At both locations the mantle below about 60 km showed a broad region with a sharp increase in conductivity attributed to just 1-2% melt. This is analogous to the melt extraction zone from the mantle that Ferguson (2011) speculates to exist at depths of 75 to 100 km, but that is beyond the penetration depth of the MT data collected here. The amount of melt required to feed this super-fast spreading centre is high, so the authors conclude that rapid episodic melt transport from the mantle is likely. Zones of partial melt in the shallow crust have also been imaged seismically below the EPR (e.g. Detrick et al., 1987; Singh et al., 1998; Kent et al., 2000). Again the magma chambers are estimated to be narrow (just 2-3 km wide and begining at a depth of 1.2 to 2.4 km below the ocean floor (Detrick et al., 1987)).

The slow spreading Mid-Atlantic Ridge (MAR) has a spreading rate of 22 mm/yr (Cannat et al., 1999), and so is a better analogue for the spreading centres in Afar. Singh et al. (2006) conducted a seismic reflection survey across the MAR at the Lucky Strike segment just south of the Azores hot-spot. They saw a reversed polarity reflection (thus indicating a reduction in P-wave velocity) at

3.25 km below the sea floor, which they interpret as an axial magma chamber 3-4 km wide and 7 km long. Unfortunately the method is insensitive to the lower extent of the low velocity zone or indeed the magnitude of the velocity anomaly, so it is not possible to place bounds on the amount of melt within the magma chamber. Another seismic survey (both reflection and wide-angle) was combined with EM measurements (controlled source and MT) on the Reykjanes ridge of the MAR at 57°45'N (Sinha et al., 1997, 1998; MacGregor et al., 1998; Navin et al., 1998). Figure 7.5 is their synoptic model showing melt accumulation and production below the ridge. They find evidence for a magma chamber in the crust directly beneath the ridge axis, which has a thin upper melt lens of pure basaltic melt underlain by a zone of crystal mush. The depth to and width of the melt lens are estimated to be 2-3 km and 3 km respectively; very similar to that of the Lucky Strike segment. The seismic imaging showed that the thickness is about 100 m, suggesting a sill like feature which is continuous along the length of the ridge (although along-axis variations are less well constrained). These observations were compatible with the results from the controlled source EM experiment, which in addition, required a large zone of very high melt fractions of at least 20% continuing from the bottom of the sill to the Moho at 6 km depth (MacGregor et al., 1998). They estimate that this contains 3 km^3 of melt per km of the rift; a volume of melt enough to supply the ridge for 20000 years, however at these shallow depths they suggest that it would likely freeze within 15000 years. This amount of melt per kilometer is comparable to the estimation of 6 km^3 per kilometre of rift from the shallow magma chamber seen on the DMS. MacGregor et al. (1998) conclude that considering that crustal magma chambers are not ubiquitous to slow-spreading ocean ridges, their findings support a model of periodic melt supply from the mantle which forms transient magma chambers and leads to a cyclic pattern of magmatic activity at the ridge crest. The MT data collected across the Reykjanes ridge did not contain high enough frequencies to resolve the crustal conductor, but did support its existence (Sinha et al., 1997;

Heinson et al., 2000). Modelling of the data did however show high conductivities in the mantle between 50 and 100 km depth, requiring a well connected melt fraction of 5% (Sinha et al., 1997). Importantly, the seismic data reveal a 'normal' discontinuity between the crust and mantle (Moho), and the MT study shows that between 10 and 40 km the upper mantle is quite resistive, leading to the conclusion that no detectable melt exists at these depths (Sinha et al., 1998). This leads to two hypotheses for melt production in the mantle. Either melt is produced and delivered cyclically within the upper mantle probably on time scales of approximately 20000 years, and at the time of the survey no melt was present. Or melt is produced in a steady state fashion below 40 km and is delivered not via percolation but sporadically through vertical conduits which are not sensed either seismically or magnetotellurically. Sinha et al. (1998) prefer the latter model on the basis of geochemical and geodynamic modelling, and the fact that their experiment shows a zone of partial melt below about 40 km. It is also supported by the experiments over the EPR where a conductive mantle was imaged over both ridge sections that do and do not contain crustal conductors (Baba et al., 2006a,b), and it is consistent with geochemical analysis of erupted products at the DMS which suggests that melt is produced at 75 to 100 km in the mantle (Ferguson, 2011).

There is a significant difference between the examples of spreading centres given above and those in Afar which is the influence of a mantle plume. The experiments conducted on the Reykjanes ridge were over 1000 km south of the proposed location of the Iceland hotspot, and Sinha et al. (1998) state that it does not affect this part of the ridge. The influence of the Afar plume on present day magma production in Afar is hotly debated (e.g. Rychert et al., 2012; Ferguson et al., 2012).

Various studies have been carried out to investigate melt production, transport and accumulation in Iceland, where it is widely accepted that a mantle plume on a

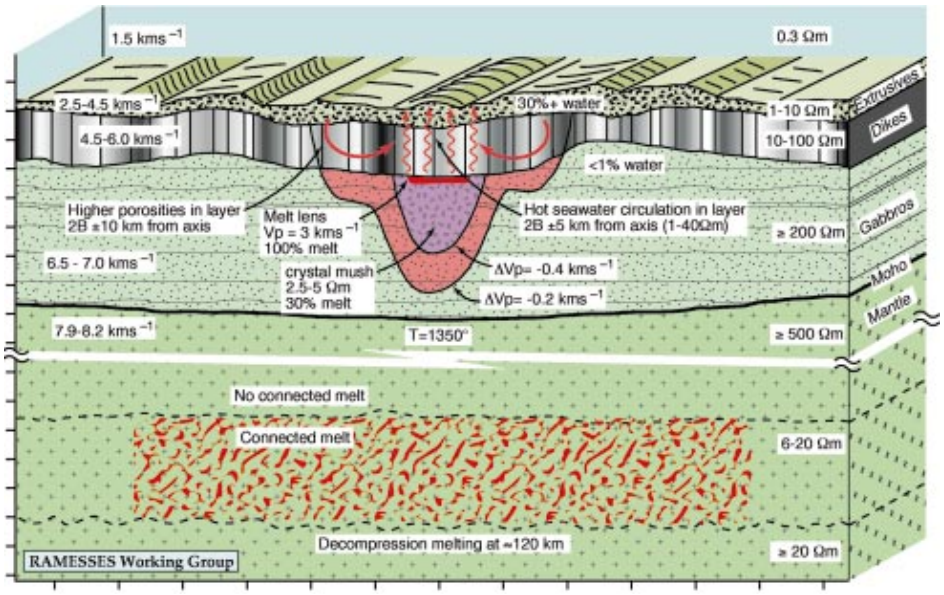

Figure 7.5: Schematic diagram of melt accumulation below the MAR constrained by seismic and EM experiments. Reproduced from Sinha et al. (1998).

spreading ridge exists (e.g. Maclennan et al., 2001), resulting in excessive melting in the mantle and a crustal thickness of between 20 and 40 km (Darbyshire et al., 1998). Widespread conductive zones have been detected across much of Iceland between approximately 5 and 15 km (Árnason et al., 2010), although this cannot be attributed to melt because there is no significant attenuation of seismic waves at these depths (Menke et al., 1995). Mamga chambers do exist, however, in the shallow crust between 3 and 5 km depth near to the Krafla caldera in NE Iceland which have been imaged both seismically and electrically (Einarsson, 1978; Árnason et al., 2010). As discussed in Chapter 2, the Krafla region underwent a rifting episode between 1975 an 1984, which was not dissimilar to the present day volcano-seismic crisis in the DMS in Afar (Wright et al., 2012). The magma chamber below the caldera is central to the zone of rifting, and subsidence at the caldera during dyke injection showed that it was directly supplying the rift (Buck et al., 2006). Detailed analysis of ground deformation has led to the suggestion that this shallow chamber was fed before, during and after dyke injection by three deeper magma chambers between 10 and 20 km depth (Tryggvason, 1986).

Although the sequence of dyke intrusions during the Krafla rifting episode seems comparable to that of the DMS in Afar, the magma supply regime must be quite different given that there is little or no evidence of subsidence or inflation of shallow magma reservoirs at the DMS.

7.4 Comparison between segments

The combined volume of melt from both melt zones below the DMS is an order of magnitude more than the HMS, regardless of which assumption is made about the axial continuity of the magma chambers. However, if it is assumed that only the axial magma chamber supplies the rift at the DMS then the amount of melt available to the rift is 50% more than for the HMS. Is this due to the periodic nature of melt supply from the mantle or is the rifting style different between these two adjacent segments? First, it should be noted that the HMS segment represents the southern most extent of the Red Sea propagator into Afar (Bridges et al., 2012). It is also the point at which the Red sea rift meets the Main Ethiopian rift. To the east, the junction with the Gulf of Aden is very poorly defined and strain is accommodated through a complex system of NW striking normal and strike slip faulting (Abbate et al., 1995). Unlike the HMS, the DMS segment is not contained within a well defined graben with recognisable active border faults. The Tendaho graben which contains the HMS is 50 km wide which is comparable to many continental rifts (e.g. the Main Ethiopian rift) and its border faults are distinct and active as demonstrated by the 1969 magnitude 5.9 earthquake at Sedo (a village about 7 km east of site 917 on the HMS profile), which ruptured an estimated 10-16 km of the NE border fault albeit with strike-slip dislocation rather than normal faulting (Kebede et al., 1989). Considering all of the above, it seems likely that more of the strain at or around the HMS is accommodated seismically than at the DMS further north, and therefore the demand for melt to

supply the rift is not so great. This of course begs the question as to whether a large melt supply drives rift segments to become a-seismic, or whether the style of rifting leads to more melt being supplied? Assuming that Ferguson (2011) and, for example, Sinha et al. (1998) are correct in their hypothesis that melt is produced in a quasi-steady-state manner not in the uppermost mantle but at depths of 50 to 100 km, then it would seem more likely that the production and delivery of melt is not 'aware' of the mechanism by which rifting is proceeding way above in the crust and is not, therefore, controlled by it. Rather, the style of rifting at the surface is determined by the magma supply rate from below.

The amount of conductive material that is in the crust as opposed to the mantle is much greater at the DMS rather than the HMS. Virtually all of the melt seen on the HMS is at a depth that straddles the Moho, whereas the axial magma chamber on the DMS is mostly within the crust. It has been speculated that the smaller melt fraction indicated by the lower conductivity values of the HMS conductor are not high enough to cross the threshold for melt migration by percolation (Hautot et al., 2012). The idea of melt pooling at the Moho until either the percolation threshold is reached or buoyancy forces overcome the resistance of the boundary is an instinctive model, supported by the shape of the observed zones of partial melt. Comparing the models for the HMS and DMS (Figure 5.3), where zones of melt are inferred to be at or straddling the Moho (i.e. the HMS and lower part of the off-axis conductor on the DMS), they tend to be horizontally elongate features of the subsurface. In contrast, where the conductive regions are clearly within the crust (as in the DMS) they are slightly stretched in the vertical direction.

It is interesting also to compare amounts of melt within the crust at the DMS and HMS to that found by Whaler and Hautot (2006) below the Main Ethiopian Rift (MER). Their MT profile is over 120 km long, crossing the continental Main Ethiopian rift SE of Addis Ababa where the crust is estimated to be 35 to 40 km think (Mackenzie et al., 2005). 2-d modelling of the data show a conductive region

at 20 km depth below the Boset magmatic segment within the rift, which is not dissimilar in dimension to that found here below the HMS (except that, although at the same depth, the conductor in the MER is well within the crust). Both conductors are centred approximately on 20 km depth, and the area enclosed by the 3% melt (or 9 Ωm) contour (shown in Figure 7.2 for the HMS profile) are about 80 and 120 km^2 respectively for the HMS and MER. Here it has been assumed that the composition of the melt is the same at both magmatic segments; (Whaler and Hautot, 2006) suggest that the melt is Gabbroic in composition (which without further detailed geochemical information can be assumed to be very similar to the basaltic melt at the HMS). Casey et al. (2006) and Keir et al. (2006) suggest that in the MER the majority of strain is accommodated magmatically, however they estimate that normal faults extend to 10 km within the crust below which magmatic intrusions (dykes) accommodate strain. Similarly, Singh et al. (2006) observe normal faults extending to depths of at least 4 km at the Lucky Strike segment of the Mid-Atlantic Ridge. On the DMS however, normal faulting is only estimated to extend to a depth of 2 km and accounts for only 8% of observed deformation (Wright et al., 2006), suggesting that here, a greater amount of strain is taken up magmatically than on the MER and Mid-Atlantic Ridge.

7.5 Summary

In summary, there are some aspects of magma production, delivery and storage, and rifting style which are common to fast and slow spreading mid-ocean ridges and the Afar rift, whilst others differ. It seems likely that, regardless of spreading rate or maturity of a rift, melt originates not in the uppermost mantle but at a depth that is approximately twice the thickness of the crust. For example, in Afar the crust has a thickness of 20 to 26 km (Hammond et al., 2011) and mantle melting occurs here not shallower than 75 km (Ferguson, 2011). Where

the crust is only about 10 km thick at the MAR, the zone of mantle melting begins at 40 km (Sinha et al., 1998). At the oceanic segments that have been studied the mantle between this point and the crust is resistive suggesting that no significant amount of connected melt exists. The majority of crustal melt storage is then in shallow magma chambers which would freeze in relatively short timescales (MacGregor et al. (1998) estimate 15000 years). This leads to a model of steady-state melt production, followed by periodic delivery to the crust and storage in transient magma chambers at very shallow depths within the crust. In contrast, the upper most mantle below the segments in Afar is, at least in places, very conductive, and crustal magma chambers are deeper, which without the vigorous hydrothermal circulation occurring at oceanic ridge crests, would take vastly longer to solidify. This leads to a model where crustal magma chambers are probably better connected to the zone of mantle melting, leading to a more steady supply of melt. Magma chambers are less transient features of the crust and possibly contain enough melt to supply the rift for much longer.

Chapter 8

Conclusion and recommendations

New audiofrequency MT data have been collected, principally along two profiles; crossing an active and an inactive magmatic spreading centre in Afar, Ethiopia. Data were also collected along a third, shorter profile near Dabbahu volcano that terminates the active rift segment. The detailed analysis of the data documented here reveals for the first time the presence of a large zone of high melt fraction partial melt well within the upper mantle, as well as a crustal magma chamber that likely fed the recent series of dyke intrusions. A considerable amount of melt has also been detected straddling the Moho on the presently inactive Hararo rift segment, but the data here do not require much conductive material within the crust.

The data collected have been shown to be largely compatible with a 2-d subsurface conductivity structure. At only one site were 3-d effects clearly present (site 809), however even if this site is omitted from subsequent modelling the results change very little. Other parts of the data set where there are indications of three-dimensionality generally correspond to poor quality data at the longest periods recorded. Groom-Bailey type decomposition and phase tensor analysis have been

carried out to find the best fitting strike direction for each of the profiles, and where possible remove the effects of galvanic distortion. With regard to the strike direction both methods agreed well.

The assumed strike direction of the causative 2-d structures aligns with the rift axis, and where seismic and MT stations are co-located, crustal seismic anisotropy is also in the same direction. The observed two-dimensionality which manifests itself as a split in the apparent resistivity and phase curves between the two MT modes, is likely to be caused by fractures and faults within the resistive, upper 10 km of the crust (some of which can be identified in the conductivity models), and/or possibly by the geometry of the conductive bodies themselves. Given that there has been much evidence in the past of elongate axial magma chambers at ocean ridge crests (e.g. Sinha et al., 1998), its seems reasonable to assume that the melt containing zones imaged here are, at least to some extent, elongate features stretched in the direction of the rift.

2-d modelling of the data has been carried out using the regularised, data space method of Siripunvaraporn and Egbert (2000). Their code REBOCC was used to carry out the inversion. Some problems were experienced with convergence and the fit of model responses to the data. However, much testing and experimentation has shown that the structures apparent in the models are robust and required by the data. Very conductive sediments usually about 1 km thick but up to 2 km in places, have been found on both the HMS and DMS rift segments. This was no surprise in the Tendaho Graben of the HMS; previous studies have found a very similar thickness of sediments (Bridges et al., 2012; Abbate et al., 1995), however such extensive deposits were not expected on the DMS where the surface of the rift is characterised by heavily faulted volcanic rock. This is evidence that at some time previous, the Tendaho graben probably existed as it does now around Semara, much further north but it has subsequently been filled with the erupted products of the rift. The oldest basalts at the surface of the rift are about 200

kyr (Ferguson, 2011), which puts a lower limit on the time since the sediments were exposed or even being deposited within the rift. The igneous cover at the DMS is seen in the MT model as a resistive layer of 100 to 200 m thickness. The sediments themselves are of very low resistivity probably dues to the presence of brines and thermal anomalies with magmatic origins.

The most important structures revealed by this study are a series of conductors within the crust and upper mantle. Many other studies have hinted at the presence of large amounts of partial melt at these depths (Wright et al., 2006; Keir et al., 2009; Hammond et al., 2011; Hamling et al., 2009; Field et al., 2012; Ferguson, 2011; Bastow et al., 2008), and so the conductors imaged here are interpreted as such. Figure 8.1 is a schematic drawing of the proposed distribution of melt below the active Dabbahu segmentand the presently inactive Hararo segment. Looking first at the conductors below the DMS where many dykes have been emplaced since 2005 (Wright et al., 2006; Belachew et al., 2011; Hamling et al., 2009), there are two distinct regions showing abnormally high conductivities. The first is directly below the rift axis (infered to be at site 811 from Rowland et al. (2007)) and centred slightly to the west of the region where dykes have recently been intruded. It starts at 8 to 10 km and extends more or less to the Moho which is at about 22 km depth here Hammond et al. (2011), and in cross-section in it is more or less circular with a slightly longer vertical axis than horizontal. The magnitude of the conductivity anomaly, together with petrological constraints, suggests a minimum melt fraction at its centre of around 20%. The second conductor is deeper (between 12 and at least 35 km deep) and off-axis to the west of the rift. The cross-sectional area is approximately five times larger than the axial conductor but it only contains about 11% melt at its centre. On the inactive HMS segment, a conductor straddling the Moho was seen. The cross-sectional area was very similar to to axial conductor on the DMS, but the maximum fraction of melt at its centre is estimated to be much

less at just 5%. The shape of the conductor here is stretched in the horizontal direction rather than the vertical, indicative of partial melt 'pooling', i.e. not being able to penetrate some boundary; most likely the Moho. Extremely high conductivities were seen in the shallow crust between about 2 and 10 km near to Dabbahu volcano. Geochemical analysis of the most recently erupted products from the volcano suggest a more evolved magma that contains a larger amount of water. These constraints and the conductivities seen in the anomaly suggest that some pure melt is probably present.

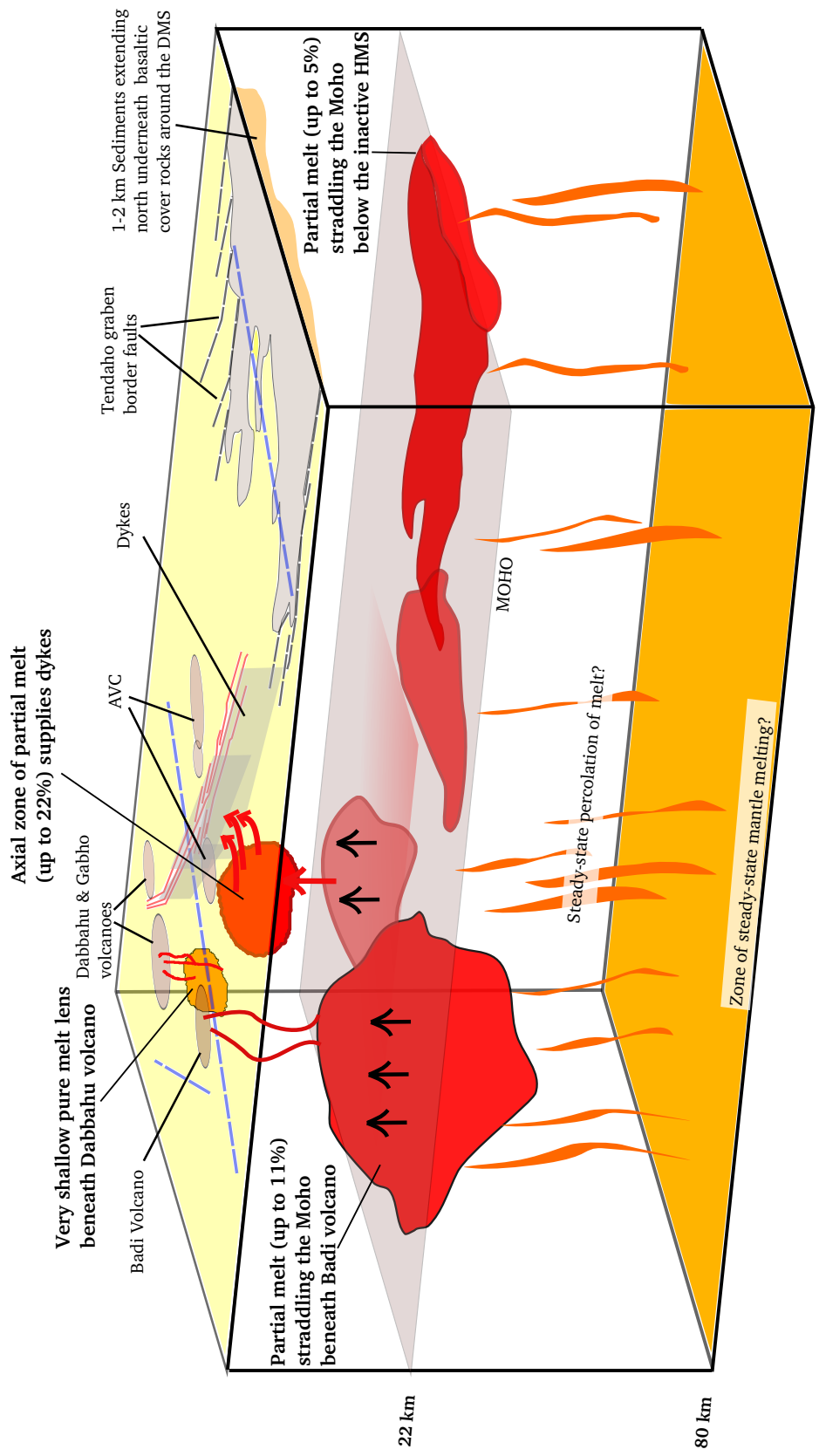

Figure 8.1: Schematic drawing showing melt distribution below the Manda-Hararo magmatic segment. Blue dashed lines show the location of the MT profiles.

Even the minimum estimate of volume of melt in the DMS axial magma chamber alone (about 35 km^3) is approximately 70 times greater than the amount required to fill the dykes that have recently been intruded. There are large uncertainties associated with estimates of the volume of melt within the magma storage zones, because the along-rift extent is not known. Boundaries are placed on these estimates by assuming spherically symmetric geometries for a minimum volume and cylinders that extend the length of the rift segments for a maximum volume. Arguments in favour of considerable along-rift continuation of the magma bodies include the fact that the data appear to be 2-dimensional; continuous axial magma chambers have been imaged at several oceanic spreading centres (Sinha et al., 1998; Singh et al., 2006); and at both the DMS and HMS rift segments a conductor is imaged at the Moho suggesting some degree of lateral continuity at that depth. The top of the axial magma chamber on the DMS is coincident with the depth upwards of which dyke opening is likely to have occurred as shown by seismicity and geodetic observations (Wright et al., 2006; Grandin et al., 2009; Belachew et al., 2011). However Belachew et al. (2011) and Hamling et al. (2009) show that dykes are very much supplied from one central location some 10 km south of the MT profile, rather than continuously along their length. This would tend to suggest that, unlike deeper melt zones, the axial magma chamber is not continuous along the length of the rift.

Another considerable uncertainty which is of great importance is the degree of connectivity between the deeper off-axis and shallower axial magma chambers on the DMS (i.e. does the deeper, more voluminous magma chamber supply material to the dykes at the rift axis?). This is important because it greatly affects the length of time for which the amount of melt seen in the crust and mantle can sustain the rift and therefore has implications for the time-scales of rifting cycles. From the conductivity model, the region between these two conductors appears to contain at least 2% melt; enough that melt could slowly

move from the lower conductor into the upper one via steady percolation. It is also possible that isolated and maybe transient high porosity conduits could transport melt as discussed in (Sinha et al., 1998). Hamling et al. (2009) state that a magma reservoir of the size and depth of the axial conductor could not alone supply the rift because if that were the case considerable deflation would be detected as dykes are injected, which does not occur. However, according to Hamling et al. (2009), if the deep zone of partial melt could also supply material via the axial one then deflation could go undetected because of the size and depth of the source. The problem with connecting the two conductors is that Ferguson (2011) states that the lavas erupted on and off-axis are chemically distinct, having undergone different patterns of fractionation.

If it is assumed that only the axial magma chamber supplies that rift, then the minimum estimate of the volume of melt there is enough to supply the rift for 2500 years. However, if we assume that either both the deeper and axial zones of partial melt supply the rift, or that the axial magma chamber is continuous along the rift, then there is enough melt to sustain spreading at present day rates for 25000 years.

The melt distribution below the inactive HMS bears more resemblance to that of the Main Ethiopian Rift, as imaged by Whaler and Hautot (2006), than that of the active DMS. The volume of melt within the crust and uppermost mantle is an order of magnitude more below the DMS, and the data from the HMS require very little melt within the crust. The best fitting model of the HMS data shows the melt at the crust-mantle boundary leading to speculations that it has stalled there. The difference between the melt distribution at the two locations in Afar most likely reflects a difference in the maturity and style of rifting rather than the observations having been made at different points in time through a rifting cycle. The difference in maturity and style of rifting between the DMS and HMS segments is highlighted by different fault patterns (Abbate et al., 1995) and amounts

of erupted lava on the surface of the rift as well as the differing patterns of melt distribution.

One of the goals of the Afar Rift Consortium is to help assess the potential threat to humanity posed by the ongoing volcanic activity around the Manda-Hararo rift segment. Although the region is generally sparsely populated, considerable development is taking place around Semara, the regional capital of Afar, which is located on the HMS. This includes the construction of many new buildings including a university, a massive 'dry dock' facility for the storage of import and export goods, and a 1.86 billion m^3 dammed reservoir for the irrigation of a 60 thousand hectare sugar cane plantation (Ayele et al., 2012). The Tendaho dam is located approximately 10 km SW of Semara close to the border faults of the Tendaho graben, and an estimated 60 thousand people living down-stream of it would be affected should it fail. Since filling in 2009 the number of seismic events around the dam has increased by a factor of eight and many leaks through the country rock have been reported (Ayele et al., 2012). Although this study does not directly contribute to hazard assessment and mitigation, it does advance the level of understanding regarding the nature of rifting on the HMS and the likely time-scales of rifting events, which are useful when considering the hazard to the local population that the rift poses.

With regard to further work required, there are some key questions left unanswered, some of which may be answered with further analysis and/or more joint analysis of data sets (including MT) already collected, and some of which may require further data collection. First, is the question of the along-rift continuity of the zones of partial melt that have been imaged here. This is important to better constrain the volume of melt within the crust and upper mantle that supplies the rift during dyke injection, and therefore make more robust statement about rifting cycles. The first approach could be to implement 3-d modelling

of the data. Using the DMS profile data and the somewhat along strike Teru profile together might constrain the extent of the magmatic bodies, at least to the north. This modelling approach may also answer the question of whether the axial magma chamber is in fact displaced to the south of the profile as an isolated conductor directly below the inferred magma supply zone, or if it is continuous along the profile. 3-d modelling was beyond the scope of this project, although recently a 'ready-to-use' 3-d code has been made available to the academic community (Siripunvaraporn et al., 2005). Along with 3-d modelling it would also be interesting to try inverting the data allowing the subsurface to be intrinsically anisotropic. Some studies have been carried out comparing the results of 2-d modelling with and without anisotropy (e.g. Miensopust et al., 2011), and they have shown that artefacts can appear in models inverted isotropically when in fact the subsurface is anisotropic. Seismic noise interferometry (e.g. Curtis et al., 2006) may also be able to resolve partial melt within the crust, and the data set already exists to facilitate such a study (although the distribution of seismic stations is sub-optimal for this sort of analysis). Other possibilities would include collecting more MT data (ideally a third profile crossing the rift) or a seismic reflection/wide angle survey. The problem with these is of course expense, and working in Afar is not cheap, especially if further helicopter access were required.

The second question that has important implications for the interpretation of our results is how well connected are the deep off-axis and axial magma chambers, and does the geochemistry really rule out the connection between the two? Also, could magma compressibility and degassing account for the lack of subsidence seen geodetically, and therefore allow the upper magma chamber to supply the dykes alone? And finally, how does the addition of up to 2 km of sediments below the DMS under a thin veneer of erupted lavas affect the modelling using elastic halfspaces of geodetic data? It is probable that directly sensing narrow, high porosity conduits between the two conductors would be very difficult via any

method. However hypothesis testing may be possible through the sort of questions just posed. Building numerical models that are informed by petrology, thermal modelling, seismics, geodetic constraints and MT may also help in answering these questions.

The final question which is interesting and key to understanding the transition from continental rifting to sea floor spreading is what is the conductivity structure of the mantle from a depth a which melting is inferred to start? (i.e. 75 to 100 km (Ferguson, 2011)). Is there a resistive layer between the conductors already imaged and the mantle melting region as discovered at oceanic spreading centres? This could only be answered by collecting long period data using fluxgate magnetometers rather than induction coils to measure the magnetic field and electrodes with stability over longer periods. The field work would be much easier, by choosing a few sites that are easily accessed and show minimum conductance in the models already produced in order to maximise depth of penetration. It would be reasonable to assume that the mantle at these depths may be more homogeneous than the upper mantle or crust so occupation of just two or three sites may be adequate to constrain the structure. Assuming that the average conductivity of the upper mantle to be in the region of 10 Ωm (from studies of the Mid-Alantic Ridge and Juan de Fuca Ridge) (Heinson et al., 2000), and if we want to image to a depth of 100 km then the skin depth equation (Equation (3.22)) tells us that periods of approximately 5000 s are needed. This is within the period range at which fluxgate magnetometers are required (Simpson and Bahr, 2005). Simpson and Bahr (2005) recommend that to achieve good quality data, time-series should be at least 100 times longer than the maximum desired time period. A simple calculation using the amount of time that sites were occupied during this study (on average about 48 hours) and the longest period of transfer function achieved (1000 s), the time series were actually about 170 times longer than highest period. Taking this upper factor, then to achieve estimate transfer

functions at 5000 s, site would need to be occupied for about 10 days. Assuming, as on previous field campaigns, three sets of recording equipment were taken to the field it would be possible to collect sufficiently long time-series at 3 sites within a two week period.

References

Abbate, E., Passerini, P., and Zan, L., Strike-slip faults in a rift area: a transect in the Afar Triangle, East Africa, *Tectonophysics*, *241*(1-2), 67–97, 1995.

Acton, G., Tessema, A., Jackson, M., and Bilham, R., The tectonic and geomagnetic significance of paleomagnetic observations from volcanic rocks from central Afar, Africa, *Earth Planet. Sci. Lett.*, *180*(3-4), 225–241, 2000.

Árnason, K., Eysteinsson, H., and Hersir, G., Joint 1D inversion of TEM and MT data and 3D inversion of MT data in the Hengill area, SW Iceland, *Geothermics*, *39*(1), 13–34, 2010.

ArRajehi, A., McClusky, S., Reilinger, R., Daoud, M., Alchalbi, A., Ergintav, S., Gomez, F., Sholan, J., Bou-Rabee, F., Ogubazghi, G., et al., Geodetic constraints on present-day motion of the Arabian Plate: Implications for Red Sea and Gulf of Aden rifting, *Tectonics*, *29*(3), 2010.

Ayele, A., Jacques, E., Kassim, M., Kidane, T., Omar, A., Tait, S., Nercessian, A., de Chabalier, J., and King, G., The volcano-seismic crisis in Afar, Ethiopia, starting September 2005, *Earth Planet. Sci. Lett.*, *255*(1-2), 177–187, 2007.

Ayele, A., Alstyne, C., Ebinger, C., and Belachew, M., Seismicity and the Tendaho Dam safety, Magmatic Rifting and Active Volcanism conference, Addis Ababa., 2012.

Baba, K., Chave, A., Evans, R., Hirth, G., and Mackie, R., Mantle dynamics beneath the East Pacific Rise at 17 S: Insights from the Mantle Electromagnetic and Tomography (MELT) experiment, *J. Geophys. Res.*, *111*, 2006.

Baba, K., Tarits, P., Chave, A., Evans, R., Hirth, G., and Mackie, R., Electrical structure beneath the northern MELT line on the East Pacific Rise at 15 45 S, *Geophys. Res. Lett.*, *33*, L22301, 2006.

Bahr, K., Interpretadon of the magnetotelluric impedance tensor: regional induction and local telluric distortion, *J. Geophys*, *62*, 119–127, 1988.

Bailey, R., Inversion of the geomagnetic induction problem, *Proceedings of the Royal Society of London. A. Mathematical and Physical Sciences*, *315*(1521), 185–194, 1970.

Balasis, G., Banks, R., and Whaler, K., Comment on understanding telluric distortion matrices by jt smith, *Geophys. J. Int*, *129*(2), 472–473, 1997.

Barberi, F., Tazieff, H., and Varet, J., Volcanism in the Afar depression: its tectonic and magmatic significance, *Tectonophysics*, *15*(1), 19–29, 1972.

Barisin, I., Leprince, S., Parsons, B., and Wright, T., Surface displacements in the September 2005 Afar rifting event from satellite image matching: Asymmetric uplift and faulting, *Geophys. Res. Lett*, *36*, L07301, 2009.

Bastow, I., Nyblade, A., Stuart, G., Rooney, T., and Benoit, M., Upper mantle seismic structure beneath the Ethiopian hot spot: Rifting at the edge of the African low-velocity anomaly, *Geochem. Geophys. Geosyst*, *9*, 12, 2008.

Bastow, I., Pilidou, S., Kendall, J., and Stuart, G., Melt-induced seismic anisotropy and magma assisted rifting in Ethiopia: evidence from surface waves, *Geochem. Geophys. Geosyst*, *11*, Q0AB05, 2010.

Belachew, M., Ebinger, C., Coté, D., Keir, D., Rowland, J., Hammond, J., and Ayele, A., Comparison of dike intrusions in an incipient seafloor-spreading segment in Afar, Ethiopia: Seismicity perspectives, *J. Geophys. Res.*, *116*(B6), B06405, 2011.

Bellahsen, N., Faccenna, C., Funiciello, F., Daniel, J., and Jolivet, L., Why did Arabia separate from Africa? insights from 3-d laboratory experiments, *Earth Planet. Sci. Lett.*, *216*(3), 365–381, 2003.

Bendick, R., McClusky, S., Bilham, R., Asfaw, L., and Klemperer, S., Distributed Nubia–Somalia relative motion and dike intrusion in the Main Ethiopian Rift, *Geophys. J. Int.*, *165*(1), 303–310, 2006.

Benoit, M., Nyblade, A., and VanDecar, J., Upper mantle P-wave speed variations beneath Ethiopia and the origin of the Afar hotspot, *Geology*, *34*(5), 329–332, 2006.

Berckhemer, H., Baier, B., Bartelsen, H., Behle, A., Burckhardt, H., Gebrande, H., Makris, J., Menzel, J., Miller, H., and Vees, R., Deep seismic soundings in the Afar region and on the highland of Ethiopia, *Afar between continental and oceanic rifting*, pp. 89–107, 1975.

Berdichevsky, M. and Dmitriev, V., Distortion of magnetic and electric fields by near surface lateral inhomogeneities, *Acta Grodaet. Geophys. Et Mantanist. Acad. Sci. Hung*, *11*, 217–221, 1976.

Beyene, A. and Abdelsalam, M., Tectonics of the Afar Depression: A review and synthesis, *Journal of African Earth Sciences*, *41*(1-2), 41–59, 2005.

Bibby, H., Analysis of multiple-source bipole-quadripole resistivity surveys using the apparent resistivity tensor, *Geophysics*, *51*(4), 972, 1986.

Bonatti, E., Punctiform initiation of seafloor spreading in the Red Sea during transition from a continental to an oceanic rift, *Nature*, *316*, 33–37, 1985.

Brasse, H. and Eydam, D., Electrical conductivity beneath the Bolivian Orocline and its relation to subduction processes at the South American continental margin, *J. Geophys. Res.*, *113*(B7), B07109, 2008.

Bridges, D., Mickus, K., Gao, S., Abdelsalam, M., and Alemu, A., Magnetic stripes of a transitional continental rift in Afar, *Geology*, *40*(3), 1–4, 2012.

Buck, W., Einarsson, P., and Brandsdóttir, B., Tectonic stress and magma chamber size as controls on dike propagation: constraints from the 1975–1984 Krafla rifting episode, *J. geophys. Res*, *111*, B12404, 2006.

Cagniard, L., Basic theory of the magneto-telluric method of geophysical prospecting, *Geophysics*, *18*, 605, 1953.

Caldwell, T., Bibby, H., and Brown, C., The magnetotelluric phase tensor, *Geophys. J. Int.*, *158*(2), 457–469, 2004.

Cannat, M., Briais, A., Deplus, C., Escartın, J., Georgen, J., Lin, J., Mercouriev, S., Meyzen, C., Muller, M., Pouliquen, G., et al., Mid-Atlantic Ridge–Azores hotspot interactions: along-axis migration of a hotspot-derived event of enhanced magmatism 10 to 4 Ma ago, *Earth Planet. Sci. Lett.*, *173*(3), 257–269, 1999.

Casey, M., Ebinger, C., Keir, D., Gloaguen, R., and Mohamed, F., Strain accommodation in transitional rifts: extension by magma intrusion and faulting in Ethiopian rift magmatic segments, *Geol. Soc. Spec. Publ.*, *259*, 143, 2006.

Chave, A. and Jones, A., *The Magnetotelluric Method; theory and practice*, Cambridge Univ. Pr., 2012.

Chave, A. and Thomson, D., Some comments on magnetotelluric response function estimation, *J. geophys. Res*, *94*(14), 215–14, 1989.

Chave, A. and Thomson, D., Bounded influence magnetotelluric response function estimation, *Geophys. J. Int.*, *157*(3), 988–1006, 2004.

Christensen, N., Poisson's ratio and crustal seismology, *J. Geophys. Res.*, *101*(B2), 3139–3156, 1996.

Christensen, N. and Mooney, W., Seismic velocity structure and composition of the continental crust: A global view, *J. Geophys. Res.*, *100*, 9761–9761, 1995.

Constable, S., Parker, R., Constable, C., et al., Occams inversion: A practical algorithm for generating smooth models from electromagnetic sounding data, *Geophysics*, *52*(3), 289–300, 1987.

Courtillot, V., Jaupart, C., Manighetti, I., Tapponnier, P., and Besse, J., On causal links between flood basalts and continental breakup, *Earth Planet. Sci. Lett.*, *166*(3), 177–195, 1999.

Curtis, A., Gerstoft, P., Sato, H., Snieder, R., and Wapenaar, K., Seismic interferometryturning noise into signal, *The Leading Edge*, *25*(9), 1082–1092, 2006.

d'Acremont, E., Leroy, S., Beslier, M., Bellahsen, N., Fournier, M., Robin, C., Maia, M., and Gente, P., Structure and evolution of the eastern Gulf of Aden conjugate margins from seismic reflection data, *Geophys. J. Int.*, *160*(3), 869–890, 2005.

Darbyshire, F., Bjarnason, I., White, R., and Flóvenz, Ó., Crustal structure above the Iceland mantle plume imaged by the ICEMELT refraction profile, *Geophys. J. Int.*, *135*(3), 1131–1149, 1998.

Davidson, A. and Rex, D., Age of volcanism and rifting in southwestern Ethiopia, *Nature*, *283*, 657–658, 1980.

Dawson, J., Neogene tectonics and volcanicity in the north tanzania sector of the gregory rift valley: contrasts with the kenya sector, *Tectonophysics*, *204*(1), 81–92, 1992.

de Groot-Hedlin, C. and Constable, S., Occam's inversion to generate smooth, two-dimensional models from magnetotelluric data, *Geophysics*, *55*(12), 1613–1624, 1990.

de Zeeuw-van Dalfsen, E., Pedersen, R., Sigmundsson, F., and Pagli, C., Satellite radar interferometry 1993–1999 suggests deep accumulation of magma near the crust–mantle boundary at the Krafla volcanic system, iceland, *Geophys. Res. Lett*, *31*, 13611, 2004.

Detrick, R., Buhl, P., Vera, E., Mutter, J., Orcutt, J., Madsen, J., and Brocher, T., Multi-channel seismic imaging of a crustal magma chamber along the East Pacific Rise, *Nature*, *326*(6108), 35–41, 1987.

Dugda, M., Nyblade, A., and Julia, J., Thin lithosphere beneath the Ethiopian Plateau revealed by a joint inversion of Rayleigh wave group velocities and receiver functions, *J. Geophys. Res.*, *112*(B8), B08305, 2007.

Dunn, R., Lekic, V., Detrick, R., and Toomey, D., Three-dimensional seismic structure of the Mid-Atlantic Ridge (35 N): Evidence for focused melt supply and lower crustal dike injection, *J. Geophys. Res.*, 2005.

Ebinger, C., Bechtel, T., Forsyth, D., and Bowin, C., Effective elastic plate thickness beneath the East African and Afar plateaus and dynamic compensation of the uplifts, *J. Geophys. Res.*, *94*(B3), 2883–2901, 1989.

Ebinger, C., Deino, A., Tesha, A., Becker, T., and Ring, U., Tectonic controls on rift basin morphology: Evolution of the Northern Malawi (Nyasa) Rift, *J. Geophys. Res.*, *98*(B10), 17821–17, 1993.

Ebinger, C., Keir, D., Ayele, A., Calais, E., Wright, T., Belachew, M., Hammond, J., Campbell, E., and Buck, W., Capturing magma intrusion and faulting processes during continental rupture: seismicity of the Dabbahu (Afar) rift, *Geophys. J. Int.*, *174*(3), 1138–1152, 2008.

Ebinger, C. J. and Sleep, N. H., Cenozoic magmatism throughout east Africa resulting from impact of a single plume, *Nature*, *395*(6704), 788–791, 1998.

Egbert, G. and Booker, J., Robust estimation of geomagnetic transfer functions, *Geophys. J. Roy. Astron. Soc.*, *87*(1), 173–194, 1986.

Einarsson, P., S-wave shadows in the Krafla caldera in NE-Iceland, evidence for a magma chamber in the crust, *Bull. Volcanol.*, *41*(3), 187–195, 1978.

Ferguson, D., *Volcanic and magmatic processes at a young spreading centre in Afar, Ethiopia*, Ph.D. thesis, 2011.

Ferguson, D., Barnie, T., Pyle, D., Oppenheimer, C., Yirgu, G., Lewi, E., Kidane, T., Carn, S., and Hamling, I., Recent rift-related volcanism in Afar, Ethiopia, *Earth Planet. Sci. Lett.*, *292*(3-4), 409–418, 2010.

Ferguson, D., Pyle, D., Plank, T., Blundy, J., and Yirgu, G., Geochemical constraints on mantle temperature and melting beneath an embryonic spreading ridge in Afar, *Submitted to Nature*, 2012.

Field, L., Blundy, J., Brooker, R., Wright, T., and Yirgu, G., Magma storage conditions beneath Dabbahu Volcano (Ethiopia) constrained by petrology, seismicity and satellite geodesy, *Bull. Volcanol.*, pp. 1–24, 2012.

Forte, A., Quéré, S., Moucha, R., Simmons, N., Grand, S., Mitrovica, J., and Rowley, D., Joint seismic-geodynamic-mineral physical modelling of African geodynamics: A reconciliation of deep-mantle convection with surface geophysical constraints, *Earth Planet. Sci. Lett.*, *295*(3-4), 329–341, 2010.

Foulger, G. and Anderson, D., A cool model for the iceland hotspot, *Journal of Volcanology and Geothermal Research*, *141*(1), 1–22, 2005.

Gaillard, F., Laboratory measurements of electrical conductivity of hydrous and dry silicic melts under pressure, *Earth Planet. Sci. Lett.*, *218*(1), 215–228, 2004.

Gaillard, F. and Marziano, G., Electrical conductivity of magma in the course of crystallization controlled by their residual liquid composition, *J. Geophys. Res*, *110*, B06204, 2005.

Gaillard, F., Malki, M., Iacono-Marziano, G., Pichavant, M., and Scaillet, B., Carbonatite melts and electrical conductivity in the asthenosphere, *Science*, *322*(5906), 1363–1365, 2008.

Gamble, T., Goubau, W., and Clarke, J., Error analysis for remote reference magnetotellurics, *Geophysics*, *44*(5), 959–968, 1979.

Gashawbeza, E., Klemperer, S., Nyblade, A., Walker, K., and Keranen, K., Shear-wave splitting in Ethiopia: Precambrian mantle anisotropy locally modified by Neogene rifting, *Geophys. Res. Lett.*, *31*, L18602, 2004.

Gianelli, G., Mekuria, N., Battaglia, S., Chersicla, A., Garofalo, P., Ruggieri, G., Manganelli, M., and Gebregziabher, Z., Water–rock interaction and hydrothermal mineral equilibria in the tendaho geothermal system, *Journal of volcanology and geothermal research*, *86*(1), 253–276, 1998.

Glover, P., Hole, M., and Pous, J., A modified Archies law for two conducting phases, *Earth Planet. Sci. Lett.*, *180*(3), 369–383, 2000.

Grandin, R., Socquet, A., Binet, R., Klinger, Y., Jacques, E., De Chabalier, J., King, G., Lasserre, C., Tait, S., Tapponnier, P., et al., September 2005 Manda Hararo-Dabbahu rifting event, Afar (Ethiopia): constraints provided by geodetic data, *J. geophys. Res*, *114*, B08404, 2009.

Griffiths, D., *Introduction to electrodynamics*, vol. 3, prentice Hall New Jersey:, 1999.

Groom, R. and Bahr, K., Corrections for near surface effects: decomposition of the magnetotelluric impedance tensor and scaling corrections for regional resistivities: a tutorial, *Surv. Geophys.*, *13*(4), 341–379, 1992.

Groom, R. and Bailey, R., Decomposition of magnetotelluric impedance tensors in the presence of local three-dimensional galvanic distortion, *J. Geophys. Res.*, *94*(B2), 1913–1925, 1989.

Groom, R. and Bailey, R., Analytic investigations of the effects of near-surface three-dimensional galvanic scatterers on MT 2sor decompositions, *Geophysics*, *56*(4), 496, 1991.

Groom, R., Kurtz, R., Jones, A., and Boerner, D., A quantitative methodology to extract regional magnetotelluric impedances and determine the dimension of the conductivity structure, *Geophys. J. Int.*, *115*(3), 1095–1118, 1993.

Gudmundsson, A., Infrastructure and mechanics of volcanic systems in Iceland, *J. Volcanol. Geoth. Res.*, *64*(1-2), 1–22, 1995.

Guidarelli, M., Stuart, G., Hammond, J., Kendall, J., Ayele, A., and Belachew, M., Surface wave tomography across Afar, Ethiopia: Crustal structure at a rift triple-junction zone, *Geophys. Res. Lett.*, *38*(24), L24313, 2011.

Hamilton, M. P., Jones, A. G., Evans, R. L., Evans, S., Fourie, C. J. S., Garcia, X., Mountford, A., Spratt, J. E., and Team, S. M., Electrical anisotropy of South African lithosphere compared with seismic anisotropy from shear-wave splitting analyses, *Phys. Earth Planet. In.*, *158*(2-4), 226–239, 2006.

Hamling, I., Ayele, A., Bennati, L., Calais, E., Ebinger, C., Keir, D., Lewi, E., Wright, T., and Yirgu, G., Geodetic observations of the ongoing Dabbahu rifting episode: new dyke intrusions in 2006 and 2007, *Geophys. J. Int.*, *178*(2), 989–1003, 2009.

Hammond, J., Kendall, J., Angus, D., and Wookey, J., Interpreting spatial variations in anisotropy: insights into the Main Ethiopian Rift from SKS waveform modelling, *Geophys. J. Int.*, *181*(3), 1701–1712, 2010.

Hammond, J., Kendall, J., Stuart, G., Keir, D., Ebinger, C., Ayele, A., and Belachew, M., The nature of the crust beneath the Afar triple junction: Evidence from receiver functions, *Geochem. Geophys. Geosyst.*, *12*(12), Q12004, 2011.

Hashin, Z. and Shtrikman, S., A variational approach to the theory of the effective magnetic permeability of multiphase materials, *J. of Appl. Phys.*, *33*(10), 3125–3131, 1962.

Hautot, S., Johnson, N., Desissa, M., Whaler, K., Dawes, G., and Fisseha, S., Melt distribution between the crust and mantle beneath the Dabbahu-Manda Hararo rift segment, Afar, from 3D magnetotelluric imaging, Magmatic Rifting and Active Volcanism conference, Addis Ababa., 2012.

Hayward, N. and Ebinger, C., Variations in the along-axis segmentation of the Afar Rift system, *Tectonics*, *15*(2), 244–257, 1996.

Heinson, G., Constable, S., and White, A., Episodic melt transort at mid-ocean ridges inferred from magnetotelluric sounding, *Geophys. Res. Lett.*, *27*, 2317–2320, 2000.

Heise, W., Bibby, H., Caldwell, T., Bannister, S., Ogawa, Y., Takakura, S., and Uchida, T., Melt distribution beneath a young continental rift: the Taupo Volcanic Zone, New Zealand, *Geophys. Res. Lett.*, *34*(14), L14313, 2007.

Hill, G., Caldwell, T., Heise, W., Chertkoff, D., Bibby, H., Burgess, M., Cull, J., and Cas, R., Distribution of melt beneath Mount St Helens and Mount Adams inferred from magnetotelluric data, *Nature Geosci.*, *2*(11), 785–789, 2009.

Hofmann, C., Courtillot, V., Feraud, G., Rochette, P., Yirgu, G., Ketefo, E., and Pik, R., Timing of the Ethiopian flood basalt event and implications for plume birth and global change, *Nature*, *389*(6653), 838–841, 1997.

Jiracek, G., Near-surface and topographic distortions in electromagnetic induction, *Surv. Geophys.*, *11*(2), 163–203, 1990.

Johnson, D., Sigmundsson, F., and Delaney, P., Comment on 'Volume of magma accumulation or withdrawal estimated from surface uplift or subsidence, with application to the 1960 collapse of Kīlauea volcano' by PT Delaney and DF McTigue, *Bull. Volcanol.*, *61*(7), 491–493, 2000.

Jones, A., Chave, A., Egbert, G., Auld, D., and Bahr, K., A comparison of techniques for magnetotelluric response function estimation, *J. geophys. Res*, *94*, 1989.

Jones, A., Lezaeta, P., Ferguson, I., Chave, A., Evans, R., Garcia, X., and Spratt, J., The electrical structure of the Slave craton, *Lithos*, *71*(2-4), 505–527, 2003.

Kebede, F., Kim, W., and Kulhánek, O., Dynamic source parameters of the March–May 1969 Serdo earthquake sequence in central Afar, Ethiopia, deduced from teleseismic body waves, *J. Geophys. Res.*, *94*(B5), 5603–5614, 1989.

Keir, D., Ebinger, C., Stuart, G., Daly, E., and Ayele, A., Strain accommodation by magmatism and faulting as rifting proceeds to breakup: Seismicity of the northern Ethiopian rift, *J. geophys. Res*, *111*, B05314, 2006.

Keir, D., Hamling, I., Ayele, A., Calais, E., Ebinger, C., Wright, T., Jacques, E., Mohamed, K., Hammond, J., Belachew, M., et al., Evidence for focused magmatic accretion at segment centers from lateral dike injections captured beneath the Red Sea rift in Afar, *Geology*, *37*(1), 59, 2009.

Keir, D., Belachew, M., Ebinger, C., Kendall, J., Hammond, J., Stuart, G., Ayele, A., and Rowland, J., Mapping the evolving strain field during continental breakup from crustal anisotropy in the Afar Depression, *Nat. Commun.*, *2*, 285, 2011.

Kent, G., Singh, S., Harding, A., Sinha, M., Orcutt, J., Barton, P., White, R., Bazin, S., Hobbs, R., Tong, C., et al., Evidence from three-dimensional

seismic reflectivity images for enhanced melt supply beneath mid-ocean-ridge discontinuities, *Nature*, *406*(6796), 614–618, 2000.

Lambiase, J., The framework of African rifting during the Phanerozoic, *Journal of African Earth Sciences (and the Middle East)*, *8*(2-4), 183–190, 1989.

Larsen, J., Removal of local surface conductivity effects from low frequency mantle response curves, *Acta Geodaet., Geophys. et Montanist. Acad. Sci. Hungary*, *12*, 183–186, 1977.

Lilley, F., Magnetotelluric tensor decomposition: Part i, theory for a basic procedure, *Geophysics*, *63*(6), 1885–1897, 1998.

MacGregor, L., Constable, S., and Sinha, M., The RAMESSES experimentIII. controlled-source electromagnetic sounding of the Reykjanes Ridge at 57 45 N, *Geophys. J. Int.*, *135*(3), 773–789, 1998.

Mackenzie, G., Thybo, H., and Maguire, P., Crustal velocity structure across the Main Ethiopian Rift: results from two-dimensional wide-angle seismic modelling, *Geophys. J. Int.*, *162*(3), 994–1006, 2005.

Maclennan, J., McKenzie, D., Gronvöld, K., and Slater, L., Crustal accretion under northern Iceland, *Earth Planet. Sci. Lett.*, *191*(3), 295–310, 2001.

Maguire, P., Keller, G., Klemperer, S., Mackenzie, G., Keranen, K., Harder, S., O Reilly, B., Thybo, H., Asfaw, L., Khan, M., et al., Crustal structure of the northern Main Ethiopian Rift from the EAGLE controlled-source survey; a snapshot of incipient lithospheric break-up, *Spec. Publ. Geol. Soc.*, *259*, 269, 2006.

Makris, J. and Ginzburg, A., The Afar depression: transition between continental rifting and sea-floor spreading, *Tectonophysics*, *141*(1), 199–214, 1987.

Marquis, G., Jones, A., and Hyndman, R., Coincident conductive and reflective middle and lower crust in southern British Columbia, *Geophys. J. Int.*, *120*(1), 111–131, 1995.

Maumus, J., Bagdassarov, N., and Schmeling, H., Electrical conductivity and partial melting of mafic rocks under pressure, *Geochim. Cosmochim. Acta*, *69*(19), 4703–4718, 2005.

McClusky, S., Reilinger, R., Ogubazghi, G., Amleson, A., Healeb, B., Vernant, P., Sholan, J., Fisseha, S., Asfaw, L., Bendick, R., et al., Kinematics of the southern Red Sea–Afar Triple Junction and implications for plate dynamics, *Geophys. Res. Lett.*, *37*, L05301, 2010.

McNeice, G. and Jones, A., Multisite, multifrequency tensor decomposition of magnetotelluric data, *Geophysics*, *66*(1), 158, 2001.

McQuarrie, N., Stock, J., Verdel, C., and Wernicke, B., Cenozoic evolution of Neotethys and implications for the causes of plate motions, *Geophys. Res. Lett.*, *30*(20), Art–No, 2003.

Menke, W., Levin, V., and Sethi, R., Seismic attenuation in the crust at the mid-Atlantic plate boundary in south-west Iceland, *Geophys. J. Int.*, *122*(1), 175–182, 1995.

Menzies, M., Baker, J., Bosence, D., Dart, C., Davison, I., Hurford, A., AlKadasi, M., McClay, K., Nichols, G., AlSubbary, A., et al., The timing of magmatism, uplift and crustal extension: preliminary observations from Yemen, *Geol. Soc. Spec. Publ.*, *68*(1), 293–304, 1992.

Menzies, M., Gallagher, K., Yelland, A., and Hurford, A., Volcanic and nonvolcanic rifted margins of the Red Sea and Gulf of Aden: Crustal cooling and margin evolution in Yemen, *Geochim. Cosmochim. Acta*, *61*(12), 2511–2527, 1997.

Mériaux, C. and Jaupart, C., Simple fluid dynamic models of volcanic rift zones, *Earth Planet. Sci. Lett.*, *136*(3), 223–240, 1995.

Meshesha, D. and Shinjo, R., Rethinking geochemical feature of the Afar and Kenya mantle plumes and geodynamic implications, *J. Geophys. Res.*, *113*(B9), B09209, 2008.

Miensopust, M., Jones, A., Muller, M., Garcia, X., and Evans, R., Lithospheric structures and Precambrian terrane boundaries in northeastern Botswana revealed through magnetotelluric profiling as part of the Southern African Magnetotelluric Experiment, *J. Geophys. Res.*, *116*(B2), B02401, 2011.

Montelli, R., Nolet, G., Dahlen, F., and Masters, G., A catalogue of deep mantle plumes: new results from finite-frequency tomography, *Geochem. Geophys. Geosyst*, *7*(11), 007, 2006.

Nabighian, M., *Electromagnetic Methods in Applied Geophysics: Applications. 2pts*, vol. 2, Soc. of Exploration Geophysicists, 1988.

Navin, D., Peirce, C., and Sinha, M., The RAMESSES experimentII. evidence for accumulated melt beneath a slow spreading ridge from wide-angle refraction and multichannel reflection seismic profiles, *Geophys. J. Int.*, *135*(3), 746–772, 1998.

Nooner, S., Bennati, L., Calais, E., Buck, W., Hamling, I., Wright, T., and Lewi, E., Post-rifting relaxation in the Afar region, Ethiopia, *Geophys. Res. Lett*, *36*, L21308, 2009.

Nyblade, A. and Robinson, S., The African superswell, *Geophys. Res. Lett.*, *21*(9), 765–768, 1994.

Owen, S., Paul Segali, M., Miklius, A., Bevis, M., and Foster, J., January 30, 1997 eruptive event on Kilauea Volcano, Hawaii, as monitored by continuous GPS, *Geophys. Res. Lett.*, *27*(17), 2757–2760, 2000.

Padilha, A., Vitorillo, I., and Rijo, L., Effects of the equatorial electrojet on magnetotelluric surveys: Field results from northwest brazil, *Geophysical research letters*, *24*(1), 89–92, 1997.

Padilha, A., Vitorello, Í., Pádua, M., and Bologna, M., Lithospheric and sublithospheric anisotropy beneath central-southeastern Brazil constrained by long period magnetotelluric data, *Phys. Earth Planet. In.*, *158*(2), 190–209, 2006.

Park, S., Hirasuna, B., Jiracek, G., and Kinn, C., Magnetotelluric evidence of lithospheric mantle thinning beneath the southern Sierra Nevada, *J. Geophys. Res.*, *101*(B7), 16241–16, 1996.

Parker, R., *Geophysical inverse theory*, Princeton Univ Pr, 1994.

Parker, R. and Booker, J., Optimal one-dimensional inversion and bounding of magnetotelluric apparent resistivity and phase measurements, *Phys. Earth Planet. In.*, *98*(3), 269–282, 1996.

Pellerin, L. and Hohmann, G., Transient electromagnetic inversion: A remedy for magnetotelluric static shifts, *Geophysics*, *55*(9), 1242–1250, 1990.

Pik, R., Deniel, C., Coulon, C., Yirgu, G., Hofmann, C., and Ayalew, D., The northwestern Ethiopian Plateau flood basalts: Classification and spatial distribution of magma types, *J. Volcanol. Geoth. Res.*, *81*(1-2), 91–111, 1998.

Pommier, A. and Le-Trong, E., SIGMELTS: A web portal for electrical conductivity calculations in geosciences, *Comput. Geosci.*, *37*(9), 1450–1459, 2011.

Pommier, A., Gaillard, F., Pichavant, M., and Scaillet, B., Laboratory measurements of electrical conductivities of hydrous and dry Mount Vesuvius melts under pressure, *J. Geophys. Res*, *113*(B5), B05205, 2008.

Prodehl, C. and Mechie, J., Crustal thinning in relationship to the evolution of the Afro-Arabian rift system: a review of seismic-refraction data, *Tectonophysics*, *198*(2-4), 311–327, 1991.

Reddy, I., Phillips, R., and Rankin, D., Three-dimensional modelling in magnetotelluric and magnetic variational sounding, *Geophys. J.*, *51*, 313–325, 1977.

Ritsema, J., Heijst, H., and Woodhouse, J., Complex shear wave velocity structure imaged beneath Africa and Iceland, *Science*, *286*(5446), 1925, 1999.

Ritter, O., Junge, A., and Dawes, G., New equipment and processing for magnetotelluric remote reference observations, *Geophys. J. Int.*, *132*(3), 535–548, 1998.

Rivalta, E. and Segall, P., Magma compressibility and the missing source for some dike intrusions, *Geophys. Res. Lett*, *35*, L04306, 2008.

Roberts, J. and Tyburczy, J., Partial-melt electrical conductivity: Influence of melt composition, *J. Geophys. Res.*, *104*(B4), 7055–7065, 1999.

Rochette, P., Tamrat, E., Feraud, G., Pik, R., Courtillot, V., Ketefo, E., Coulon, C., Hoffmann, C., Vandamme, D., and Yirgu, G., Magnetostratigraphy and timing of the Oligocene Ethiopian traps, *Earth Planet. Sci. Lett.*, *164*(3-4), 497–510, 1998.

Rowland, J., Baker, E., Ebinger, C., Keir, D., Kidane, T., Biggs, J., Hayward, N., and Wright, T., Fault growth at a nascent slow-spreading ridge: 2005 Dabbahu rifting episode, Afar, *Geophys. J. Int.*, *171*(3), 1226–1246, 2007.

Rychert, C., Hammond, J., Harmon, N., Kendall, J., Keir, D., Ebinger, C., Bastow, I., Ayele, A., Belachew, M., and Stuart, G., Volcanism in the Afar Rift sustained by decompression melting with minimal plume influence, *Nature Geosci.*, 2012.

Sato, H. and Ida, Y., Low frequency electrical impedance of partially molten gabbro: the effect of melt geometry on electrical properties, *Tectonophysics*, *107*(1-2), 105–134, 1984.

Schmeling, H., Numerical models on the influence of partial melt on elastic, anelastic and electrical properties of rocks. part II: electrical conductivity, *Phys. Earth Planet. In.*, *43*(2), 123–136, 1986.

Schock, R., Duba, A., and Shankland, T., Electrical conduction in olivine, *J. Geophys. Res.*, *94*(B5), 5829–5839, 1989.

Shankland, T. and Waff, H., Partial melting and electrical conductivity anomalies in the upper mantle, *J. Geophys. Res.*, *82*(33), 5409–5417, 1977.

Sigmundsson, F., *Iceland geodynamics: crustal deformation and divergent plate tectonics*, Springer Verlag, 2006.

Simpson, F. and Bahr, K., *Practical magnetotellurics*, Cambridge Univ. Pr., 2005.

Sims, W., Bostick Jr, F., and Smith, H., The estimation of magnetotelluric impedance tensor elements from measured data, *Geophysics*, *36*, 938, 1971.

Singh, S., Kent, G., Collier, J., Harding, A., and Orcutt, J., Melt to mush variations in crustal magma properties along the ridge crest at the southern East Pacific Rise, *Nature*, *394*(6696), 874–878, 1998.

Singh, S., Crawford, W., Carton, H., Seher, T., Combier, V., Cannat, M., Canales, J., Düsünür, D., Escartin, J., and Miranda, J., Discovery of a magma chamber and faults beneath a Mid-Atlantic ridge hydrothermal field, *Nature*, *442*(7106), 1029–1032, 2006.

Sinha, M., Navin, D., MacGregor, L., Constable, S., Peirce, C., White, A., Heinson, G., and Inglis, M., Evidence for accumulated melt beneath the slow–spreading Mid–Atlantic Ridge, *Philosophical Transactions of the Royal Society of London. Series A: Mathematical, Physical and Engineering Sciences*, *355*(1723), 233–253, 1997.

Sinha, M., Constable, S., Peirce, C., White, A., Heinson, G., MacGregor, L., and Navin, D., Magmatic processes at slow spreading ridges: implications of the RAMESSES experiment at 57 45 n on the Mid-Atlantic Ridge, *Geophys. J. Int.*, *135*(3), 731–745, 1998.

Siripunvaraporn, W. and Egbert, G., An efficient data-subspace inversion method for 2-D magnetotelluric data, *Geophysics*, *65*(3), 791–803, 2000.

Siripunvaraporn, W., Egbert, G., Lenbury, Y., and Uyeshima, M., Three-dimensional magnetotelluric inversion: data-space method, *Phys. Earth Planet. In.*, *150*(1), 3–14, 2005.

Smith, J., Understanding telluric distortion matrices, *Geophys. J. Int.*, *122*(1), 219–226, 1995.

Smith, J. and Booker, J., Rapid inversion of two-and three-dimensional magnetotelluric data, *J. Geophys. Res.*, *96*(B3), 3905–3922, 1991.

Solon, K., Jones, A., Nelson, K., Unsworth, M., Kidd, W., Wei, W., Tan, H., Jin, S., Deng, M., Booker, J., et al., Structure of the crust in the vicinity of the Banggong-Nujiang suture in central Tibet from INDEPTH magnetotelluric data, *J. Geophys. Res*, *110*, B10102, 2005.

Sternberg, B., Washburne, J., and Pellerin, L., Correction for the static shift in magnetotellurics using transient electromagnetic soundings, *Geophysics*, *53*(11), 1459–1468, 1988.

Stork, A., Stuart, G., Henderson, C., and Keir, D., Uppermost mantle (p_n) velocity model for the Afar region, Ethiopia: An insight into rifting processes, *Submitted to Geophys. J. Int.*, 2012.

Sutarno, D. and Vozoff, K., Phase-smoothed robust M-estimation of magnetotelluric impedance functions, *Geophysics*, *56*(12), 1999, 1991.

Swift, C., *A magnetotelluric investigation of an electrical conductivity anomaly in the Southwestern United States.*, Ph.D. thesis, 1967.

Ten Grotenhuis, S., Drury, M., Spiers, C., and Peach, C., Melt distribution in olivine rocks based on electrical conductivity measurements, *J. Geophys. Res.*, *110*, B12201–doi, 2005.

Tryggvason, E., Multiple magma reservoirs in a rift zone volcano: ground deformation and magma transport during the September 1984 eruption of Krafla, Iceland, *J. Volcanol. Geoth. Res.*, *28*(1-2), 1–44, 1986.

Tyburczy, J. and Waff, H., Electrical conductivity of molten basalt and andesite to 25 kilobars pressure: Geophysical significance and implications for charge transport and melt structure, *J. Geophys. Res.*, *88*(B3), 2413–2430, 1983.

Ukstins, I., Renne, P., Wolfenden, E., Baker, J., Ayalew, D., and Menzies, M., Matching conjugate volcanic rifted margins: 40ar/39ar chrono-stratigraphy of pre-and syn-rift bimodal flood volcanism in Ethiopia and Yemen, *Earth Planet. Sci. Lett.*, *198*(3-4), 289–306, 2002.

Vigny, C., de Chabalier, J., Ruegg, J., Huchon, P., Feigl, K., Cattin, R., Asfaw, L., and Kanbari, K., Twenty-five years of geodetic measurements along the Tadjoura–Asal rift system, Djibouti, East Africa, *J. geophys. Res*, *112*, B06410, 2007.

Waff, H., Theoretical considerations of electrical conductivity in a partially molten mantle and implications for geothermometry, *J. Geophys. Res.*, *79*(26), 4003–4010, 1974.

Wannamaker, P., Anisotropy versus heterogeneity in continental solid earth electromagnetic studies: fundamental response characteristics and implications for physicochemical state, *Surv. Geophys.*, *26*(6), 733–765, 2005.

Weaver, J., *Mathematical methods for geo-electromagnetic induction*, Research studies press, 1994.

Whaler, K. and Hautot, S., The electrical resistivity structure of the crust beneath the northern Main Ethiopian Rift, *Geol. Soc. Spec. Publ.*, *259*, 293, 2006.

White, R., Magmatism during and after continental break-up, *Geol. Soc. Spec. Publ.*, *68*(1), 1–16, 1992.

White, R. and McKenzie, D., Magmatism at rift zones: the generation of volcanic continental margins and flood basalts, *J. Geophys. Res.*, *94*(B6), 7685–7729, 1989.

Wolfenden, E., Ebinger, C., Yirgu, G., Renne, P., and Kelley, S., Evolution of a volcanic rifted margin: Southern Red Sea, Ethiopia, *Geol. Soc. Am. Bull.*, *117*(7-8), 846, 2005.

Wright, T., Ebinger, C., Biggs, J., Ayele, A., Yirgu, G., Keir, D., and Stork, A., Magma-maintained rift segmentation at continental rupture in the 2005 Afar dyking episode, *Nature*, *442*(7100), 291–294, 2006.

Wright, T., Sigmundsson, F., Pagli, C., Belachew, M., Hamling, I., Brandsdóttir, B., Keir, D., Pedersen, R., Ayele, A., Ebinger, C., et al., Geophysical constraints on the dynamics of spreading centres from rifting episodes on land, *Nature Geosci.*, *5*(4), 242–250, 2012.

Wu, X., Ferguson, I., and Jones, A., Magnetotelluric response and geoelectric structure of the Great Slave Lake shear zone, *Earth Planet. Sci. Lett.*, *196*(1), 35–50, 2002.

Zhao, D., Seismic structure and origin of hotspots and mantle plumes, *Earth Planet. Sci. Lett.*, *192*(3), 251–265, 2001.